Coupling solidification model with CALPHAD data for the prediction of macrosegregation and solidification structures

THÈSE

présentée et soutenue publiquement le 5 mai 2022

pour l'obtention du titre de

Docteur de l'Université de Lorraine

(mention Science et ingéniérie des matériaux et métallurgie)

par

Savya SACHI

Composition du jury

Président :	Sabine DENIS	Professeur, Université de Lorraine
Rapporteurs :	Menghuai WU	Chair of Simulation and Modelling of Metallurgical Processes, Montanuniversität Leoben
	Benoit GOYEAU	Professeur, Université de Paris - Saclay
Examinatrices :	Olga BUDENKOVA	Chargé de recherche CNRS, , Institut Polytechnique de Grenoble-PHELMA - SIMaP
	Marie BEDEL	Maître de conférences, Arts et Métiers ParisTech - Laboratoire MSMP
Invité :	Laurent CARROZ	Ingénieur R&D, ArcelorMittal - Industeel, Le Creusot
Encadrant :	Charles-André GANDIN	Directeur de recherche CNRS, CEMEF
Directeur de thèse :	Hervé COMBEAU	Professeur, Université de Lorraine
Co-directeurs de thèse :	Miha ZALOŽNIK	Chargé de recherche CNRS, Institut Jean Lamour

"Don't ever, for any reason, do anything, to anyone, for any reason, ever, no matter what, no matter where, or who, or who you are with, or where you are going, or where you've been, ever, for any reason whatsoever..." - **Michael Scott**

Résumé étendu

Introduction

Le moulage est l'un des premiers procédés industriels de l'histoire qui a contribué de manière significative à la croissance et au développement de l'humanité. La plupart des dispositifs mécaniques de tous les jours sont constitués de composants métalliques qui sont fabriqués par un procédé de moulage. Dans ce type de procédé, le métal en fusion est versé dans la cavité d'un moule, où il est refroidi et ensuite extrait du moule. Un phénomène fondamental au cours du procédé de coulée est la solidification, c'est-à-dire la transformation de la matière de la phase liquide à la phase solide. Les espèces chimiques, en général, ont une solubilité plus faible dans la phase liquide que dans la phase solide. Ainsi, à mesure que la solidification progresse, les espèces chimiques sont rejetés par le solide et diffusent dans les phases solide et liquide. Ce phénomène qui se développe à une petite échelle, typiquement l'échelle des dendrites, est appelé microségrégation. La ségrégation à l'échelle des grandes pièces industrielles est appelée macroségrégation. La macroségrégation peut entraîner une variation du chemin de solidification qui se traduit par une variation de la distribution finale des phases formées suivant le point où l'on se place dans la pièce. Les conditions locales de solidification affectent également les structures de solidification. Ainsi, il existe une corrélation très forte entre les structures de solidification et les macroségrégations d'un produit, comme illustré sur la figure 1 dans le cas d'un lingot d'acier de 65 tonnes. Les propriétés finales d'un produit coulé sont le résultat de l'interaction complexe entre les ségrégations (micro, macro) et les structures de solidification. Par conséquent, des produits élaborés à partir d'un même alliage peuvent avoir des structures finales et des performances fonctionnelles distinctes s'ils sont solidifiés dans des conditions différentes.
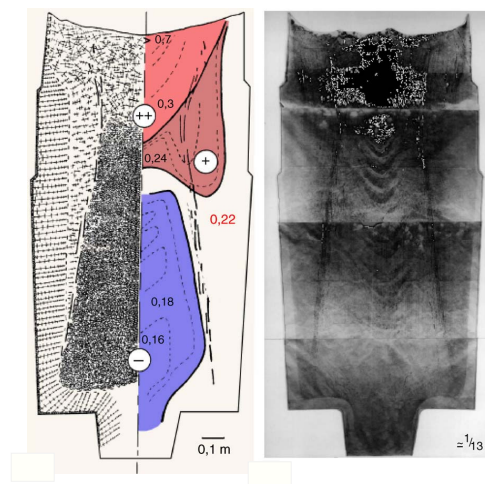

Fig.1 - Schéma de gauche : structures de solidification et carte de composition moyenne en carbone d'un lingot de 65t coulé par Industeel Mittal ; empreinte Baumann révélant les hétérogénéités de composition observées sur le même lingot [1]

Outre la macroségrégation, les défauts rencontrés lors d'une coulée industrielle sont les porosités, les criques, les canaux de ségrégation, etc. Pour les applications critiques où les exigences en matière de contrôle de la qualité sont très strictes, un petit nombre de ces défauts peut rendre une pièce inutilisable, après quoi le métal doit être refondu ou mis au rebut. Ces deux options entraînent des pertes substantielles pour l'industrie. L'analyse post-mortem d'une pièce ne fournit que des informations sur l'état final au mieux en fin de solidifica-

tion et ne fournit qu'une quantité limitée d'informations sur les différents phénomènes qui se sont déroulés pendant l'étape de solidification. Quant aux observations in-situ, elles sont associées à une petite taille des échantillons et à des régimes de convection limités. Ainsi, les résultats des observations in-situ ne peuvent pas être transposés aux procédés de solidification tels que les lingots d'acier. C'est pourquoi, la modélisation et la simulation numérique sont essentiels pour comprendre les différents phénomènes pertinents et responsables de la structure finale de solidification et des macroségrégations pour des pièces massives. Une fois mis au point ces outils peuvent contribuer à une amélioration de la qualité d'un produit.

Modélisation

L'état de l'art

Le code de calcul SOLID® est un modèle de solidification applicable à l'échelle d'un procédé comme la coulée de lingots d'acier. Il est développé à l'Institut Jean Lamour (IJL), Nancy, France. Ce modèle contient deux parties:

— un modèle de transport macroscopique (à l'échelle du produit) qui tient compte de la conservation de la quantité de mouvement, de la masse, de la chaleur, de la masse du soluté et des populations de grains

— un modèle de germination/ croissance des structures de solidification à l'échelle microscopique
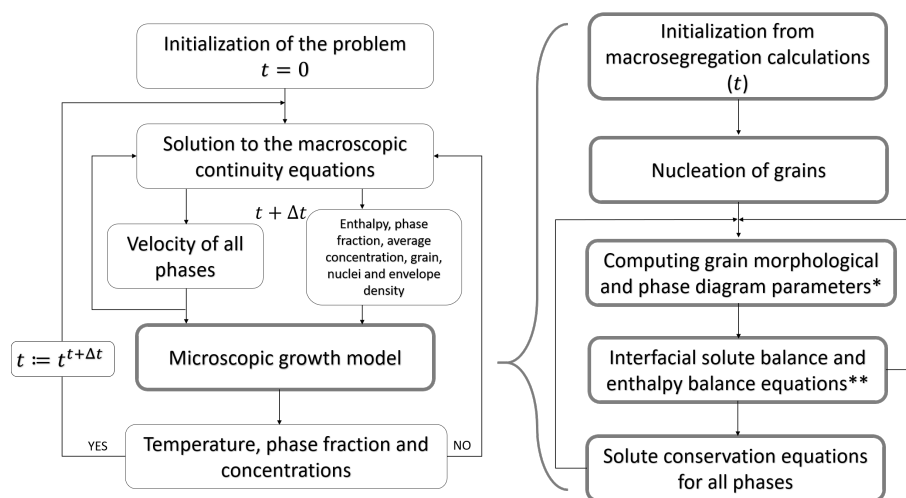

Fig.2 - Schéma du principe de couplage du modèle de croissance microscopique avec les équations de conservation macroscopiques

La Fig. 2 montre le cadre général de couplage du modèle de germination/croissance microscopique avec les équations de conservation macroscopiques. Nous supposons que le pas de temps utilisé au cours de la modélisation est Δt. En utilisant les informations au temps t, ous calculons les variables dans le bloc macro : vitesse moyenne des phases liquide et solide, pression moyenne (supposée égale dans les phases liquide et solide), enthalpie moyenne et concentrations moyennes des solutés au temps $t + \Delta t$. Les variations locales ainsi obtenues : enthalpie et concentrations moyennes des solutés sont utilisées pour en déduire dans le bloc micro de germination croissance, les grandeurs : température, fraction de phase et concentration moyenne en éléments d'alliage dans les phases solide et liquide.

Dans le bloc macro, le mouvement de la phase liquide et des grains équiaxes est modélisé en prenant en compte : les forces d'inertie, les forces aux interfaces solide-liquide et la poussée d'Archimède. Ainsi, le mouvement de ces phases est principalement induit par la variation de densité du liquide (convection thermosolutale) et la différence de densité entre le liquide et le solide. Les grains colonnaires sont supposés immobiles. Les fragments des grains colonnaires sont la source de nouveaux grains équiaxes. Ils sont introduits en avant du front colonnaire à l'aide d'une densité de flux de fragments prédéfinie activée lorsque le gradient thermique local passe en dessous d'une valeur critique. Une fois apparus à partir de ces fragments, les grains équiaxes se développent tout d'abord en tant qu'une phase solide dispersée et ils se déplacent librement. Un bilan de population des grains permet de déterminer l'évolution locale de la densité volumique des grains. Deux types de grains sont considérés : colonnaire et équiaxe. La croissance des grains quel que soit leur type est décrite par la croissance d'une enveloppe qui délimite une frontière entre le grain et le liquide à l'extérieur du grain. A l'intérieur de l'enveloppe, la solidification est calculée en prenant en compte la diffusion des espèces chimiques et l'équilibre thermodynamique. Lorsque la fraction d'enveloppe des grains équiaxes est supérieure à une fraction limite d'empilement, les grains sont bloqués et le régime d'écoulement passe d'un écoulement diphasique avec une phase dispersée à un écoulement en milieu poreux. La transition d'une structure colonnaire allongée à la périphérie des pièces moulées à une structure équiaxe plus fine au centre est appelée "transition colonnaire à équiaxe" (TCE). Deux phénomènes responsables de la TCE sont considérés : "le blocage mécanique" et "le blocage solutal". Le "blocage mécanique" se produit lorsque la fraction de grains équiaxes dans la zone de mélange atteint une valeur critique qui peut varier de 0,2 à 1. Le "blocage solutal" se produit lorsque la surfusion chimique diminue suffisamment pour empêcher la croissance du front colonnaire, le bloquant effectivement. La transition "équiaxe-colonne" (TEC) qui est observée au sommet des lingots d'acier industriels, est également modélisée. Les phénomènes principaux pris en compte dans le modèle sont représentés sur la Fig. 3.
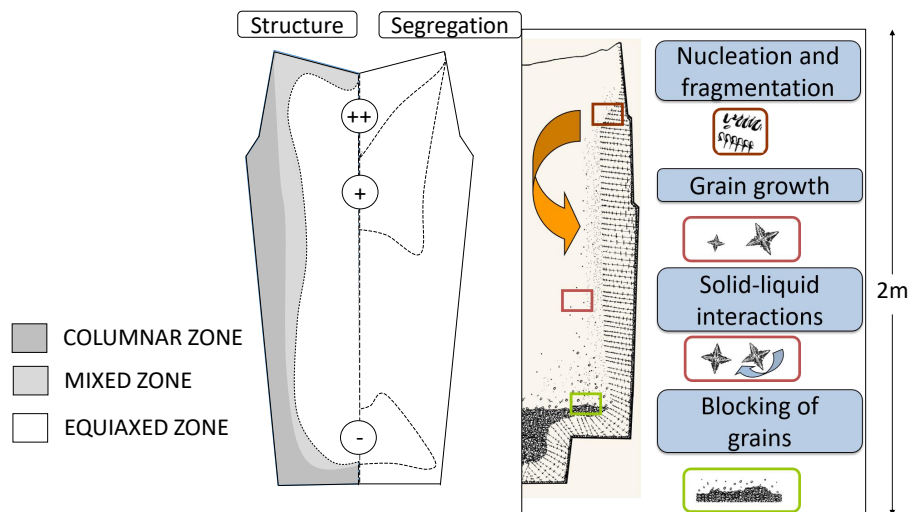
Fig.3 - Phénomènes principaux pris en compte dans le code de calcul SOLID®

Les disparités d'échelle spatiales et temporelles des phénomènes de transfert de chaleur, de masse et de quantité de mouvement, ainsi que les diverses interactions entre les phases qui se produisent en raison de la morphologie complexe des interfaces obligent à adopter une méthode de prise de moyenne à une échelle intermédiaire afin d'obtenir des équations de transport moyennées sur un volume élémentaire représentatif. Pour faire face aux défis posés par la modélisation de la solidification, nous utilisons la méthode de la prise de

moyenne volumique. Les équations de conservation microscopiques sont moyennées sur un volume moyen qui est grand par rapport à l'échelle microscopique et petit par rapport à l'échelle macroscopique. Grâce à cette approche, nous pouvons modéliser le système à l'échelle macroscopique et incorporer les effets des phénomènes microscopiques par le biais de divers termes sources (termes de transfert interphase) dans les équations moyennées. L'application de la méthode de prise de moyenne volumique est illustrée ci-dessous pour l'équation de conservation de la masse du soluté dans une phase.

— Équations de conservation de la masse du soluté à l'échelle microscopique:

— dans la phase liquide:

$$\frac{\partial \left(\rho_l c_l\right)}{\partial t} + \nabla \cdot \left(\rho_l c_l \vec{v_l}\right) = \nabla \cdot \left(\rho_l D_l \nabla c_l\right)$$

— dans la phase solide:

$$\frac{\partial \left(\rho_s c_s\right)}{\partial t} + \nabla \cdot \left(\rho_s c_s \vec{v_s}\right) = \nabla \cdot \left(\rho_s D_s \nabla c_s\right)$$

— Équations de conservation de la masse du soluté moyennées (la diffusion à l'échelle macroscopique et la germination hétérogène sont négligés dans ces équations)

— dans la phase liquide:

$$\frac{\partial}{\partial t} \left(g_l \rho \left\langle c_l \right\rangle^l\right) + \nabla \cdot \left(g_l \rho \left\langle c_l \right\rangle^l \left\langle \vec{v}_l \right\rangle^l\right) = -\Gamma_s c_l^\star + \frac{\rho S_v^s D_l}{\delta_l} \left(c_l^\star - \left\langle c_l \right\rangle^l\right)$$

— dans la phase solide:

$$\frac{\partial}{\partial t} \left(g_s \rho \left\langle c_s \right\rangle^l\right) + \nabla \cdot \left(g_s \rho \left\langle c_s \right\rangle^l \left\langle \vec{v}_s \right\rangle^s\right) = \Gamma_s c_s^\star + \frac{\rho S_v^s D_s}{\delta_s} \left(c_s^\star - \left\langle c_s \right\rangle^l\right)$$

Dans les deux bilans moyennés ci-dessus, les termes en rouge correspondent aux termes de transfert entre les phases liquide et solide.

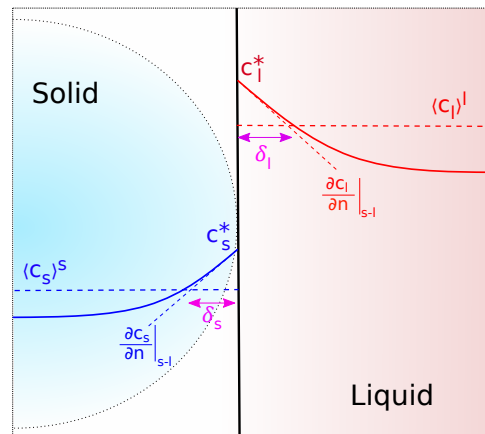Fig. 4 - Profils de composition chimique dans les phases solide et liquide dans la région de l'interface entre ces phases illustrant les transferts de matière dans le cas du modèle de croissance à deux phases

Un modèle de croissance de grain à deux phases solide (s) et liquide (l) a tout d'abord été abordé dans ce travail. Les termes de transferts entre phases correspondant à ce modèle sont illustrés sur la figure 4. Le

changement de phase pendant la solidification primaire est principalement contrôlé par le transfert d'espèces chimiques à l'interface solide/liquide ainsi que par l'extraction de chaleur du système. Les équations suivantes correspondent aux équations principales du modèle de croissance:

$$c_1^{*i}\big(k^i - 1\big)\frac{\Gamma_{s/l}}{\rho} + c_1^{*i}\Big(\frac{S_v^s D_1^i}{\delta_1^i} + k^i \frac{S_v^s D_s^i}{\delta_s^i}\Big) = \langle c_1^i \rangle^1 \frac{S_v^s D_1^i}{\delta_1^i} + \langle c_s^i \rangle^s \frac{S_v^s D_s^i}{\delta_s^i}$$

$$\Delta \langle h \rangle = C_p \Delta T + L_f \Delta g_l$$

$$T = T_f + \sum_i m_1^i c_1^{*i} \qquad k^i = \frac{c_s^{*i}}{c_1^{*i}}$$

La première équation correspond au calcul de l'enthalpie moyenne dans le volume de prise de moyenne en supposant les chaleurs spécifiques des phase constantes et égales. La deuxième équation est un bilan de masse de soluté aux interfaces liquide/solide. Enfin, la troisième relation correspond à l'expression de l'équilibre thermodynamique local en supposant une pente de liquidus constante pour toutes les espèces chimiques. Les paramètres surlignés en bleu sont les paramètres du diagramme de phase, ceux en vert sont les paramètres obtenus à partir de relations de fermeture. Les grandeurs surlignées en rouge sont les variables pour lesquelles les équations sont résolues. Dans l'état initial du modèle au début de la thèse, le diagramme de phase est supposé être linéaire (comme le montre la Fig. 5), de sorte que les paramètres du diagramme de phase sont constants et que les enthalpies des phases ne dépendent que de la température. Une modélisation précise de la macroségrégation nécessite de prendre en compte le diagramme de phase "réel" et de tenir compte de l'effet de la composition sur les enthalpies de phase. C'est la question qui a été posée dans ce travail : quel est l'impact des simplifications faites sur le diagramme de phase et sur le calcul des enthalpies sur la prédiction des macroségrégations.
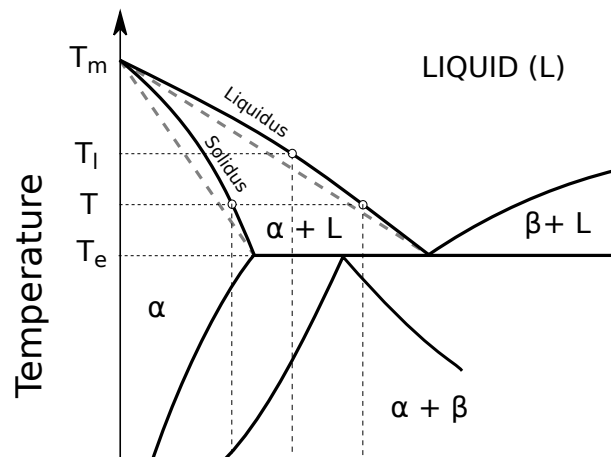

Fig. 5 - Diagramme d'équilibre thermodynamique réel et diagramme d'équilibre simplifié en linéarisant les courbes de liquidus et de solidus

Développements effectués dans ce travail

   – **Couplage avec les données du diagramme de phase**

   Pour tenir compte des paramètres variables du diagramme de phase, le modèle de croissance micro

de croissance de grain a été modifié. Alors que les bilans de masse de soluté aux interfaces liquide solide n'ont pas été modifiés, le calcul de l'enthalpie moyenne et les équations relatives à l'équilibre thermodynamique ont été modifiés. Ces modifications sont les suivantes :

$$\Delta\langle h\rangle = A + B + C$$

$$A = L_f \Delta g_{\mathrm{l}}$$

$$B = \sum_i \left[g_{\mathrm{l}}\Big(\frac{\partial\langle h_{\mathrm{l}}\rangle^{\mathrm{l}}}{\partial\langle c_{\mathrm{l}}^i\rangle^{\mathrm{l}}}\Big)\Delta\langle c_{\mathrm{l}}^i\rangle^{\mathrm{l}} + \Big(1 - g_{\mathrm{l}}\Big)\Big(\frac{\partial\langle h_{\mathrm{s}}\rangle^{\mathrm{s}}}{\partial\langle c_s^i\rangle^{\mathrm{s}}}\Big)\Delta\langle c_{\mathrm{s}}^i\rangle^{\mathrm{s}} \right]$$

$$C = \left[g_{\mathrm{l}}C_{p,l} + \Big(1 - g_{\mathrm{s}}\Big)C_{p,s} \right]\Delta T$$

Les paramètres du diagramme de phase ainsi que les enthalpies des phases sont obtenus par calcul à l'aide du logiciel Thermo-Calc®

La prise en compte de paramètres thermodynamiques variables pour la simulation de la solidification à grande échelle nécessite un accès efficace aux données de Thermo-Calc®. Les approches actuelles pour coupler les simulations de solidification avec Thermo-Calc® sont les suivantes:

- Calcul direct avec Thermo-Calc® par le biais de l'interface TQ-Interface®
- Approche par tabulation couplée à une interpolation multilinéaire (données tabulées produites avec TQ-Interface®)

Tab. 1 - Liste des différentes fonctions de régression générées et du type de fichier de données

Inputs	Outputs	Description	File type
$T, \langle c_\phi^1\rangle^\phi ... \langle c_\phi^i\rangle^\phi$	$\langle h_\phi\rangle^\phi$	Enthalpy of phase	Phase data file
$T, \langle c_\phi^1\rangle^\phi ... \langle c_\phi^i\rangle^\phi$	$\left(\frac{\partial\langle h_\phi\rangle^\phi}{\partial T}\right)_{\langle c_\phi^i\rangle^\phi}$	Specific heat capacity of phase	Phase data file
$T, \langle c_\phi^1\rangle^\phi ... \langle c_\phi^i\rangle^\phi$	$\left(\frac{\partial\langle h_\phi\rangle^\phi}{\partial\langle c_\phi^i\rangle}\right)_{T, \langle c_\phi^{j\neq i}\rangle^\phi}$	Composition effect on phase enthalpy	Phase data file
$\langle h_{\mathrm{l}}\rangle^{\mathrm{l}}, \langle c_{\mathrm{l}}^1\rangle^{\mathrm{l}} ... \langle c_{\mathrm{l}}^i\rangle^{\mathrm{l}}$	T_{l}	Temperature of liquid phase	Phase data file
$\langle h_{\mathrm{s}}\rangle^{\mathrm{s}}, \langle c_{\mathrm{s}}^1\rangle^{\mathrm{s}} ... \langle c_{\mathrm{s}}^i\rangle^{\mathrm{s}}$	T_{s}	Temperature of solid phase	Phase data file
$c_{\mathrm{l}}^{*1} ... c_{\mathrm{l}}^{*i}$	T	Interfacial temperature	Interface equlib. data file
$c_{\mathrm{l}}^{*1} ... c_{\mathrm{l}}^{*i}$	$k_p^1 ... k_p^i$	Partition coefficients	Interface equlib. data file
$c_{\mathrm{l}}^{*1} ... c_{\mathrm{l}}^{*i}$	$m_{\mathrm{l}}^1 ... m_{\mathrm{l}}^i$	Liquidus slope	Interface equlib. data file

Ces deux approches sont coûteuses en termes de temps de calcul. C'est pourquoi, nous avons proposé de générer des fonctions de régression pour les différentes fonctions thermodynamiques (listées dans le Tab. 1) en utilisant des données tabulées générées par un logiciel de type CALPHAD comme Thermo-Calc®. Les "données de phase" font référence aux valeurs thermodynamiques du diagramme

de phase qui sont tabulées pour l'ensemble de l'espace température-composition, alors que les "données d'équilibre interfacial" font référence aux valeurs tabulées de compositions d'équilibre thermodynamique des phases.
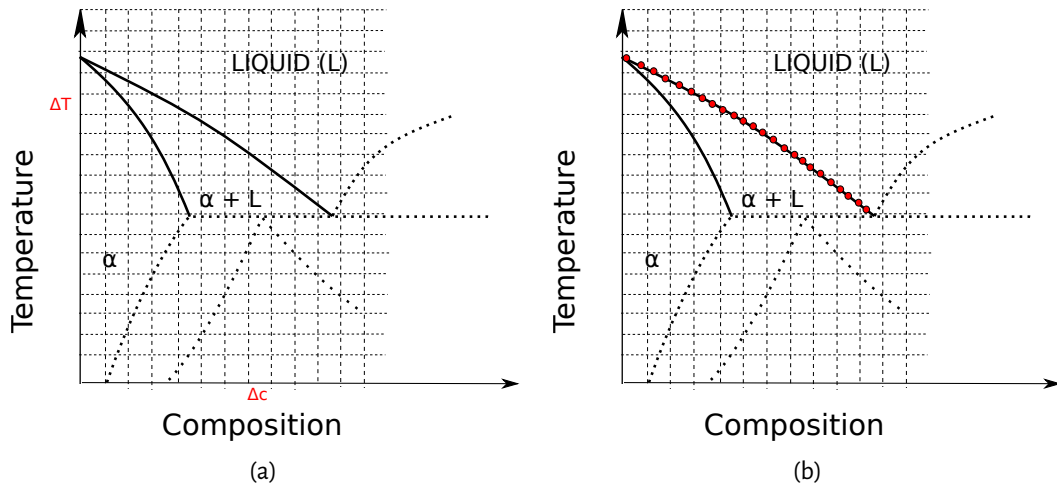

Fig. 6 - Illustration du domaine (composition, température) dans lequel les données thermodynamiques sont tabulées. Les grilles correspondent aux points où ces données sont calculées

Les fonctions de régression sont générées à l'aide d'un réseau neuronal artificiel (ANN) - perceptron multicouche (MLP). Les MLP sont une classe de réseaux neuronaux à action directe. Les MLP sont composés de plusieurs neurones (ou nœuds) répartis dans une couche d'entrée, une ou plusieurs couches cachées et une ou plusieurs couches de sortie.
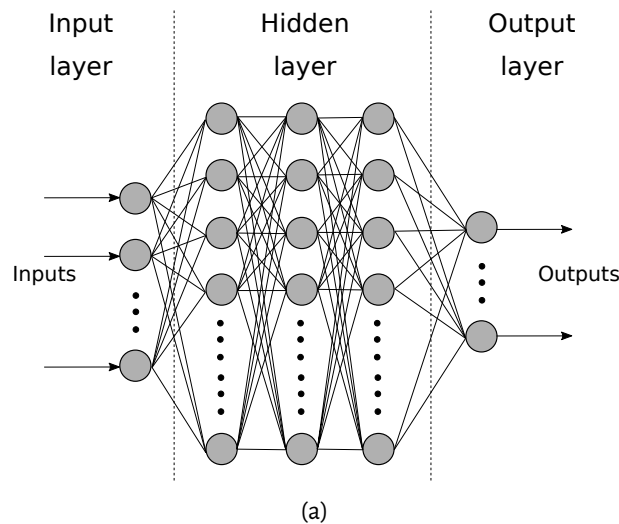

Fig. 7 - Représentation schématique d'un réseau neuronal à perceptron multicouche (MLP)

Pour un MLP-ANN à une seule couche cachée, la formulation mathématique est donnée par:

$$y_k(\mathbf{x}, \mathbf{w}) = \sum_{j=0}^{m_1} w_{kj}^{(2)} h \left(\sum_{i=1}^{n} w_{ji}^{(1)} x_i + w_{j0}^{(1)} \right) + w_{k0}^{(2)}$$

Où l'ensemble de toutes les matrices de poids et de biais ont été regroupées dans le vecteur w. Ainsi,

le réseau neuronal est simplement une fonction non linéaire d'un ensemble de variables d'entrée $\{x_i\}$ à un ensemble de variables de sortie $\{y_k\}$ contrôlé par un vecteur $\{w\}$ de paramètres ajustables. La fonction h fait référence à la fonction d'activation, qui dans le cadre de notre travail est la fonction tanh. La précision des fonctions de régression est calculée à l'aide de la mesure de l'erreur quadratique moyenne (EQM). Pour le système Fe-C-Cr, les fonctions de régression de la pente du liquidus ont été validées en traçant le rapport entre la valeur prédite et la valeur réelle dans le domaine de composition souhaité, comme le montre la Fig. 8. Le modèle ANN-MLP a été couplé avec succès au modèle de croissance des grains pour prédire les résultats de solidification de Scheil obtenus à l'aide de Thermo-Calc®.
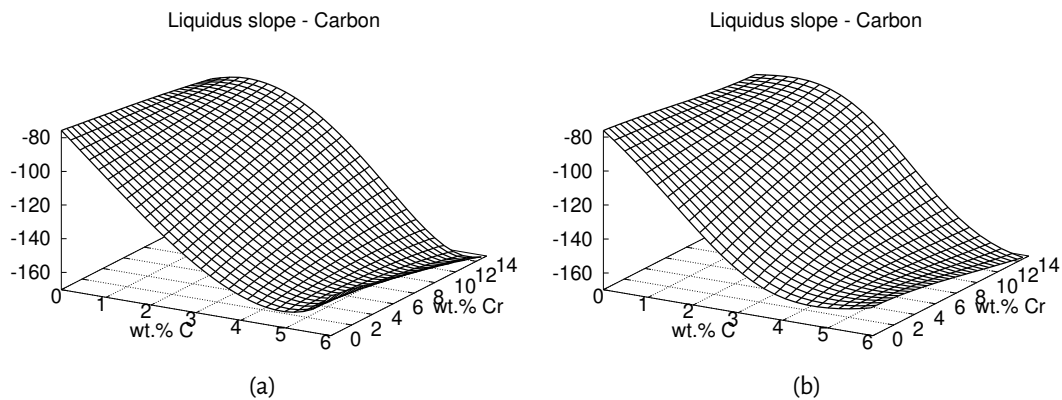
Fig. 8 - Rapport de la pente de liquidus données par la régression avec le modèle AMN-MLP à la pente de liquidus calculée par le logiciel Thermo-Calc® à gauche pour le carbone, à droite pour le chrome
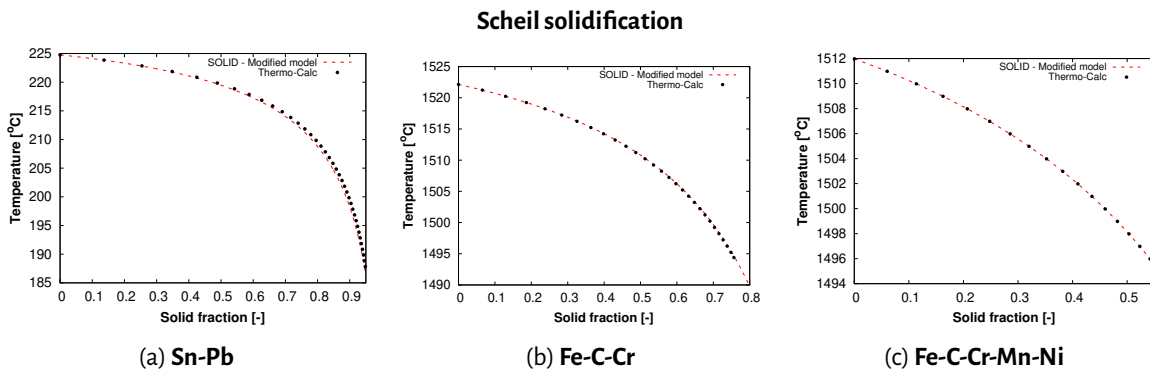
Fig. 9 - Chemins de solidification pour trois alliages (binaire, ternaire, quinaire) calculées par le logiciel Thermo-Calc® (points) et à partir des données issues de la régression avec le modèle AMN-MLP (courbe pointillées rouges)

— **Modification de la longueur de diffusion du liquide** es modèles de croissance de grains reposent sur une représentation aussi fidèle que possible des grandeurs géométriques des structures de solidification telle que la morphologie des grains et du profil de soluté dans les phases. L'estimation de la morphologie des grains pour les grains globulaires équiaxes est simple. Cependant, le profil de solutés dans les phases, qui détermine le flux de soluté à l'interface s/l et finalement la vitesse de l'interface s/l, nécessite le calcul des gradients de composition des solutés à l'interface s/l. Ces

x

gradients de composition G_c ont calculés à l'aide de l'équation suivante:

$$G_c = \frac{c_1^* - \langle c_1 \rangle^1}{\delta_1}$$

Ces gradients de composition sont estimés en définissant une longueur de diffusion caractéristique (δ_1). Une représentation précise du profil de soluté dans la phase liquide permet de décrire la cinétique de la solidification en tenant compte de la compétition entre la germination et la croissance des grains. Cette compétition est critique car elle détermine : (i) le nombre de grains qui germent (ii) la surfusion atteinte pendant la solidification. Les transferts à l'échelle macroscopique dépendent fortement de ces paramètres et ainsi la macroségrégation. Le déplacement de l'interface s/l et de la convection rendent difficile une description précise de la longueur de diffusion δ_1. La plupart des modèles présents dans la littérature ne prennent en compte ces phénomènes que de façon incomplète, en particulier la convection de la phase liquide, même si la croissance des grains est significativement affectée par celle-ci.

Tab. 2 - Synthèse des modèles de la littérature pour le calcul de la longueur de diffusion dans la phase liquide lorsque la convection est négligée

| Reference	Expression for δ_1
Fixed interface models	
Ni & Beckermann [Ni1991] Wu & Ludwig [Wu2009]	R^*
Wu *et al.* [Wu2013]	$R^*\left(1 - \frac{R^*}{R_f}\right)$
Mobile interface models	
Wu & Ludwig [Wu2019]	$\mathbf{min}(\delta_v, R^*, R_f - R^*)$
Wang & Beckermann [Wang1993]	$\frac{R_f}{Pe}\left\{1 - 3\left(\frac{R_f}{R^*}\right)^3 \exp\left(-Pe\frac{R^*}{R_f}\right)\int_{R^*/R_f}^{1}\left[x^2\exp\left(\frac{Pe(R^*/R_f)^2}{x}\right)\right]dx\right\}$
Martorano *et al.* [Martorano2003]	$\frac{R^{*2}}{(R_f^3 - R^{*3})}\left\{\exp\left(-\frac{R_f - R^*}{\delta_v}\right)\left(\delta_v^2 + R_f\delta_v - R_f^2\right) - \left(\delta_v^2 + R^*\delta_v - \frac{R_f^3}{R}\right) + \frac{R_f^3}{\delta_v}\exp\left(\frac{R^*}{\delta_v}\right)\left[E_1\left(\frac{R_f}{\delta_v}\right) - E_1\left(\frac{R^*}{\delta_v}\right)\right]\right\}$
Tveito *et al.* [Tveito2012,Bedel2014]	$\left\{\frac{1}{R^*} + \frac{\frac{R_f^2 - R^{*2}}{2\delta_v}}{\frac{R_f^2 - R^{*2}}{2} - \delta_v\left(R^* + \delta_v - (R_f + \delta_v)\exp\left(-\frac{R_f - R^*}{\delta_v}\right)\right)}\right\}^{-1}$
Guillemot & Gandin [Guillemot2015]	Post computation from an analytical solution for liquid solute profile
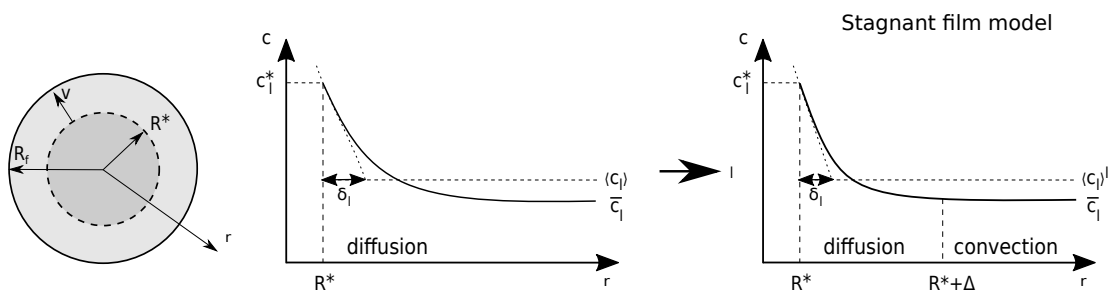
Fig. 10 - Schémas illustrant les différentes grandeurs introduites pour le développement du modèle basé sur un film stagnant

Divers modèles pour la longueur de diffusion du liquide ont été proposés dans la littérature. Pour le cas de la diffusion pure, les modèles ont été listés dans le Tab. 2. Les "modèles d'interface fixe" ne tiennent pas compte du mouvement de l'interface s/l. Les modèles surlignés en rouge sont des

solutions analytiques de l'équation:

$$v\frac{\partial c_{\mathrm{l}}}{\partial r} = \frac{D_{\mathrm{l}}}{r^2}\frac{\partial}{\partial r}\left[r^2\frac{\partial c_{\mathrm{l}}}{\partial r}\right] \text{ with } \begin{cases} c_{\mathrm{l}}(R^*) = c_{\mathrm{l}}^* \\[2mm] \langle c_{\mathrm{l}}\rangle^{\mathrm{l}} = \frac{1}{\frac{4}{3}\pi\left(R_{\mathrm{f}}^3 - R^{*3}\right)}\int_{R^*}^{R_{\mathrm{f}}} c_{\mathrm{l}}(r)4\pi r^2\,\mathrm{d}r \end{cases}$$

La différence entre les différentes expressions provient de la différence des hypothèses utilisées pour résoudre l'équation de diffusion écrite ci-dessus. [Martorano2003] correspond à la solution la plus précise et utilisable dans un code de calcul de macroségrégation. Cependant, ce modèle ne prend pas en compte l'effet de la convection. Ce modèle a été étendu pour tenir compte de la convection de la phase liquide en employant une approche de film stagnant. La Fig. 11 montre une représentation schématique du profil du soluté dans la phase liquide extragranulaire. Dans l'approche du film stagnant, le liquide est séparé en deux régions. Le transfert de soluté dans la région du film stagnant proche de l'interface s/l (r=R^*) est supposé être contrôlé par la diffusion uniquement. Cette région a une épaisseur Δ. La convection domine au-delà de cette zone où le liquide est alors supposé être homogène en composition. Il est ainsi possible de déterminer une expression de δ_{l} qui tient compte du mouvement de l'interface s/l, de la présence d'autres grains et de la convection:

$$\delta_{\mathrm{l}} = \frac{R^{*2}\exp\left(\frac{R^*}{\delta_v}\right)\mathbf{C}}{\delta_v} \qquad \text{où}$$

$$\mathbf{C} = \left(\frac{\exp\left(-\frac{R^*}{\delta_v}\right)}{\left(\frac{R^*}{\delta_v}\right)} - \mathrm{E}_1\left(\frac{R^*}{\delta_v}\right)\right) - \frac{\left(R_{\mathrm{f}}^3 - R_{\mathrm{c}}^3\right)}{\left(R_{\mathrm{f}}^3 - R^{*3}\right)}\left[\left(\frac{\exp\left(-\frac{R_{\mathrm{c}}}{\delta_v}\right)}{\left(\frac{R_{\mathrm{c}}}{\delta_v}\right)} - \mathrm{E}_1\left(\frac{R_{\mathrm{c}}}{\delta_v}\right)\right)\right] - \frac{\delta_v^3}{\left(R_{\mathrm{f}}^3 - R^{*3}\right)}$$

$$\left[\left[\exp\left(-\frac{R_{\mathrm{c}}}{\delta_v}\right)\left(\left(\frac{R_{\mathrm{c}}}{\delta_v}\right)^2 - \frac{R_{\mathrm{c}}}{\delta_v} - 1\right) - \left(\frac{R_{\mathrm{c}}}{\delta_v}\right)^3\mathrm{E}_1\left(\frac{R_{\mathrm{c}}}{\delta_v}\right)\right] - \left[\exp\left(-\frac{R^*}{\delta_v}\right)\left(\left(\frac{R^*}{\delta_v}\right)^2 - \frac{R^*}{\delta_v} - 1\right) - \left(\frac{R^*}{\delta_v}\right)^3\mathrm{E}_1\left(\frac{R^*}{\delta_v}\right)\right]\right]$$

En plus du modèle proposé, d'autres modèles de longueur de diffusion liquide qui tiennent compte de la convection sont donnés dans le Tab. 3, où ils ont été regroupés suivant qu'ils prennent en compte ou non le mouvement de l'interface s/l.

Résultats

Les développements présentés dans la partie précédente ont été implémentés dans le code de calcul SOLID®. Deux cas d'application sont présentés dans cette partie:

– Cas de référence 'Hebditch-Hunt'

– Lingot industriel Q550

Cas de référence Hebditch-Hunt

Hebditch et Hunt (H&H) ont réalisés des alliages Sn-Pb et Pb-Sn des expériences de solidification dans un moule à section mince dont les dimensions intérieures sont de 100 mm x 60 mm x 10 mm, et qui est représenté sur la Figure 11. Toutes les faces sont complètement isolées thermiquement, à l'exception de la face gauche par

Tab. 3 - Synthèse des modèles de la littérature pour le calcul de la longueur de diffusion dans la phase liquide lorsque la convection est prise en compte

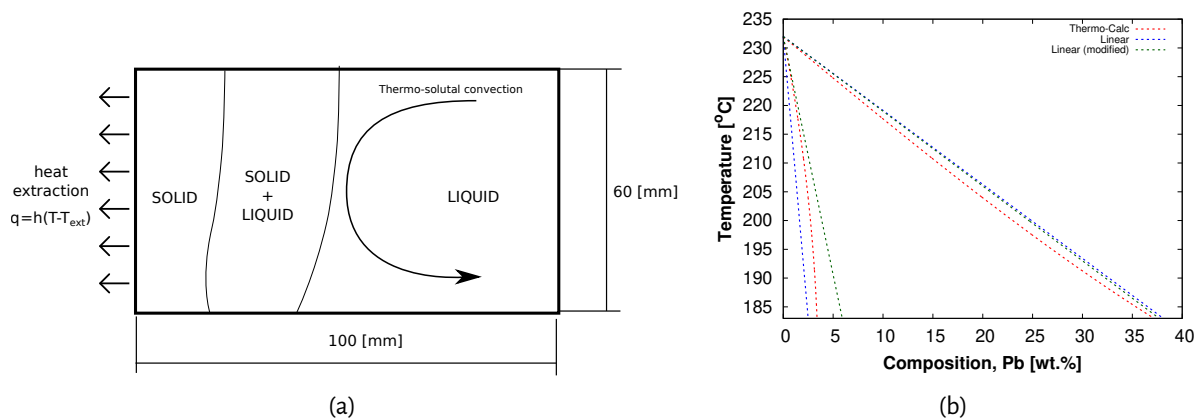| Reference	Expression for δ_l
Fixed interface models	
Ni & Beckermann [Ni1993]	$R^* \left[\frac{1}{1-g_s^{1/3}} + \frac{\mathrm{Sc}^{1/3}\mathrm{Re}^a}{3g_l} \right]^{-1} \quad a = \frac{2\mathrm{Re}^{0.28}+4.65}{3(\mathrm{Re}^{0.28}+4.65)}$
Wang & Beckermann [Wang1996]	$\frac{2R}{2+0.865\left(\frac{C}{g_l}\right)^{1/3}\mathrm{Pe}^{1/3}} \quad C = \frac{2+\frac{4}{3}(g_s)^{5/3}}{2-3g_s^{1/3}+3g_s^{5/3}-2g_s^2}$
Appolaire $et\ al.$ [Appolaire2008]	$\mathbf{min}\left(\delta_v, \frac{2R^*}{\mathrm{Sh}}\right) \; \mathrm{Sh} = 2 + 0.6\mathrm{Sc}^{1/3}\mathrm{Re}^{1/2}$
Wang $et\ al.$(2019) [Wang2019]	$\mathbf{min}\left[R^* \left[\frac{1}{1-(g_s)^{1/3}} + \frac{\mathrm{Sc}^{1/3}\mathrm{Re}^a}{3g_l} \right]^{-1}, \delta_v \right] \; a = \frac{2\mathrm{Re}^{0.28}+4.65}{3(\mathrm{Re}^{0.28}+4.65)}$
Mobile interface models	
Tveito $et\ al.$ [Tveito2012,Bedel2014]	$\delta_v \left[\frac{\delta_v}{R^*} - \frac{f(R^*,\Delta)+g(R_f,R^*,\Delta)}{\delta_v[R^*+\delta_v-(R^*+\Delta+\delta_v)e^{-\Delta/\delta_v}]-f(R^*,\Delta)+(e^{-\Delta/\delta_v}-1)g(R_f,R^*,\Delta)} \right]^{-1}$

Fig. 11 - Partie gauche : schema du domaine dans lequel l'alliage Sn-Pb se solidifie pour le cas référence H&H; partie droite : partie du diagramme d'équilibre Sn-Pb calculé avec le logiciel Thermo-Calc® et par différentes approches simplifiées

laquelle le lingot est refroidi. La distribution de la concentration moyenne à différentes étapes a été mesurée. L'expérience de H&H illustre l'importance de la convection thermo-solutale sur la formation de la macroségrégation. Les structures de solidification ont été caractérisées et des structures colonnaires sont majoritairement présentes sauf dans la zone de fin de solidification. Ainsi, toute ségrégation due à la sédimentation des grains équiaxes peut être négligée et on peut supposer que la macroségrégation est principalement due à la convection de la phase liquide. Des simulations ont été effectuées pour l'alliage Sn-5% en poids de Pb avec le diagramme de phase linéarisé (valeurs standard des données du diagramme de phase), le diagramme de phase réel et un diagramme de phase linéarisé modifié (comme indiqué sur la Fig. 11). Pour l'ensemble de ces simulations, la phase solide a été supposée fixe.

La Fig. 12 montre la carte finale de ségrégation du Pb pour la solidification colonnaire dans le cas de référence H&H. Nous avons montré que les résultats obtenus en tenant de la forme réelle du diagramme d'équilibre sont plus proches des résultats expérimentaux, ce qui souligne l'importance de tenir compte des
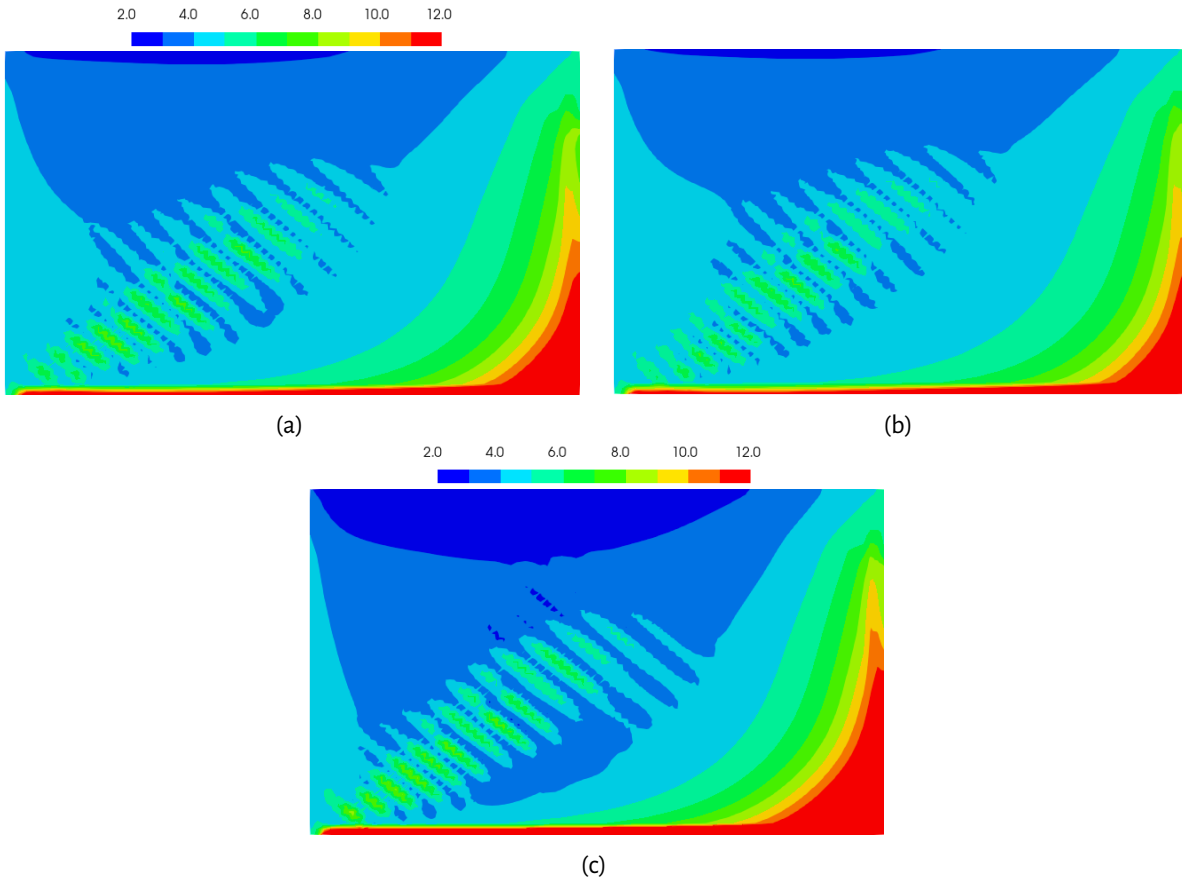
(a)

(b)

(c)

Fig. 12 : Cartes de composition Moyenne locale en fin de solidification pour le cas H&H Sn-5%Pb, a) données thermodynamiques obtenues par régression, b) données thermodynamique constante mais adaptée, c) données thermodynamique constante telles qu'employées dans la littérature
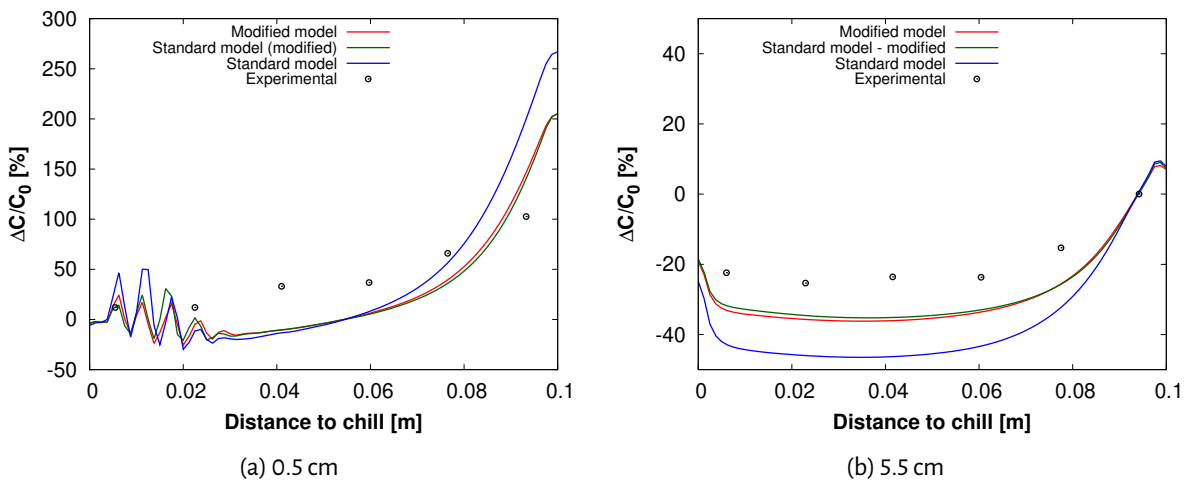

(a) 0.5 cm

(b) 5.5 cm

Fig. 13 - Profils de composition en Pb le long de deux lignes horizontales

paramètres variables du diagramme de phase. Nous avons également montré qu'il était possible d'utiliser des données thermodynamiques constantes mais qu'il fallait les modifier par rapport aux valeurs utilisées dans la littérature pour avoir le meilleur accord possible avec l'expérience. Les profils de composition en Pb le long de deux lignes horizontales présentés sur la Fig. 13 illustrent la qualité de la prédiction des simulations en

fonctions des hypothèses adoptées.

Nous avons montré que la fraction de phase formée çà la température eutectique dépend fortement des données thermodynamiques adoptées. Les fractions de phase formées à la température eutectique sont présentées sur la Fig. 14. Pour les deux simulations où les données thermodynamiques sont prises constantes, c'est le jeu de valeur conduisant aux moins bonnes prédictions de la ségrégation en plomb qui conduisent aux meilleures prédictions de la quantité de phase formée à la température eutectique. Ainsi, on peut conclure que si le résultat de la ségrégation peut être amélioré en modifiant les paramètres du diagramme de phase, la prédiction correcte de la fraction de phase formée à la température eutectique nécessite un couplage avec le diagramme de phase.
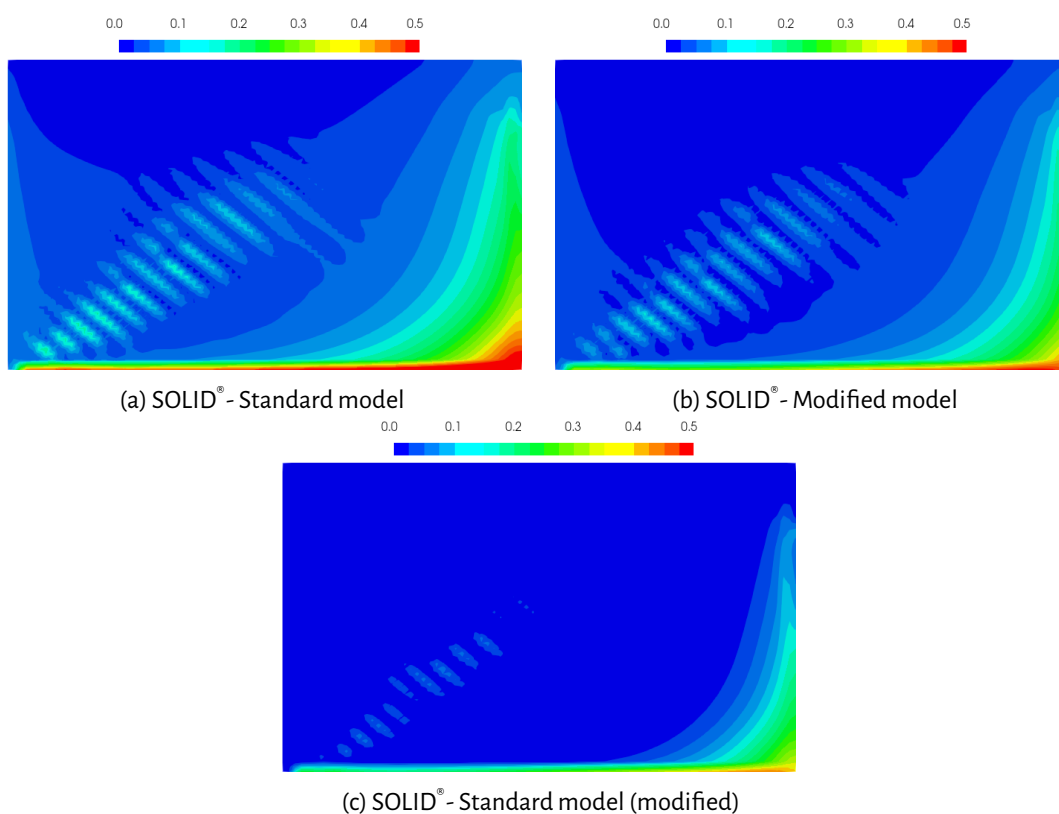

(a) SOLID® - Standard model

(b) SOLID® - Modified model

(c) SOLID® - Standard model (modified)

Fig. 14 - Fraction de phase formées à la température eutectique

Lingot industriel Q550

Des simulations ont été réalisées pour le lingot industriel Q550 pour une nuance acier 18MND5. Dans les simulations présentées, nous avons considéré un alliage ternaire Fe-C-Cr comme souligné en rouge dans le tableau 4. Les autres éléments d'alliage figurant en noir dans ce tableau n'ont pas été pris en compte. Dans le cadre de notre modèle, nous avons considéré une géométrie 2D axisymétrique, comme illustré à la Figure 15. Le maillage utilisé pour la simulation est illustré sur la Figure 15. La taille de maille au centre du lingot est de 1 cm×3 cm.

La Fig. 16 montre l'impact du couplage avec les données CALPHAD. Deux résultats de simulation sont présentés sur cette figure : une première où les données thermodynamiques sont prises constantes et la deuxième où elles sont obtenues par régression avec des données provenant de calculs avec le logiciel Thermo-Calc®. On observe que les cartes de ségrégation du carbone et du chrome obtenues avec les deux simulations
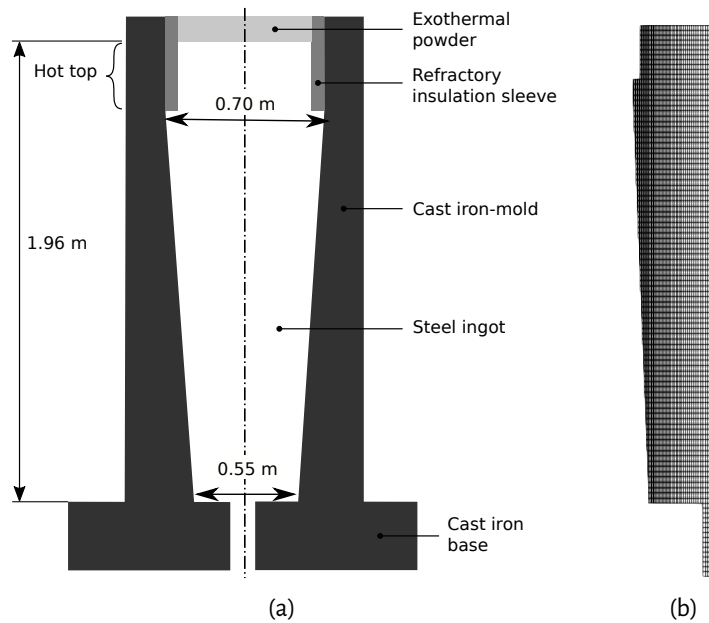
Fig. 15 - a) Schéma de la lingotière du lingot Q550 ; b) maillage du lingot Q550 adopté pour les simulations.

Tab. 4 - Composition en éléments d'alliage de la nuance 18MND5 coulée avec le lingot Q550

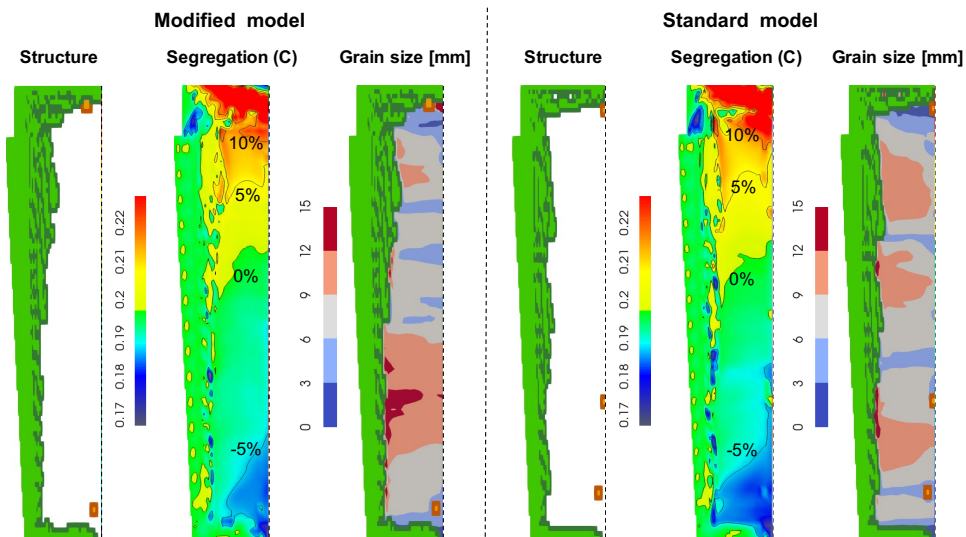| C	Mn	Ni	Cr	Mo
0.197	1.5	0.7	0.18	0.5

Fig. 16 - A gauche : résultat de la simulation avec des données thermodynamiques obtenues par régression avec des données issues de calculs avec le logiciel Thermo-Calc® ; à droite : résultat de la simulation en prenant des données thermodynamiques constantes

sont très similaires, à l'exception d'un cône de ségrégation négatif légèrement plus grand à la base pour le calcul avec régression. La principale différence réside dans la prédiction des structures de solidification. Nous avons montré que ces différences pouvaient être attribuées à la description des enthalpies des phases solide

et liquide. La taille des grains équiaxes et leur morphologie diffèrent et sont une conséquence directe de la différence des conditions de transfert de chaleur et d'écoulement de la phase liquide dans le lingot. Ainsi, les paramètres du diagramme de phase qui affectent les enthalpies de phase sont critiques.
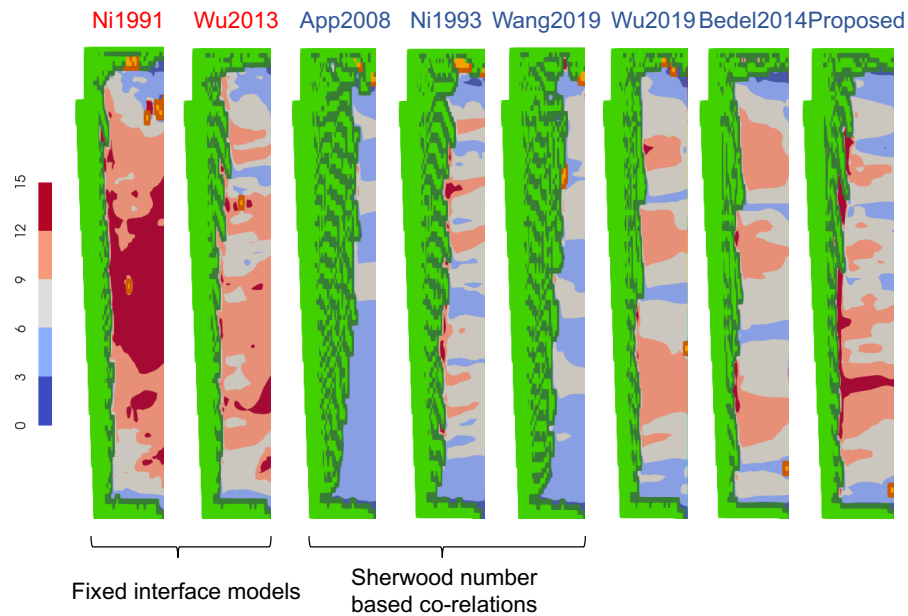
(a)
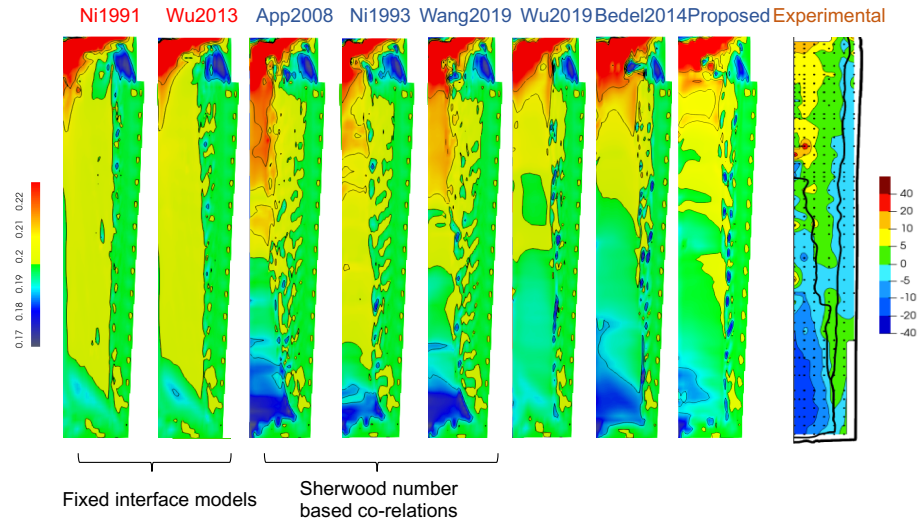
(b)

Fig. 17 - Résultats de simulations en utilisant différents modèles pour calculer la longueur de diffusion dans la phase liquide. Ligne supérieur structures de solidification, ligne inférieure cartes finales de composition en carbone

La figure 17 montre l'impact de la longueur de diffusion du liquide sur la ségrégation finale et la structure du lingot de coulée. Nous avons montré que les modèles à interface fixe introduisent une erreur significative dans la prédiction de la macroségrégation.

Conclusions et recommendations

Des modifications à l'implémentation actuelle du modèle SOLID® ont été proposées pour prendre en compte les paramètres variables du diagramme de phase et améliorer la description du profil du soluté dans la phase liquide grâce au modèle de calcul de la longueur de diffusion dans la phase liquide. Le modèle ainsi modifié a été appliqué à deux cas de solidification. Les deux simulations soulignent l'importance de coupler le modèle avec les données de Thermo-Calc®. Bien que l'importance relative de certains paramètres du diagramme de phase dépende du système d'alliage, le couplage des modèles avec les données de Thermo-Calc® a permis d'améliorer les résultats par rapport aux simulations avec des paramètres constants du diagramme de phase. Au cours de cette étude, des valeurs améliorées correspondant à des paramètres fixes du diagramme de phase ont été suggérées pour le cas Sn-5%Pb. Bien que ces paramètres améliorés ne reproduisent pas complètement les résultats d'une simulation avec tous les diagrammes de phase variables, ils améliorent les résultats de la simulation. Le nouveau modèle de longueur de diffusion proposé constitue également une amélioration par rapport au modèle de longueur de diffusion utilisés précédemment. Ainsi Le modèle de régression ANN-MLP s'avère être un outil efficace et précis pour générer des fonctions de régression pour diverses données thermodynamiques.

Même si le code SOLID® a pu être amélioré par ces apports, il reste encore des points ouverts à des améliorations conséquentes ainsi qu'à une analyse plus approfondie de divers aspects du modèle. Plusieurs propositions peuvent être faites:

- Application du nouveau modèle à des alliages quaternaire, quinaire . . . . ;

- Incorporation des données de densité des phases liquide et solide issues de Thermo-Calc® ;

- Prise e, compte de la transformation péritectique;

- Application d'algorithmes de régression avancés.

Contents

Acknowledgments

Nomenclature

Most of the variables are defined within the text. For clearance a nomenclature with all the variables is given below.

Latin symbols :	
δt	Micro time-step
Δt	Macro time-step
n_{mic}	Number of micro time-steps
$\mathbf{G}$	Temperature gradient
c_0	Nominal concentration
c_{ref}	Reference concentration
$\langle h \rangle$	Average enthalpy
$\langle h_{\mathrm{l}} \rangle^{\mathrm{l}}, \langle h_{\mathrm{s}} \rangle^{\mathrm{s}}$	Intrinsic enthalpy of the solid and liquid phase respectively
$\langle c \rangle$	Average solute concentration
$\langle c_{\mathrm{l}} \rangle^{\mathrm{l}}, \langle c_{\mathrm{s}} \rangle^{\mathrm{s}}$	Intrinsic solute concentration of the liquid and solid phase respectively
$c_{\mathrm{l}}^*, c_{\mathrm{s}}^*$	Equilibrium solute concentration of the liquid and solid phase respectively
$\langle C_{\mathrm{l}} \rangle^{le}$	Intrinsic solute concentration in the extradendritic liquid
T	Temperature
T_f	Melting temperature of a pure substance
T_{sol}	Solidus temperature
T_{liq}	Liquidus temperature
T_{sol0}	End of solidification temperature
C_d	Drag coefficient
C_p	Specific heat capacity
L_f	Latent heat
$D_{\mathrm{l}}, D_{\mathrm{s}}$	Diffusion coefficient in liquid and in solid, respectively
d_g	Grain diameter
g	Normal terrestrial gravity
$g_{\mathrm{s}}, g_{\mathrm{l}}$	Solid and liquid volumetric fractions, respectively
g_{env}	Envelope fraction

g_i	Internal solid fraction
$g_{\mathrm{e}}, g_{\mathrm{d}}$	Extragranular and intragranular liquid fractions respectively
g_e^{block}	Solid fraction packing limit (two-phase globular model) or envelope fraction packing limit (three-phase dendritic model)
R_{arm}	Grain arm length
R_{env}	Envelope radius
$g_{ep}^{\max}$	Maximum packing envelope/solid fraction.
k	Partition coefficient
m_{l}	Liquidus slope
T^{∞}	Far-field temperature
$k, k_{\mathrm{l}}, k_{\mathrm{s}}$	Thermal conductivity, averaged, in liquid and in solid, respectively
K	Permeability
K_k	Kozeny constant
$\Delta T, \Delta T_c, \Delta T_t$	Total undercooling, solutal undercooling and thermal undercooling respectively
$\vec{M}_k^d, \vec{M}_k^{\Gamma}, \vec{M}_k^{\phi}$	Interfacial momentum exchange of the phase k due to drag, solid growth and nucleation, respectively
N_{nuc}	Volumetric density of nuclei
N_g	Volumetric density of grains
$Q_k, Q_k^{\Gamma}, Q_k^{\Phi}$	Interfacial energy exchange of the phase k due to diffusion, grain growth and grain nucleation
p	Pressure
R^*	Averaged grain radius
R_{tip}	Tip radius
$S_v^{\mathrm{env}}, S_v^{\mathrm{s}}$	Specific surface area for envelope and solid, respectively
ΔT_{nuc}	Nucleation undercooling
V_0	Initial volume of a nucleated grain
V_g	Velocity of the solid-liquid interface in case of spherical shaped front
v_{tip}	Tip velocity
$\langle \vec{v}_{\mathrm{l}} \rangle^l, \langle \vec{v}_{\mathrm{s}} \rangle^s$	Averaged intrinsic velocity of the liquid and solid phases, respectively
v_i	Velocity of the solid-liquid interface
R	Molar gas constant

Greek symbols :	
α_t	Slurry/porous flow regime transition function
α	Coefficient for slurry/porous flow regime transition function
λ_1	Primary dendrite arm spacing
λ_2	Secondary dendrite arm spacing
β_T, β_C	Thermal and solutal expansion coefficients
β_{sh}	Shrinkage coefficient
Γ_{s}	Mass transfer rate from liquid to solid phase
Γ_{env}	Volumetric transfer rate to envelope phase
Φ_{s}	Mass transfer rate to the solid phase due to nucleation
Φ_{env}	Volumetric transfer rate to the envelope phase due to nucleation
$\delta_{\mathrm{l}}, \delta_{\mathrm{s}}$	Diffusion lengths for liquid and solid, respectively
$\mu_{\mathrm{l}}, \mu_{\mathrm{s}}$	Dynamic viscosities for the liquid and solid phases, respectively
ν_{l}	Liquid kinematic viscosity
ρ	Density
ρ_{ref}	Reference density
$\rho_{\mathrm{l}}, \rho_{\mathrm{s}}$	Liquid and solid densities, respectively
τ	Tortuosity

Chapter 1 : Introduction

Contents

1.1   Solidification and its macroscopic modeling

Casting of metals is an ever evolving process with ancient roots. It is one of the earliest industrial processes in history which has had a significant contribution to the growth and development of the human race. Even today, most of the every-day mechanical devices we use have metal parts, which are manufactured through the casting process. The final cast product is characterised by its structure and segregation which affect its quality and performance. In this process, molten metal is poured into a mold cavity, where it is cooled and later extracted from the mold. The key concept behind casting is solidification, the transformation of matter from liquid to solid state. Solidification is the result of several physical phenomena occurring simultaneously at different length scales. Atomic vibrations at the nano scale determine the diffusion of atoms across a single phase (solid or liquid) as well as the atomic rearrangement at the solid-liquid (s/l) interface, which determines the interface movement at the micro-scale. Interaction between phases at the meso-scale to the liquid/solid movement at the macro-scale determine the final distribution of the phases. Fig. 1.1 illustrates the various physical phenomena which interact to produce the final cast product along with the employed modeling and simulation approaches for the associated length scales.
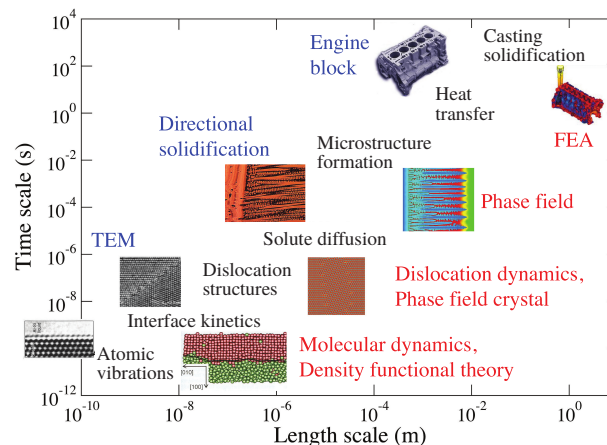
Figure 1.1 – Illustration of physical phenomena and simulation approach for the associated length scales [2]

The primary casting routes used in the steel industry are ingot casting (Fig. 1.2a) and continuous casting (Fig. 1.2b). In the recent past, many industrial facilities have replaced ingot casting with continuous casting due to advantages such as improvement of steel quality, better yield, energy saving and manpower. However, ingot casting continues to be used considerably in industry for large forgings and rolled products. The quality and performance of the product depends on the grain structure and chemical composition variation (segregation) across cast products. The structure and composition variations are highly interlinked. In continuous casting, faster cooling conditions prevail due to the geometry of the cast as well as the cooling conditions employed. Continuous cast products are associated with strong centreline segregation as shown in Fig. 1.3. The amount of segregation is heavily dependent on the cooling rate [3]. Similarly, in ingot casting, there are zones of strong negative segregation at the bottom of ingot and positive segregation at the top of ingot **??**. Segregation and non-uniform structure distribution results in reduced performance of the product. Thus, the ability to predict macrosegregation and the associated structures is essential for many industrial applications. Control over solidification requires understanding of various phenomena occurring over several length scales.
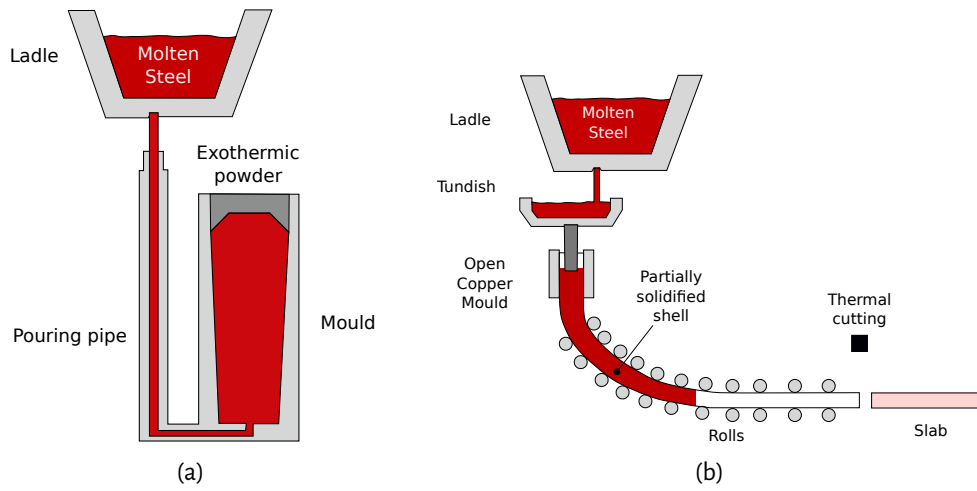
Figure 1.2 – Schematics of main steel casting processes by a) ingot casting and b) continuous casting [4].
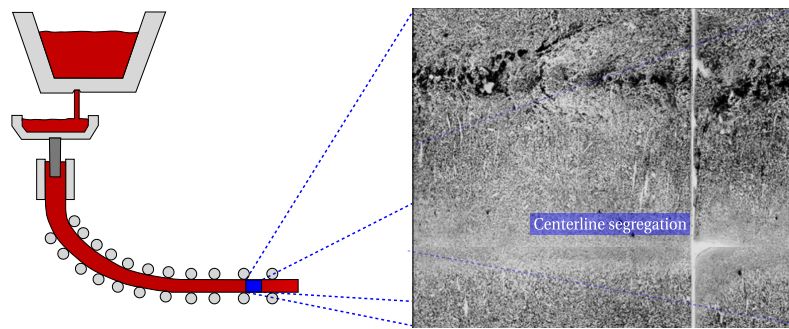
Figure 1.3 – Centreline segregation in continuous cast product [4].
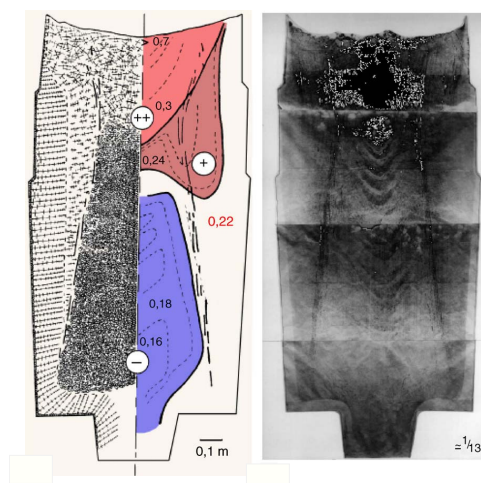
Figure 1.4 – Sulphur print of the longitudinal section of 65 ton steel ingot showing macrosegregation patterns and its intensity as well as the solidification structures [1]
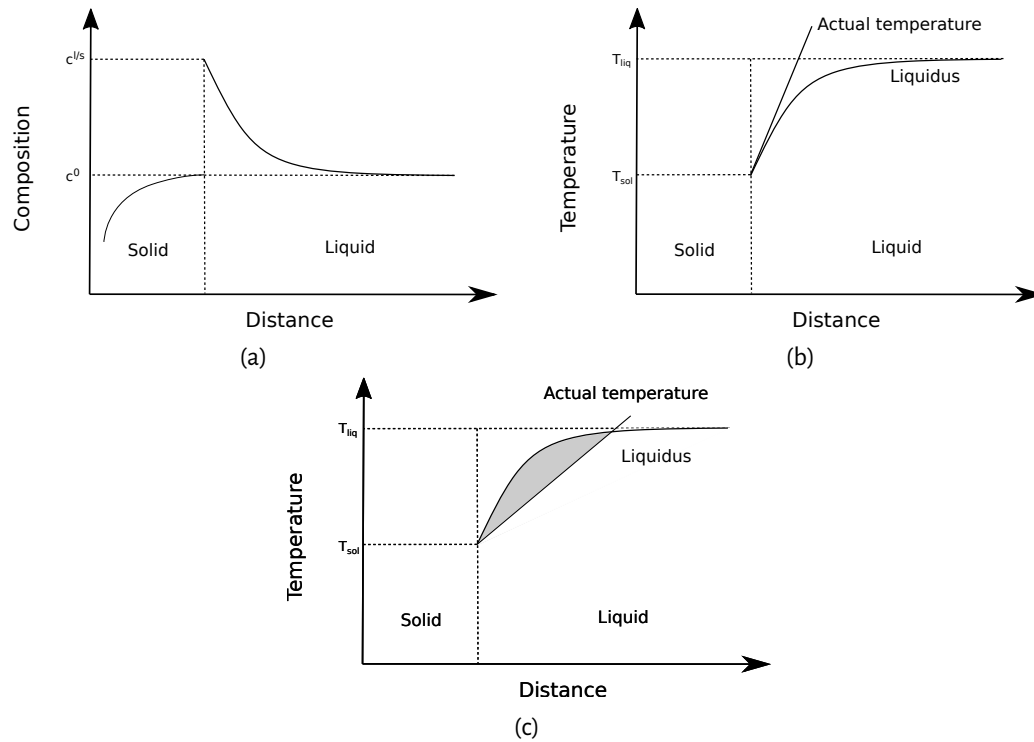
Figure 1.5 – Illustration of constitutional undercooling during directional solidification of binary alloy with planar front initially, (a) composition profile and solute enrichment layer ahead of the steady state planar solidification (for the case when solute element is rejected by solid phase) front (b) stable condition for planar growth (c) unstable condition for planar growth.

1.2   Solid-liquid interface

In classical theory of solidification, the interface between solid and liquid during directional solidification of pure metal is considered to be planar. The propagation of the interface is mainly controlled by the temperature gradient **G** in the liquid at the interface and the velocity **v** of the interface. If **G** is positive, as encountered in the case of directional solidification of pure metal, the interface has a planar morphology. However, if **G** is negative, as encountered during equiaxed solidification of pure metal, the interface is not stable and it turns to dendritic morphology. This analysis becomes more complicated for alloys. Solute elements, in general, have a lower solubility in the liquid phase as compared to solid. Thus, as solidification progresses, solute elements are rejected by solid and diffuse into the liquid phase. The solute profile in the liquid phase is shown in Fig.1.5a. The shape of the solute profile depends on the velocity, **v**, and it can be seen that the solute concentration gradient is negative at the interface. This results in the lowering of the liquidus temperature (T_{liq}) as shown in Fig. 1.5b. The stationary solute profile in the liquid depends on the diffusion coefficient of the element and the velocity of the solid-liquid interface. The solid-liquid interface is stable if the temperature gradient ahead of the interface is high, such that the actual temperature is above the local liquidus temperature, corresponding to the case of Fig1.5b. However, if the temperature gradient is low, the actual temperature is below the liquidus temperature which results in 'consitutional undercooling' of the region ahead of the interface as shown by the gray zone in Fig. 1.5c. The undercooling of the melt ahead of the solid/liquid interface is the driving force for solidification. Tiller *et al.* [5, 2] explained that in the absence of an undercooled zone, any perturbation to the interface remelts and the planar interface remains stable during growth. In the presence of an undercooled

zone, the interface is unstable and breaks down into cellular or dendritic morphology.

Dendritic microstructure is the most prominent microstructure observed in industrial castings in which the solid/liquid interface adopts a tree-like shape. There are two types of dendritic microstructure: i) columnar and ii) equiaxed, as shown in Fig.1.6 for an Al-Cu alloy. The transition from columnar to equiaxed dendritic is referred to as 'Columnar to Equiaxed Transition' (CET) which is an important phenomena in castings and will be discussed in detail in section 1.3.3. Each of the above mentioned dendritic structures offer advantages over another depending on the application of the cast product. Columnar dendrites offer excellent creep resistance for high temperature applications. For example, directionally solidified single-crystal materials contain no grain boundaries along the longitudinal direction and are widely used for aircraft engines. Equiaxed regions contain a large number of grain boundaries and offer high strength, ductility and isotropic mechanical properties, making it the preferred choice of material for automobiles, machinery and construction. For such applications, the steelmakers promote CET as early as possible. Thus, it becomes critical to understand the origin of these dendritic structures and the conditions which control this transition.

1.3 Solidification structures

(a)   (b)
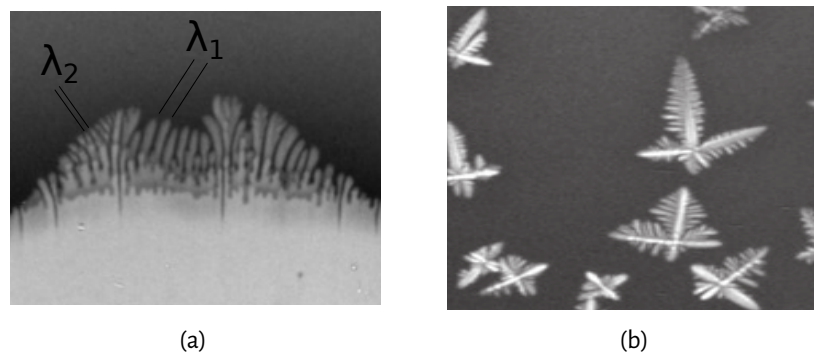
Figure 1.6 – In-situ observation of (a) columnar microstructure for Al-5wt.%Cu alloy [6] & (b) equiaxed microstructure for Al-10wt.%Cu alloy [7]

1.3.1 Columnar structure

1.3.1.1 Description of columnar structure

Columnar grains are observed close to the chill surface where high thermal gradients favour directional solidification. Columnar dendrites are characterized by primary dendrite arm spacing (PDAS), λ_1, and secondary dendrite arm spacing(SDAS), λ_2, as shown in Fig.1.6a. PDAS is the spacing between the primary trunks and SDAS is the spacing between arms that are perpendicular to the primary trunks. The thermal gradient in front of the columnar front is positive. It constrains the grains to adopt a columnar morphology as schematized in Fig. 1.7 with the notable exception at the end of columnar growth after which CET occurs [8].

1.3.1.2 Origin of columnar structure

The columnar structure originates from the equiaxed crystals that nucleate on the chill surface when the hot metal comes in contact with the mold wall. If these equiaxed crystals stay attached to the mold wall, they
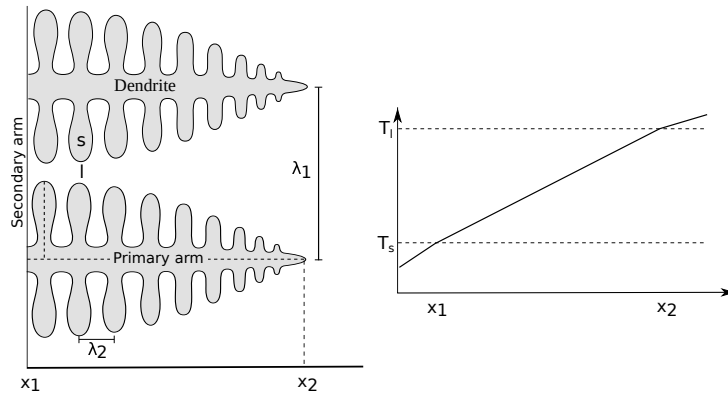
Figure 1.7 – Schematic of columnar grains and the thermal profile during solidification

Growth direction
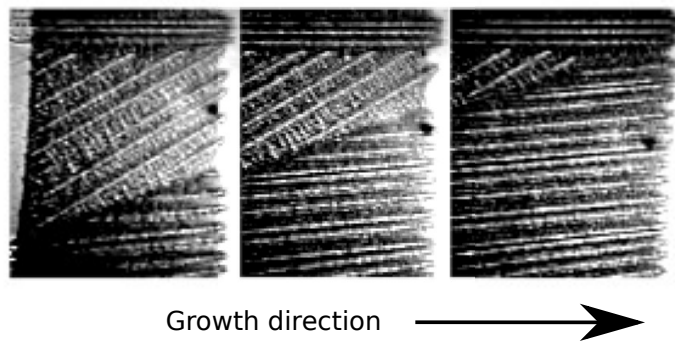
Figure 1.8 – Columnar grain growth competition in Pb-Ag alloy [9]
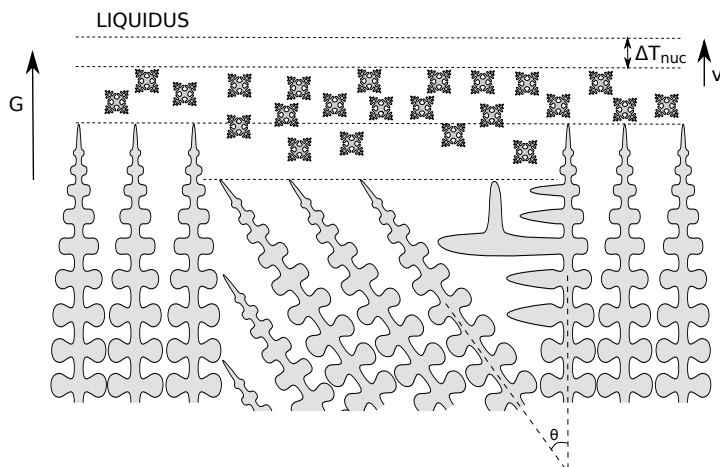
Figure 1.9 – Schematic illustration of grain growth mechanisms occurring in dendritic alloy with non-uniform temperature. ΔT_{nuc} is the nucleation undercooling for equiaxed grains (redrawn from [10])

grow as columnar grains, else they act as source of equiaxed grains as discussed in the following section. The thermal gradient ahead of the columnar front is the driving force for the growth of columnar grains. Columnar grains whose crystallographic direction is best aligned with the thermal gradient grow preferably over other grains, which are eventually blocked as is shown in Fig. 1.8. The explanation given by Rappaz and Gandin [10] is shown in Fig.1.9. The grain growth competition can be summarized as the best alignment corresponding to the minimum undercooling. The interface velocity is assumed to be dependent on the undercooling. In Fig.

1.9, the left and the right dendrites are aligned with the temperature gradient and hence perpendicular to the liquidus isotherm (dashed). The two grains grow with the same velocity as that of the liquidus isotherm v_L. The middle dendrite is aligned at an angle θ to the temperature gradient direction. Thus, the growth velocity of the middle grain is $v_\theta = v_L/\cos\theta$ so that the component of growth velocity along the temperature gradient direction is v_L. This results in the undercooling at the dendrite tip of the middle grain to be larger than the surrounding grains, hence the dendrite tip has a lower temperature compared to the surrounding grains. And since the temperature gradient is fixed, the lower the temperature, the farther away the dendrite tip for the middle grain lies from the liquidus isotherm which results in the middle grain lagging behind. This results in:

- The primary tips of the less favourably oriented grain hit the side of the best oriented grains and are stopped at the converging grain boundary

- The extensions of secondary arms of the grain on the right can continue growing into the space at the diverging grain boundary and evolve into new primary branches

1.3.2 Equiaxed structure

1.3.2.1 Description of equiaxed structure
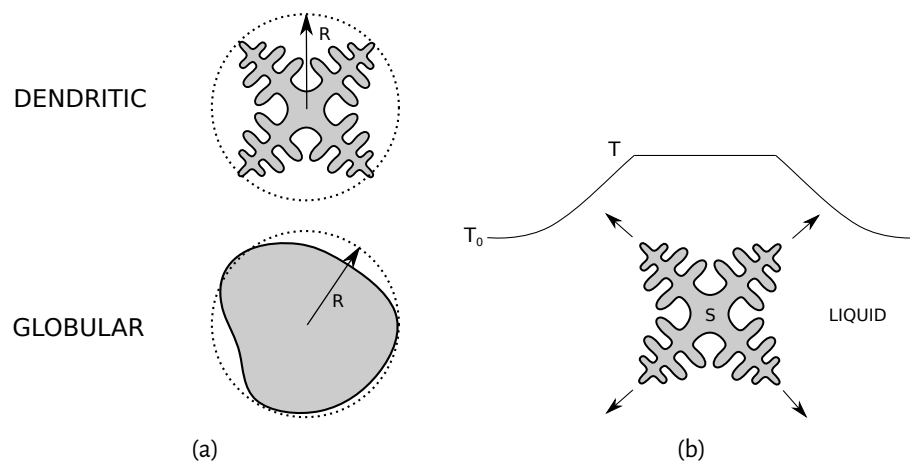
Figure 1.10 – Schematic of equiaxed grains and the thermal profile across a grain during solidification

Fig. 1.10a represents the two kinds of morphologies which distinguish the equiaxed structures: i) globular ii) dendritic. Fig. 1.10b describes the thermal profile during solidification of equiaxed structures. We notice that unlike the case of columnar solidification, the heat must be evacuated through the surrounding liquid and the solid is at a higher temperature than the liquid phase. Since the equiaxed grains nucleate and grow in undercooled liquid, equiaxed growth is referred to as "unconstrained growth". The growth of the equiaxed grains depends on the undercooling in the surrounding liquid.

1.3.2.2 Origin of equiaxed structures

A number of mechanisms have been proposed for the formation of equiaxed grains. The dominant mechanisms differ in regards to the hypothesis regarding the origin of the equiaxed grains in the context of the solidification setup and flow conditions prevailing within the setup. The understanding of these phenomena
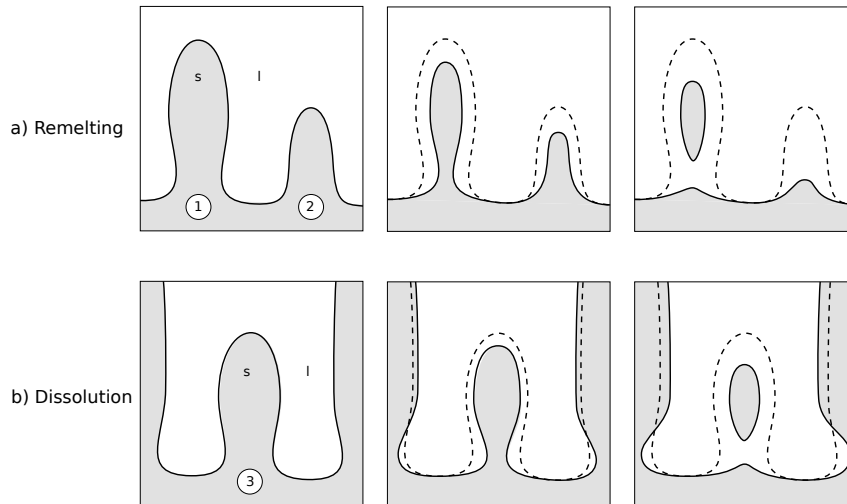
Figure 1.11 – Schematic of the dendritic fragmentation mechanisms: a) remelting and b) dissolution. In the case of remelting, both arms remelt, but only arm 1 is detached. In the case of dissolution, the arms on either side of arm 3 are larger in diameter resulting in this arm to dissolve [11]

is evolving, thanks to the more controlled experimental setups. However, the major types of identified mechanism are:

– **Heterogeneous nucleation** - This hypothesis was initially proposed by Northcott [12] and later by Winegard & Chalmers [13] who assumed that solute accumulation ahead of the columnar front results in constitutional supercooling. When a critical undercooling is exceeded, heterogeneous nucleation occurs. In the case of inoculated alloys, the supercooling is directly related to the size of equiaxed grains which nucleate. However, it is now accepted that heterogeneous nucleation is not the source of equiaxed grains in non-inoculated alloys such as steel ingots as the undercooling criteria are not satisfied.

– **Pre-existing solid crystals** - This phenomenon assumes pre-existing solid crystals in the liquid before any significant solidification has occurred. This hypothesis was proposed by Chalmers [14] and is called the "Big Bang" hypothesis. This phenomena occurs while filling the mould, when the hot metal comes into contact with the cool walls. High thermal supercooling results in nucleation of equiaxed crystals on the mold walls which can be transported by the liquid flow. The subsequent survival of these crystals in the bulk liquid depends on the local thermal conditions. If these crystals do not remelt because of high superheat, they subsequently grow into equiaxed grains. A similar mechanism was proposed by Ohno *et al.* [15].

– **Fragmentation** - Experimental observations by Jackson *et al.* [16] on the solidification of cyclohexanol (an analogue of a pure metal) and cyclohexanol with fluorescein (a mixture analogue of a metallic alloy) concluded that dendrites of pure metal differ from those of an alloy. In pure metals, the diameter of the main stem and branches are similar unlike alloys where the branch broadens after having grown through the solute boundary layer of the main stem. This results in the branch being attached to the main stem by a narrow neck, a shape that is conducive to detachment. Dendrite fragmentation is the phenomenon of detachment of branches (secondary arms) from the main stem (primary arms). Pilling and Hellawell [17] have shown that the detachment is not due to any mechanical stresses acting on the secondary arms. Fragmentation depends strongly on the local

conditions (thermal gradients, solute concentration gradients, growth rate of dendrites etc.) that are dictated by the casting conditions. Several mechanisms have been proposed for the secondary arm fragmentation:

– Local dissolution at the base of the arms [18]

– Remelting of the arms [19]

– Unconstrained growth of dendrite - This mechanism will be discussed along with constrained to unconstrained growth mechanism for CET in the section 1.3.3.

1.3.3 Columnar to equiaxed transition (CET)

The transition from elongated columnar structure at the periphery of castings to finer equiaxed structure at the centre is termed as "Columnar to equiaxed transition" (CET). CET is very important because a better understanding of this phenomenon enables industry to engineer the microstructure to the needs of the product. Thus, CET has been fascinating academia and industry for more than 50 years which has resulted in extensive experimentation and numerical modelling of CET. Some of the prominent experiments conducted are:

– Ares & Schvezov [20] studied the effect of alloy composition and cooling rate on CET during upward directional solidification of Pb-Sn alloy. CET occured when the temperature gradient ahead of the columnar front dropped below 0.8 Kcm^{-1} with a gradual transition from pure columnar to pure equiaxed within a thickness of 1 cm. Similar observations were made for Zn-Al [21] and Al-Cu [22] alloys.

– Spinelli *et al.* [23] studied the influence of liquid melt convection on CET during downward directional solidification of Sn-Pb alloys. Liquid convection transports dendrite fragments into bulk liquid which promotes equiaxed nucleation and growth and a subsequent CET. The critical cooling rate was found to be 0.03 Ks^{-1}. Hachani *et al.* [24, 25] performed directional solidification experiments for Sn-Pb alloy with varying composition and cooling rates. It was observed that the size of the equiaxed zone increased with increasing solute concentration.

– Liu *et al.* [26] studied directional solidification under microgravity with both refined and unrefined Al-7 wt%. Si alloys with different pulling velocities. They observed that CET was gradual for lower pulling velocity and sharp for higher pulling velocity. At low pulling velocities, the constitutional undercooling ahead of the front is low which results in slow growth of equiaxed grains. At high pulling velocities, the undercooling is high which causes fast growth of equiaxed grains and a sharp CET. Liu *et al.* [27] further observed that the thickness of the undercooled liquid region is responsible for a sharp or progressive CET. A thick undercooled region promotes a sharp CET. Reinhart *et al.* [28] performed simulations and experiments of CET in upward directional solidification of Al-3.5 wt%. Ni alloys. The CET position was extracted from X-ray radiographs and was modeled using 2D CAFE (Cellular automata finite element) model in the presence and absence of liquid convections. The CET prediction agreed with simulation results when liquid convection was considered.

During the course of these experiments, various mechanisms have been proposed to explain CET. Some of primary mechanisms are as follows:

– **Mechanical blocking** - Hunt [29] proposed the first CET mechanism which is now referred to as 'mechanical blocking'. As discussed in earlier sections, the region ahead of the columnar dendrites are

constitutionally undercooled in which equiaxed grains can nucleate. If these equiaxed grains nucleate and are given enough time to grow, when the volume fraction of the equiaxed grains becomes greater than 0.49, equiaxed grains will mechanically block the further advancement of the front resulting in CET. This criteria has been widely used in literature to predict CET with considerable success. However, the mathematical derivation of the criterion is based on empirical relations and the grain fraction figure of 0.49 is arbitrary. Biscuola and Martorano [30] showed for Al-Si alloys that using a value of 0.2 for equiaxed blocking fraction results in CET predictions that are in better agreement with experiments.

– **Constrained to unconstrained growth** - As mentioned in earlier sections, columnar growth is referred to as 'constrained growth' and equiaxed growth is referred to as 'un-constrained growth' due to the role of temperature gradient ahead of the dendrite tip. Mahapatra and Weinberg first suggested that when the thermal gradient ahead of the columnar front becomes sufficiently weak, the shape of the dendrite could become unstable which could result on slowing of the dendrite tip, thus promoting the growth of equiaxed grains which have been generated through heterogeneous nucleation. Subsequently, Gandin [8] proposed the mechanism of destabilization of the columnar front based on directional solidification experiments on Al-Si ingots. He found out that during the initial stages of solidification when thermal gradient is high, the growth is constrained and the tip velocity increases with time. Later, when the thermal gradient is small, the latent heat released by the growing front can now be partly removed via the liquid phase which results in a local negative gradient and unconstrained growth. This transition to unconstrained growth indicates the destabilization of the columnar front.

Reduction in thermal gradient results in slowing of the columnar front and fragmentation of the columnar secondary arm as suggested by Jackson *et al.* [16]. The production of fragments is further favoured by reorganisation in the columnar structure as the PDAS depends on the columnar front velocity. This effect has been demonstrated by Pollock and Murphy [31] during freckle formation in nickel based alloys.
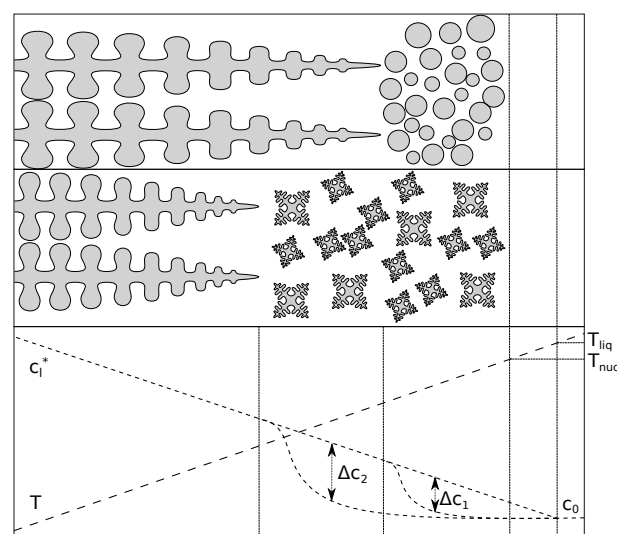
Figure 1.12 – Schematic illustration of the solutal interaction between columnar dendrites and equiaxed grains during CET. Case 1 is for high equiaxed grain density and case 2 is for low grain density. The temperature gradient and nucleation undercooling is same in both the cases (redrawn from [32])

– **Solutal blocking** - In contrast to the previous mechanism which assumes direct contact between the columnar and equiaxed grains, the solutal blocking mechanism is called "soft blocking" as it implies the blocking of the columnar front even before direct contact with the equiaxed grains. Equiaxed grains reject solute during solidification. Martorano *et al.* [32] showed that when the equiaxed grain density is sufficient such that the rejected solutes reduce the driving force for the growth of columnar grains, CET occurs.

1.4 Segregation

Segregation is the non-uniform distribution of solute elements which is a consequence of the difference in solubility of the solute in the solid and liquid phases resulting in the partitioning of the solute species. Segregation occurs at various length scales and is the direct result of the length scale specific physical phenomena which cause mass transfer. Microsegregation occurs on a length scale of a few hundreds micrometres and is the result of solute diffusion and solid/liquid interface movement. Macrosegregation is the result of long range advection of solute elements due to relative movement between segregated liquid and solid during solidification and can occur over a length scale of millimetres to metres. The various causes of macrosegregation in casting processes are:

– **Thermo-solutal convection** - The temperature and solute gradients produced during solidification results in spatial variation in the liquid density. Generally for steels, an increase in temperature results in lower liquid phase density and vice versa. However, the correlation between the liquid composition and its density varies from one alloy to another. These variations in the thermal and solutal fields create a driving force of liquid convection during which redistribution of chemical species occurs resulting in macrosegregation.

– **Movement of equiaxed grains** - Equiaxed grains generated through any of the mechanisms mentioned in section 1.3.2.2, are transported by the liquid flow and can float or sediment depending on the prevailing conditions. As equiaxed grains grow, they continuously reject solute into the bulk liquid and grow denser than the surrounding liquid, instead tend to sink and settle [33]. In large industrial ingots, a negative macrosegregation zone is detected close to the bottom which is the result of the settling of these solute depleted equiaxed grains and is the dominant macrosegregation phenomena in large ingots.

– **Solidification shrinkage** - As liquid metal solidifies into solid, there is an increase in density for most alloys. The liquid moves towards the interface to compensate for the volume difference caused by phase change. Contraction due to decrease in temperature also induces the liquid flow. The liquid flow brings in solute rich liquid towards the solidifying areas which results in positive segregation. Negative segregation at the centre of ingot and positive segregation at the surface during DC casting of Al alloys are prime examples of shrinkage induced flow.

– **Solid deformation** - As solidification progresses, various stresses of thermal and mechanical nature develop in the cast product. Deformation of the semi-solid network due to these stresses along with metallostatic head causes a relative solid-liquid movement leading to segregation. During continuous casting of steels and twin roll casting of aluminium, it has been observed that deformation imposed by rolls lead to centerline macrosegregation in the final cast product [33, 34, 35].

– **Forced flow** - Imposed flow due to pouring, electromagnetic stirring etc. changes the liquid flow
pattern which results in modification of the segregation. Chu and Jacoby [36] demonstrated that
ingot cast by level pour method has an approximate 15% improvement in the negative centerline
segregation as compared to bi-level transfer method and the improvement was attributed to dif-
ference in flow pattern introduced. Further investigation indicated that optimizing the metal en-
trance conditions resulted in significant reduction in centerline segregation [37] as fragmentation
is reduced which results in reduction of volume of sedimenting grains.
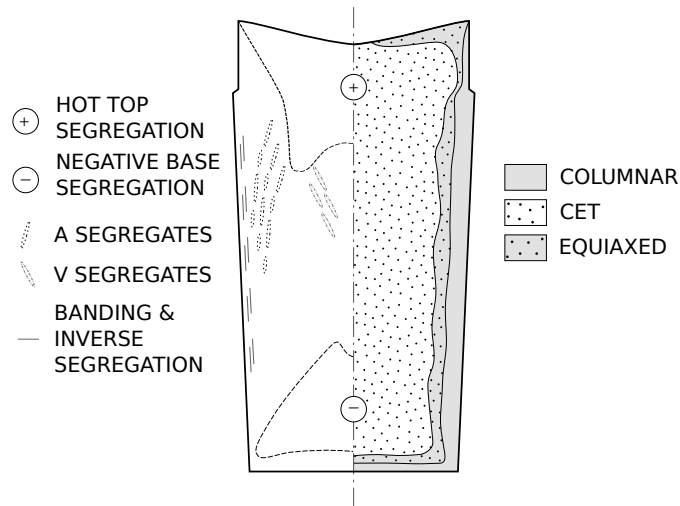
Figure 1.13 – Schematic representation of different zones of segregation and structures observed in large in-
gots

In between macrosegregation and microsegregation, there is mesosegregation. Mesosegregation repre-
sents a form of segregation, where composition variation occurs over a length scale of few grains. Such lo-
calized segregation occupies only certain parts of the ingot, such as segregation channels, V-shaped segrega-
tions, reverse segregations or bands [38, 39]. The different types of segregation encountered in large ingots
have been schematically represented in Fig.1.13.

– **Negative segregation cone** - This negative segregation is caused due to sedimentation of equiaxed
grains. This phenomenon has already been discussed while describing movement of equiaxed grains
as one of the primary segregation mechanisms.

– **Positive "hot top" segregation** - This is an intense segregation zone at the head of the ingot. This
zone is the last part to solidify and contains the most enriched liquid as the enriched liquid is less
dense and tends to rise. Poor insulation of the head can create negative temperature gradients
which accentuates the segregation [42, 43].

– **Positive "A segregates"** - These are segregation channels which form in the mushy zone of the steel
ingots and is the result of thermo-solutal convection [44]. Several studies have established links
between segregation channels, thermal gradient and the solidification rate. Low thermal gradient
and solidification rate promote channel formation. Giamei and Kear [45] observed the formation of
segregation channels in nickel based superalloys only beyond a critical distance from the skin. Close
to the skin, the thermal gradient and solidification rate are too high. Common and Bastien [46]
compared segregation in ingots of different sizes. The "A segregation" was much less pronounced
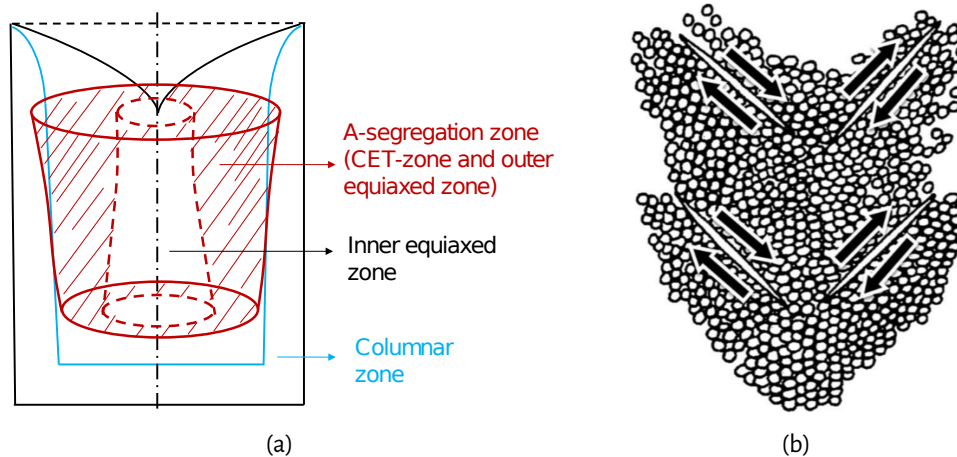
Figure 1.14 – Schematic illustration of (a) A-segregation in 500 kg ingot [40] (b) formation of V-shaped segregations due to the appearance of cracks within the first network of equiaxed grains [41]

in small ingots as compared to larger ingots due to similar reasons as before. The position of these channels are also influenced by the permeability which depends on the PDAS. The channels form preferentially where PDAS are the largest due to higher permeability. Chen *et al.* [40] illustrate the zone in which segregation channels can form in low carbon and high carbon low alloy steel ingots as shown in Fig. 1.14a

— **Positive "V segregates"** - The "V segregates" look similar to "A" segregates but are closer to the centre of the ingot and in the opposite direction. The mechanism of formation of "V" segregates differs from that of "A" segregates. "V" segregates form at an advanced stage of solidification when the equiaxed grains have grown, settled and coalesced to form a solid network with pockets of enriched liquid. This solid network is still fragile and can crack due to metallostatic pressure and stresses due to shear and solidification shrinkage. Once cracked, the entrapped enriched liquid is free to flow and form segregation channels which later solidify as "V segregates". This mechanism has been illustrated in Fig. 1.14b.

Macrosegregation can be quantified using chemical analysis methods on samples taken from ingots or direct measurement on a cut of the ingot. Several methods can be employed to quantify composition of elements in the alloy. One of the methods used is optical emission spectroscopy (OES) with a spark source. A spark discharge is applied to the surface of the alloy which results in emission of spectral radiation by surface atoms. These radiations are quantified to know the composition. Carbon and sulphur are difficult to quantify using this method. Thus, these elements are quantified through combustion for which small chips of the alloy are produced by drilling small holes in the ingot. These chips are placed in a crucible and heated until they burn and produce CO_2 and SO_2 gases. These gases can be analysed and quantified using infra-red (IR) absorption of CO_2 and ulta-violet (UV) of SO_2. By repeating the above procedure over specifically chosen points of the cast (Fig. 1.15a), a macrosegregation map can be generated (Fig. 1.15b). It has to be noted that the size of the samples used for these analyses is usually in the range of 1[cm]. The sample size is important as it has to be large enough so that it averages out local composition variations due to microsegregation and mesosegregation. Another technique used to generate macrosegregation maps is X-ray fluorescence. It has the benefits that it is a non-destructive method and does not require tedious sample preparation. However, it suffers from the disadvantage that it cannot measure carbon concentration and high carbon steels have background radi-

(a)   (b)
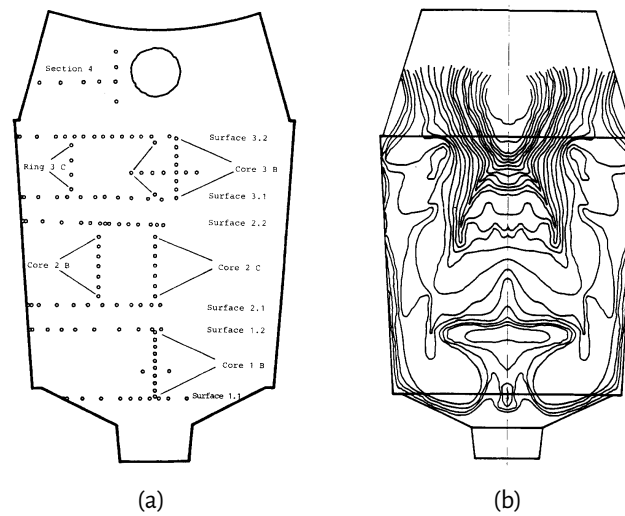
Figure 1.15 – (a) Location of points of analysis in 180 ton ingot of 20 MnMoNi 5 5 alloy and (b) iso-concentration carbon lines post composition analysis [47]

ations due to carbon which introduces error in measurement of composition for other elements.

(a)   (b)
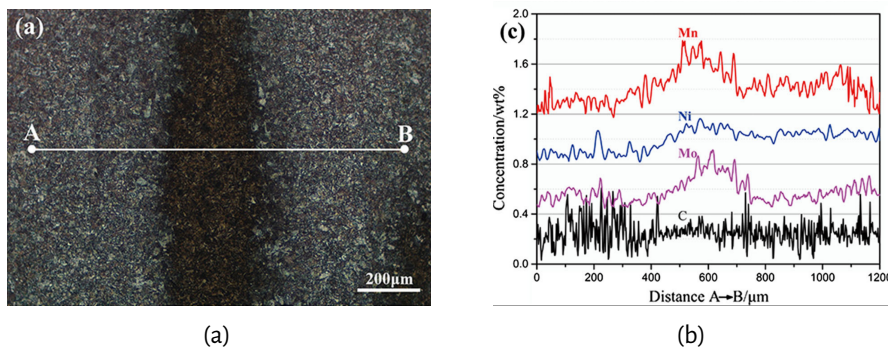
Figure 1.16 – (a) Optical micrograph of the line analyzed and (b) EPMA linescan result [48]

One of the methods to measure microsegregation is using Electron Probe Micro Analyser (EPMA). It is based on the chemical analysis of the X-ray spectrum emitted by a small volume element in the order of [μm^3] under the action of localized electron bombardment. The analysis of the X-ray spectrum allows for the identification of elements. Both qualitative and quantitative analyses are possible. EPMA can be used in various configurations. One such configuration has been employed by Yan *et al.* [48] where they use EPMA analysis along a line and shown in Fig. 1.16.

1.5   Project context and objectives

1.5.1   Context

Steel is one of the most innovative and flexible alloys which can be customized for many requirements. Variants of steel are used in various sectors ranging from housing and transportation to critical sectors such as nuclear energy which has resulted in huge demand for steel. Fig. 1.17 shows the increase in global steel production between 1980 and 2013. The Chinese steel industry has grown significantly in the past few decades
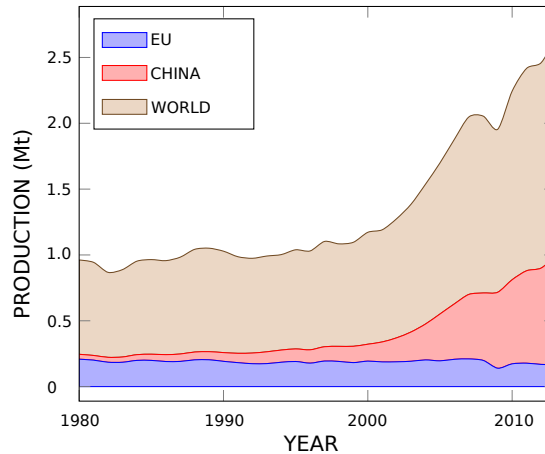
Figure 1.17 – Evolution of crude steel production [4]

(a)   (b)
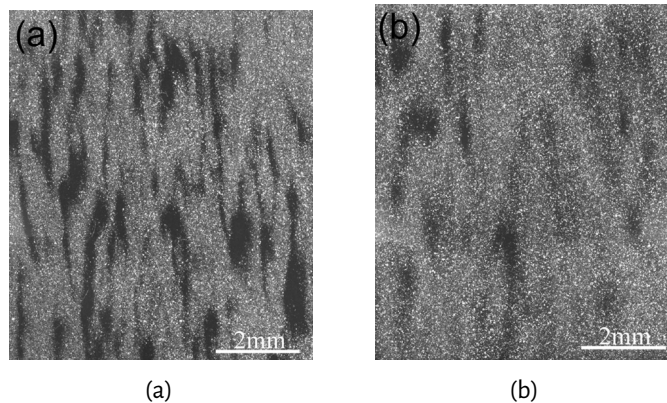
Figure 1.18 – Dark and white contract produced after etching. The dark zone represent segregation zones[48]

and its primary focus lies in steel for less critical sectors. The European Union steel production mostly focuses on steel for critical applications where quality constraints are severe. Faced with global competition, French steelmakers must constantly innovate in order to offer increasingly efficient products. One of the current challenges, in particular for these critical sectors is manufacturing steels with highly homogeneous properties:

– **Minimization of segregation** - Segregation poses problems to the structural integrity of the cast product. Reheating treatments are usually employed to homogenize the solute concentration heterogeneities produced from microsegregation through increased solid state diffusion and makes the mechanical properties more uniform. Yan *et al.* [48] presents the effect of homogenisation on the mechanical properties of pressure vessel steel. After the heat treatment, the chemical composition has become more homogeneous (Fig. 1.18): the concentration of alloying elements has decreased in positive bands and increased in negative bands along with more homogeneous hardness, better impact toughness and tensile properties. However, solute heterogeneities produced from macro/meso segregations span a much larger distance and cannot be removed by any kind of post treatment. Thus, macro/meso segregation is an irreversible defect and failure to prevent or reduce their intensity during solidification results in reduced performance of the cast product.

Various authors have established the link between segregation, composition and the dimension of the ingot. Acting correctly on these factors can reduce segregation. For example, reducing the in-

got size increases the thermal gradient, reduces the solidification time which results in reduction of segregation [49]. Since reduction of size of ingots is economically infeasible for steelmakers, the composition of the alloy can be varied such that the difference between the liquidus and solidus is reduced resulting in smaller mushy zone thickness and lower solidification time which reduces the segregation [50]. Silicon is a light element which encourages natural convection within the liquid and increases segregation [50]. Silicon is also attributed to reduced segregation in vacuum cast ingots with carbon deoxidation as compared to silicon killed steel ingots [47].

| (a) | (b) | (c) |
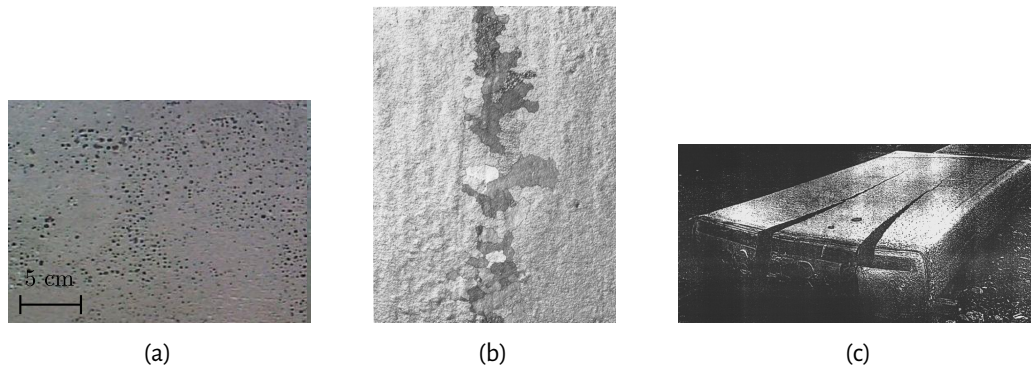
Figure 1.19 – Solidification related defects found in cast product: a) surface cavities in ingot casting [51] b) freckle in the form of chain of equiaxed crystals in Ni-base superalloy investment casting [45] and c) crack during continuous casting [52]

- **Absence of defects** - Other than macrosegregation, defects which are encountered during industrial casting are pores, crack, segregation channels etc. For critical sectors where quality control requirements are very strict, a small number of such defects can render the cast useless, following which the metal has to be recast again or is scrapped. Both of these options result in substantial loss for the industry.

  - **Porosity** - Porosity is the most common casting defect. Porosity is any void or hole in the casting and these form inside the casting or at the outer surface. Porosities are attributed to two factors: shrinkage porosity and gas porosity. Shrinkage porosity is caused due to the difference between the solid and liquid and occurs in sections of the cast which solidify later than the surrounding sections. These sections do not have enough metal flow which results in the formation of pores. Gas porosity occurs because the liquid metal has much higher solubility for gas as compared to solid. Thus, as solidification occurs, these gases come out and form pores. These gases could either be initially in the melt, created by reaction between metal and water in air or trapped in grooves at the mould surface or introduced through turbulence while filling the mold.

  - **Hot tearing** - It is the undesired formation of irregular cracks in metal casting during solidification. It is generally attributed to development of thermally induced tensile stresses and strains as molten metal contracts due to solidification shrinkage and solid state shrinkage. Preferential sites for crack initiation are locations where liquid feeding is difficult. These include corners or fillets of casting geometries. Factors that influence hot tearing are the alloy composition as well as the process parameters for casting.

  - **Segregation channels/freckles** - Freckles are macroscopic segregated channels and they

usually appear as a long trail of equiaxed grains as shown in Fig. 1.19b. Freckles are the product of thermo-solutal convection in the inter-dendritic liquid during solidification where the convection is primarily driven by density inversion occuring in the mushy zone as a result of microsegregation. As solute accumulates in these channels, the solidification of these channels are further delayed. The local conditions prevailing in the channel promote fragmentation of the solid dendrite network which introduces equiaxed grains which later solidify in the solute enriched liquid and leads to the formation of distinct crystal chain patterns.

– **Homogeneous grain structure with a large equiaxed zone** - As the industrial partners are working in the domain of steels for automobile, aeronautic and energy applications, castings with large equiaxed zones are preferred. As mentioned earlier, columnar grains are associated with anisotropic response to external loads such as mechanical and thermal stresses which causes premature failure of the component. Equiaxed grains have the benefit of increased soundness due to better permeability of liquid metal into the mushy zone. This results in homogeneously distributed porosities, reduced hot tearing susceptibility, better mechanical performance and an easier and homogeneous mechanical working into the final product. Success in producing fine equiaxed grain structures limits the constraints and opens the possibility to improve the design of the castings.

For this, a key manufacturing step lies in the solidification of the ingots which strongly inter-links the structure-segregation requirements. Thus, to better understand the solidification kinetics during casting and the effect of various processing parameters on the final cast product, various steelmakers spend considerable time and money on research and development (R&D). Industrial trials are expensive and infeasible due to which, simulation softwares dedicated to alloy casting are one of the primary areas of focus. The steelmakers work with academic partners in development of such softwares which cater to the general casting issues as well as steelmaker specific issues.

Charles Darwin said, "In the long history of humankind, those who learned to collaborate and improvise most effectively have prevailed". It is within this spirit of collaboration that **SOFT-DEFIS** (**SOFT**ware for the **DE**velopement of **F**ine **I**ngot **S**tructure) brought together 11 partners as shown in Fig. 1.20. The main tasks within this project are:

– **Experimental investigation performed by the manufacturing partners**

– **Model developments by academic partners**

– **Model integration into simulation software by software partners**

– **Validation of the developments by the manufacturing partners**

During the course of this project, many advancements have been made towards achieving the final aim of steels with homogeneous properties. One of the primary aims achieved in the project has been the continued development and integration of solidification models in SOLID® and THERCAST® solidification softwares.

1.5.2 Objectives

A critical element for successful modeling of solidification is the knowledge of the phase diagram of alloys. Fig. 1.21 shows an eutectic binary alloy phase diagram. For a binary alloy, the solid and liquid composition at equilibrium is given by the tie line and is represented by the horizontal dashed line at temperature T which
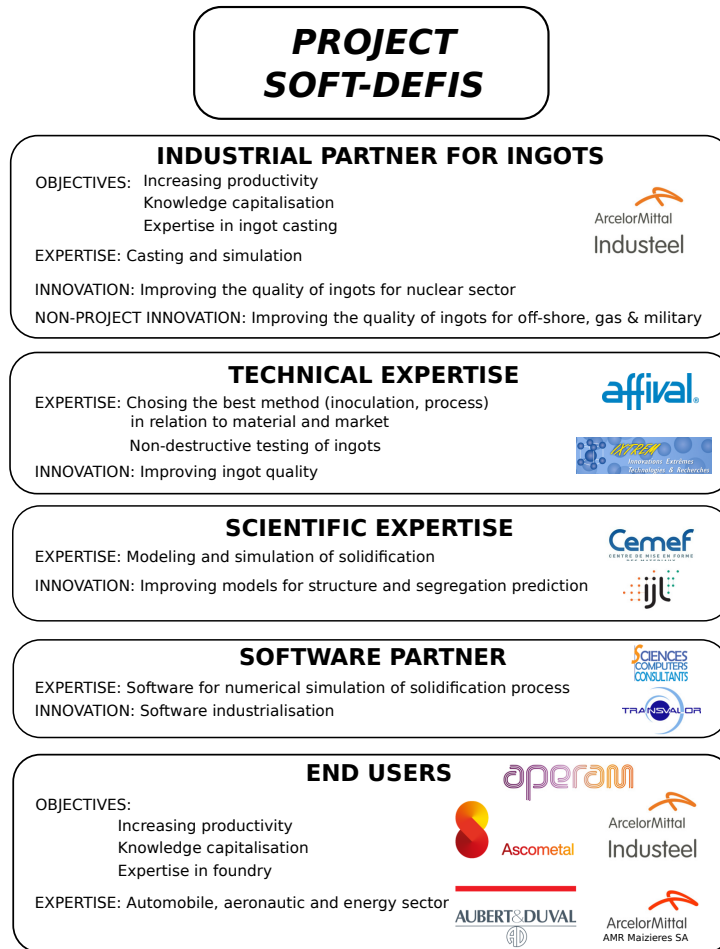
Figure 1.20 – Overview of partner role and interactions

intersects the solidus and liquidus lines. For most solidification models, simplified phase diagrams are used and are represented by the linearized solidus and liquid given by the gray lines in Fig. 1.21. For each phase, the relationship between composition at the interface and that in the bulk depends on the degree of homogenization of the composition by solute transport. In solid, diffusion is the primary mode of solute transfer whereas diffusion and convection are the primary mode of solute transfer in liquid phase. All of these phenomena are accounted for in a microsegregation model. Various microsegregation models are proposed and have been discussed in the next chapter. Accurate modeling of microsegregation is critical as it affects the microstructure, grain morphology and macrosegregation, hence the final mechanical properties of the alloy.

The tie lines are usually known for common binary alloys. But such data is usually not known experimentally for higher order alloys over a wide range of temperature and composition. Thus, extending the approximation of using linearized phase diagram data for higher order systems by extending linearized phase diagram data for binary sub-systems, a common practice in solidification modeling is unacceptable. Thus, there is a need for using data from thermodynamically sound extrapolation techniques. This methodology is called **CALPHAD** (**CAL**culation of **PHA**se **D**iagram) and is briefly discussed in the following chapter. Within the CALPHAD approach, experimental and calculated data are used to model various functions for phases which are stored in CALPHAD databases generated by Thermo-Calc®. The present thesis has the primary objective of improving the prediction of macrosegregation during the solidification process. This is achieved through improved prediction of solidification path for multicomponent industrial alloys by accounting for variable phase
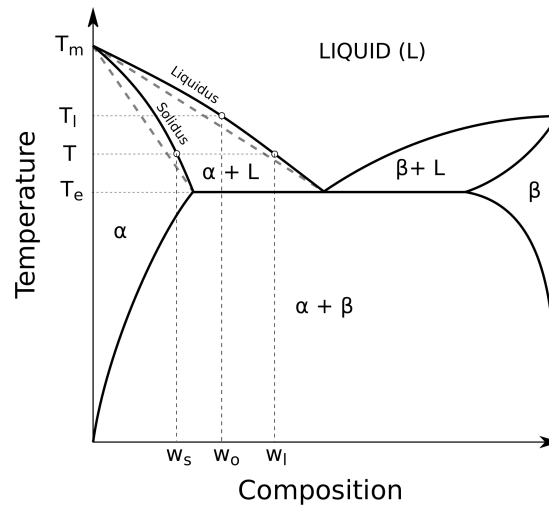
Figure 1.21 – Phase diagram of eutectic binary alloy showing the real solidus and liquidus along with the corresponding linear approximations (dashed grey lines). T_m and T_e are the melting point of the solvent and the eutectic temperature of the alloy respectively

diagram parameters by coupling the solidification models in SOLID®with CALPHAD databases.

SOLID®is a multiphase, volume averaged, euler-euler process scale model of solidification developed at Institut Jean Lamour (IJL), Nancy (Université de Lorraine) and is marketed by SCC® (Sciences Computers Consultants) (www.scconsultants.com). It is a 2D numerical simulation software used for the modeling of ingot and continuous casting. The model consists of two parts: a macroscopic part with mass, momentum, energy, solute mass and grain population conservation equations. The microscopic model describes the nucleation and growth of globular and dendritic grains. The complete model is described in Combeau *et al.* [38] and Zaloznik and Combeau [53]. Fig. 1.22 highlights the various sub-domains in the SOLID®model. The primary work of this thesis focuses on improving the phase thermodynamics (in blue) description and to study its eventual impact on various macro phenomenons.

Previous studies have focused on coupling the micro-model with CALPHAD data, as well as using the micro-model to simulate directional solidification of alloys to study various phenomena. However, the novelty of the current work with respect to the predecessors lies in using the CALPHAD coupled micro-model to simulate the macrosegregation in large industrial ingots accounting for grain motion. As will be described in the Chapter 2, the algorithm to simulate solidification with grain motion is already computationally expensive. Coupling the model with CALPHAD data increases the computational cost further. The approaches used in literature for coupling simulations with CALPHAD data are by using a tabulation approach [54] or direct coupling with Thermo-Calc®. Both of these approaches are computationally expensive if the number of solute elements goes beyond 2. Thus, we propose a novel approach to couple the CALPHAD data with the solidification model using neural networks.

1.6 Outline

The manuscript consists of 5 chapters. In chapter 2, a short review introduces the state-of-art in the literature of macroscopic modeling of solidification. The macroscopic transport equations are presented along with the microscopic model and the various constitutive relationships used to complete the model. Chapter 3 presents the various modifications required to couple the solidification model with CALPHAD data. Further, an efficient
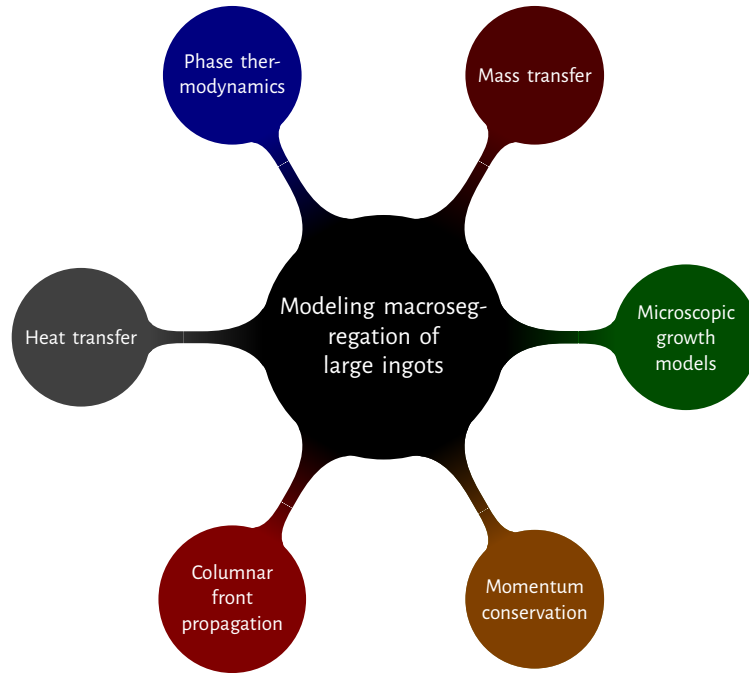
Figure 1.22 – A graphical representation of the main elements of multiscale modeling of solidifcation

approach to obtain the CALPHAD data is presented. Chapter 4 focuses on the constitutive models for the liquid diffusion length. An improvement over the already proposed liquid diffusion length model is presented. Chapter 5 employs the proposed modification to the implementation of the microscopic growth model (chapter 3), the efficient approach to obtain the CALPHAD data (chapter 3) and the new liquid diffusion length model (chapter 4) to model the solidification of experimental and industrial ingots. Chapter 6 presents the final conclusions and the future perspectives .

Chapter 2 : Volume averaging method for solidification modeling

Contents

Chapter 1 introduces the diversity of physical phenomena and their interactions involved in the creation of segregation and structure during casting. Thus, numerical modeling of solidification has always been a challenging problem. In the current section, the focus is on the advances in the mathematical modeling of solidification.

2.1   Review of macrosegregation modeling

The first studies that modeled the development of macrosegregation during alloy solidification were done by Flemings and his coworkers [55, 56, 57] in the 1960's which laid the foundation of future macrosegregation theory. Flemings and Nereo [55] proposed the local solute redistribution equation (LSRE) which modeled the solute redistribution in a mushy zone due to shrinkage induced flow at a prescribed cooling rate in unidirectional solidification. The local solute redistribution between solid and liquid was based on the assumption of perfect mixing of solute in the liquid phase and no mixing in the solid phase (Gulliver-Scheil model). The model gave a general expression for macrosegregation as a function of shrinkage flow velocity, thermal gradient in the mush and the cooling rate and enabled them to propose qualitative explanations for macrosegregation patterns in castings. The LSRE was further modified by Mehrabian *et al.* [58]. They accounted for gravity and thermal buoyancy by calculating the change in liquid density through a temperature gradient in the mushy zone. The liquid flow through the mushy zone was calculated using Darcy's law. This work was further extended to account for diffusion in solid [59, 60]. However, the fluid flow in the bulk liquid and mushy zone were still not coupled. This limitation was overcome by using multi-domain models.

The first multi-domain model was proposed by Ridder *et al.* [61]. For the mushy zone, they solved the coupled set of equations which described liquid motion due to thermal convection and shrinkage, the energy transfer and the LSRE. For the bulk liquid, the momentum and energy equations were solved. The two regions were coupled by imposing a boundary condition at the interface. The macrosegregation prediction compared favourably to the experimental measurements. The interface position is fixed in steady state solidification. However, for non-steady state solidification, interface tracking is required along with mesh size adaptation which are difficult and the biggest drawback of these models [62]. Single domain models were proposed to avoid the difficulties associated with the front tracking.

In contrast to the multi-domain models where the liquid, mushy zone and solid regions were modeled by separate equations and coupled via boundary conditions at the interface, single domain models are based on equations that are valid in all regions. Two separate approaches were adopted. The first approach was referred to as continuum mixture models. Mixture quantities, defined in terms of weighted mass or volume fraction of the phases (solid and liquid) were the dependent variables in the governing equations. Bennon, Incropera and Prescot [63, 64, 65] developed the first continuum mixture model accounting for advection-diffusion transport of mass, momentum, energy and species. Ni and Incropera [66, 67] further extended the continuum model to account for various microscopic phenomena which have an important impact on the macroscopic process by implementing the two phase grain growth models (to be reviewed later in this chapter). Vreeman *et al.* [68] extended the continuum model to account for equiaxed grain motion and its consequent effect on macrosegregation in grain refined casting. Within the mushy zone, separate momentum equations for the slurry (dispersed solid phase) and porous (fixed solid phase network) regions were employed. The transition from slurry to porous region was modeled by switching between the equations at a fixed solid fraction. Krane [69, 70] extended the work to account for ternary alloys. However, a major drawback with these continuum models was not accounting the interaction between the solid and liquid phases which resulted in poor resolution of grain

motion. Significant discrepancies were found between the model results and experimental data and to overcome the difficulties, a volume averaging model was proposed.

In order to obtain a system of equations at the macroscopic scale, the volume averaging approach proposed by Whitaker [71] involves integrating the local governing equations on a representative elementary volume (REV). It combines a volume averaging operator to smooth the space and a phase indicator function to distinguish between the fluid and solid phases. The equations for each phase are therefore true across the entire domain when the fluid and solid phases are replaced by an analogous continuous medium. At the macroscopic level, the spatial smoothing process generates open terms involving local quantities. These terms must be closed, and this approach's key challenge is establishing out closure models. This volume averaging method provides information on the porous medium's effective macroscopic properties and is successfully applied to a wide range of transfer problems. The establishment of the model is largely related to earlier research on the development of a volume-averaged solidification model by Ni and Beckermann [72], to the modeling of porous media flows by Whitaker [73], to the modeling of porous media formed by dendritic mushy zones by Goyeau *et al.* [74] and to Bousquet-Melou *et al.* [75]. Other significant works on application of volume averaging to solidification modeling were developed by Beckermann and coworkers [76, 77, 78] and by Ganesan and Poirier [79]. Volume averaging method is used for the conservation equations of mass, momentum and solute which results in separate volume average conservation equations for each phase. They are further supplemented with constitutive models. A comprehensive description of the volume averaging model is available in section 2.4. The main advantage of volume averaging two-phase models is the natural incorporation of the microscopic interphase phenomena and the clear link between the microscopic conservation equations (section 2.3) and the macroscopic volume averaged equations [80].

The earlier versions of the volume averaged models had several simplifications. These simplifications did not account for different length scales of diffusion in the liquid phase. This simplification further prohibited modeling of movement of equiaxed grains. It was common knowledge that the liquid between dendrites were more homogeneous as compared to the bulk liquid. Rappaz and Thevoz [81] proposed solute diffusion models for equiaxed dendritic growth by accounting for an additional phase, intragranular liquid to distinguish between the two liquid phases, the bulk liquid and the liquid between the dendrites. The advantage of this model was the ability to couple the model with macroscale models. Multiphase models proposed by Wang and Beckermann [82, 83, 84] incorporated the three phase description of the equiaxed grains which enabled better description of the grain morphology. Dendritic structures could now be modeled as compared to only globular structures in the previous models. Schneider and Beckermann [85] extended the model to multicomponent alloys. Incorporation of intragranular liquid meant that bulk liquid did not need to be homogeneous. Solute gradients could exist in the bulk liquid which resulted in constitutional supercooling in liquid and hence nucleation and growth of equiaxed grains. Until then, either complete mixing in the solid and liquid phase (lever rule) or Gulliver-Scheil model were used to determine the evolution of phase composition and phase fraction which did not allow for undercooled liquid. The microstructure growth model now related the phase change due to solidification to the local enthalpy change as well as the solute flux into the various phases. Using this approach, solute gradients in the bulk liquid could also exist for globular two phase models. Combeau *et al.* [38], Založnik and Combeau[86], Kumar *et al.* [87] highlight the importance of grain morphology on segregation and structure of large ingots. They compared experimental macrosegregation profiles to model predictions and found significant discrepancies when the equiaxed grains were assumed to be globular. Wu and Ludwig [88, 89] proposed a modified volume averaged equiaxed solidification model. The model considered two hydrodynamic phases (extragranular liquid and the equiaxed grain envelope) along with three thermo-

dynamic phases (solid, intragranular liquid and extragranular liquid). The intragranular liquid was not considered to be homogeneous. The model also accounted for globular to dendritic transition (GDT) of equiaxed grains. The model was further developed to account for columnar solidification [90, 91] which resulted in 5 thermodynamic phases (columnar solid, columnar intragranular liquid, extragranular liquid, equiaxed solid and equiaxed intragranular liquid) along with 3 hydrodynamic phases (columnar grain envelope, extragranular liquid and equiaxed grain envelope). Založnik and Combeau [53] proposed the splitting algorithm to model equiaxed solidification using two phase globular model which was extended by Tveito *et al.* [92] and Bedel *et al.* [93] to model flow of inoculants and study its impact on macrosegregation. Further, Tveito *et al.* [94] proposed a simplified three phase dendritic solidification model by assuming uniform composition of the intragranular liquid. This model will be discussed in more detail in this chapter. Recently, Ge *et al.* [95] extended the three phase model to four phase model. The fourth phase is "air" and it has been incorporated to account for shrinkage of liquid metal during solidification.

2.2 Numerical modeling of macrosegregation
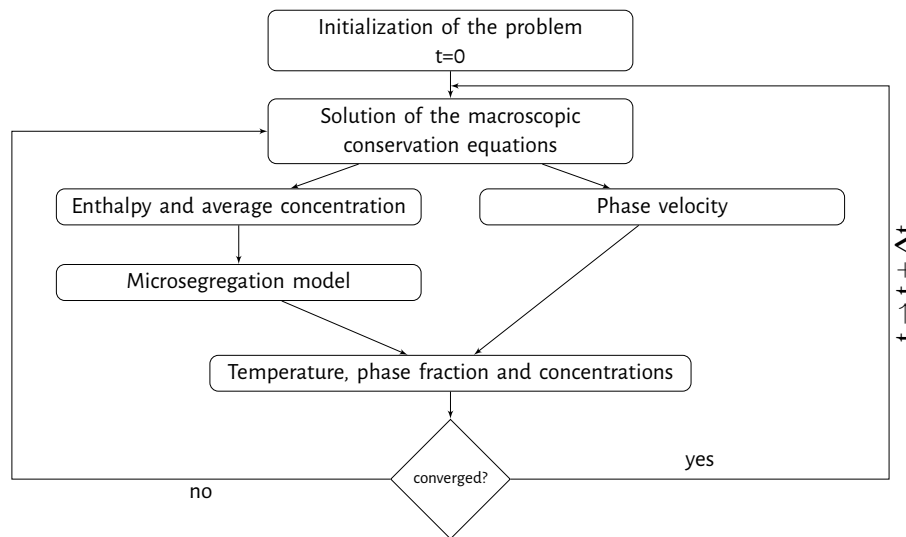
Figure 2.1 – Algorithm for modeling of macrosegregation

The goal of macrosegregation modeling is to predict the inhomogeneities in solute concentration at the scale of the cast product. Such modeling requires the resolution of continuity equations at the macroscopic scale. It is assumed that the time step used during modeling is Δt. Using the information at time t, the following variables are computed: average fluid and solid velocity, pressure, specific enthalpy and average solute concentration at time $t + \Delta t$. The local known variations of the enthalpy and average solute concentration is used to deduce the local solidification path through which temperature, phase fraction and average concentration of solid and liquid are obtained. This algorithm has been shown in Fig. 2.1. The local solidification paths are modeled through various microscopic models which account for solute and enthalpy partitioning between the solid and liquid phases during solidification. The diversity of physical phenomena involved in the creation of macrosegregation along with their complex interaction makes numerical modeling of macrosegregation a challenging problem to solve. Some of the challenges encountered during modeling (as mentioned in Založnik [96]) are:

– **Multiple scales:** As mentioned in the previous chapter, macrosegregation is a multiscale phenomena. The solute partitioning between the solid and liquid phases occurs at the scale of s/l interface ($\sim$1nm) [97]. The solute redistribution occurs at the length scale of dendritic structures ($\sim$10 μm) in the time scale equivalent with the total solidification time. Macroscopic solute transport along with heat and momentum transport occur at the length scale of the cast product ($\sim$1m).

– **Coupling of solidification with transport:** As shown in Fig. 2.1, the microscopic model determines the local parameters such as temperature, phase composition and phase fraction which subsequently affects the transport of mass, momentum, heat and solute. Thus, there is a strong coupling between the local solidification dynamics and the global transport of mass, momentum, heat and solute.

– **Numerical solution:** The solidification model that would be presented in the following section results in a complex system of coupled partial differential equations (PDE). A consistent approach to solve these PDEs is critical to insure numerical stability of the computed fields, specially in cases when steep gradients occur in an otherwise smooth field. These issues can arise in the mushy zone, in the boundary layers and across the bulk liquid due to unstable liquid convection patterns.

Scale disparities at the microscopic and macroscopic transport along with the various interphase interactions which arise due to the complex interface morphology make the use of microscopic conservation equations to model solidification impractical. To cope with the challenges posed by solidification modeling, the volume averaging method is employed which takes advantage of the large scale disparities. The microscopic conservation equations are averaged over an averaging volume that is large compared to the scale of the microscopic phenomena and small compared to the scale of macroscopic phenomena (more details in section 2.4). Using this approach, the macroscopic system is modeled and incorporate the effects of the microscopic phenomena through various source terms in the volume averaged equations linked to phenomenological models. In the next section, the microscopic conservation equations are discussed after which the volume averaged macroscopic conservation equations.

2.3   Microscopic conservation equations

In fluid mechanics, microscopic conservation equations are applied over a fixed volume of space called control volumes by employing Reynolds transport theorem which provides the link between systems in continuum mechanics and control volumes in fluid mechanics. For any extensive property ψ of phase ϕ, the microscopic transport equation is

$$\frac{\partial (\psi_\phi)}{\partial t} + \nabla \cdot (\psi_\phi \vec{v_\psi}) = -\nabla \cdot J_\psi + S_\psi \tag{2.1}$$

where $\vec{v_\phi}$ is the phase velocity, J is a tensor which accounts for diffusion of momentum, heat or species and S is the source term. The microscopic conservation equations for total mass, momentum, energy and mass of species for a phase ϕ are

$$\frac{\partial \rho_\phi}{\partial t} + \nabla \cdot (\rho_\phi \vec{v_\phi}) = 0 \tag{2.2}$$

$$\frac{\partial (\rho_\phi \vec{v_\phi})}{\partial t} + \nabla \cdot (\rho_\phi \vec{v_\phi} \vec{v_\phi}) = -\nabla p + \nabla \cdot \tau_\phi + \vec{b_\phi} \tag{2.3}$$

$$\frac{\partial (\rho_\phi h_\phi)}{\partial t} + \nabla \cdot (\rho_\phi h_\phi \vec{v_\phi}) = -\nabla \cdot (-k_\phi \nabla T) \tag{2.4}$$

$$\frac{\partial\left(\rho_\phi c_\phi\right)}{\partial t} + \nabla \cdot \left(\rho_\phi c_\phi \vec{v_\phi}\right) = -\nabla \cdot \left(-\rho_\phi D_\phi \nabla c_\phi\right) \tag{2.5}$$

where ρ_ϕ is the density, p is the pressure, τ is the tangential stress tensor, $\vec{b}$ is the body force, h_ϕ is the specific enthalpy, k_ϕ is the thermal conductivity, T is the temperature, c_ϕ is the mass fraction concentration of solute and D_ϕ is the diffusion coefficient, all for phase ϕ. The heat and mass diffusion fluxes are modeled using the Fourier and Ficks law respectively. In multiphase systems, these equations must be solved for boundary conditions located at one of more phase interfaces. Modeling of solute diffusion and microstructure formation requires a detailed solution of a boundary value problem. However, for large scale solidification simulations, the interfacial configuration is complex. A detailed solution of the boundary value problem is impossible and/or computationally expensive as the characteristic length scale over which the point variables undergo significant variation is small compared to the length over which macroscopic observations are made. In such cases, knowledge of volume averaged quantities is sufficient.

2.4   Volume averaging method

According to Whitaker (1999), the majority of porous media with practical significance have a hierarchical structure, or more than one length scale. The volume averaging method can be used to study the hierarchical structure when these length scales are dissimilar. The microscopic conservation equations are averaged over a macroscopic scale. The averaging is performed over a 'Representative Elementary Volume' (REV) of volume V with the following dimensional constraint: the element should be able to account for the average microscopic fluctuations while being smaller than the scale of macroscopic variation. By using this REV, the microscopic conservation equations are upscaled to be used for macroscopic solidification modeling. This has been depicted in Fig. 2.2 which shows a porous media with a length scale L composed of the solid and liquid phases and a REV of length scale l with $l \ll L$. The process scale L is in the range of 10^{-1} - 10^{0} m while the length scale for the interfacial structures (inside the enlarged area) is in the range of 10^{-5} - 10^{-4} m . Thus, the length scale of the REV is in the range of 10^{-3} - 10^{-2} m.
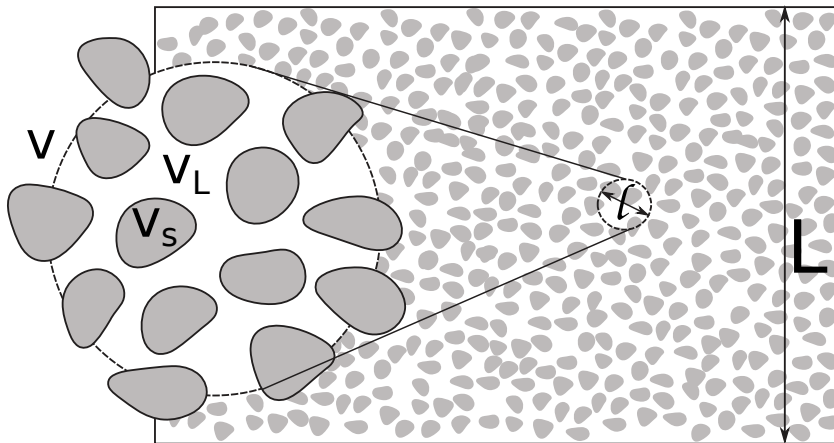
Figure 2.2 – Illustration of volume averaging method

The volume average of any physical quantity ψ in the system is

$$\langle\psi\rangle = \frac{1}{V}\int_V \psi\,\mathrm{d}V \tag{2.6}$$

where V is the volume of the REV. The local value of the variable is

$$\psi = \langle\psi\rangle + \hat{\psi} \tag{2.7}$$

where $\langle\psi\rangle$ is the average over an REV centered in the point of interest and $\hat{\psi}$ is the local deviation from the average in the point of interest. Hence,

$$\langle\hat{\psi}\rangle = 0 \tag{2.8}$$

A phase indicator function for any phase ϕ in a multiphase system is introduced and is defined as:

$$X_\phi(\vec{x}, t) = \begin{cases} 1 & \text{where position } \vec{x} \text{ is in phase } \phi \text{ at time } t \\ \\ 0 & \text{otherwise} \end{cases} \tag{2.9}$$

The phase indicator function X_ϕ picks out the phase ϕ such that $\psi_\phi = X_\phi\psi$. The volume averaging of the phase function in the REV is the phase volume fraction g_ϕ:

$$\langle X_\phi\rangle = \frac{1}{V}\int_V X_\phi\,\mathrm{d}V = \frac{V_\phi}{V} = g_\phi \tag{2.10}$$

The gradient of X_ϕ is zero everywhere except at the phase interface where the magnitude is equal to the Dirac delta function, δ, in a direction normal to the phase interface into the phase ϕ, $\vec{n_\phi}$,:

$$\nabla X_\phi = \left(\frac{\partial X_\phi}{\partial n}\right)\vec{n_\phi} = \delta\left(\vec{x} - \vec{x_i}\right)\vec{n_\phi} \tag{2.11}$$

The general properties of the function $\dfrac{\partial X_\phi}{\partial n}$ are:

$$\int_V \frac{\partial X_\phi}{\partial n}\psi\,\mathrm{d}V = \int_{A_\phi}\psi\,\mathrm{d}A \tag{2.12}$$

$$\left\langle\frac{\partial X_\phi}{\partial x}\right\rangle = \frac{1}{V}\int_V \frac{\partial X_\phi}{\partial x}\,\mathrm{d}V = \frac{1}{V}\int_{A_\phi}\mathrm{d}A = \frac{A_i}{V} = S_i \tag{2.13}$$

where A_i is the phase interface area and S_i is the volumetric interface density. Further, Drew [80] shows that the phase indicator function obeys the relationship

$$\frac{\partial X_\phi}{\partial t} + \vec{v_i}.\nabla X_\phi = 0 \tag{2.14}$$

where $\vec{v_i}$ is the local relative phase interface velocity. The volume average of ψ in phase ϕ over volume V is defined by:

$$\langle\psi_\phi\rangle = \frac{1}{V}\int_V X_\phi\psi\,\mathrm{d}V = \langle X_\phi\psi\rangle \tag{2.15}$$

and the intrinsic volume average, the average value of ψ inside phase ϕ is defined as:

$$\langle \psi_\phi \rangle^\phi = \frac{1}{V_\phi} \int_V X_\phi \psi \, \mathrm{d}V = \frac{\langle \psi_\phi \rangle}{g_\phi} \tag{2.16}$$

Further, the volume averaging operation is applied to temporal and spatial derivation operators.

    – Temporal derivative operator:

$$\langle \left(\frac{\partial \psi}{\partial t} \right)_\phi \rangle = \frac{\partial \left(g_\phi \langle \psi \rangle^\phi \right)}{\partial t} + \frac{1}{V} \int_{A_\phi} \psi_\phi \vec{v}_i . \vec{n}_\phi \, \mathrm{d}A \tag{2.17}$$

    – Spatial derivative operator:

$$\langle \nabla \psi_\phi \rangle = g_\phi \nabla \langle \psi_\phi \rangle^\phi - \frac{1}{V} \int_{A_\phi} \psi_\phi \vec{n}_\phi \, \mathrm{d}A \tag{2.18}$$

where $\vec{n}_\phi$ is the direction normal to the interface and the surface integral terms in Eqs.2.17 and 2.18 express the exchanges between the phases across the interface. Using these equations, the microscopic conservation equations are upscaled and subsequently used to derive macroscopic conservation equations which are used within the framework of solidification modeling as shown in Fig. **??** and described in the following section.

2.5   Volume averaged macroscopic conservation equations

In this section, the macroscopic conservation equations implemented in SOLID®are presented which have been described by the authors for two phase globular and three phase dendritic models [38, 53]. The authors use an operator splitting scheme to split and combine the contribution of the microscopic and macroscopic solidification phenomena. In this scheme, the total variation of phase and solute concentration during solidification is due to the macroscopic transport phenomena and the microscopic nucleation and growth phenomena. The operator splitting scheme will be discussed in more detail in section 2.7. However, in accordance with the operator splitting scheme, the macroscopic conservation equations are presented and followed with the microscopic growth model.

2.5.1   Hypothesis

The following general assumptions are applied to the model:

    – Densities are assumed to be constant and equal in all phases except in the buoyancy terms (However, the equations presented in the chapter distinguish between ρ_s and ρ_l so as to be more generic)

    – The diffusion fluxes obey Fick's law

    – No creation of solute

    – In metallic alloys, thermal diffusion is very fast compared to chemical diffusion. Thus, the temperature is assumed to be homogeneous

    – Thermodynamic equilibrium at the s/l interface

2.5.2 Mass conservation

The volume averaged mass conservation equations for phase ϕ is obtained by applying the volume averaging laws to Eq. 2.2. The temporal term is written as:

$$\left\langle X_\phi \frac{\partial (\rho)}{\partial t} \right\rangle = \frac{\partial \left(g_\phi \langle \rho_\phi \rangle^\phi \right)}{\partial t} + \frac{1}{V} \int_{A_\phi} \rho_\phi \vec{v_i} . \vec{n_\phi} \, \mathrm{d}A \tag{2.19}$$

The advective term is written as:

$$\left\langle X_\phi \nabla \cdot (\rho \vec{v}) \right\rangle = \nabla \cdot \left(g_\phi \langle \rho_\phi \rangle^\phi \langle \vec{v}_\phi \rangle^\phi \right) + \nabla \cdot \left(\langle g_\phi \rangle^\phi \langle \hat{\rho}_\phi \hat{\vec{v}}_\phi \rangle^\phi \right) - \frac{1}{V} \int_{A_\phi} \rho_\phi \vec{v_\phi} . \vec{n_\phi} \, \mathrm{d}A \tag{2.20}$$

It can be assumed that the contribution of density fluctuations on the averaged product of density and any quantity ψ is small,

$$\langle \hat{\rho}_\phi \psi_\phi \rangle \approx 0 \qquad \langle \hat{\rho}_\phi \hat{\psi}_\phi \rangle \approx 0 \tag{2.21}$$

Using Eq. 2.21 and combining the last two terms in Eqs. 2.19 and 2.20,

$$\frac{1}{V} \int_{A_\phi} \rho_\phi \left(\vec{v_\phi} - \vec{v_i}\right) . \vec{n_\phi} \, \mathrm{d}A = \Gamma_\phi \tag{2.22}$$

where Γ_ϕ is the mass transfer rate of phase ϕ across the phase interface due to relative movement of the interface and is termed as 'interfacial phase change rate'. The mass transfer rate due to "nucleation" of new grains which is denoted by Φ_ϕ is also accounted for. There "nucleation" and "grain growth" phenomena are microscopic phenomena and their modeling will be discussed in section 2.6. The final volume averaged mass conservation equation for phase ϕ is written as:

$$\frac{\partial \left(g_\phi \rho_\phi \right)}{\partial t} + \nabla \cdot \left(g_\phi \rho_\phi \langle \vec{v}_\phi \rangle^\phi \right) = \Gamma_\phi + \Phi_\phi \tag{2.23}$$

where $\langle \rho \rangle^\phi$ is replaced with ρ_ϕ as they are equivalent. The one phase formulation can be obtained by adding the continuity equations for the solid and liquid phase. Accounting for mass conservation at the s/l interface

$$\Gamma_\mathrm{s} + \Phi_\mathrm{s} + \Gamma_\mathrm{l} + \Phi_\mathrm{l} = 0 \tag{2.24}$$

$$\frac{\partial (\rho_\mathrm{m})}{\partial t} + \nabla \cdot (\rho_\mathrm{m} \langle \vec{v} \rangle) = 0 \tag{2.25}$$

where ρ_m is the average density

$$\rho_\mathrm{m} = (g_\mathrm{s} \rho_\mathrm{s} + g_\mathrm{l} \rho_\mathrm{l}) \tag{2.26}$$

and $\langle \vec{v} \rangle$ is the mixture velocity

$$\langle \vec{v} \rangle = \left(\frac{\rho_\mathrm{s}}{\rho_\mathrm{m}}\right) g_\mathrm{s} \langle \vec{v_\mathrm{s}} \rangle^\mathrm{s} + \left(\frac{\rho_\mathrm{l}}{\rho_\mathrm{m}}\right) g_\mathrm{l} \langle \vec{v_\mathrm{l}} \rangle^\mathrm{l} \tag{2.27}$$

2.5.3   Energy conservation

The volume averaged energy conservation equations for phase ϕ is obtained by applying the volume averaging laws to Eq. 2.4 The temporal term is written as:

$$\left\langle X_\phi \frac{\partial (\rho h)}{\partial t} \right\rangle = \frac{\partial \left(g_\phi \langle \rho_\phi h_\phi \rangle^\phi \right)}{\partial t} + \frac{1}{V} \int_{A_\phi} \rho_\phi h_\phi \vec{v_i}.\vec{n_\phi} \, \mathrm{d}A$$

$$\implies \left\langle X_\phi \frac{\partial (\rho h)}{\partial t} \right\rangle = \frac{\partial \left(g_\phi \langle \rho_\phi \rangle^\phi \langle h_\phi \rangle^\phi \right)}{\partial t} + \overbrace{\frac{\partial \left(g_\phi \langle \hat{\rho_\phi} \hat{h_\phi} \rangle \right)}{\partial t}}^{\approx 0} + \frac{1}{V} \int_{A_\phi} \rho_\phi h_\phi \vec{v_i}.\vec{n_\phi} \, \mathrm{d}A \qquad (2.28)$$

The advective term is written as:

$$\left\langle X_\phi \nabla \cdot (\rho h \vec{v}) \right\rangle = \nabla \cdot \left(g_\phi \langle \rho_\phi h_\phi \vec{v_\phi} \rangle^\phi \right) - \frac{1}{V} \int_{A_\phi} \rho_\phi h_\phi \vec{v_\phi}.\vec{n_\phi} \, \mathrm{d}A$$

$$\implies \left\langle X_\phi \nabla \cdot (\rho h \vec{v}) \right\rangle = \nabla \cdot \left(g_\phi \langle \langle \rho_\phi \rangle^\phi \langle h_\phi \vec{v_\phi} \rangle^\phi \rangle^\phi \right) + \overbrace{\nabla \cdot \left(g_\phi \langle \hat{\rho_\phi} \widehat{h_\phi \vec{v_\phi}} \rangle^\phi \right)}^{\approx 0} - \frac{1}{V} \int_{A_\phi} \rho_\phi h_\phi \vec{v_\phi}.\vec{n_\phi} \, \mathrm{d}A$$

$$\implies \left\langle X_\phi \nabla \cdot (\rho h \vec{v}) \right\rangle = \nabla \cdot \left(g_\phi \langle \rho_\phi \rangle^\phi \langle h_\phi \rangle^\phi \langle \vec{v_\phi} \rangle^\phi \right) + \nabla \cdot \left(g_\phi \langle \rho_\phi \rangle^\phi \langle \hat{h_\phi} \hat{\vec{v_\phi}} \rangle^\phi \right) - \frac{1}{V} \int_{A_\phi} \rho_\phi h_\phi \vec{v_\phi}.\vec{n_\phi} \, \mathrm{d}A$$
$$(2.29)$$

The diffusive term is written as:

$$\left\langle X_\phi \nabla \cdot (k \nabla T) \right\rangle = \nabla \cdot \left(g_\phi \langle k_\phi \nabla T \rangle^\phi \right) - \frac{1}{V} \int_{A_\phi} k_\phi \nabla T_\phi.\vec{n_\phi} \, \mathrm{d}A$$

$$\left\langle X_\phi \nabla \cdot (k \nabla T) \right\rangle = \nabla \cdot \left(g_\phi \langle k_\phi \rangle^\phi \langle \nabla T_\phi \rangle^\phi \right) + \nabla \cdot \left(g_\phi \langle \hat{k_\phi} \widehat{\nabla T_\phi} \rangle^\phi \right) \qquad (2.30)$$

The final volume averaged energy conservation equation for phase ϕ is

$$\frac{\partial \left(g_\phi \langle \rho_\phi \rangle^\phi \langle h_\phi \rangle^\phi \right)}{\partial t} + \nabla \cdot \left(g_\phi \langle \rho_\phi \rangle^\phi \langle h_\phi \rangle^\phi \langle \vec{v_\phi} \rangle^\phi \right) = \nabla \cdot \left(g_\phi \langle k_\phi \rangle^\phi \langle \nabla T_\phi \rangle^\phi \right)$$
$$+ Q_\phi{}^\Gamma + Q_\phi{}^j + \nabla \cdot \left(\vec{q_\phi}{}^t \right) + \nabla \cdot \left(g_\phi \langle \vec{q_\phi}{}^d \rangle^\phi \right) \qquad (2.31)$$

where $Q_\phi{}^\Gamma$ is the energy exchange due to movement of the phase interface, $Q_\phi{}^j$ is the diffusive heat flux across the interface, $\vec{q_\phi}{}^t$ is the tortuosity flux and $\langle \vec{q_\phi}{}^d \rangle^\phi$ is the dispersion flux. In the context of solidification, the dispersion and tortuosity terms can be neglected [96]. Further, similar to the mass conservation, the heat flux due to nucleation, $Q_\phi{}^\Phi$ is introduced. The final energy conservation equation is

$$\frac{\partial \left(g_\phi \rho_\phi \langle h_\phi \rangle^\phi \right)}{\partial t} + \nabla \cdot \left(g_\phi \rho_\phi \langle h_\phi \rangle^\phi \langle \vec{v_\phi} \rangle^\phi \right) = \nabla \cdot \left(g_\phi \langle k_\phi \rangle^\phi \langle \nabla T_\phi \rangle^\phi \right)$$
$$+ Q_\phi{}^\Gamma + Q_\phi{}^j + Q_\phi{}^\Phi \qquad (2.32)$$

However, local thermal equilibrium in the REV is assumed. Thus, there is no need to separately model the heat transport in the two phases, allowing to switch from a two phase formulation to a single phase formulation. Since energy is conserved, the interfacial exchange terms cancel out.

$$Q_s{}^\Gamma + Q_l{}^\Gamma + Q_s{}^j + Q_l{}^j + Q_s{}^\Phi + Q_l{}^\Phi = 0 \tag{2.33}$$

Defining the average mixture enthalpy $\langle h \rangle$ as

$$\langle h \rangle = \left(\frac{\rho_s}{\rho_m} \right) g_s \langle h_s \rangle^s + \left(\frac{\rho_l}{\rho_m} \right) g_l \langle h_l \rangle^l \tag{2.34}$$

and k_m as the average mixture conductivity,

$$k_m = \left(g_s \langle k_s \rangle^s + g_l \langle k_l \rangle^l \right) \tag{2.35}$$

by adding the average energy equations in the two phases.

$$\frac{\partial \left(\rho_m \langle h \rangle \right)}{\partial t} + \nabla \cdot \left(g_s \rho_s \langle h_s \rangle^s \langle \vec{v}_s \rangle^s + g_l \rho_l \langle h_l \rangle^l \langle \vec{v}_l \rangle^l \right) = \nabla \cdot (k_m \nabla T) \tag{2.36}$$

2.5.4 Solute conservation

The volume averaged energy conservation equations for phase ϕ is obtained by applying the volume averaging laws to Eq. 2.5. The temporal term is written as:

$$\left\langle X_\phi \frac{\partial (\rho c)}{\partial t} \right\rangle = \frac{\partial \left(g_\phi \langle \rho_\phi \rangle^\phi \langle c_\phi \rangle^\phi \right)}{\partial t} + \frac{1}{V} \int_{A_\phi} \rho_\phi c_\phi \vec{v}_i . \vec{n_\phi} \, \mathrm{d}A \tag{2.37}$$

The advective term is written as:

$$\left\langle X_\phi \nabla \cdot (\rho c \vec{v}) \right\rangle = \nabla \cdot \left(g_\phi \langle \rho_\phi \rangle^\phi \langle c_\phi \rangle^\phi \langle \vec{v}_\phi \rangle^\phi \right) + \nabla \cdot \left(\langle g_\phi \rangle^\phi \langle \rho_\phi \rangle^\phi \langle \hat{c}_\phi \hat{\vec{v}}_\phi \rangle^\phi \right) - \frac{1}{V} \int_{A_\phi} \rho_\phi c_\phi \vec{v}_\phi . \vec{n_\phi} \, \mathrm{d}A \tag{2.38}$$

The diffusive term is written as:

$$\left\langle X_\phi \nabla \cdot (\rho D \nabla c) \right\rangle = \nabla \cdot \left(g_\phi \langle \rho_\phi \rangle^\phi \langle D_\phi \rangle^\phi \nabla \langle c_\phi \rangle^\phi \right) - \nabla \cdot \left(\langle \rho_\phi \rangle^\phi \langle D_\phi \rangle^\phi \frac{1}{V} \int_{A_\phi} \hat{c}_\phi \vec{n_\phi} \, \mathrm{d}A \right)$$
$$- \frac{1}{V} \int_{A_\phi} \rho_\phi D_\phi \nabla c_\phi \vec{n_\phi} \, \mathrm{d}A \tag{2.39}$$

The final volume averaged solute conservation equation for phase ϕ is written as:

$$\frac{\partial \left(g_\phi \langle \rho_\phi \rangle^\phi \langle c_\phi \rangle^\phi \right)}{\partial t} + \nabla \cdot \left(g_\phi \langle \rho_\phi \rangle^\phi \langle c_\phi \rangle^\phi \langle \vec{v}_\phi \rangle^\phi \right) = \nabla \cdot \left(g_\phi \langle \rho_\phi \rangle^\phi \langle D_\phi \rangle^\phi \nabla \langle c_\phi \rangle^\phi \right)$$
$$\underbrace{J_\phi^\tau + J_\phi^j + J_\phi^\Phi}_{\text{microscopic transport}} + \underbrace{\vec{J}_\phi^{\,t} + \nabla \cdot \left(g_\phi \langle \vec{J}_\phi^d \rangle^\phi \right)}_{\text{macroscopic transport}} \tag{2.40}$$

where J_ϕ^τ is the solute flux due to movement of the phase interface, J_ϕ^j is the solute flux due to diffusion across the interface, J_ϕ^Φ is the solute flux due to nucleation/remelting of solid grains (further explained in section

2.6.2.1), $\vec{J}_\phi^{\,t}$ is the tortuosity flux and $\langle \vec{J_\phi^d} \rangle^\phi$ is the dispersion flux and are given by:

$$J_\phi^\tau = \frac{1}{V} \int_{A_\phi} \rho_\phi c_\phi \left(\vec{v_i} - \vec{v_\phi} \right).\vec{n_\phi}\,\mathrm{d}A \tag{2.41}$$

$$J_\phi^j = \frac{1}{V} \int_{A_\phi} \rho_\phi D_\phi \nabla c_\phi \vec{n_\phi}\,\mathrm{d}A \tag{2.42}$$

$$\vec{J}_\phi^{\,t} = -\langle \rho_\phi \rangle^\phi \langle D_\phi \rangle^\phi \frac{1}{V} \int_{A_\phi} \hat{c}_\phi \vec{n_\phi}\,\mathrm{d}A \tag{2.43}$$

$$\langle \vec{J_\phi^d} \rangle^\phi = -\langle \rho_\phi \rangle^\phi \langle \hat{c}_\phi \hat{\vec{v}}_\phi \rangle^\phi \approx \langle \rho_\phi \hat{c}_\phi \hat{\vec{v}}_\phi \rangle^\phi \tag{2.44}$$

and are obtained through various constitutive models. The one phase formulation of solute conservation is

$$\frac{\partial \left(\rho_\mathrm{m} c_\mathrm{m} \right)}{\partial t} + \nabla \cdot \left(\rho_\mathrm{m} c_\mathrm{m} \vec{v}_\mathrm{m} \right) = \nabla \cdot \left(\rho_\mathrm{m} D_\mathrm{m} \nabla c_\mathrm{m} \right)$$
$$+\nabla \cdot \left[\rho_\mathrm{m} c_\mathrm{m} \vec{v}_\mathrm{m} - g_\mathrm{s} \langle \rho_\mathrm{s} \rangle^\mathrm{s} \langle c_\mathrm{s} \rangle^\mathrm{s} \langle \vec{v}_\mathrm{s} \rangle^\mathrm{s} - g_\mathrm{l} \langle \rho_\mathrm{l} \rangle^\mathrm{l} \langle c_\mathrm{l} \rangle^\mathrm{l} \langle \vec{v}_\mathrm{l} \rangle^\mathrm{l} \right] \tag{2.45}$$
$$+\nabla \cdot \left[\rho_\mathrm{m} D_\mathrm{m} \nabla c_\mathrm{m} - g_\mathrm{s} \langle \rho_\mathrm{s} \rangle^\mathrm{s} D_\mathrm{s} \langle c_\mathrm{s} \rangle^\mathrm{s} - g_\mathrm{l} \langle \rho_\mathrm{l} \rangle^\mathrm{l} D_\mathrm{l} \langle c_\mathrm{l} \rangle^\mathrm{l} \right]$$

As will be discussed in the following sections, the two phase formulation of the solute conservation equation is eventually employed.

2.5.5   Momentum conservation

The volume averaged energy conservation equations for phase ϕ is obtained by applying the volume averaging laws to Eq. 2.3. The temporal and advective terms for the momentum conservation equations are analogous to those for energy conservation with the only difference being that the h term is replaced with $\vec{v}$. Thus the first two terms are

$$\left\langle X_\phi \frac{\partial \left(\rho \vec{v} \right)}{\partial t} \right\rangle = \frac{\partial \left(g_\phi \langle \vec{v}_\phi \rangle^\phi \langle h_\phi \rangle^\phi \right)}{\partial t} + \frac{1}{V} \int_{A_\phi} \rho_\phi \vec{v}_\phi \vec{v_i}.\vec{n_\phi}\,\mathrm{d}A \tag{2.46}$$

$$\left\langle X_\phi \nabla \cdot \left(\rho \vec{v} \vec{v} \right) \right\rangle = \nabla \cdot \left(g_\phi \langle \rho_\phi \rangle^\phi \langle \vec{v}_\phi \rangle^\phi \langle \vec{v_\phi} \rangle^\phi \right) + \nabla \cdot \left(g_\phi \langle \rho_\phi \rangle^\phi \langle \hat{\vec{v}}_\phi \hat{\vec{v}}_\phi \rangle^\phi \right) - \frac{1}{V} \int_{A_\phi} \rho_\phi \vec{v}_\phi \vec{v_\phi}.\vec{n_\phi}\,\mathrm{d}A \tag{2.47}$$

The pressure term is averaged as

$$-\langle X_\phi \nabla p \rangle = -\nabla \left(g_\phi \langle p_\phi \rangle^\phi \right) + \frac{1}{V} \int_{A_\phi} p_\phi \vec{n_\phi}\,\mathrm{d}A = -\nabla \left(g_\phi \langle p_\phi \rangle^\phi \right) + \vec{M}_\phi^\mathrm{P} \tag{2.48}$$

where $\vec{M}_\phi^\mathrm{P}$ is the interfacial pressure force. The tangential stress term is averaged as

$$\langle X_\phi \nabla \cdot \tau \rangle = \nabla \cdot \left(g_\phi \langle \tau_\phi \rangle^\phi \right) - \frac{1}{V} \int_{A_\phi} \tau_\phi.\vec{n_\phi}\,\mathrm{d}A = \nabla \cdot \left(g_\phi \langle \tau_\phi \rangle^\phi \right) + \vec{M}_\phi^\mathrm{d} \tag{2.49}$$

where $\vec{M}_\phi^{\mathrm{d}}$ is the interfacial drag force. The body force (buoyancy) term is averaged as

$$\langle X_\phi \vec{b} \rangle = g_\phi \langle b_\phi \rangle^\phi \tag{2.50}$$

The interfacial pressure force $\vec{M}_\phi^{\mathrm{p}}$ and interfacial drag force $\vec{M}_\phi^{\mathrm{d}}$ are added together and referred to as $\vec{M}_\phi^\tau$. The interface momentum exchange due to phase change is

$$\frac{1}{V} \int_{A_\phi} \rho_\phi \vec{v}_\phi \left(\vec{v}_i - \vec{v}_\phi \right) . \vec{n_\phi} \, \mathrm{d}A = \vec{M}_\phi^\Gamma \tag{2.51}$$

The second term in Eq. 2.47 arises from the averaging of the velocity fluctuations and is written as a stress τ_ϕ^t [72], analogous to the Reynolds turbulent stress in modeling of turbulent flow.

$$-\nabla \cdot \left(g_\phi \langle \rho_\phi \rangle^\phi \langle \hat{\vec{v}}_\phi \hat{\vec{v}}_\phi \rangle^\phi \right) = \nabla \cdot \left(g_\phi \langle \tau_\phi^t \rangle^\phi \right) \tag{2.52}$$

Bousquet-Melou *et al.* [75] have shown that $\nabla \cdot \left(g_\phi \langle \tau_\phi^t \rangle^\phi \right)$ can be neglected. There are other simplifications which are possible and not discussed here. Readers are referred to Bousquet-Melou *et al.* [75] and Založnik [96] for more information. Mechanical equilibrium is assumed such that $\langle p_{\mathrm{s}} \rangle^{\mathrm{s}} = \langle p_{\mathrm{l}} \rangle^{\mathrm{l}} = p$. The final volume averaged momentum equation for phase ϕ after incorporating the interface momentum exchange due to nucleation ($\vec{M}_\phi^\Phi$) is written as

$$\frac{\partial \left(g_\phi \rho_\phi \langle \vec{v}_\phi \rangle^\phi \right)}{\partial t} + \nabla \cdot \left(g_\phi \rho_\phi \langle \vec{v}_\phi \rangle^\phi \langle \vec{v}_\phi \rangle^\phi \right) = -g_\phi \nabla(p) + \nabla \cdot \left(g_\phi \langle \tau_\phi \rangle^\phi \right) +$$
$$g_\phi \langle b_\phi \rangle^\phi + \vec{M}_\phi^\Gamma + \vec{M}_\phi^\Phi + \vec{M}_\phi^{\mathrm{d}} \tag{2.53}$$

Two approaches have been implemented to model the momentum conservation:

- **Approach 1** [53]: In this approach, for the solid momentum conservation equation, the inertial terms are neglected, viscous term, nucleation term and the phase change term. The equation for the solid momentum conservation reduces to

$$-g_{\mathrm{s}} \nabla(p) + g_{\mathrm{s}} \langle b_{\mathrm{s}} \rangle^{\mathrm{s}} + \vec{M}_{\mathrm{s}}^{\mathrm{d}} = \vec{0} \tag{2.54}$$

  For the liquid phase, the nucleation and phase change terms are neglected.

$$\frac{\partial \left(g_{\mathrm{l}} \rho_{\mathrm{l}} \langle \vec{v}_{\mathrm{l}} \rangle^{\mathrm{l}} \right)}{\partial t} + \nabla \cdot \left(g_{\mathrm{l}} \rho_{\mathrm{l}} \langle \vec{v}_{\mathrm{l}} \rangle^{\mathrm{l}} \langle \vec{v}_{\mathrm{l}} \rangle^{\mathrm{l}} \right) = -g_{\mathrm{l}} \nabla(p) + \nabla \cdot \left(g_{\mathrm{l}} \langle \tau_{\mathrm{l}} \rangle^{\mathrm{l}} \right) + g_{\mathrm{l}} \langle b_{\mathrm{l}} \rangle^{\mathrm{l}} + \vec{M}_{\mathrm{l}}^{\mathrm{d}} \tag{2.55}$$

  Eqs. 2.54 and 2.55 added together gives

$$\frac{\partial \left(g_{\mathrm{l}} \rho_{\mathrm{l}} \langle \vec{v}_{\mathrm{l}} \rangle^{\mathrm{l}} \right)}{\partial t} + \nabla \cdot \left(g_{\mathrm{l}} \rho_{\mathrm{l}} \langle \vec{v}_{\mathrm{l}} \rangle^{\mathrm{l}} \langle \vec{v}_{\mathrm{l}} \rangle^{\mathrm{l}} \right) = -\nabla(p) + \nabla \cdot \left(g_{\mathrm{l}} \langle \tau_{\mathrm{l}} \rangle^{\mathrm{l}} \right) + \left(g_{\mathrm{s}} \langle b_{\mathrm{s}} \rangle^{\mathrm{s}} + g_{\mathrm{l}} \langle b_{\mathrm{l}} \rangle^{\mathrm{l}} \right) \tag{2.56}$$

  Eq. 2.56 and the mass conservation equations are solved simultaneously to compute $\langle \vec{v}_{\mathrm{l}} \rangle^{\mathrm{l}}$. Substituting $\vec{M}_{\mathrm{s}}^{\mathrm{d}}$ in Eq. 2.54 with the appropriate expression derived from the constitutional models, an explicit expression for the velocity of the solid phase $\langle \vec{v}_{\mathrm{s}} \rangle^{\mathrm{s}}$ is obtained.

- **Approach 2** [98]: In this approach, the interfacial exchange terms due to nucleation are only neglected for the solid and liquid phase. The conservation equations for the solid and liquid phase are

$$\frac{\partial \left(g_{\mathrm{s}}\rho_{\mathrm{s}}\langle\vec{v}_{\mathrm{s}}\rangle^{\mathrm{s}}\right)}{\partial t} + \nabla\cdot\left(g_{\mathrm{s}}\rho_{\mathrm{s}}\langle\vec{v}_{\mathrm{s}}\rangle^{\mathrm{s}}\langle\vec{v}_{\mathrm{s}}\rangle^{\mathrm{s}}\right) = -g_{\mathrm{s}}\nabla(p) + \nabla\cdot\left(g_{\mathrm{s}}\langle\tau_{\mathrm{s}}\rangle^{\mathrm{s}}\right) + g_{\mathrm{s}}\langle b_{\mathrm{s}}\rangle^{\mathrm{s}} + \vec{M}_{\mathrm{s}}^{\Gamma} + \vec{M}_{\mathrm{s}}^{\mathrm{d}}$$

$$(2.57)$$

$$\frac{\partial \left(g_{\mathrm{l}}\rho_{\mathrm{l}}\langle\vec{v}_{\mathrm{l}}\rangle^{\mathrm{l}}\right)}{\partial t} + \nabla\cdot\left(g_{\mathrm{l}}\rho_{\mathrm{l}}\langle\vec{v}_{\mathrm{l}}\rangle^{\mathrm{l}}\langle\vec{v}_{\mathrm{l}}\rangle^{\mathrm{l}}\right) = -g_{\mathrm{l}}\nabla(p) + \nabla\cdot\left(g_{\mathrm{l}}\langle\tau_{\mathrm{l}}\rangle^{\mathrm{l}}\right) + g_{\mathrm{l}}\langle b_{\mathrm{l}}\rangle^{\mathrm{l}} + \vec{M}_{\mathrm{l}}^{\Gamma} + \vec{M}_{\mathrm{l}}^{\mathrm{d}}$$

$$(2.58)$$

For flow modeling distinguishes between two flow regimes: slurry and porous regimes. In the slurry regime, the solid phase is in the form of dispersed particles and is considered to move freely in the surrounding liquid. The second flow regime is the porous regime in which the solid phase is modeled as a fixed rigid porous structure. The two regimes are distinguished based on critical packing value $g_{\mathrm{s}}^{\mathrm{pack}}$ as defined by Založnik and Combeau [53]

$$\begin{cases} g_{\mathrm{s}} < g_{\mathrm{s}}^{\mathrm{pack}} & \text{Slurry regime} \\[2ex] g_{\mathrm{s}} \geq g_{\mathrm{s}}^{\mathrm{pack}} & \text{Porous regime} \end{cases} \qquad (2.59)$$

2.5.5.1   Constitutive models for momentum conservation

The constitutive models for momentum conservation are briefly described taking into account the two flow regimes:

– **Buoyancy force:** The buoyancy force is given by

$$\langle b_{\phi}\rangle^{\phi} = \vec{g}\rho_{\phi}^{b} \qquad (2.60)$$

where $\vec{g}$ is the gravity acceleration and ρ_{ϕ}^{b} is the modified density of phase ϕ which takes into account the temperature and composition variation for the liquid phase and shrinkage for the solid phase. The liquid density in the buoyancy terms is modeled as

$$\rho_{\mathrm{l}}^{b} = \rho_{\mathrm{ref}}\left[1 - \beta_{\mathrm{T}}\left(T - T_{\mathrm{ref}}\right) - \sum_{i}\beta_{\mathrm{c}}^{i}\left(\langle c_{\mathrm{l}}^{i}\rangle^{\mathrm{l}} - c_{\mathrm{ref}}^{i}\right)\right] \qquad (2.61)$$

Eq. 2.61 is referred to as Boussinesq assumption where ρ_{ref} is the density at reference temperature T_{ref} and composition c_{ref}^{i}, β_{T} is the thermal expansion coefficient and β_{c} is the solutal expansion coefficient. The solid density in the buoyancy term is modeled as

$$\rho_{\mathrm{s}}^{b} = \frac{\rho_{\mathrm{ref}}}{1 - \beta_{\mathrm{sh}}} \qquad (2.62)$$

where β_{sh} is the shrinkage coefficient. Note that in all the other equations, $(\rho_{\mathrm{s}} = \rho_{\mathrm{l}} = \rho)$, thus not allowing to account for solidification shrinkage driven flow.

– **Interfacial momentum flux due to nucleation:** The momentum exchange at the interface due to
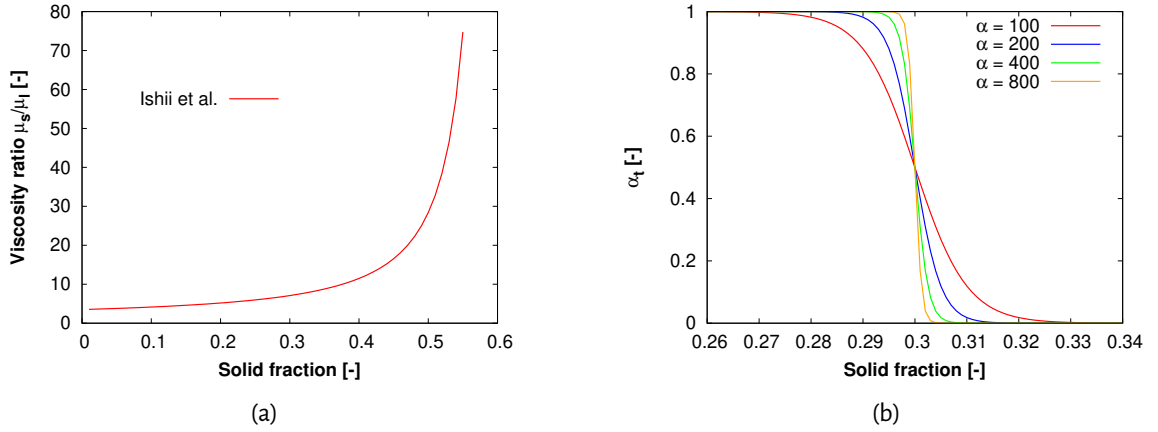
Figure 2.3 – Variation of a) viscosity ratio evolution with solid fraction obtained from Ishii *et al.* [99] and b) indicative function for different values of α and $g_s^{\mathrm{pack}} = 0.3$.

nucleation is negligible compared to other terms such that

$$\vec{M}_\phi^\Phi = 0 \tag{2.63}$$

- **Tangential stress:** The liquid and solid phases are modeled as a Newtonian fluid. Thus, the tangential stress term is

$$\nabla \cdot \left(g_\phi \langle \tau_\phi \rangle^\phi \right) = \nabla \cdot \left(\mu_\phi \nabla \left(g_\phi \langle \vec{v}_\phi \rangle^\phi \right) \right) \tag{2.64}$$

In order to take into account the contact between the grains, the solid phase is modeled as a pseudo-fluid. The viscosity of the solid phase is calculated according to Ishii *et al.* [99]. This approach has already been used by Ni and Beckermann [100], Ludwig and Wu [101] and Vreeman *et al.* [68].

$$\mu_s = \frac{\mu_l}{g_s} \left[\left(1 - \frac{g_s}{g_s^{b,max}} \right)^{-2.5 g_s^{b,max}} - (1 - g_s) \right] \tag{2.65}$$

where $g_s^{b,max}$ is the maximum stacking fraction. This value is taken to be equal to the fraction of random stacking of monodisperse spheres, i.e. $g_s^{b,max} = 0.6$. Fig. 2.3a shows the evolution of viscosity ratio between solid and liquid (μ_s / μ_l) obtained from the Ishii model. At a solid fraction of 0.5, the viscosity ratio is ~ 28. Thus at high solid fraction, the solid phase would introduce a strong resistance to movement and slow down the flow.

- **Interfacial drag force:** As mentioned earlier, there are two flow regimes. The interfacial drag force is dependent on the flow regime. For numerical implementation, a transition from one interfacial drag force model to another may cause numerical issues. Thus, an indicative function proposed by Založnik [96] and Nguyen [102] is used which causes a smooth transitioning between the two flow regimes:

$$\alpha_t = 1 - 0.5 \left(1 - \tanh \left[\alpha \left(g_s^{\mathrm{pack}} - g_s \right) \right] \right) \tag{2.66}$$

where α is an arbitrary value. The indicative function satisfies the criteria

$$\alpha_t = \begin{cases} 1 & \text{slurry regime } \left(g_{\mathrm{s}} < g_{\mathrm{s}}^{\mathrm{pack}} \right) \\ \\ 0 & \text{porous regime } \left(g_{\mathrm{s}} > g_{\mathrm{s}}^{\mathrm{pack}} \right) \end{cases} \tag{2.67}$$

The transition between the two regimes is dependent on α. Smaller value of α results in a smoother transition and vice versa. Fig. 2.3b shows the shape of the indicative function for different values of α and $g_{\mathrm{s}}^{\mathrm{pack}} = 0.3$. However, Založnik and Combeau [53] and Heyvaert *et al.* [103] use a sharp transition criteria.

In the slurry flow regime, interfacial drag force is modeled as

$$\vec{M}_{\mathrm{s}}^{\mathrm{d}} = -\vec{M}_{\mathrm{l}}^{\mathrm{d}} = K^{\mathrm{d,slurry}} \left(\langle \vec{v}_{\mathrm{l}} \rangle^{\mathrm{l}} - \langle \vec{v}_{\mathrm{s}} \rangle^{\mathrm{s}} \right) \tag{2.68}$$

$$K^{\mathrm{d,slurry}} = \frac{3 g_{\mathrm{s}} \rho_{\mathrm{l}} C_{\mathrm{d}}}{4 d_{\mathrm{g}}} \left| \langle \vec{v}_{\mathrm{l}} \rangle^{\mathrm{l}} - \langle \vec{v}_{\mathrm{s}} \rangle^{\mathrm{s}} \right| \tag{2.69}$$

where d_{g} is the grain diameter, C_{d} is the drag coefficient. The drag coefficient is modeled as proposed by Ni and Beckermann [100] which is based on the model of Agarwal and O'Neil [104]

$$C_{\mathrm{d}} = \frac{48 C_{ke} \left(1 - g_{\mathrm{l}} \right)}{\mathrm{Re}} + C_{ie} \tag{2.70}$$

$$\mathrm{Re} = \frac{\rho g_{\mathrm{l}} d_{\mathrm{g}}}{\mu_{\mathrm{l}}} \left| \langle \vec{v}_{\mathrm{l}} \rangle^{\mathrm{l}} - \langle \vec{v}_{\mathrm{s}} \rangle^{\mathrm{s}} \right| \tag{2.71}$$

$$C_{ke} \begin{cases} \frac{25}{6} & g_{\mathrm{l}} \leq 0.5 \\ \\ \frac{1}{2} \left(\frac{g_{\mathrm{l}}^3}{1-g_{\mathrm{l}}} \right) \left(\frac{1+4.7(1-g_{\mathrm{l}})}{1-1.83(1-g_{\mathrm{l}})} \right) & g_{\mathrm{l}} > 0.5 \end{cases} \tag{2.72}$$

$$C_{ie} \begin{cases} \frac{7}{3} & g_{\mathrm{l}} \leq 0.5 \\ \\ \frac{24 \left(10^{E} - 1 \right)}{\mathrm{Re} \left[1 - 0.9 (g_{\mathrm{l}} - 0.25)^{1/3} (1-g_{\mathrm{l}})^{2/3} \right]^3} & g_{\mathrm{l}} > 0.5 \end{cases} \tag{2.73}$$

$$E = 0.261 \mathrm{Re}^{0.369} - 0.105 \mathrm{Re}^{0.431} - \frac{0.124}{1 + (\log_{10} \mathrm{Re})^2} \tag{2.74}$$

The drag coefficient proposed by Ni and Beckermann [100] reduces to one for a single sphere as $g_{\mathrm{s}} \to 0$. If $g_{\mathrm{s}} \to 0$ and $\mathrm{Re} \to 0$, the drag coefficient reduces to the Stokes law, $C_{\mathrm{d}} = 24/\mathrm{Re}$.

In the porous regime, the solid phase is fixed, $\langle \vec{v}_{\mathrm{s}} \rangle^{\mathrm{s}} = 0$. The interfacial drag force depends on the permeability and morphology of the porous media and is modeled according to Darcy model

$$\vec{M}_{\mathrm{l}}^{\mathrm{d}} = -K^{\mathrm{d,porous}} \langle \vec{v}_{\mathrm{l}} \rangle^{\mathrm{l}} \tag{2.75}$$

$$K^{\text{d,porous}} = \frac{g_l^2 \mu_l}{K} \tag{2.76}$$

where K is the hydrodynamic permeability which is modeled by the Kozeny-Carman relationship

$$K = \frac{g_l^3}{(1 - g_l^2)} \left(\frac{l_c^2}{\pi^2 K_k \tau^2} \right) \tag{2.77}$$

where K_k is the Kozeny constant, l_c is the characteristic length of the porosity and τ is the porous media tortuosity. Values for a packed bed of sphere are commonly used: $K_k = 5$ and $\tau = \frac{6}{\pi}$. Incorporation of indicator function as well as the constants $K^{\text{d,slurry}}$ and $K^{\text{d,porous}}$ allows us to write the different momentum equation for the different regimes in a single equation

$$\vec{M}_s^d = \left[\left(\alpha_t K^{\text{d,slurry}} \right) + \left((1 - \alpha_t) K^{\text{d,porous}} \right) \right] \left(\langle \vec{v}_l \rangle^l - \langle \vec{v}_s \rangle^s \right) \tag{2.78}$$

– **Interfacial momentum flux due to phase change:** Assuming that the average fluctuating solid velocity is negligibly small during ingot solidification [98], the interfacial momentum flux due to phase change is modeled as

$$\vec{M}_s^\Gamma = -\vec{M}_l^\Gamma = \langle \vec{v}_s \rangle^s \Gamma_s \tag{2.79}$$

To summarize, two phase formulations of the volume averaged conservation equations for mass, momentum and solute conservation and a one phase formulation for the energy conservation equation are employed.

2.6 Microscopic growth model

The solidification rate, hence the solid phase fraction is determined by the mass transfer at the interface along with the cooling rate imposed due to casting and is modeled through microsegregation models. Microsegregation models relate the local enthalpy and solute concentration to the local temperature, phase fraction and their solute composition. Založnik & Combeau [53] showed through non-dimensional analysis that the macroscopic terms i.e. the transient and the advective terms have the same scale and this scale is considerably greater than the microscopic terms which account for nucleation and grain growth. Thus, nucleation and grain growth are solved locally using a micro time step. n_{mic} is the number of sub-divisions of the macro time step (Δt) such that the micro time step is given by:

$$\delta t = \frac{\Delta t}{n_{\text{mic}}} \tag{2.80}$$

The temperature and solid fraction in the control volume are linked to the specific enthalpy of the solid-liquid mixture with the relationship:

$$\langle h \rangle = g_s \langle h_s \rangle^s + g_l \langle h_l \rangle^l \tag{2.81}$$

The intrinsic enthalpies of the phases are only dependent on temperature. The specific heat capacity (C_p) of solid and liquid phase are assumed to be equal and constant.

$$\langle h_s \rangle^s = C_p T \quad \langle h_l \rangle^l = C_p T + L_f \tag{2.82}$$

where L_f is the latent heat of the liquid phase. Latent heat is also assumed to be constant. Eq. 2.81 and 2.82 together gives

$$\langle h \rangle = C_p T + L_f \left(1 - g_{\mathrm{s}} \right) \tag{2.83}$$

With the assumption of the interface at equilibrium, the temperature is linked to the interfacial composition by a simplified linearized multicomponent phase diagram

$$T = T_f + \sum_i m_{\mathrm{l}}^i c_{\mathrm{l}}^{*i} \tag{2.84}$$

where c_{l}^{*i} is the interfacial liquid composition and m_{l}^i is the liquidus slope for species i $\left(\left. \dfrac{\partial T}{\partial c_{\mathrm{l}}^i} \right|_{P.c_{\mathrm{l}}^{j \neq i}} \right)$ and it is assumed to be constant. The solidification interval ranges from the liquidus temperature T_{liq} to the maximum of the two temperatures: solidus temperature T_{sol} and the eutectic temperature (T_{eut}). T_{liq} is given by:

$$T_{\mathrm{liq}} = T_f + \sum_i m_{\mathrm{l}}^i \langle c_{\mathrm{l}}^i \rangle^{\mathrm{l}} \tag{2.85}$$

and the temperature evolution during solidification is given by:

$$T = \begin{cases} T_f + \sum_i m_{\mathrm{l}}^i c_{\mathrm{l}}^{*i} & \text{if} \quad T > \max(T_{\mathrm{sol}}, T_{\mathrm{eut}}) \\[2mm] \max(T_{\mathrm{sol}}, T_{\mathrm{eut}}) & T < \max(T_{\mathrm{sol}}, T_{\mathrm{eut}}) \end{cases} \tag{2.86}$$

Egns. 2.83 and 2.84 together gives

$$\langle h \rangle = C_p \left(T_f + \sum_i m_{\mathrm{l}}^i c_{\mathrm{l}}^{*i} \right) + L_f \left(1 - g_{\mathrm{s}} \right) \tag{2.87}$$

Eq. 2.87 in the discretized form is

$$\delta \langle h \rangle = \left(C_p \left(T_f + \sum_i m_{\mathrm{l}}^i c_{\mathrm{l}}^{*i} \right) - T_0 \right) - L_f \left(\frac{\Gamma_{\mathrm{s}} \delta t}{\rho} \right) \tag{2.88}$$

where $\delta \langle h \rangle$ is the enthalpy change in δt and T_0 is a previous temperature at time $t - \delta t$. Hence, the need for a model which links the interfacial composition to the phase fraction so as to obtain a closed system of equations. The models which link the interfacial composition to the phase fractions are called "microsegregation models".

2.6.1 Microsegregation models

As discussed in the previous chapter, microsegregation occurs over a length scale of a few hundred microns. The structures relevant for the solute redistribution are the secondary dendrite arms. Thus, microsegregation models are usually implemented over a control volume perpendicular to the dendrite arms as shown in Fig. 2.4a [97]. The main assumptions across the large majority of microsegregation models are:

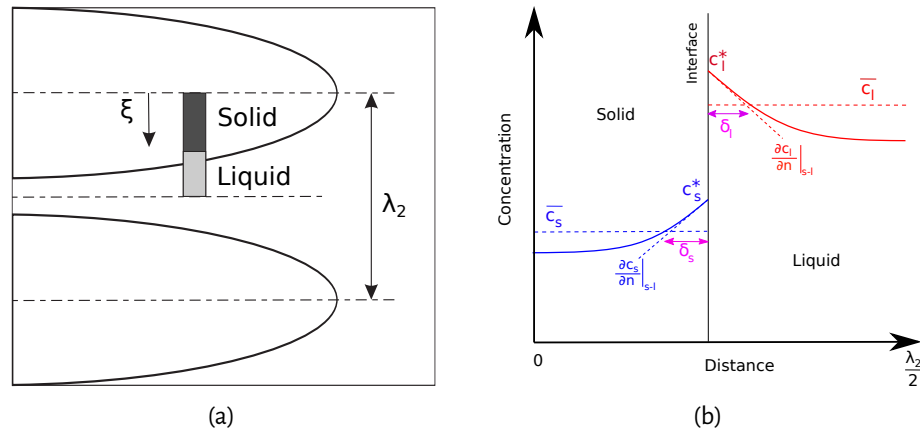- Temperature is uniform across the control volume

Figure 2.4 – (a) Control volume for microsegregation and (b) concentration profile at the secondary arm scale. λ_2 is the secondary dendrite arm spacing (SDAS). δ_l and δ_s are the diffusion lenghts in the liquid and solid phase

- Densities of the liquid and solid phases are equal and constant

- Local thermodynamic equilibrium at the s/l interface

- Closed system

Microsegregation results from the partitioning of solute elements between the solid and liquid phase which is expressed by the equilibrium partition coefficient (k_p) for every solute:

$$k_p = \frac{c_s^*}{c_l^*} \tag{2.89}$$

where c_s^* and c_l^* are the interfacial solute concentration in solid and liquid phase respectively (Fig. 2.4b). Most of the industrial alloys usually have $k_p < 1$, *i.e.* solute element atoms are rejected into the liquid phase. Solid formation depends on the ability of solute diffusion in the liquid and solid phases. Diffusion is a kinetic phenomenon. As solidification progresses, solute element atoms build up in the liquid ahead of the s/l interface which has a solute content higher than the bulk liquid. There are three distinct zones of solute transfer:

- solid phase: solute transfer only by diffusion

- s/l interface: solute diffusion boundary layer of thickness δ_l (diffusion length) as shown in Fig. 2.4b. Diffusion is the predominant mass transfer phenomena in this zone

- bulk liquid phase: solute transport by diffusion and liquid convection

Solute transfer in the solid phase cannot be altered by external parameters. However, natural convection and mechanical mixing can increase the solute transfer in liquid phase, subsequently reducing δ_l and homogenizing the liquid phase. Microsegregation models should be able to account for all of the above mentioned phenomena.

Mathematically, the microsegregation model is formulated as a Stefan problem. The solute diffusion in the solid and liquid phases are modeled according to the Fick's diffusion law:

$$\frac{\partial c_\phi}{\partial t} = D\nabla^2 c_\phi \tag{2.90}$$

with the Neumann boundary condition at both ends of the control volume.

$$\left.\frac{\partial c_\mathrm{s}}{\partial x}\right|_{x=0} = 0 \quad \text{and} \quad \left.\frac{\partial c_\mathrm{l}}{\partial x}\right|_{x=\frac{\lambda_2}{2}} = 0 \tag{2.91}$$

As the interface advances, the velocity of the moving interface ($v_i = \frac{dx_i}{dt}$) is defined by solute balance at the interface

$$(c_\mathrm{l}^* - c_\mathrm{s}^*)\frac{dx_i}{dt} = D_\mathrm{s}\left.\frac{\partial c_\mathrm{s}}{\partial x}\right|_{x=x_i} - D_\mathrm{l}\left.\frac{\partial c_\mathrm{l}}{\partial x}\right|_{x=\frac{\lambda_2}{2}} \tag{2.92}$$

The above equation is also referred to as Stefan condition. This model is limited to diffusion in the solid and liquid phase and does not consider the effect of liquid convection. The ratio of diffusion coefficient for solute elements in the solid and liquid phase within the solidification interval $D_\mathrm{s}/D_\mathrm{l} \approx 10^{-3}$-$10^{-4}$. Hence, most of the microsegregation models assume complete mixing in the liquid phase ($\delta_l \to 0$). Applying this approximation and further using the boundary conditions, Eqn. 2.92 can be written as:

$$-(1 - k_p)c_\mathrm{l}^*\frac{dg_\mathrm{s}}{dt} + \frac{2D_\mathrm{s}}{\lambda_2}\frac{\partial c_\mathrm{s}(x^*, t)}{\partial x} + (1 - g_\mathrm{s})\frac{dc_\mathrm{l}^*}{dt} = 0 \tag{2.93}$$

Microsegregation models become more complex when accounting for eutectic reactions at the end of solidification. These models are not discussed. Readers interested in such models are referred to the work of Combeau *et al.* [105, 106]. The microsegregation models can be generally categorized as:

- Analytical model

- Numerical model

- Machine learning based model

- Volume averaging based microsegregation model

2.6.1.1   Analytical model

Various analytical models have been established. These models differ with regards to the transient diffusion in solid (back diffusion), given by the second term in Eqn. 2.93. Two limiting models are proposed: lever rule which assumes perfect equilibrium and Gulliver-Scheil model which is non-equilibrium. In between these two models are various models which assume finite back diffusion.

- **Lever rule:** Lever rule assumes local thermodynamic equilibrium of the solid and liquid phases (equivalent to infinitely fast diffusion in both phases) due to which the phase compositions are homogeneous. The average composition of the phase is only a function of temperature/phase fraction and is obtained from the phase diagram. The compositions are given by:

$$\bar{c}_\mathrm{l} = c_\mathrm{l}^* = \frac{c_\mathrm{s}^*}{k_p} = \frac{\bar{c}_\mathrm{s}}{k_p} \tag{2.94}$$

$$\bar{c}_\mathrm{s} = c_\mathrm{s}^* = \frac{k_p c_0}{k_p g_\mathrm{s} + (1 - g_\mathrm{s})} \tag{2.95}$$

  where $\bar{c}_\mathrm{s}$ and $\bar{c}_\mathrm{l}$ are the average concentration of the solid and liquid phases and g_s is the solid phase fraction.

– **Gulliver-Scheil model:** This model is the other limiting case. Fourier number for diffusion in solid, $\mathrm{Fo_s}$ is defined using the solid diffusion coefficient D_s, local solidification time t_s and the SDAS and is given by:

$$\mathrm{Fo_s} = \frac{D_\mathrm{s} t_s}{\left(\lambda_2/2\right)^2} \tag{2.96}$$

When $\mathrm{Fo_s} \ll 1$, the transient diffusion term in Eqn. 2.93 can be neglected. This is true when the solidification time is small or D_s is small in the case of substitutional elements. In such cases, diffusivity in the solid phase is assumed to be small enough such that it can be neglected at the space and time scales of solidification structures, the Gulliver-Scheil model is obtained which is given by:

$$\bar{c}_\mathrm{l} = c_1^* = c_0 \left(1 - g_\mathrm{s}\right)^{k_p - 1} \tag{2.97}$$

$$\bar{c}_\mathrm{s} = \frac{c_0 - \left(\bar{c}_\mathrm{l}\left(1 - g_\mathrm{s}\right)\right)}{g_\mathrm{s}} \tag{2.98}$$

– **Finite back diffusion:** At intermediate cooling rates or high D_s as in the case of interstitial elements, $\mathrm{Fo_s} \sim \mathcal{O}(1)$. In such cases, the transient diffusion in solid has to be accounted for. A number of models have been proposed in the framework of analytical models which account for solute diffusion in solid. The first model to do so was the Brody-Flemings model [107] which was based on the differential solute balance equation for a parabolic growth rate

$$\bar{c}_\mathrm{l} = c_1^* = \frac{c_\mathrm{s}^*}{k_p} \tag{2.99}$$

$$c_\mathrm{s}^* = k_p c_0 \left[1 - \left(1 - 2\mathrm{Fo_s} k_p\right) g_\mathrm{s}\right]^{\frac{k_p - 1}{1 - 2\mathrm{Fo_s} k}} \tag{2.100}$$

The Gulliver-Scheil rule is recovered when $\mathrm{Fo_s} = 0$ in Eq. 2.100. However, the lever rule is not obtained when $\mathrm{Fo_s} \to \infty$. Lever rule is recovered when $\mathrm{Fo_s} = 0.5$. This is due to non-conservation of solute in the model. Thus Brody-Flemings model is most accurate when $\mathrm{Fo_s} < 0.1$ when back diffusion is less important. Numerous models were developed to extend and improve the Brody-Flemings model. Interested readers are referred to the following non-exhaustive list of publications: Clyne and Kurz [108], Ohnaka [109], Kobayashi [110], Voller and Beckermann [111].

2.6.1.2 Numerical model

Analytical models are restricted by their simplifying assumptions. However, in numerical models, various assumptions concerning variable thermo-physical quantities, cooling rates, phase diagram, coarsening phenomena and undercooling can be considered within a 1D simulation setup. One of the first numerical models for microsegregation was proposed by Ueshima *et al.* [112]. The model considered finite diffusion in the solid γ and δ phase and complete equilibrium in the liquid phase. Sundarraj and Voller [113] proposed a numerical model which considered non-constant phase diagram parameters. They only modeled primary solidification, however they accounted for finite diffusion in the liquid phase. Further, coarsening of dendrites was also accounted for. Thuinet and Combeau [114] extended the model by accounting for secondary solid phase and coupling the model with phase diagram data using a tabular approach. This approach of coupling with thermodynamic data will be discussed in more detail in the next chapter. While no nucleation undercooling was

accounted for, tip undercooling is accounted for. The advantage of the numerical model is that the solute profile in the phase is obtained and no approximations are made in regards to the solute profile in the phases which was the case with analytical models. Fig. 2.5 shows the solute profile for carbon and nickel during solidification of a ternary Fe-C-Ni steel alloy. The model is able to capture the gradient in the Ni solute profile which is caused due to ferrite regression. The interfacial composition of Ni in δ is less than the point behind the interface. Such solute profiles are also observed for substitutional elements during remelting of the primary solidification phase.
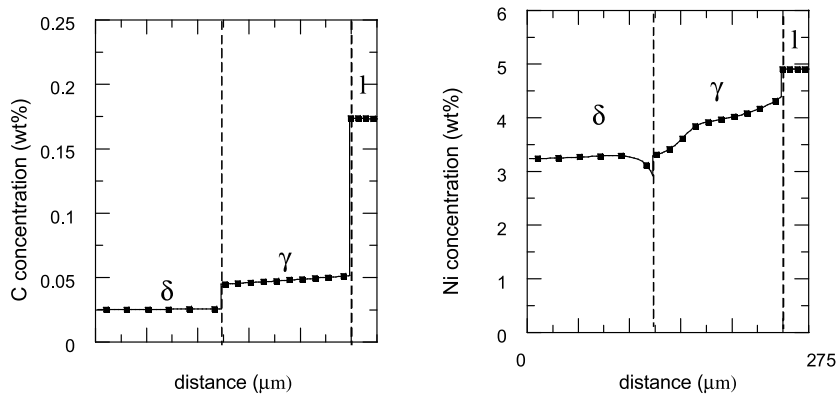

Figure 2.5 – Solute profile for carbon and nickel in δ and γ phase during solidification [115]

2.6.1.3   Machine learning based model

Machine learning is a method of data analysis that automates regression model building. Various models and algorithms are available that can be employed such that the system can learn from data, identify patterns and make predictions. Ohno *et al.* [116] used results of numerical microsegregation models as described earlier, to train the algorithm. The numerical microsegregation models assumed finite diffusion in the liquid and solid phases. The algorithm was able to successfully predict the segregation results for various Fe based alloys as shown in Fig. 2.6. Further, they improved the algorithm by training it on phase field simulation results [117].
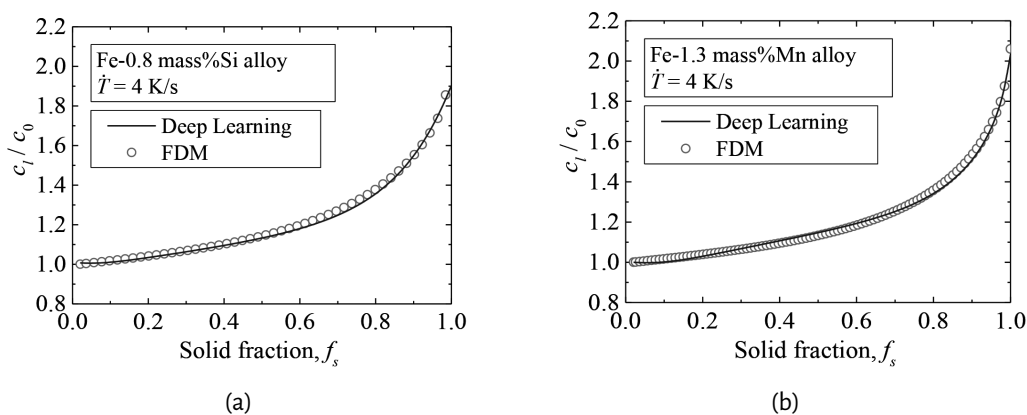

Figure 2.6 – Comparison between results of deep learning and FDM model for (a) Fe-0.8 wt%.Si alloy cooled at $\dot{T}$ =4 K.s^{-1} and (b) Fe-1.3 wt%.Mn alloy cooled at $\dot{T}$ =4 K.s^{-1} [116]

2.6.1.4 Need for volume averaging based microsegregation model

The above mentioned two types of microsegregation models: analytical model and machine learning based model cannot be used to determine the interface exchange terms for volume averaged solute conservation equations: solute flux due to interface diffusion (J_ϕ^{ij}), phase change ($J_\phi^{i\Gamma}$) and nucleation ($J_\phi^{i\Phi}$). Numerical models can provide these values, however, they are computationally expensive which makes them infeasible for large cases of solidification modeling. The requirement for all the interphase exchange terms mentioned is due to the fact that a two phase formulation for the macroscopic volume averaged solute conservation equations are used. Similar to the energy conservation equation, the one phase formulation for the solute (Eq. 2.45) conservation equation is used. In such cases, the above mentioned microsegregation models are emplyed to compute the temperature, phase fraction and their compositions.

Extensive literature is available on analytical models being used to model macrosegregation. Dong *et al.* [118] used various analytical microsegregation models to predict macrosegregation in continuous cast round billet. Fig. 2.7 shows the segregation profiles for carbon and phosphorus in round billets for various microsegregation models. The results obtained from the microsegregation model of Voller-Beckermann were closest to the experimentally observed solute profiles. It also highlights the importance of accounting for back diffusion when compared to lever rule and Gulliver-Scheil models. Thuinet and Combeau [119] used a numerical seg-
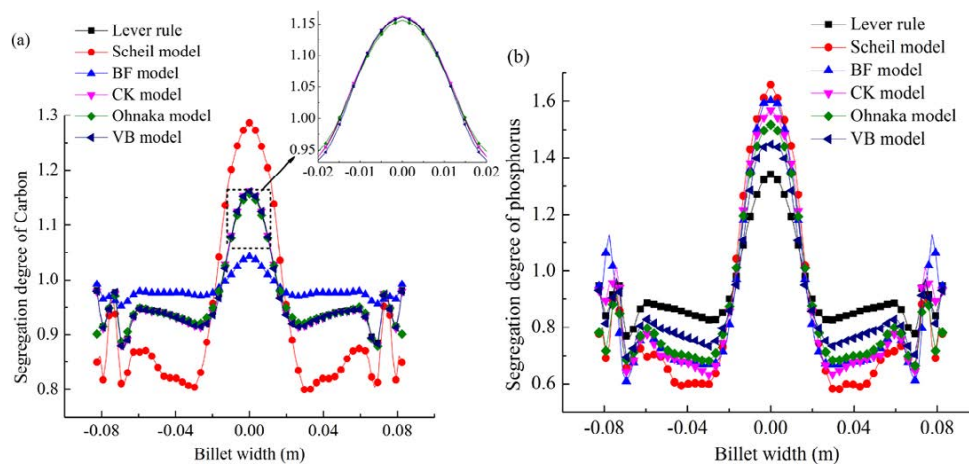

Figure 2.7 – Centerline segregation profile for carbon and phosphorous predicted by different microsegregation models for a round billet [118]

regation model for prediction of macrosegregation in a large ingot. This work primarily focused on studying the impact of peritectic transformation on macrosegregation. Ohno *et al.* [117] used machine learning based models to predict macrosegregation. Each of these microsegregation models have certain limitations which restrict their applicability to special simulation cases. The primary limitations are as follows:

- **Undercooling:** All the analytical models assume complete mixing in the liquid phase due to which they can only be used to model columnar solidification. Since equiaxed grains nucleate and grow in undercooled melt, simulating equiaxed solidification is infeasible. Numerical models can be used to model equiaxed solidification. Application of machine learning based microsegregation models, in theory, can be applied to model equiaxed solidification as it uses numerical microsegregation models to train the algorithm. However, there is no literature which has used these microsegregation models to model equiaxed solidification.

- **Nucleation kinetics:** All the models assume presence of solid phase at the liquidus temperature.

This does not allow for accurate representation of the competition between nucleation and grain growth. This competition is critical as it determines: i) number of grains which nucleate and ii) undercooling achieved during solidification.

– **Computational cost:** Numerical models are computationally expensive which make it infeasible to couple these models with large macrosegregation simulations. Analytical models are cheap. The computational cost of the machine learning based microsegregation models depends on the complexity of the final model obtained from the algorithms.

– **Grain morphology:** In the previous chapter, different morphologies of columnar and equiaxed grains were illustrated. Combeau *et al.* [38] showed the importance of morphology on the final segregation pattern of large ingots. All the above models are only applicable to globular grains. Hence, they do not provide any information on the grain morphology which is a huge disadvantage, specially when modeling equiaxed solidification.

– **Sensitivity to microsegregation models:** Fig. 2.8 shows the composition profile for Pb during solidification of Sn-5 wt%. Pb alloy in a rectangular cavity. It is observed that using lever rule results in formation of segregation channels which are not observed when using microsegregation models which account for finite diffusion in liquid. Thus, the segregation channels are strongly dependent on the microsegregation model employed. Assumption of full equilibrium results in the mushy zone being less stable and more favourable to the formation of segregation channels.

(a)   (b)
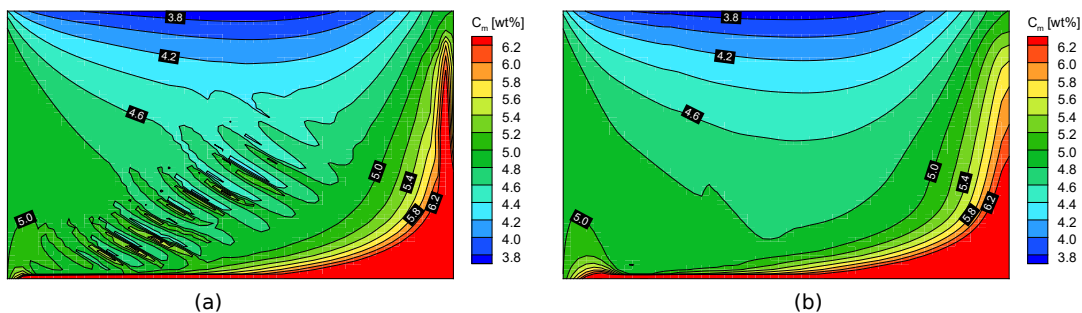
Figure 2.8 – Composition profile for Pb in solidified Sn-5 wt%.Pb ingot using a) full equilibrium and b) finite diffusion in liquid approximations [120]

Thus, the above-mentioned microsegregation model has several restrictions which makes its applicability to wide ranges of solidification simulation impossible. Volume averaging based microsegregation models resolve the various restrictions imposed by other microsegregation models and can be used in a two phase formulation of the macroscopic volume averaged solute conservation equation.

2.6.2   Volume averaging based microsegregation model

Wang and Beckermann [82] developed a general approach to model equiaxed solidification. They used the volume averaging method to solve the microsegregation problem. The averaging volume consisted of primary dendritic structure and the surrounding liquid. The advantage of this approach is that it allows for consideration of complex geometries and the effect of undercooling on the dendritic growth. The model was extended by Tourret and Gandin [121] to account for concurrent primary, peritectic and eutectic solidification. In the following section, the microscopic model for nucleation and growth as implemented in SOLID® is presented.
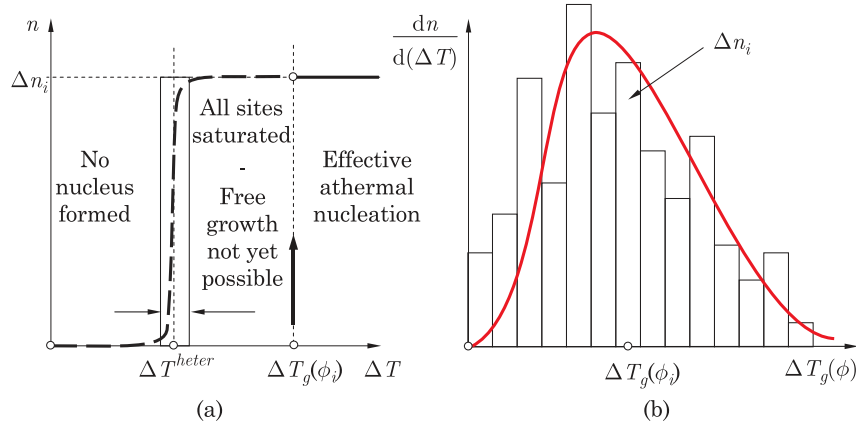
Figure 2.9 – (a) Evolution of grain density as a function of undercooling for a constant cooling rate when (a) one class of nuclei are considered (b) continuous distribution of nuclei are considered [2]

2.6.2.1 Nucleation

As discussed in the previous chapter, the primary source of nuclei for equiaxed grains are:

– **Heterogeneous nucleation:** Heterogeneous nucleation occurs from the nuclei already present in liquid. The nuclei are in the form of inoculants which are used during casting. Use of inoculants is a common practice in the aluminium casting industry. Nucleation occurs when the local conditions are favourable. It is modeled by an instantaneous nucleation model when the local grain density is zero at a predefined undercooling below the liquidus temperature. The domain has a predefined nuclei density N_{nuc} which nucleates instantaneously. Thus, the number of new grains introduced through nucleation is given by:

$$
\dot{N} = \begin{cases} N_{\mathrm{nuc}}\delta t, & \text{if } \Delta T \geq \Delta T_{\mathrm{nuc}} \quad \text{and} \quad N_g = 0 \\ 0, & \text{otherwise} \end{cases} \tag{2.101}
$$

where ΔT is the local undercooling and ΔT_{nuc} is the undercooling that allows free growth of the grains. The solid mass transfer rates due to grain nucleation are:

$$
\Phi_{\mathrm{s,nuc}} = \rho V_{\mathrm{g0}}\dot{N} \tag{2.102}
$$

where $\Phi_{\mathrm{s,nuc}}$ is the rate of solid formation due to nucleation, $V_{\mathrm{g0}} = (4\pi r_{\mathrm{g0}}^3)/3$ is the volume of the nucleated grains and r_{g0} is the nucleation radius of the nucleated grains. The nucleation model was further improved by Bedel [122]. Nuclei densities are classified by their size and are generated depending upon the undercooling as shown in Fig. 2.9. The modified mass transfer rate is given by:

$$
\Phi_{\mathrm{s,nuc}} = \sum_j \Phi_{\mathrm{s,nuc}}^j \quad \text{where} \quad \Phi_{\mathrm{s,nuc}}^j = \rho V_{\mathrm{g0}}\dot{N}^j \tag{2.103}
$$

where j is the number of classes of nuclei, Φ_{s}^j is the mass transfer rate due to each nuclei class with a grain density of $\dot{N}^j$.

– **Fragmentation:** Fragmentation occurs in the presence of columnar grains. Readers are suggested to

refer to the thesis of Leriche [123] for information about the 2D framework of modeling of columnar growth, columnar front tracking and the implementation of the fragmentation of columnar grains. However, the contribution of fragmentation at a point 'p' depends on the state of its neighbours 'i'. Each of the neighbours can inject a surface flux of fragments. The total mass transfer rate due to fragmentation is given by:

$$\Phi_{\text{s,frag}} = \frac{1}{V_0} \iint_{\partial\Omega_{p/i}} \phi_{\text{frag}} \, dS_i \tag{2.104}$$

where $\partial\Omega_{p/i}$ is the contact surface between 'p' and neighbour 'i'. The surface flux is only calculated when the columnar front is not blocked i.e. CET has not occured.

The total mass transfer rate due to nucleation and fragmentation is:

$$\Phi_{\text{s}} = \Phi_{\text{s,nucl}} + \Phi_{\text{s,frag}} \tag{2.105}$$

and solute transfer rate of the solid and liquid phases is :

$$J_{\text{s}}^{i,\Phi} = \Phi_{\text{s}} \left(k_p^i \langle c_l^i \rangle^1 \right) \tag{2.106}$$

$$J_{\text{l}}^{i,\Phi} = -J_{\text{s}}^{i,\Phi} \tag{2.107}$$

with the assumption that the grains nucleating have a composition $k_p^i \left(\langle c_l^i \rangle^1 \right)$.

2.6.2.2   Grain growth

Once nucleated, grain growth occurs which is primarily controlled by solute diffusion. Local thermodynamic equilibrium at the s/l interface is assumed. As mentioned in section 2.1, early versions of volume averaging models only accounted for two phases in the microscopic growth model. Subsequently, the microscopic growth model was extended to three phases which allowed for better description of the grain morphology and segregation patterns observed in industrial ingots.

2.6.2.2.1   Two phase model   The two phase grain growth model consists of two phases: solid and liquid $(g_{\text{s}} + g_{\text{l}} = 1)$ and is illustrated in Fig. 2.10. The mass and solute transfer rate for each phase is given by:

$$\begin{cases} \frac{\partial(\rho g_{\text{s}})}{\partial t} = \Gamma_{\text{s}} \\[2mm] \frac{\partial(\rho g_{\text{l}})}{\partial t} = \Gamma_{\text{l}} \end{cases} \tag{2.108}$$

$$\begin{cases} \frac{\partial(\rho g_{\text{s}} \langle c_{\text{s}}^i \rangle^{\text{s}})}{\partial t} = J_{\text{s}}^{i,\Gamma} + J_{\text{s}}^{i,j} = \Gamma_{\text{s}} c_{\text{s}}^{*i} + \frac{\rho S_v^{\text{s}} D_{\text{s}}^i}{\delta_{\text{s}}^i} \left(c_{\text{s}}^{*i} - \langle c_{\text{s}}^i \rangle^{\text{s}} \right) \\[3mm] \frac{\partial(\rho g_{\text{l}} \langle c_{\text{l}}^i \rangle^1)}{\partial t} = J_{\text{l}}^{i,\Gamma} + J_{\text{l}}^{i,j} = \Gamma_{\text{l}} c_{\text{l}}^{*i} + \frac{\rho S_v^{\text{s}} D_{\text{l}}^i}{\delta_{\text{l}}^i} \left(c_{\text{l}}^{*i} - \langle c_{\text{l}}^i \rangle^1 \right) \end{cases} \tag{2.109}$$
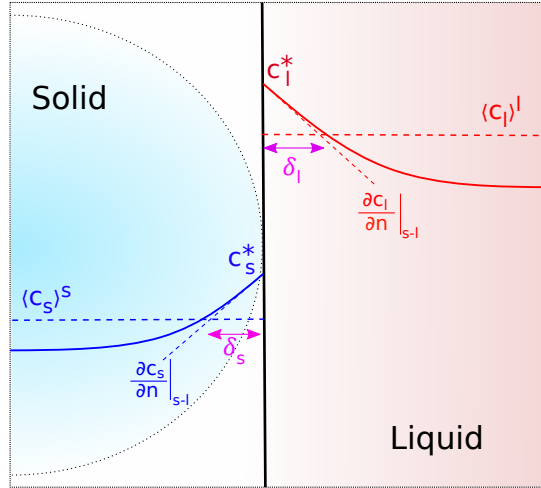
Figure 2.10 – Schematic of the solute diffusion in the two phase approach

where Γ_ϕ is the mass flux, c_ϕ^{i*} is the interface composition, δ_ϕ is the diffusion length, D_ϕ is the diffusion coefficient, all for phase ϕ and S_v^s is the volumetric interfacial area density.

$$S_v^s = 4\pi R^2 N_g \tag{2.110}$$

$$R = \left(\frac{3g_s}{4\pi N_g} \right)^{1/3} \tag{2.111}$$

where R is the grain radius and N_g is the volumetric grain density. Applying the conditions of local thermodynamic equilibrium at the s/l interface along with the mass and solute balance in the REV results in

$$c_s^{*i} = k_p^i c_l^{*i} \tag{2.112}$$

$$\Gamma_s = -\Gamma_l \tag{2.113}$$

$$J_s^{i,\Gamma} + J_s^{i,j} = -\left(J_l^{i,\Gamma} + J_l^{i,j} \right)$$

$$\implies c_l^{*i}\left(k^i - 1\right)\frac{\Gamma_s}{\rho} + c_l^{*i}\left(\frac{S_v^s D_l^i}{\delta_l^i} + k^i \frac{S_v D_s^i}{\delta_s^i} \right) = \langle c_l^i \rangle^l \frac{S_v^s D_l^i}{\delta_l^i} + \langle c_s^i \rangle^s \frac{S_v^s D_s^i}{\delta_s^i} \tag{2.114}$$

The solute profile in the phases are approximated through various analytical relationships for the diffusion length in the phases. As mentioned earlier, diffusion is the only phenomena through which solute transfer in solid occurs and the ratio of diffusion coefficients for solute elements in the solid is orders of magnitude lower than that in the liquid phase. Thus, exact evaluation of the diffusion length in solid is not critical and a simplified approximation for the diffusion length could be used, e.g. :

$$\delta_s = \frac{R}{5} \tag{2.115}$$

However, for the liquid phase, various analytical models have been proposed. These liquid diffusion length
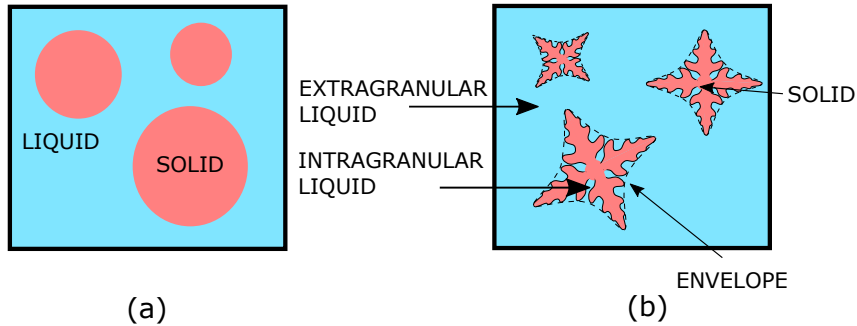
models will be discussed in the Chapter 4.

Figure 2.11 – Representation of a) two phase and b) three phase model

2.6.2.2.2 Three phase model In the two phase grain growth model, the equiaxed grains are assumed to be globular. It is not realistic as in most solidification cases, the morphology of equiaxed grains is more complicated. This results in higher interfacial surface area which affects the solute balance at the interfaces. Further, the motion of the grains also depends on its morphology. All these consequences result in the two phase model over predicting macrosegregation as reported by Combeau *et al.* [38]. A three phase dendritic grain consists of solid dendrite which is surrounded by an intragranular (d) liquid phase as shown in Fig. 2.11. This liquid phase is separated from the extragranular liquid (e) phase by an envelope whose surface passes over the tips of the primary and the secondary dendrite arms. Introduction of the envelope allows to separate the liquid in the immediate vicinity of the solid (d) from the liquid further from the grain (e). Grain growth is no longer linked to the advance of one but of two interfaces: the microscopic equations of growth are therefore modified.

The conservation of the mass of the three phases s (solid), d (intragranular liquid) and e (extragranular
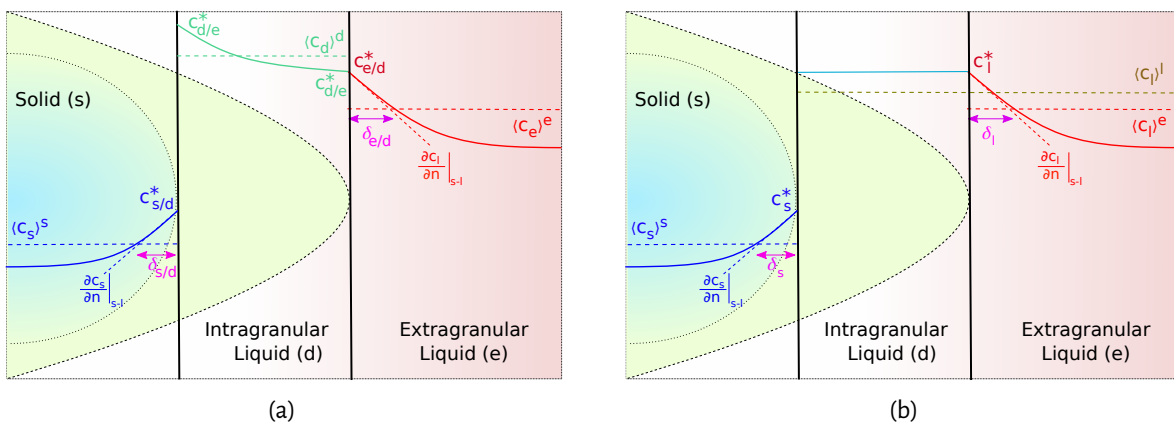

Figure 2.12 – Schematic of the solute diffusion in the a) three phase model b) simplified three phase model

liquid) is written:

$$
\begin{cases}
\frac{\partial(\rho g_{\mathrm{s}})}{\partial t} = \Gamma_{\mathrm{s}} \\[2mm]
\frac{\partial(\rho g_{\mathrm{d}})}{\partial t} = \Gamma_{\mathrm{env}} - \Gamma_{\mathrm{s}} \\[2mm]
\frac{\partial(\rho g_{\mathrm{e}})}{\partial t} = -\Gamma_{\mathrm{env}}
\end{cases}
\tag{2.116}
$$

The growth of the intragranular phase therefore depends on both the growth of the solid and the envelope. The mass and solute transfer rate for each phase is given by:

$$
\begin{cases}
\frac{\partial(\rho g_{\mathrm{s}}\langle c_{\mathrm{s}}^{i}\rangle^{\mathrm{s}})}{\partial t} = \Gamma_{\mathrm{s}} c_{\mathrm{s/d}}^{*i} + \frac{\rho S_{v}^{\mathrm{s}} D_{\mathrm{s}}^{i}}{\delta_{\mathrm{s}}^{i}}\left(c_{\mathrm{s/d}}^{*i} - \langle c_{\mathrm{s}}^{i}\rangle^{\mathrm{s}}\right) \\[2mm]
\frac{\partial(\rho g_{\mathrm{d}}\langle c_{\mathrm{d}}^{i}\rangle^{\mathrm{d}})}{\partial t} = -\Gamma_{\mathrm{s}} c_{\mathrm{d/s}}^{*i} + \Gamma_{\mathrm{env}} c_{\mathrm{d/e}}^{*i} + \frac{\rho S_{v}^{\mathrm{s}} D_{\mathrm{l}}^{i}}{\delta_{\mathrm{d/s}}^{i}}\left(c_{\mathrm{d/s}}^{*i} - \langle c_{d}^{i}\rangle^{\mathrm{d}}\right) + \frac{\rho S_{v}^{\mathrm{env}} D_{\mathrm{l}}^{i}}{\delta_{\mathrm{d/e}}^{i}}\left(c_{\mathrm{d/e}}^{*i} - \langle c_{\mathrm{d}}^{i}\rangle^{\mathrm{d}}\right) \\[2mm]
\frac{\partial(\rho g_{\mathrm{e}}\langle c_{\mathrm{e}}^{i}\rangle^{\mathrm{e}})}{\partial t} = -\Gamma_{\mathrm{env}} c_{\mathrm{e/d}}^{*i} + \frac{\rho S_{v}^{\mathrm{env}} D_{\mathrm{l}}^{i}}{\delta_{\mathrm{e/d}}^{i}}\left(c_{\mathrm{e/d}}^{*i} - \langle c_{\mathrm{e}}^{i}\rangle^{\mathrm{e}}\right)
\end{cases}
\tag{2.117}
$$

and solute conservation at the $\mathrm{s/d}$ and $\mathrm{d/e}$ interfaces are given by:

$$
\begin{cases}
\Gamma_{\mathrm{s}}\left(c_{\mathrm{d/s}}^{*i} - c_{\mathrm{s/d}}^{*i}\right) = \frac{\rho S_{v}^{\mathrm{s}} D_{\mathrm{s}}^{i}}{\delta_{\mathrm{s}}^{i}}\left(c_{\mathrm{s/d}}^{*i} - \langle c_{\mathrm{s}}^{i}\rangle^{\mathrm{s}}\right) + \frac{\rho S_{v}^{\mathrm{s}} D_{\mathrm{l}}^{i}}{\delta_{\mathrm{d/s}}^{i}}\left(c_{\mathrm{d/s}}^{*i} - \langle c_{d}^{i}\rangle^{\mathrm{d}}\right) \\[2mm]
\Gamma_{\mathrm{env}}\left(c_{\mathrm{e/d}}^{*i} - c_{\mathrm{d/e}}^{*i}\right) = \frac{\rho S_{v}^{\mathrm{env}} D_{\mathrm{l}}^{i}}{\delta_{\mathrm{d/e}}^{i}}\left(c_{\mathrm{d/e}}^{*i} - \langle c_{d}^{i}\rangle^{\mathrm{d}}\right) + \frac{\rho S_{v}^{\mathrm{env}} D_{\mathrm{l}}^{i}}{\delta_{\mathrm{e/d}}^{i}}\left(c_{\mathrm{e/d}}^{*i} - \langle c_{\mathrm{e}}^{i}\rangle^{\mathrm{e}}\right)
\end{cases}
\tag{2.118}
$$

Applying the conditions of local thermodynamic equilibrium at the s/d interface, equal interfacial composition for d/e interface along with the mass and solute balance in the REV results in:

$$
\begin{cases}
\Gamma_{\mathrm{s}} c_{\mathrm{d/s}}^{*i}\left(1 - k\right) = \frac{\rho S_{v}^{\mathrm{s}} D_{\mathrm{s}}^{i}}{\delta_{\mathrm{s}}^{i}}\left(k c_{\mathrm{d/s}}^{*i} - \langle c_{\mathrm{s}}^{i}\rangle^{\mathrm{s}}\right) + \frac{\rho S_{v}^{\mathrm{s}} D_{\mathrm{l}}^{i}}{\delta_{\mathrm{d/s}}^{i}}\left(c_{\mathrm{d/s}}^{*i} - \langle c_{d}^{i}\rangle^{\mathrm{d}}\right) \\[2mm]
0 = \frac{\rho S_{v}^{\mathrm{env}} D_{\mathrm{l}}^{i}}{\delta_{\mathrm{d/e}}^{i}}\left(c_{\mathrm{d/e}}^{*i} - \langle c_{d}^{i}\rangle^{\mathrm{d}}\right) + \frac{\rho S_{v}^{\mathrm{env}} D_{\mathrm{l}}^{i}}{\delta_{\mathrm{e/d}}^{i}}\left(c_{\mathrm{d/e}}^{*i} - \langle c_{\mathrm{e}}^{i}\rangle^{\mathrm{e}}\right)
\end{cases}
\tag{2.119}
$$

Further, the three phase model is simplified by assuming perfect diffusion in the intragranular liquid such that:

$$
\frac{S_{v}^{\mathrm{s}} D_{\mathrm{l}}^{i}}{\delta_{\mathrm{d/s}}^{i}} \to \infty \qquad \frac{S_{v}^{\mathrm{env}} D_{\mathrm{l}}^{i}}{\delta_{\mathrm{e/d}}^{i}} \to \infty
\tag{2.120}
$$

This assumption results in the average composition of the intragranular liquid to become equal to the interfacial composition:

$$
\langle c_{\mathrm{d}}^{i}\rangle^{\mathrm{d}} = c_{\mathrm{d/e}}^{*i} = c_{\mathrm{e/d}}^{*i} = c_{\mathrm{l}}^{*i}
\tag{2.121}
$$

The two liquid phases are treated as the same hydrodynamic phases such that the intragranular and extragranular liquid velocity can be replaced with the averaged liquid velocity:

$$
\langle \vec{v_{\mathrm{l}}}\rangle^{\mathrm{d}} = \langle \vec{v_{\mathrm{l}}}\rangle^{\mathrm{e}} = \langle \vec{v_{\mathrm{l}}}\rangle^{\mathrm{l}}
\tag{2.122}
$$
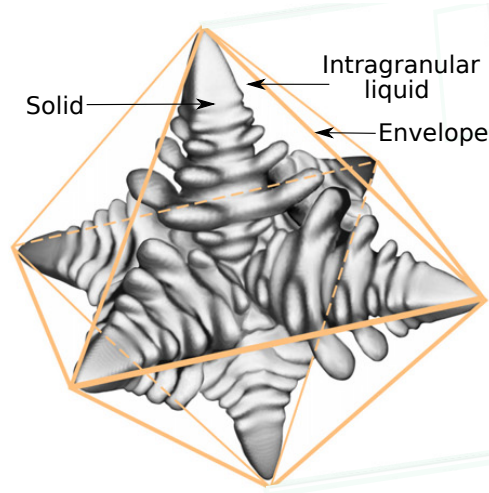
Figure 2.13 – Representation of the octahedral shape of dendritic grain with solid, intragranular liquid and envelope, $g_{\mathrm{env}} = g_{\mathrm{s}} + g_{\mathrm{d}}$ [124]

Also, the temporal evolution of the intragranular liquid composition is neglected without introducing a significant error on the estimate of the maximum supercooling as proposed by Tveito *et al.* [94]. This assumption results in slight overestimation of the dendrization of grains. The average composition of the extragranular liquid is related to the composition at the interface and the average composition of the entire liquid phase and is given by:

$$\langle c_{\mathrm{l}}^i \rangle^{\mathrm{e}} = \frac{g_{\mathrm{l}} \langle c_{\mathrm{l}}^i \rangle^{\mathrm{l}} - g_{\mathrm{d}} c_{\mathrm{l}}^{*i}}{g_{\mathrm{e}}} \tag{2.123}$$

where g_{e} is the extragranular liquid composition. The solute conservation equations for the solid and the liquid phase is written as follows:

$$\frac{\partial (g_{\mathrm{s}} \langle c_{\mathrm{s}}^i \rangle^{\mathrm{s}})}{\partial t} = \mathrm{J}_{\mathrm{s}}^{i,\Gamma} + \mathrm{J}_{\mathrm{s}}^{i,j} = \frac{\Gamma_{\mathrm{s}}}{\rho} k_p^i c_{\mathrm{l}}^{*i} + \frac{S_v^{\mathrm{s}} D_{\mathrm{s}}}{\delta_{\mathrm{s/d}}^i} \left(k_p^i c_{\mathrm{l}}^{*i} - \langle c_{\mathrm{s}}^i \rangle^{\mathrm{s}} \right) \tag{2.124}$$

$$\frac{\partial (g_{\mathrm{l}} \langle c_{\mathrm{l}}^i \rangle^{\mathrm{l}})}{\partial t} = \mathrm{J}_{\mathrm{l}}^{i,\Gamma} + \mathrm{J}_{\mathrm{l}}^{i,j} = -\frac{\Gamma_{\mathrm{s}}}{\rho} c_{\mathrm{l}}^{*i} + \frac{S_v^{\mathrm{env}} D_{\mathrm{l}}}{\delta_{\mathrm{e/d}}^i} \frac{g_{\mathrm{l}}}{g_{\mathrm{e}}} \left(c_{\mathrm{l}}^{*i} - \langle c_{\mathrm{l}}^i \rangle^{\mathrm{l}} \right) \tag{2.125}$$

The specific surface of the envelope and the ratio of the liquid fraction to the extragranular liquid fraction are used to characterize the morphology of the grains, and the interface balance is reduced to a two-phase system (and replacing the notation $(\mathrm{e/d} \rightarrow \mathrm{l})$ and $(\mathrm{s}) \rightarrow \mathrm{s})$:

$$\left(k_p^i - 1 \right) c_{\mathrm{l}}^{*i} \frac{\Gamma_{\mathrm{s}}}{\rho} + c_{\mathrm{l}}^{*i} \left(\frac{S_v^{\mathrm{env}} D_{\mathrm{l}}^i}{\delta_{\mathrm{l}}^i} \frac{g_{\mathrm{l}}}{g_{\mathrm{e}}} + \frac{S_v^s D_{\mathrm{s}}^i}{\delta_{\mathrm{s}}^i} k_p^i \right) = \frac{S_v^{\mathrm{env}} D_{\mathrm{l}}^i}{\delta_{\mathrm{l}}^i} \left(\frac{g_{\mathrm{l}}}{g_{\mathrm{e}}} \right) [\langle c_{\mathrm{l}}^i \rangle^{\mathrm{l}}] + \frac{S_v^s D_{\mathrm{s}}^i}{\delta_{\mathrm{s}}^i} \langle c_{\mathrm{s}}^i \rangle^{\mathrm{s}} \tag{2.126}$$

The envelope specific surface area S_v^{env} is determined by assuming the grain envelope as octahedrons as shown in Fig. 2.13

$$S_v^{\mathrm{env}} = 4\sqrt{3} R_{\mathrm{arm}}^2 N_g \tag{2.127}$$
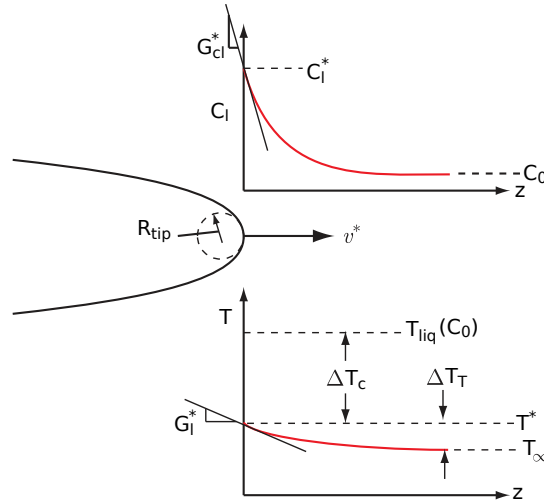
Figure 2.14 – Schematic illustration of the LGK model portraying the solutal undercooling ΔT_C and the thermal undercooling ΔT_T [2]

where R_{arm} denotes the grain arm length

$$R_{\mathrm{arm}} = \left(\frac{3 g_{\mathrm{env}}}{4 N_g} \right)^{1/3} \tag{2.128}$$

The solid specific surface area S_v^{s} is obtained through the expression proposed by Appolaire [124]

$$S_v^{\mathrm{s}} = \frac{4}{\lambda_2} \sqrt{g_i} g_{\mathrm{env}} \left(1 - g_i^m \right) + g_i^m S_v^{\mathrm{env}} \tag{2.129}$$

where λ_2 is the secondary arm spacing $\left(\lambda_2 = \frac{R_{\mathrm{env}}}{5} \right)$, R_{env} is the equivalent envelope radius

$$R_{\mathrm{env}} = 4 \pi N_g \left(3 g_{\mathrm{env}} \right)^{1/3} \tag{2.130}$$

g_{env} is the envelope phase fraction ($g_{\mathrm{env}} = g_{\mathrm{s}} + g_{\mathrm{d}}$), g_{i} is the internal solid fraction ($g_{\mathrm{i}} = g_{\mathrm{s}}/g_{\mathrm{env}}$) and the coefficient m is equal to 6 according to Nielsen *et al.* [125].

2.6.2.2.3 Dendrite tip growth model As mentioned earlier, the driving force for solidification in the two phase grain growth model is the solute diffusion across the s/l interface. In the three phase grain growth model, the growth of the solid phase is determined by the solute diffusion across the s/l interface whereas the growth of the envelope is determined by dendrite tip growth kinetics. The solution for dendritic growth of a pure substance in an undercooled melt was first proposed by Ivantsov [126] and was later generalized by Horvay and Cahn [127]. The dendrite tip which is assumed to be paraboloidal in shape grows in an undercooled melt with a far field temperature T^∞ at a constant velocity v_{tip} in a shape preserving way. The geometry of the paraboloid is characterized by the radius of the curvature at the tip, R_{tip}.

The growth of the dendrite is controlled by the existence of undercooling in the extragranular liquid. The most important undercooling in a metallic alloy is of chemical origin, and it comes from the diffusion of solute at the interface. It is further referred to as 'solutal undercooling'. The solutal undercooling, ΔT_c, is expressed

as

$$\Delta T_c = -m_{\mathrm{l}}\left(c_{\mathrm{l}}^* - c_{\mathrm{l}}^\infty\right) = m_{\mathrm{l}}c_{\mathrm{l}}^\infty\left[1 - \frac{1}{1-(1-k_p)\,\Omega_c}\right] \tag{2.131}$$

where Ω_c is the chemical supersaturation given by

$$\Omega_c = \frac{c_{\mathrm{l}}^* - c_{\mathrm{l}}^\infty}{c_{\mathrm{l}}^*\left(1-k_p\right)} \tag{2.132}$$

c_{l}^∞ is the liquid composition far from the interface. In the current implementation, c_{l}^∞ is approximated as $\langle c_{\mathrm{e}}\rangle^{\mathrm{e}}$. Eqn. 2.131 assumes thermodynamic equilibrium at the interface. There is also an undercooling of thermal origin due to diffusion of latent heat into the liquid. The 'thermal undercooling', ΔT_t is given by

$$\Delta T_t = \Omega_t \frac{L_f}{C_p} \tag{2.133}$$

where Ω_t is the thermal supersaturation. For metallic alloys, the undercoolings due to the effect of kinetics and curvature of the dendrite tips can be neglected. The total undercooling (ΔT)is given by:

$$\Delta T = \Delta T_c + \Delta T_t \tag{2.134}$$

Following the work of Papapetrou [128], Ivantsov [126] proposed an analytical model to describe the growth of a dendrite tip whose shape is assumed to be parabolic. It was initially proposed for a purely thermal dendrite (without chemical undercooling), and was later extended to binary alloys. Assuming the the dendrite is isolated and growing in an infinite liquid in a purely diffusive regime,

$$\Omega_c = Iv(\mathrm{Pe_c}) \tag{2.135}$$

where $\mathrm{Pe_c}$ is the solutal Péclet number linked to the tip growth, and is given by

$$\mathrm{Pe_c} = \frac{R_{tip}v_{tip}}{2D_{\mathrm{l}}} \tag{2.136}$$

The Ivantsov function Iv is

$$Iv(\mathrm{Pe}) = \mathrm{Pe.E}_1(\mathrm{Pe}).\exp(\mathrm{Pe}) \tag{2.137}$$

here E_1 is the exponential integral function. Using these sets of equations does not yield unique values for R_{tip} and v_{tip}, rather a solution in terms of the product $(R_{tip}v_{tip})$. Thus, a second relationship is employed. The most widely used relationship is the "marginal stability criteria" which was initially proposed by Langer and Krumbhaar. Employing the relationship results in [2]:

$$R_{tip} = \frac{\Gamma}{(\sigma^*)^2} \frac{1}{\frac{2Pe_{\mathrm{th}}L_f}{C_p} - \frac{2Pe_c m_{\mathrm{l}}c_{\mathrm{l}}^\infty(1-k)}{1-(1-k)Iv(Pe_c)}} \tag{2.138}$$

where Pe_{th} is the thermal Péclet number and is given by

$$Pe_{\mathrm{th}} = \frac{R_{tip}v_{tip}}{2\alpha} \tag{2.139}$$

where α is the thermal diffusivity. σ^* is the constant of marginal stability and is equal to $\left(4\pi^2\right)^{-1}$. The model

developed by Lipton *et al.*, commonly called LGK model, integrates the relationship of Ivantsov and marginal stability to propose a growth model for the dendrite tips valid for low growth rates. For high growth rates ($v_{tip} > 1$ cm/s), Kurz *et al.* [129] developed an extension to the previous model. The model was called the KGT model and it was developed on the hypothesis that thermodynamic equilibrium at the interface is no longer valid. Bobadilla *et al.* extended the KGT model to account for multicomponent systems.

The above mentioned models assume a purely diffusive growth regime and neglect the influence of convection on the growth of dendrite tips. Due to the complexity introduced by the flow, and in particular the direction of the flow, few growth models have been proposed which account for convection. Ananth and Gill [130] proposed an analytical solution for an isolated dendrite whose growth direction is exactly opposite to the flow. The solutal supersaturations is given by:

$$\Omega_c \left(\text{Pe}_\text{c}, \text{Pu}_\text{c}, \text{Re}_\text{c}\right) = 2\text{Pe}_\text{c} \int_1^\infty \exp\left[-\ln\left(\eta\right) + \left(1 - \eta^2\right) - \frac{2\text{Pu}_\text{c}}{E_1\left(\text{Re}_\text{c}\right)} \left(1 - \eta^2 + \ln\left(\eta\right)\left(1 + \eta^2\right)\right)\right] d\eta \quad (2.140)$$

where Pu_c is the flow Péclet number.

$$\text{Pu}_\text{c} = \frac{R_{tip}\left|\langle\vec{v}_s\rangle^\text{s} - \langle\vec{v}_\text{l}\rangle^\text{l}\right|}{2D_\text{l}} \quad \text{Re}_\text{c} = \frac{Pe + Pu}{Sc}$$

with $Pr = \frac{C_p \mu_\text{l}}{k}$ is the Prandtl number, $Sc = \frac{\mu_\text{l}}{\rho D_\text{l}}$ is the Schmidt number and Re_c is the Reynolds number: Unlike the model of Ananth and Gill [130], the model of Gandin *et al.* [131] proposes to take into account the influence of the relative orientation of the flow. The model is based on the idea of a convective boundary layer developed by Cantor and Vogel [132]. The authors suggest:

$$\Omega_c = Pe_\text{c}\exp(Pe_\text{c}) \left[E_1\left(Pe_\text{c}\right) - E_1\left(Pe_\text{c}\left(1 + \frac{4}{A\left(2\text{Re}_\text{tip}\right)^B \text{Sc}^C \sin\left(\frac{\theta}{2}\right)}\right)\right)\right] \quad (2.141)$$

where θ is the angle between the dendrite growth direction and velocity of the liquid, A = 0.5773, B = 0.6593 and C=0.5249. The envelope growth rate, Γ_env, for an octahedral envelope morphology, is given by:

$$\Gamma_\text{env} = \frac{1}{\sqrt{3}} S_v^\text{env} v_{tip} \quad (2.142)$$

2.7 Coupling micromodels with macromodels

The solidification model presented above leads to a complex set of coupled, non-linear partial differential equations (PDE). A consistent approach to solve these PDEs is critical to ensure numerical stability of computed fields. Various time integration schemes have been proposed in literature. They use iterative methods to couple these PDEs without going into the finer details of the algorithms. Wu *et al.* [133] have implemented a fully implicit scheme as shown in Fig. 2.15a which suggests that the PDEs of the micromodel are fully coupled with the PDEs of the macromodel. Wang *et al.* [134] have implemented a scheme as shown in Fig. 2.15b. The interfacial exchange terms for the solute and mass balances are computed from the converged values at time t if the conditions from primary solidification are satisfied at time t. The computed values are then used to solve the macroscopic transport equations at time $t + \Delta t$.

Založnik and Combeau [53] proposed an operator splitting scheme for the solution of the coupled system as shown in Fig. **??**. It is based on the concept of separation of scales on the solution level. For each iteration, in
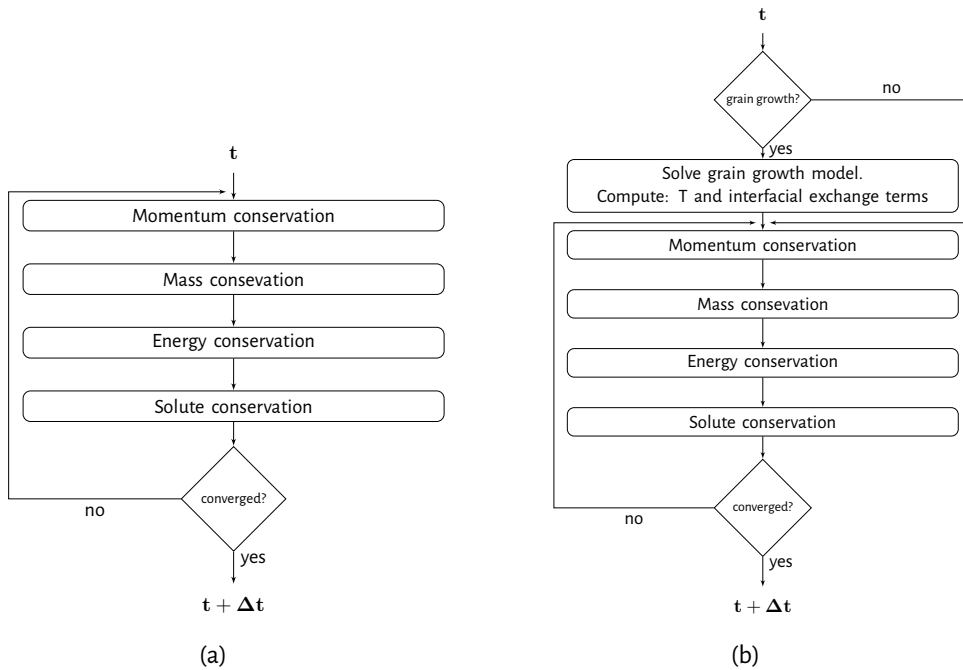
Figure 2.15 – Algorithms for multi-scale modeling of solidification adopted by a) Wu *et al.* [133] and b) Wang *et al.* [134]

the first stage of this time integration scheme, all advective contributions to the energy and solute conservation equations are resolved globally using a macro time step (Δt). The interfacial exchange parameters due to nucleation and grain growth are neglected. This stage is referred to as the 'transport stage'. In the second stage, interfacial exchange terms due to nucleation and grain growth are computed locally using the grain growth. The solution proceeds through micro time steps (δt) assuming that there is no evolution of the global quantities such as average composition and total enthalpy and is shown in Fig. 2.16b. This stage is referred to as the "growth stage". Subsequently, the contributions are added to obtain the total variation. Finally the momentum equations are solved using the macro time step (Δt) to compute the velocity fields. Thus, all the required values are computed at iteration $\mathbf{v + 1}$.

The total variation of a quantity ψ due to macroscopic transport and microscopic processes such as nucleation and growth is

$$\frac{\partial \psi}{\partial t} = A\psi + B\psi + C\psi \tag{2.143}$$

where A, B and C are the operators representing advection, nucleation and grain growth respectively. Within a macro timestep $[t, t + \Delta t]$, the operator splitting scheme is organized as

<table>
<tr><td></td><td>Initial value:</td><td>Final value:</td><td></td></tr>
</table>

$$\frac{\partial \psi^{\mathrm{tr}}}{\partial t} = A\psi^{\mathrm{tr}} \qquad {}^{t+\Delta t}[\psi]_0^{\mathrm{tr}} = {}^{t}[\psi]^{\mathrm{gr}} \qquad {}^{t+\Delta t}[\psi]^{\mathrm{tr}} \tag{2.144}$$

$$\frac{\partial \psi^{\mathrm{nuc}}}{\partial t} = B\psi^{\mathrm{nuc}} \qquad {}^{t+\Delta t}[\psi]_0^{\mathrm{nuc}} = {}^{t}[\psi]^{\mathrm{tr}} \qquad {}^{t+\Delta t}[\psi]^{\mathrm{nuc}} \tag{2.145}$$
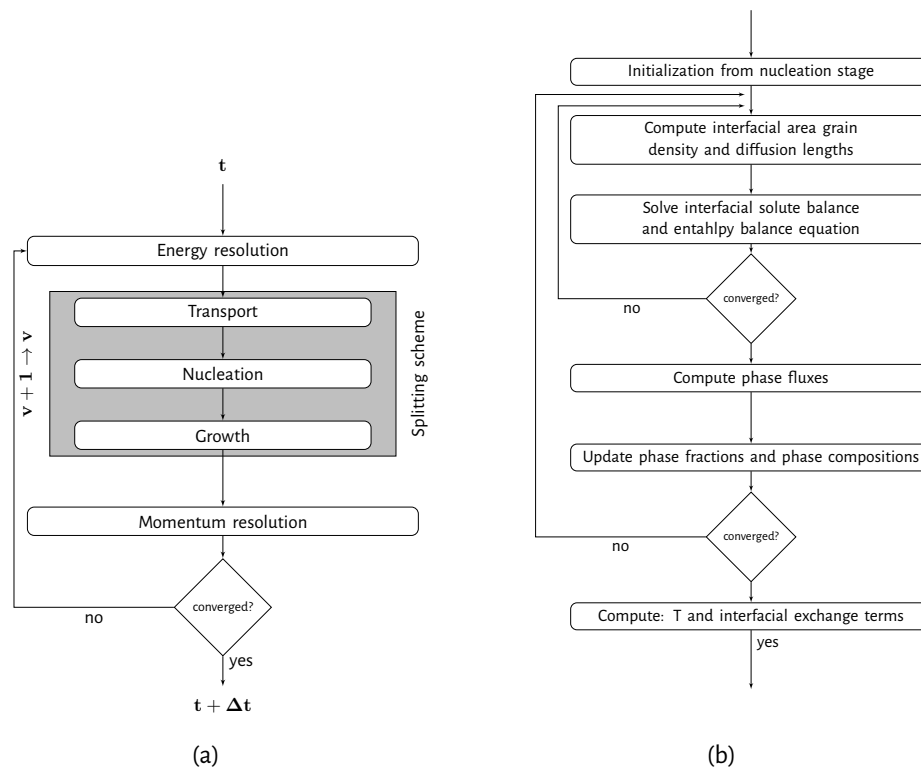
Figure 2.16 – Algorithms for a) multi-scale modeling of solidification in the splitting scheme and (b) growth stage [53]

$$\frac{\partial \psi^{\mathrm{gr}}}{\partial t} = C\psi^{\mathrm{gr}} \qquad {}^{\mathrm{t}+\Delta\mathrm{t}}[\psi]_0^{\mathrm{gr}} = {}^{\mathrm{t}}[\psi]^{\mathrm{nuc}} \qquad {}^{\mathrm{t}+\Delta\mathrm{t}}[\psi]^{\mathrm{gr}} \tag{2.146}$$

where the superscripts tr, nuc and gr represent the values obtained from the transport, nucleation and growth stages respectively at a fixed time. The values obtained after the growth stage account for the changes due to transport, nucleation and growth, however with a slight error. The mathematical error introduced due to Eqns. 2.144, 2.145 and 2.146 should be small in order for the scheme to be applicable. For solidification systems, the authors have demonstrated through scaling analysis that the error introduced through the operator splitting scheme is small under the condition:

$$\left(\left| \frac{\partial \psi}{\partial t} \right| \sim |A\psi| \right) \gg |B\psi|, |C\psi| \tag{2.147}$$

Several authors ([103, 135, 136]) have adopted the operator splitting scheme in solidification modeling. A detailed resolution of the algorithm is shown in Fig. 3.3. Using the operator splitting scheme, for the two phase

model, the mass and solute conservation equations for transport stage and nucleation and growth stage are

$$\text{Transport stage} \begin{cases} \frac{\partial(\rho g_s)}{\partial t} + \nabla.(\rho g_s \langle \vec{v_s} \rangle^l) = 0 \\[2ex] g_s + g_l = 1 \\[2ex] \frac{\partial(\rho g_s \langle c_s^i \rangle^s)}{\partial t} + \nabla.(\rho g_s \langle c_s^i \rangle^s \langle \vec{v_s} \rangle^s) = 0 \\[2ex] \frac{\partial(\rho g_l \langle c_l^i \rangle^l)}{\partial t} + \nabla.(\rho g_l \langle c_l^i \rangle^l \langle \vec{v_l} \rangle^l) = 0 \end{cases} \tag{2.148}$$

$$\text{Nucleation and growth stage} \begin{cases} \frac{\partial(\rho g_s)}{\partial t} = \Gamma_s + \Phi_s \\[2ex] g_s + g_l = 1 \\[2ex] \frac{\partial(\rho g_s \langle c_s^i \rangle^s)}{\partial t} = J_s^{i,\Phi} + J_s^{i,\Gamma} + J_s^{i,j} \\[2ex] \frac{\partial(\rho g_l \langle c_l^i \rangle^l)}{\partial t} = -\left(J_s^{i,\Phi} + J_s^{i,\Gamma} + J_s^{i,j} \right) \end{cases} \tag{2.149}$$

Using the simplified three phase model, it is possible to easily take into account a third phase in the current two-phase model. The model presented here allows this separation of scales while maintaining a macroscopic two-phase model. The transport stage is not modified and the growth stage is very slightly modified. The mass and solute conservation equations for transport stage and nucleation and growth stage for the three phase model are given by:

$$\text{Transport stage} \begin{cases} \frac{\partial(\rho g_s)}{\partial t} + \nabla.(\rho g_s \langle \vec{v_s} \rangle^l) = 0 \\[2ex] \frac{\partial(\rho g_{env})}{\partial t} + \nabla.(\rho g_{env} \langle \vec{v_s} \rangle^l) = 0 \\[2ex] \underbrace{g_s + g_d}_{g_{env}} + g_e = 1 \\[2ex] \frac{\partial(\rho g_l)}{\partial t} + \nabla.(\rho g_l \langle \vec{v_l} \rangle^l) = 0 \\[2ex] \frac{\partial(\rho g_s \langle c_s^i \rangle^s)}{\partial t} + \nabla.(\rho g_s \langle c_s^i \rangle^s \langle \vec{v_s} \rangle^s) = 0 \\[2ex] \frac{\partial(\rho g_l \langle c_l^i \rangle^l)}{\partial t} + \nabla.(\rho g_l \langle c_l^i \rangle^l \langle \vec{v_l} \rangle^l) = 0 \end{cases} \tag{2.150}$$

$$
\text{Nucleation and growth stage}
\begin{cases}
\dfrac{\partial(\rho g_{\mathrm{s}})}{\partial t} = \Gamma_{\mathrm{s}} \\[2ex]
\dfrac{\partial(\rho g_{\mathrm{d}})}{\partial t} = -\Gamma_{\mathrm{s}} + \Gamma_{\mathrm{env}} \\[2ex]
\dfrac{\partial(\rho g_{\mathrm{e}})}{\partial t} = -\Gamma_{\mathrm{env}} \\[2ex]
\dfrac{\partial(\rho g_{\mathrm{s}}\langle c_{\mathrm{s}}^{i}\rangle^{\mathrm{s}})}{\partial t} = \mathrm{J}_{\mathrm{s}}^{i,\Phi} + \mathrm{J}_{\mathrm{s}}^{i,\Gamma} + \mathrm{J}_{\mathrm{s}}^{i,j} \\[2ex]
\dfrac{\partial(\rho g_{\mathrm{l}}\langle c_{\mathrm{l}}^{i}\rangle^{\mathrm{l}})}{\partial t} = -\left(\mathrm{J}_{\mathrm{s}}^{i,\Phi} + \mathrm{J}_{\mathrm{s}}^{i,\Gamma} + \mathrm{J}_{\mathrm{s}}^{i,j} \right)
\end{cases}
\tag{2.151}
$$

The microscopic growth model describing the growth of columnar grains is similar to the microscopic growth model for equiaxed grains. However, modeling of columnar solidification requires tracking the position of the columnar front. This is done using a columnar front tracking algorithm. For cell containing columnar and equiaxed grains, special treatment is required and is referred to as the "six phase model". The "six phase model" and the columnar front tracking algorithm will not be discussed here. Interested readers are referred to Leriche [123] for an in-detailed discussion on these models.

2.8 Summary

In this chapter, the multi-scale approach to modeling of solidification is reviewed. Volume averaging approach is used and its principles are summarized. Using this approach, a solidification model is proposed in terms of macroscopic conservation equations. Lower length scale information is accounted for through the source terms in the macroscopic conservation equations. These source terms are computed by a microscopic model which also employs various constitutive relationships. Thus, the final solidification model is a complex set of coupled, non-linear PDE's, which are solved within the operator splitting scheme [53] in SOLID®.

Chapter 3 : Coupling solidification model with CALPHAD data

Contents

3.1 State of the art

Modeling of macrosegregation during solidification requires coupling of the volume averaged macroscopic conservation equations pertaining to mass, momentum, energy and solute composition with the microscopic growth model as discussed in the previous chapter. For the sake of reference, the main macroscopic equations are again presented.

$$\frac{\partial \left(\sum_\phi g_\phi \rho_\phi \right)}{\partial t} + \nabla \cdot \left(\sum_\phi g_\phi \rho_\phi \langle \vec{v}_\phi \rangle^\phi \right) = 0 \tag{3.1}$$

$$\frac{\partial \left(g_\phi \rho_\phi \langle \vec{v}_\phi \rangle^\phi \right)}{\partial t} + \nabla \cdot \left(g_\phi \rho_\phi \langle \vec{v}_\phi \rangle^\phi \langle \vec{v}_\phi \rangle^\phi \right) = -g_\phi \nabla (p) + \nabla \cdot \left(g_\phi \langle \tau_\phi \rangle^\phi \right) + $$
$$g_\phi \langle b_\phi \rangle^\phi + \vec{M}_\phi^\Gamma + \vec{M}_\phi^\Phi + \vec{M}_\phi^{\mathrm{d}} \tag{3.2}$$

$$\frac{\partial \left(\langle \rho \rangle \langle h \rangle \right)}{\partial t} + \nabla \cdot \left(\sum_\phi g_\phi \rho_\phi \langle h_\phi \rangle^\phi \langle \vec{v}_\phi \rangle^\phi \right) = \nabla \cdot (k_{\mathrm{m}} \nabla T) \tag{3.3}$$

$$\frac{\partial \left(g_\phi \rho_\phi \right)}{\partial t} + \nabla \cdot \left(g_\phi \rho_\phi \langle \vec{v}_\phi \rangle^\phi \right) = \Gamma_\phi + \Phi_\phi \tag{3.4}$$

$$\frac{\partial \left(g_\phi \langle \rho_\phi \rangle^\phi \langle c_\phi^i \rangle^\phi \right)}{\partial t} + \nabla \cdot \left(g_\phi \langle \rho_\phi \rangle^\phi \langle c_\phi^i \rangle^\phi \langle \vec{v}_\phi \rangle^\phi \right) = \nabla \cdot \left(g_\phi \langle \rho_\phi \rangle^\phi \langle D_\phi^i \rangle^\phi \nabla \langle c_\phi^i \rangle^\phi \right) + J_\phi^{i,\Gamma} + J_\phi^{i,j} + J_\phi^{i,\Phi} \tag{3.5}$$

The intrinsic phase enthalpy $\langle h_\phi \rangle^\phi$ in Eqn. 3.3 along with interfacial exchange terms in Eqns. 3.4 and 3.5 are dependent on the phase diagram parameters. Currently, all the models simulating multi-component ingot solidification with solid grain motion assume a linearized phase diagram. Quoting from Schneider *et al.* [137], 'realistic prediction of macrosegregation in multi-component alloys requires accurate modeling of phase equilibrium, solidification path and microsegregation'. In ternary and higher order systems, the phase diagram parameters are highly dependent on the phase, temperature and composition. Thus, coupling solidification models with 'real' phase diagram parameters is critical. Phase diagram parameters can be obtained from various CALPHAD functions. The intrinsic phase enthalpy $\langle h_\phi \rangle^\phi$ in Eqn. 3.3 as well as the phase diagram parameters used in various constitutive models to compute the interfacial exchange terms in Eqns. 3.4 and 3.5 can be obtained from CALPHAD functions (and are thus highlighted in blue). Table 3.1 lists the constitutive models used for the phase diagram parameters in the linearized phase diagram approach as well as its equivalent CALPHAD functions. The list of CALPHAD functions in table 3.1 is non-exhaustive.

The CALPHAD approach along with its implementation in the current solidification model framework will be discussed in more details in the proceeding sections. However, as presented earlier, coupling the model with CALPHAD functions modifies Eqns. 3.3, 3.4 and 3.5 (highlighted in blue). Modification to Eqn. 3.3 only modifies the values used in the equation to solve the equation. Modifications to Eqns. 3.4 and 3.5 requires modifications to microscopic growth model which was presented in the previous chapter. Thus, in this chap-

Table 3.1 – CALPHAD function equivalents for various linearized phase diagram parameters

Outputs	Linearized phase diagram	CALPHAD function
$\langle h_\phi \rangle^\phi$	$\begin{cases} C_p T & : \text{solid} \\ C_p T + L_f & : \text{liquid} \end{cases}$	$f_1\left(T, \langle c_\phi \rangle^\phi\right)$
T^*	$T_f + \sum_i m_1^i c_1^{*i}$	$f_2\left(c_1^{*i}\right)$
c_s^{*i}	$k_p^i c_1^{*i}$	$f_3\left(c_1^{*i}\right)$

ter, we first present the modification pertaining to the energy conservation equation (Eq. 3.3) in section 3.3. Subsequently, we present the new microscopic growth model along with the solution scheme employed in section 3.4.

3.2 Coupling between microscopic and macroscopic scales
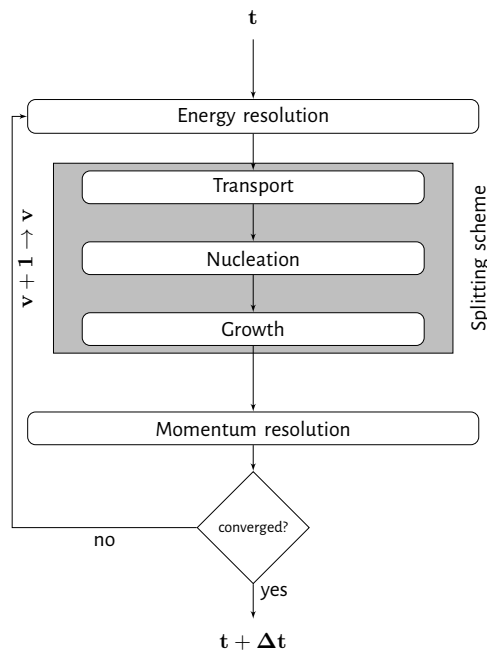
Figure 3.1 – Algorithm for multi-scale modeling of solidification in the splitting scheme[53]

In the previous chapter, the operator splitting scheme developed by Založnik and Combeau [53] was introduced. Highlighting the main point of the operator splitting scheme again (Fig. 3.1), each iteration $\mathbf{v}$ begins with the resolution of the energy and the solute transport equations using a macro time-step Δt. The nucleation and the growth terms are neglected. The solutions obtained are indicated with the superscript $\mathbf{v+1}$ along with an additional superscript tr for the transport stage. The nucleation and growth stages are solved locally with variables initialized from the transport stage at $\mathbf{v+1}$, assuming that the average composition

and the total enthalpy does not evolve within these stages. Nucleation occurs depending on the local conditions and the solution of the model is indicated with the superscript $\mathbf{v+1}$ along with an additional superscript nuc for the nucleation stage. The solution of the nucleation model are the inputs for the microscopic growth model which uses an iterative scheme with micro time-steps (δt). The solution of the growth model is indicated with a superscript $\mathbf{v+1}$ along with an additional superscript gr for the growth stage. Finally, the solution of the growth model is used to solve the momentum equations to compute the velocity fields at $\mathbf{v+1}$. This resolution algorithm for solidification is currently implemented in SOLID® and is schematized in Fig. 3.2.

3.3 Macrosegregation model - energy conservation equation

3.3.1 Formulation

In order to facilitate the numerical solution of Eq. 3.3, the diffusive term is expressed in terms of the leading variable $\langle h \rangle$

$$\nabla \cdot (k_\mathrm{m} \nabla T) = \nabla \cdot \left(k_\mathrm{m} \left(\frac{\partial T}{\partial \langle h \rangle} \right)_{\langle c_\phi^i \rangle^\phi} \nabla \langle h \rangle \right) - \left(\nabla \cdot \left(k_\mathrm{m} \left(\left(\frac{\partial T}{\partial \langle h \rangle} \right)_{\langle c_\phi^i \rangle^\phi} \right) \nabla \langle h \rangle \right) - k_\mathrm{m} \nabla T \right) \quad (3.6)$$

We also add and subtract the term $(\nabla \cdot (\langle \rho \rangle \langle h \rangle \langle \vec{v} \rangle))$ on both sides of the equation. The final equation is

$$\frac{\partial (\langle \rho \rangle \langle h \rangle)}{\partial t} + (\nabla \cdot (\langle \rho \rangle \langle h \rangle \langle \vec{v} \rangle)) - \nabla \cdot \left(k_\mathrm{m} \left(\frac{\partial T}{\partial \langle h \rangle} \right)_{\langle c_\phi^i \rangle^\phi} \nabla \langle h \rangle \right) = \nabla \cdot (k_\mathrm{m} \nabla T) -$$

$$\nabla \cdot \left(k_\mathrm{m} \left(\frac{\partial T}{\partial \langle h \rangle} \right)_{\langle c_\phi^i \rangle^\phi} \nabla \langle h \rangle \right) \left[\nabla \cdot (\langle \rho \rangle \langle h \rangle \langle \vec{v} \rangle) - \nabla \cdot (g_\mathrm{s} \rho_\mathrm{s} \langle h_\mathrm{s} \rangle^\mathrm{s} \langle \vec{v}_\mathrm{s} \rangle^\mathrm{s}) - \nabla \cdot \left(g_\mathrm{l} \rho_\mathrm{l} \langle h_\mathrm{l} \rangle^\mathrm{l} \langle \vec{v}_\mathrm{l} \rangle^\mathrm{l} \right) \right] \quad (3.7)$$

3.3.2 Discretization

In SOLID®, the energy conservation equation (Eqn. 3.7) is discretized in the following way:

$$\frac{\partial (\langle \rho \rangle^{\mathbf{v+1}} \langle h \rangle)}{\partial t} + \left(\nabla \cdot \left(\langle \rho \rangle^{\mathbf{v+1}} \langle h \rangle \langle \vec{v} \rangle \right) \right) - \nabla \cdot \left(k_\mathrm{m} \left(\frac{\partial T}{\partial \langle h \rangle} \right)_{\langle c_\phi^i \rangle^\phi} \nabla \left(^{\mathbf{v+1}} \langle h \rangle \right) \right) = \nabla \cdot (k_\mathrm{m} \nabla T) -$$

$$\nabla \cdot \left(k_\mathrm{m} \left(\frac{\partial T}{\partial \langle h \rangle} \right)_{\langle c_\phi^i \rangle^\phi} \nabla \langle h \rangle \right) \left[\nabla \cdot (\langle \rho \rangle \langle h \rangle \langle \vec{v} \rangle) - \nabla \cdot (g_\mathrm{s} \rho_\mathrm{s} \langle h_\mathrm{s} \rangle^\mathrm{s} \langle \vec{v}_\mathrm{s} \rangle^\mathrm{s}) - \nabla \cdot \left(g_\mathrm{l} \rho_\mathrm{l} \langle h_\mathrm{l} \rangle^\mathrm{l} \langle \vec{v}_\mathrm{l} \rangle^\mathrm{l} \right) \right] \quad (3.8)$$

and is solved for $^{\mathbf{v+1}} \langle h \rangle$ (highlighted in red). $\mathbf{v+1}$ denotes the current iteration and $\mathbf{v}$ the previous iteration. All the parameters except for $\langle h \rangle$ on the LHS of Eqn. 3.7 corresponds to iteration $\mathbf{v}$ which has been omitted here for the sake of clarity of the equation. $\langle \vec{v} \rangle$ is the mixture velocity calculated from the conservative phase velocities, $\langle \vec{v}_\mathrm{s} \rangle^\mathrm{s}$ and $\langle \vec{v}_\mathrm{l} \rangle^\mathrm{l}$, obtained after pressure correction in the preceding iteration $\mathbf{v}$. Phase fractions and densities are also calculated after the growth stage of the preceding iteration $\mathbf{v}$. The terms on the LHS of Eqn. 3.7 are solved implicitly and the RHS terms are explicit. The mixture density $\langle \rho \rangle$, mixture velocity $\langle \vec{v} \rangle$ and the
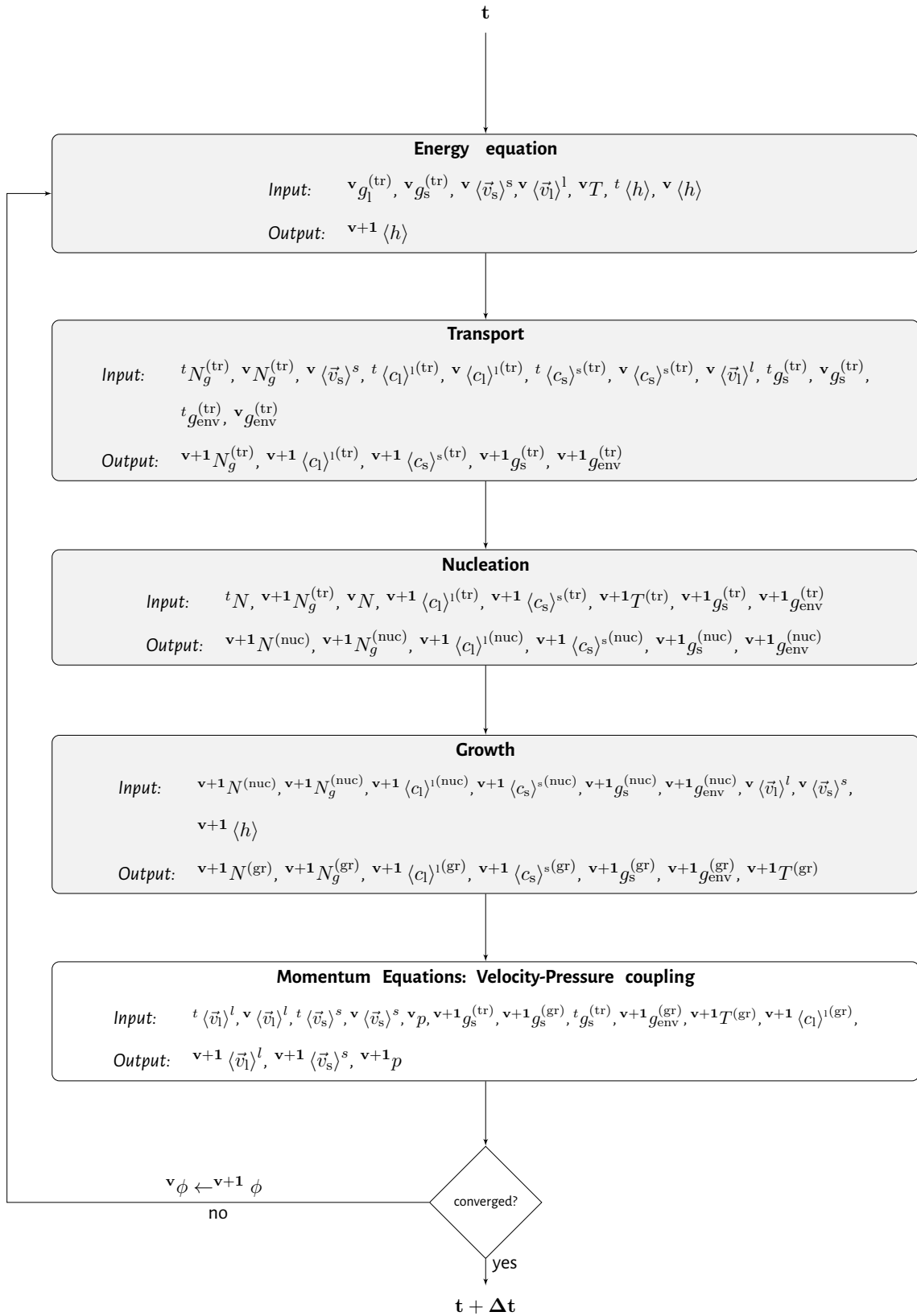
$$t$$

Energy   equation

Input: $^{\mathbf{v}}g_{\mathrm{l}}^{(\mathrm{tr})}$, $^{\mathbf{v}}g_{\mathrm{s}}^{(\mathrm{tr})}$, $^{\mathbf{v}}\langle\vec{v}_{\mathrm{s}}\rangle^{\mathrm{s}}$, $^{\mathbf{v}}\langle\vec{v}_{\mathrm{l}}\rangle^{\mathrm{l}}$, $^{\mathbf{v}}T$, $^{t}\langle h\rangle$, $^{\mathbf{v}}\langle h\rangle$

Output: $^{\mathbf{v+1}}\langle h\rangle$

Transport

Input: $^{t}N_{g}^{(\mathrm{tr})}$, $^{\mathbf{v}}N_{g}^{(\mathrm{tr})}$, $^{\mathbf{v}}\langle\vec{v}_{\mathrm{s}}\rangle^{s}$, $^{t}\langle c_{\mathrm{l}}\rangle^{\mathrm{l}(\mathrm{tr})}$, $^{\mathbf{v}}\langle c_{\mathrm{l}}\rangle^{\mathrm{l}(\mathrm{tr})}$, $^{t}\langle c_{\mathrm{s}}\rangle^{\mathrm{s}(\mathrm{tr})}$, $^{\mathbf{v}}\langle c_{\mathrm{s}}\rangle^{\mathrm{s}(\mathrm{tr})}$, $^{\mathbf{v}}\langle\vec{v}_{\mathrm{l}}\rangle^{l}$, $^{t}g_{\mathrm{s}}^{(\mathrm{tr})}$, $^{\mathbf{v}}g_{\mathrm{s}}^{(\mathrm{tr})}$,

              $^{t}g_{\mathrm{env}}^{(\mathrm{tr})}$, $^{\mathbf{v}}g_{\mathrm{env}}^{(\mathrm{tr})}$

Output: $^{\mathbf{v+1}}N_{g}^{(\mathrm{tr})}$, $^{\mathbf{v+1}}\langle c_{\mathrm{l}}\rangle^{\mathrm{l}(\mathrm{tr})}$, $^{\mathbf{v+1}}\langle c_{\mathrm{s}}\rangle^{\mathrm{s}(\mathrm{tr})}$, $^{\mathbf{v+1}}g_{\mathrm{s}}^{(\mathrm{tr})}$, $^{\mathbf{v+1}}g_{\mathrm{env}}^{(\mathrm{tr})}$

Nucleation

Input: ^{t}N, $^{\mathbf{v+1}}N_{g}^{(\mathrm{tr})}$, $^{\mathbf{v}}N$, $^{\mathbf{v+1}}\langle c_{\mathrm{l}}\rangle^{\mathrm{l}(\mathrm{tr})}$, $^{\mathbf{v+1}}\langle c_{\mathrm{s}}\rangle^{\mathrm{s}(\mathrm{tr})}$, $^{\mathbf{v+1}}T^{(\mathrm{tr})}$, $^{\mathbf{v+1}}g_{\mathrm{s}}^{(\mathrm{tr})}$, $^{\mathbf{v+1}}g_{\mathrm{env}}^{(\mathrm{tr})}$

Output: $^{\mathbf{v+1}}N^{(\mathrm{nuc})}$, $^{\mathbf{v+1}}N_{g}^{(\mathrm{nuc})}$, $^{\mathbf{v+1}}\langle c_{\mathrm{l}}\rangle^{\mathrm{l}(\mathrm{nuc})}$, $^{\mathbf{v+1}}\langle c_{\mathrm{s}}\rangle^{\mathrm{s}(\mathrm{nuc})}$, $^{\mathbf{v+1}}g_{\mathrm{s}}^{(\mathrm{nuc})}$, $^{\mathbf{v+1}}g_{\mathrm{env}}^{(\mathrm{nuc})}$

Growth

Input: $^{\mathbf{v+1}}N^{(\mathrm{nuc})}$, $^{\mathbf{v+1}}N_{g}^{(\mathrm{nuc})}$, $^{\mathbf{v+1}}\langle c_{\mathrm{l}}\rangle^{\mathrm{l}(\mathrm{nuc})}$, $^{\mathbf{v+1}}\langle c_{\mathrm{s}}\rangle^{\mathrm{s}(\mathrm{nuc})}$, $^{\mathbf{v+1}}g_{\mathrm{s}}^{(\mathrm{nuc})}$, $^{\mathbf{v+1}}g_{\mathrm{env}}^{(\mathrm{nuc})}$, $^{\mathbf{v}}\langle\vec{v}_{\mathrm{l}}\rangle^{l}$, $^{\mathbf{v}}\langle\vec{v}_{\mathrm{s}}\rangle^{s}$,

              $^{\mathbf{v+1}}\langle h\rangle$

Output: $^{\mathbf{v+1}}N^{(\mathrm{gr})}$, $^{\mathbf{v+1}}N_{g}^{(\mathrm{gr})}$, $^{\mathbf{v+1}}\langle c_{\mathrm{l}}\rangle^{\mathrm{l}(\mathrm{gr})}$, $^{\mathbf{v+1}}\langle c_{\mathrm{s}}\rangle^{\mathrm{s}(\mathrm{gr})}$, $^{\mathbf{v+1}}g_{\mathrm{s}}^{(\mathrm{gr})}$, $^{\mathbf{v+1}}g_{\mathrm{env}}^{(\mathrm{gr})}$, $^{\mathbf{v+1}}T^{(\mathrm{gr})}$

Momentum Equations: Velocity-Pressure coupling

Input: $^{t}\langle\vec{v}_{\mathrm{l}}\rangle^{l}$, $^{\mathbf{v}}\langle\vec{v}_{\mathrm{l}}\rangle^{l}$, $^{t}\langle\vec{v}_{\mathrm{s}}\rangle^{s}$, $^{\mathbf{v}}\langle\vec{v}_{\mathrm{s}}\rangle^{s}$, $^{\mathbf{v}}p$, $^{\mathbf{v+1}}g_{\mathrm{s}}^{(\mathrm{tr})}$, $^{\mathbf{v+1}}g_{\mathrm{s}}^{(\mathrm{gr})}$, $^{t}g_{\mathrm{s}}^{(\mathrm{tr})}$, $^{\mathbf{v+1}}g_{\mathrm{env}}^{(\mathrm{gr})}$, $^{\mathbf{v+1}}T^{(\mathrm{gr})}$, $^{\mathbf{v+1}}\langle c_{\mathrm{l}}\rangle^{\mathrm{l}(\mathrm{gr})}$,

Output: $^{\mathbf{v+1}}\langle\vec{v}_{\mathrm{l}}\rangle^{l}$, $^{\mathbf{v+1}}\langle\vec{v}_{\mathrm{s}}\rangle^{s}$, $^{\mathbf{v+1}}p$

$^{\mathbf{v}}\phi \leftarrow {}^{\mathbf{v+1}}\phi$

no

converged?

yes

$$t + \mathbf{\Delta t}$$

Figure 3.2 – Transport-growth resolution algorithm for the three phase model

mixture enthalpy $\langle h \rangle$ are defined as

$$\langle \rho \rangle = g_{\mathrm{s}}\rho_{\mathrm{s}} + g_{\mathrm{l}}\rho_{\mathrm{l}} \tag{3.9}$$

$$\langle \vec{v} \rangle = \frac{\rho_{\mathrm{s}}}{\langle \rho \rangle} g_{\mathrm{s}}\langle \vec{v}_{\mathrm{s}} \rangle^{\mathrm{s}} + \frac{\rho_{\mathrm{l}}}{\langle \rho \rangle} g_{\mathrm{l}}\langle \vec{v}_{\mathrm{l}} \rangle^{\mathrm{l}} \tag{3.10}$$

$$\langle h \rangle = \frac{\rho_{\mathrm{s}}}{\langle \rho \rangle} g_{\mathrm{s}}\langle h_{\mathrm{s}} \rangle^{\mathrm{s}} + \frac{\rho_{\mathrm{l}}}{\langle \rho \rangle} g_{\mathrm{l}}\langle h_{\mathrm{l}} \rangle^{\mathrm{l}} \tag{3.11}$$

where $\langle h_{\mathrm{l}} \rangle^{\mathrm{l}}$ and $\langle h_{\mathrm{s}} \rangle^{\mathrm{s}}$ are intrinsic phase enthalpies obtained from CALPHAD function f_1 in Table 3.1. $(\partial T/\partial \langle h \rangle)$ is also calculated using CALPHAD functions. However, $(\partial T/\partial \langle h \rangle)$ does not need to be calculated exactly since the two terms of Eqn. 3.8 that contain this coefficient cancel out upon convergence. $(\partial T/\partial \langle h \rangle)$ can be approximated such that the better the approximation, the faster is the convergence. For non-solidifying materials and for solidifying materials in fully liquid or fully solid state $(\partial T/\partial \langle h \rangle) = 1/C_{\mathrm{pm}}$ where C_{pm} is the specific heat capacity of the mixture and is given by

$$C_{\mathrm{pm}} = g_{\mathrm{s}} \left(\frac{\partial \langle h_{\mathrm{s}} \rangle^{\mathrm{s}}}{\partial T} \right)_{\langle c_{\mathrm{s}}^i \rangle^{\mathrm{s}}} + (1 - g_{\mathrm{s}}) \left(\frac{\partial \langle h_{\mathrm{l}} \rangle^{\mathrm{l}}}{\partial T} \right)_{\langle c_{\mathrm{l}}^i \rangle^{\mathrm{l}}} \tag{3.12}$$

$$\frac{\partial \langle h_\phi \rangle^\phi}{\partial T} = f_4 \left(T, \langle c_\phi \rangle^\phi \right) \tag{3.13}$$

where f_2 is a CALPHAD function. For solidifying materials within the solidification interval, approximations are made using values of the previous iteration.

3.4 Microsegregation model

3.4.1 Model formulation

3.4.1.1 Nucleation

Heterogeneous nucleation occurs when nuclei are present and the local undercooling (ΔT) conditions are satisfied. Coupling the nucleation model with CALPHAD functions does not change the solid mass flux due to nucleation (Φ_{s}), however the solute flux due to nucleation and the point at which nucleation occurs is modified due to modifications in the partition coefficient and the liquidus temperature. The solute flux due to nucleation is given by

$$\mathrm{J}_{\mathrm{s}}^{i,\Phi} = \Phi_{\mathrm{s}} \left(k_p^i \langle c_{\mathrm{l}}^i \rangle^{\mathrm{l}} \right) \tag{3.14}$$

where

$$\Delta T = f_2 \left(\langle c_{\mathrm{l}}^i \rangle^{\mathrm{l}} \right) - T \tag{3.15}$$

f_2 computes the liquidus temperature for the liquid with composition $\langle c_{\mathrm{l}}^i \rangle^{\mathrm{l}}$.

3.4.1.2 Grain growth

3.4.1.2.1 Enthalpy balance equation: The total enthalpy of the system is:

$$\langle h \rangle = g_{\mathrm{s}} \langle h_{\mathrm{s}} \rangle^{\mathrm{s}} + g_{\mathrm{l}} \langle h_{\mathrm{l}} \rangle^{\mathrm{l}} \tag{3.16}$$

Differentiating the above equation and re-arranging the terms, we get:

$$\mathrm{d}\langle h \rangle = \left(\langle h_{\mathrm{l}} \rangle^{\mathrm{l}} - \langle h_{\mathrm{s}} \rangle^{\mathrm{s}} \right) \mathrm{d}g_{\mathrm{l}} + g_{\mathrm{s}} \left(\mathrm{d}\langle h_{\mathrm{s}} \rangle^{\mathrm{s}} \right) + g_{\mathrm{l}} \left(\mathrm{d}\langle h_{\mathrm{l}} \rangle^{\mathrm{l}} \right) \tag{3.17}$$

The first term in Eqn. 3.17 is the contribution of solid phase change (dg_{s}) to the total enthalpy change. The second and the third term corresponds to the intrinsic variation in the enthalpy of phases due to change in temperature and composition.

$$\mathrm{d}\langle h_{\mathrm{s}} \rangle^{\mathrm{l}} = \left(\frac{\partial \langle h_{\mathrm{s}} \rangle^{\mathrm{s}}}{\partial T} \right)_{\langle c_{\mathrm{s}}^i \rangle^{\mathrm{s}}} \mathrm{d}T + \sum_i \left(\frac{\partial \langle h_{\mathrm{s}} \rangle^{\mathrm{s}}}{\partial \langle c_{\mathrm{s}}^i \rangle^{\mathrm{s}}} \right)_T \mathrm{d}\langle c_{\mathrm{s}}^i \rangle^{\mathrm{s}} \tag{3.18}$$

$$\mathrm{d}\langle h_{\mathrm{l}} \rangle^{\mathrm{s}} = \left(\frac{\partial \langle h_{\mathrm{l}} \rangle^{\mathrm{l}}}{\partial T} \right)_{\langle c_{\mathrm{l}}^i \rangle^{\mathrm{l}}} \mathrm{d}T + \sum_i \left(\frac{\partial \langle h_{\mathrm{l}} \rangle^{\mathrm{l}}}{\partial \langle c_{\mathrm{l}}^i \rangle^{\mathrm{l}}} \right)_T \mathrm{d}\langle c_{\mathrm{l}}^i \rangle^{\mathrm{l}} \tag{3.19}$$

Thus, the final enthalpy balance equation is

$$\mathrm{d}\langle h \rangle = A + B + C \tag{3.20}$$

$$A = \left(\langle h_{\mathrm{l}} \rangle^{\mathrm{l}} - \langle h_{\mathrm{s}} \rangle^{\mathrm{s}} \right) \mathrm{d}g_{\mathrm{l}}$$

$$B = \left[g_{\mathrm{s}} \left(\frac{\partial \langle h_{\mathrm{s}} \rangle^{\mathrm{s}}}{\partial T} \right)_{\langle c_{\mathrm{s}}^i \rangle^{\mathrm{s}}} + (1 - g_{\mathrm{s}}) \left(\frac{\partial \langle h_{\mathrm{l}} \rangle^{\mathrm{l}}}{\partial T} \right)_{\langle c_{\mathrm{l}}^i \rangle^{\mathrm{l}}} \right] \mathrm{d}T$$

$$C = \left[g_{\mathrm{s}} \sum_i \left(\frac{\partial \langle h_{\mathrm{s}} \rangle^{\mathrm{s}}}{\partial \langle c_{\mathrm{s}}^i \rangle^{\mathrm{s}}} \right)_T \mathrm{d}\langle c_{\mathrm{s}}^i \rangle^{\mathrm{s}} + (1 - g_{\mathrm{s}}) \sum_i \left(\frac{\partial \langle h_{\mathrm{l}} \rangle^{\mathrm{l}}}{\partial \langle c_{\mathrm{l}}^i \rangle^{\mathrm{l}}} \right)_T \mathrm{d}\langle c_{\mathrm{l}}^i \rangle^{\mathrm{l}} \right]$$

Contribution 'A' corresponds to the effect of phase transformation on enthalpy. Contribution 'B' and 'C' corresponds to the contribution of composition and temperature change on the enthalpy. Contribution 'B' was not accounted for in the earlier models. The constant latent heat, L_f, in the earlier model is replaced with $\left(\langle h_{\mathrm{l}} \rangle^{\mathrm{l}} - \langle h_{\mathrm{s}} \rangle^{\mathrm{s}} \right)$, which does not correspond to the standard definition of 'latent heat' that are defined for pure metals.

3.4.1.2.2 Interface solute mass balance equation: The interface solute mass balance equation is not modified. As presented in the previous chapter, the interface solute mass balance equation for solute i is written as:

$$c_{\mathrm{l}}^{*i} \left(k_p^i - 1 \right) \frac{\Gamma_{\mathrm{s/l}}}{\rho} + c_{\mathrm{l}}^{*i} \left(\frac{S_v^{\mathrm{s}} D_{\mathrm{l}}^i}{\delta_{\mathrm{l}}^i} + k_p^i \frac{S_v D_{\mathrm{s}}^i}{\delta_{\mathrm{s}}^i} \right) = \langle c_{\mathrm{l}}^i \rangle^{\mathrm{l}} \frac{S_v^{\mathrm{s}} D_{\mathrm{l}}^i}{\delta_{\mathrm{l}}^i} + \langle c_{\mathrm{s}}^i \rangle^{\mathrm{s}} \frac{S_v^{\mathrm{s}} D_{\mathrm{s}}^i}{\delta_{\mathrm{s}}^i} \tag{3.21}$$

The above equation is non-linear as the left most term is the product of the unknowns $\Gamma_{\mathrm{s/l}}$ and c_{l}^{*i} which makes the equation non-linear. Further, the partition coefficient (k_p^i) is obtained from the CALPHAD function

f_3 from Table. 3.1.

3.4.1.2.3   Interface equilibrium relationship   The interface composition and temperature follow from the interface equilibrium and the local thermal equilibrium in the REV. In the earlier models, the equilibrium interface composition was linked to the temperature by a simplified multi-component phase diagram where the liquidus temperature is described by the linear dependence on the alloy composition and the liquidus slope for each element i

$$T^* = T_f + \sum_i m_1^i c_{1/s}^{*,i} \tag{3.22}$$

However, this assumption of linear dependence is not valid for variable phase diagram parameters. Thus, this relation is written in its differential form as

$$\mathrm{d}T = \sum_i m_1^i . \mathrm{d}c_{1/s}^{*,i}$$

where m_1^i is obtained from CALPHAD function. The equations listed above are used in conjunction with the solute balance equations in the solid and liquid phase

$$\frac{\partial}{\partial t}\left(g_s \langle c_s^i \rangle^s\right) = \frac{\Gamma_{s/l} k_p^i c_1^{*i}}{\rho} + \frac{S_v^s D_s^i}{\delta_s^i}\left(k_p^i c_1^{*i} - \langle c_s^i \rangle^s\right) \tag{3.23}$$

$$\frac{\partial}{\partial t}\left(g_l \langle c_l^i \rangle^l\right) = -\frac{\Gamma_{s/l} c_1^{*i}}{\rho} + \frac{S_v^s D_l^i}{\delta_l^i}\left(c_1^{*i} - \langle c_l^i \rangle^l\right) \tag{3.24}$$

to obtain the parameters: $c_1^{*i}, \Gamma_{s/l}, T^*, \langle c_l^i \rangle^l$ and $\langle c_s^i \rangle^s$

3.4.2   Model implementation

Fig. 3.3 schematizes the resolution algorithm for primary solidification currently implemented in SOLID® and will be further referred to as 'Approach SOLID'. In fig. 3.3, the variables corresponding to transport, nucleation and growth stage are denoted with index 'tr', 'nuc' and 'gr'. The solution of the transport stage at the iteration $\mathbf{v+1}$ is used to initialize the variables for the nucleation stage. The solution of the nucleation model is used as inputs for the grain growth model. As mentioned earlier, the microscopic grain growth model uses micro time-steps δt such that

$$\delta t = \frac{\Delta t}{n_{\mathrm{mic}}} \tag{3.25}$$

where n_{mic} is the number of micro time-steps. For the microscopic grain growth model, it is assumed that there is a linear variation of enthalpy over each micro time-step between time $(t, t + \Delta t)$

$$\delta \langle h \rangle = \frac{{}^{\mathbf{v+1}}\langle h \rangle - {}^{\mathbf{t}}\langle h \rangle}{n_{\mathrm{mic}}} \tag{3.26}$$

$\delta \langle h \rangle$ is used as an input for the enthalpy balance equation.

The enthalpy balance equation is discretized in the following way:

$$\delta \langle h \rangle = {}^{\mathbf{t+\delta t}}\langle h \rangle - {}^{\mathbf{t}}\langle h \rangle \tag{3.27}$$

Nucleation stage solution
$$^{\mathbf{v+1}}[\langle c_{\mathrm{s}}^i \rangle^{\mathrm{s}}]^{\mathrm{nuc}}$$
$$^{\mathbf{v+1}}[\langle c_{\mathrm{l}}^i \rangle^{\mathrm{l}}]^{\mathrm{nuc}}$$
$$^{\mathbf{v+1}}[g_{\mathrm{s}}]^{\mathrm{nuc}}$$
$$^{\mathbf{v+1}}[N]^{\mathrm{nuc}}$$
$$^{\mathbf{v+1}}[N_{\mathrm{nuc}}]^{\mathrm{nuc}}$$

Transport stage solution
$$^{\mathbf{v+1}}\langle h \rangle$$
$$^{\mathbf{v+1}}[\langle c_{\mathrm{s}}^i \rangle^{\mathrm{s}}]^{\mathrm{tr}}$$
$$^{\mathbf{v+1}}[\langle c_{\mathrm{l}}^i \rangle^{\mathrm{l}}]^{\mathrm{tr}}$$
$$^{\mathbf{v+1}}[g_{\mathrm{s}}]^{\mathrm{tr}}$$
$$^{\mathbf{v+1}}[N]^{\mathrm{tr}}$$
$$^{\mathbf{v+1}}[N_{\mathrm{nuc}}]^{\mathrm{tr}}$$

Initialization for growth model
$$\delta t = \frac{\Delta t}{n_{\mathrm{mic}}} \quad \delta \langle h \rangle = \frac{\Delta \langle h \rangle}{n_{\mathrm{mic}}} \quad {}^{\mathbf{t+\delta t}}T = {}^{(t)}T$$
$$^{\mathbf{t+\delta t}}c_{\mathrm{l}}^{*i} = {}^{(t)}c_{\mathrm{l}}^{*i} \quad {}^{\mathbf{t+\delta t}}\Gamma_{\mathrm{s}} = {}^{(t)}\Gamma_{\mathrm{s}}$$
$$^{\mathbf{t+\delta t}}[\langle c_{\mathrm{s}}^i \rangle^{\mathrm{s}}]^{\mathrm{gr}} = {}^{\mathbf{v+1}}[\langle c_{\mathrm{s}}^i \rangle^{\mathrm{s}}]^{\mathrm{nuc}}$$
$$^{\mathbf{t+\delta t}}[\langle c_{\mathrm{l}}^i \rangle^{\mathrm{l}}]^{\mathrm{gr}} = {}^{\mathbf{v+1}}[\langle c_{\mathrm{l}}^i \rangle^{\mathrm{l}}]^{\mathrm{nuc}}$$
$$^{\mathbf{t+\delta t}}[g_{\mathrm{s}}]^{\mathrm{gr}} = {}^{\mathbf{v+1}}[g_{\mathrm{s}}]^{\mathrm{nuc}}$$
$$^{\mathbf{t+\delta t}}[N]^{\mathrm{gr}} = {}^{\mathbf{v+1}}[N]^{\mathrm{nuc}}$$
$$^{\mathbf{t+\delta t}}[N_{\mathrm{nuc}}]^{\mathrm{nuc}} = {}^{\mathbf{v+1}}[N_{\mathrm{nuc}}]^{\mathrm{nuc}}$$

Primary solidif.

YES

Initialization
$$^{\mathbf{n}}c_{\mathrm{l}}^{*i} = {}^{\mathbf{t+\delta t}}c_{\mathrm{l}}^{*i} \quad {}^{\mathbf{n}}\Gamma_{\mathrm{s}} = {}^{\mathbf{t+\delta t}}\Gamma_{\mathrm{s}}$$
$$^{\mathbf{n}}[\langle c_{\mathrm{s}}^i \rangle^{\mathrm{s}}]^{\mathrm{gr}} = {}^{\mathbf{t+\delta t}}[\langle c_{\mathrm{s}}^i \rangle^{\mathrm{s}}]^{\mathrm{gr}}$$
$$^{\mathbf{n}}[\langle c_{\mathrm{l}}^i \rangle^{\mathrm{l}}]^{\mathrm{gr}} = {}^{\mathbf{t+\delta t}}[\langle c_{\mathrm{l}}^i \rangle^{\mathrm{l}}]^{\mathrm{gr}}$$
$$^{\mathbf{n}}[g_{\mathrm{s}}]^{\mathrm{gr}} = {}^{\mathbf{t+\delta t}}[g_{\mathrm{s}}]^{\mathrm{gr}}$$
$$^{\mathbf{n}}[N]^{\mathrm{gr}} = {}^{\mathbf{t+\delta t}}[N]^{\mathrm{gr}}$$
$$^{\mathbf{n}}[N_{\mathrm{nuc}}]^{\mathrm{gr}} = {}^{\mathbf{t+\delta t}}[N_{\mathrm{nuc}}]^{\mathrm{gr}}$$
Compute phase diagram parameters

Update
$$t \leftarrow t + \delta t$$
$$^{\mathbf{t+\delta t}}[\langle c_{\mathrm{s}}^i \rangle^{\mathrm{s}}]^{\mathrm{gr}} = {}^{\mathbf{n+1}}[\langle c_{\mathrm{s}}^i \rangle^{\mathrm{s}}]^{\mathrm{gr}}$$
$$^{\mathbf{t+\delta t}}[\langle c_{\mathrm{l}}^i \rangle^{\mathrm{l}}]^{\mathrm{gr}} = {}^{\mathbf{n+1}}[\langle c_{\mathrm{l}}^i \rangle^{\mathrm{l}}]^{\mathrm{gr}}$$
$$^{\mathbf{t+\delta t}}[g_{\mathrm{s}}]^{\mathrm{gr}} = {}^{\mathbf{n+1}}[g_{\mathrm{s}}]^{\mathrm{gr}}$$
$$^{\mathbf{t+\delta t}}[N]^{\mathrm{gr}} = {}^{\mathbf{n+1}}[N]^{\mathrm{gr}}$$
$$^{\mathbf{t+\delta t}}[N_{nuc}]^{\mathrm{gr}} = {}^{\mathbf{n+1}}[N_{nuc}]^{\mathrm{gr}}$$
$$^{\mathbf{t+\delta t}}c_{\mathrm{l}}^{*i} = {}^{\mathbf{n+1}}c_{\mathrm{l}}^{*i}$$
$$^{\mathbf{t+\delta t}}\Gamma_{\mathrm{s}} = {}^{\mathbf{n+1}}\Gamma_{\mathrm{s}}$$

Compute morphological parameters
(Eqns. in section 2.6.2.2)
$$^{\mathbf{j}}c_{\mathrm{l}}^{*i} = {}^{\mathbf{n}}c_{\mathrm{l}}^{*i} \quad {}^{\mathbf{j}}\Gamma_{\mathrm{s}} = {}^{\mathbf{n}}\Gamma_{\mathrm{s}} \quad {}^{\mathbf{j}}T = {}^{\mathbf{t+\delta t}}T$$

Solve for $^{\mathbf{j+1}}\Gamma_{\mathrm{s}}$, $^{\mathbf{j+1}}c_{\mathrm{l}}^{*i}$ and $^{\mathbf{j+1}}T$
(Eqns. 3.31, 3.33, 3.34)

Convergence NO

Iteration **j**

YES

$$^{\mathbf{n+1}}\Gamma_{\mathrm{s}} = {}^{\mathbf{j+1}}\Gamma_{\mathrm{s}}$$
$$^{\mathbf{n+1}}c_{\mathrm{l}}^{*i} = {}^{\mathbf{j+1}}c_{\mathrm{l}}^{*i}$$
$$^{\mathbf{t+\delta t}}T = {}^{\mathbf{j+1}}T$$
Solve for $^{\mathbf{n+1}}[g_{\mathrm{s}}]^{\mathrm{gr}}$, $^{\mathbf{n+1}}[\langle c_l^i \rangle^{\mathrm{l}}]^{\mathrm{gr}}$,
$^{\mathbf{n+1}}[\langle c_s^i \rangle^{\mathrm{s}}]^{\mathrm{gr}}$, $^{\mathbf{n+1}}[N]^{\mathrm{gr}}$ and $^{\mathbf{n+1}}[N_{nuc}]^{\mathrm{gr}}$
(Eqns. 3.35, 3.36)

Iteration **n**

Convergence NO

YES

$$t + \delta t < t + \Delta t$$ YES

NO

Solution of the growth stage
$$^{\mathbf{v+1}}[\langle c_{\mathrm{s}}^i \rangle^{\mathrm{s}}]^{\mathrm{gr}} = {}^{\mathbf{n+1}}[\langle c_{\mathrm{s}}^i \rangle^{\mathrm{s}}]^{\mathrm{gr}}$$
$$^{\mathbf{v+1}}[\langle c_{\mathrm{l}}^i \rangle^{\mathrm{l}}]^{\mathrm{gr}} = {}^{\mathbf{n+1}}[\langle c_{\mathrm{l}}^i \rangle^{\mathrm{l}}]^{\mathrm{gr}}$$
$$^{\mathbf{v+1}}[g_{\mathrm{s}}]^{\mathrm{gr}} = {}^{\mathbf{n+1}}[g_{\mathrm{s}}]^{\mathrm{gr}}$$
$$^{\mathbf{v+1}}[N]^{\mathrm{gr}} = {}^{\mathbf{n+1}}[N]^{\mathrm{gr}}$$
$$^{\mathbf{v+1}}[N_{nuc}]^{\mathrm{gr}} = {}^{\mathbf{n+1}}[N_{nuc}]^{\mathrm{gr}}$$
$$^{\mathbf{v+1}}T = {}^{\mathbf{t+\delta t}}T$$

Figure 3.3 – Resolution algorithm for primary solidification in two phase globular model- Approach SOLID®

$$\implies \delta\langle h\rangle = \left(^{\mathbf{t+\delta t}}g_{\mathrm{s}}\right) {}^{\mathbf{t+\delta t}}\langle h_{\mathrm{s}}\rangle^{\mathrm{s}} + \left(^{\mathbf{t+\delta t}}g_{\mathrm{l}}\right) {}^{\mathbf{t+\delta t}}\langle h_{\mathrm{l}}\rangle^{\mathrm{l}} - \left(^{\mathbf{t}}g_{\mathrm{s}}\right) {}^{\mathbf{t}}\langle h_{\mathrm{s}}\rangle^{\mathrm{s}} - \left(^{\mathbf{t}}g_{\mathrm{l}}\right) {}^{\mathbf{t}}\langle h_{\mathrm{l}}\rangle^{\mathrm{l}}$$

$$\implies \delta\langle h\rangle = \left(^{\mathbf{t+\delta t}}g_{\mathrm{l}} - {}^{\mathbf{t}}g_{\mathrm{l}}\right)\left(^{\mathbf{t+\delta t}}\langle h_{\mathrm{l}}\rangle^{\mathrm{l}} - {}^{\mathbf{t+\delta t}}\langle h_{\mathrm{s}}\rangle^{\mathrm{s}}\right) + {}^{\mathbf{t}}g_{\mathrm{l}}\left(\delta\langle h_{\mathrm{l}}\rangle^{\mathrm{l}}\right) + {}^{\mathbf{t}}g_{\mathrm{s}}\left(\delta\langle h_{\mathrm{s}}\rangle^{\mathrm{s}}\right) \tag{3.28}$$

where

$$\delta\langle h_{\mathrm{l}}\rangle^{\mathrm{l}} = {}^{\mathbf{t+\delta t}}\langle h_{\mathrm{l}}\rangle^{\mathrm{l}} - {}^{\mathbf{t}}\langle h_{\mathrm{l}}\rangle^{\mathrm{l}}$$

$$\implies \delta\langle h_{\mathrm{l}}\rangle^{\mathrm{l}} = \left(\frac{\partial\langle h_{\mathrm{l}}\rangle^{\mathrm{l}}}{\partial T}\right)_{\langle c_{\mathrm{l}}^{i}\rangle^{\mathrm{l}}}\left(^{\mathbf{t+\delta t}}T - {}^{\mathbf{t}}T\right) + \sum_{i}\left(\frac{\partial\langle h_{\mathrm{l}}\rangle^{\mathrm{l}}}{\partial\langle c_{\mathrm{l}}^{i}\rangle^{\mathrm{l}}}\right)_{T}\left(^{\mathbf{t+\delta t}}\langle c_{\mathrm{l}}^{i}\rangle^{\mathrm{l}} - {}^{\mathbf{t}}\langle c_{\mathrm{l}}^{i}\rangle^{\mathrm{l}}\right) \tag{3.29}$$

$$\delta\langle h_{\mathrm{s}}\rangle^{\mathrm{l}} = {}^{\mathbf{t+\delta t}}\langle h_{\mathrm{s}}\rangle^{\mathrm{l}} - {}^{\mathbf{t}}\langle h_{\mathrm{s}}\rangle^{\mathrm{l}}$$

$$\implies \delta\langle h_{\mathrm{s}}\rangle^{\mathrm{s}} = \left(\frac{\partial\langle h_{\mathrm{s}}\rangle^{\mathrm{s}}}{\partial T}\right)_{\langle c_{\mathrm{s}}^{i}\rangle^{\mathrm{s}}}\left(^{\mathbf{t+\delta t}}T - {}^{\mathbf{t}}T\right) + \sum_{i}\left(\frac{\partial\langle h_{\mathrm{s}}\rangle^{\mathrm{s}}}{\partial\langle c_{\mathrm{s}}^{i}\rangle^{\mathrm{s}}}\right)_{T}\left(^{\mathbf{t+\delta t}}\langle c_{\mathrm{s}}^{i}\rangle^{\mathrm{s}} - {}^{\mathbf{t}}\langle c_{\mathrm{s}}^{i}\rangle^{\mathrm{s}}\right) \tag{3.30}$$

Thus, the final enthalpy balance equation in the discretized form is given by:

$$\delta\langle h\rangle = A + B + C \tag{3.31}$$

$$A = \delta g_{\mathrm{l}}\left(^{\mathbf{t+\delta t}}\langle h_{\mathrm{l}}\rangle^{\mathrm{l}} - {}^{\mathbf{t+\delta t}}\langle h_{\mathrm{s}}\rangle^{\mathrm{s}}\right)$$

$$B = \sum_{i}\left[{}^{\mathbf{t}}g_{\mathrm{s}}\left(\frac{\partial\langle h_{\mathrm{s}}\rangle^{\mathrm{s}}}{\partial\langle c_{\mathrm{s}}^{i}\rangle^{\mathrm{s}}}\right)_{T}\left(^{\mathbf{t+\delta t}}\langle c_{\mathrm{s}}^{i}\rangle^{\mathrm{s}} - {}^{\mathbf{t}}\langle c_{\mathrm{s}}^{i}\rangle^{\mathrm{s}}\right) + \left(1 - {}^{\mathbf{t}}g_{\mathrm{s}}\right)\left(\frac{\partial\langle h_{\mathrm{l}}\rangle^{\mathrm{l}}}{\partial\langle c_{\mathrm{l}}^{i}\rangle^{\mathrm{l}}}\right)_{T}\left(^{\mathbf{t+\delta t}}\langle c_{\mathrm{l}}^{i}\rangle^{\mathrm{l}} - {}^{\mathbf{t}}\langle c_{\mathrm{l}}^{i}\rangle^{\mathrm{l}}\right)\right]$$

$$C = \left(^{\mathbf{t+\delta t}}T - {}^{\mathbf{t}}T\right)\left[\left(1 - {}^{\mathbf{t}}g_{\mathrm{s}}\right)\left(\frac{\partial\langle h_{\mathrm{l}}\rangle^{\mathrm{l}}}{\partial T}\right)_{\langle c_{\mathrm{l}}^{i}\rangle^{\mathrm{l}}} + {}^{\mathbf{t}}g_{\mathrm{s}}\left(\frac{\partial\langle h_{\mathrm{s}}\rangle^{\mathrm{s}}}{\partial T}\right)_{\langle c_{\mathrm{s}}^{i}\rangle^{\mathrm{s}}}\right]$$

where δg_{l} is the change in liquid phase fraction due to transport, nucleation and grain growth during each micro times step and is given by

$$\delta g_{\mathrm{l}} = \delta g_{\mathrm{l}}^{\mathrm{tr}} + \delta g_{\mathrm{l}}^{\mathrm{nuc}} + \delta g_{\mathrm{l}}^{\mathrm{gr}}$$

$$\implies \delta g_{\mathrm{l}} = -\left(\delta g_{\mathrm{s}}^{\mathrm{tr}} + \delta g_{\mathrm{s}}^{\mathrm{nuc}} + \delta g_{\mathrm{s}}^{\mathrm{gr}}\right)$$

$$\implies \delta g_{\mathrm{l}} = -\left(\frac{^{\mathbf{v+1}}g_{\mathrm{s}}^{\mathrm{tr}} - {}^{\mathbf{t}}g_{\mathrm{s}}^{\mathrm{tr}}}{n_{\mathrm{mic}}} + \frac{\frac{^{\mathbf{t+\Delta t}}\Theta_{s}}{\rho}}{n_{\mathrm{mic}}} + \frac{^{\mathbf{t+\delta t}}\Gamma_{\mathrm{s/l}}\delta t}{\rho}\right) \tag{3.32}$$

The other equations are discretized as follows:

$$^{t+\delta t}c_1^{*i}\left(k_p^i - 1\right)\frac{^{t+\delta t}\Gamma_{s/l}}{\rho} + {}^{t+\delta t}c_1^{*i}\left(\frac{S_v^s D_1^i}{\delta_1^i} + k_p^i\frac{S_v D_s^i}{\delta_s^i}\right) = {}^{t+\delta t}\langle c_1^i\rangle^l\frac{S_v^s D_1^i}{\delta_1^i} + {}^{t+\delta t}\langle c_s^i\rangle^s\frac{S_v^s D_s^i}{\delta_s^i} \quad (3.33)$$

$$^{t+\delta t}T - {}^tT = \sum_i m_l^i\left({}^{t+\delta t}c_1^{*i} - {}^tc_1^{*i}\right) \quad (3.34)$$

$$\frac{\left({}^{t+\delta t}g_s\,{}^{t+\delta t}\langle c_s^i\rangle^s\right) - \left({}^tg_s\,{}^t\langle c_s^i\rangle^s\right)}{\delta t} = \frac{^{t+\delta t}\Gamma_{s/l}k_p^i\,{}^{t+\delta t}c_1^{*i}}{\rho} + \frac{S_v^s D_s^i}{\delta_s^i}\left(k_p^i\,{}^{t+\delta t}c_1^{*i} - {}^{t+\delta t}\langle c_s^i\rangle^s\right) \quad (3.35)$$

$$\frac{\left({}^{t+\delta t}g_l\,{}^{t+\delta t}\langle c_1^i\rangle^l\right) - \left({}^tg_l\,{}^t\langle c_1^i\rangle^l\right)}{\delta t} = -\frac{^{t+\delta t}\Gamma_{s/l}\,{}^{t+\delta t}c_1^{*i}}{\rho} + \frac{S_v^s D_1^i}{\delta_1^i}\left({}^{t+\delta t}c_1^{*i} - {}^{t+\delta t}\langle c_1^i\rangle^l\right) \quad (3.36)$$

3.4.3   Solution scheme for primary solidification

The resolution algorithm schematized in Fig. 3.3 is described in this section. The focus of this section pertains to primary solidification (the red box in the Fig. 3.3). Hence, the indexes 'tr', 'nuc' and 'gr' are avoided for the sake of clarity. Eqns. 3.31, 3.33, 3.34, 3.35 and 3.36 are solved to obtain the parameters $^{t+\delta t}c_1^{*i}$, $^{t+\delta t}\Gamma_{s/l}$, $^{t+\delta t}T$, $^{t+\delta t}\langle c_1^i\rangle^l$ and $^{t+\delta t}\langle c_s^i\rangle^s$. There are various approaches to solve these implicit equations. We employ an iterative scheme which is as follows:

Table 3.2 – Function calls for various CALPHAD functions

CALPHAD variables	Function call
k_p^i, m_l^i	Beginning of micro time-step
$\langle h_l\rangle^l, \langle h_s\rangle^s, \left(\frac{\partial\langle h_l\rangle^l}{\partial T}\right)_{\langle c_1^i\rangle^l}, \left(\frac{\partial\langle h_s\rangle^s}{\partial T}\right)_{\langle c_s^i\rangle^s}, \left(\frac{\partial\langle h_l\rangle^l}{\partial\langle c_1^i\rangle^l}\right)_T, \left(\frac{\partial\langle h_s\rangle^s}{\partial\langle c_s^i\rangle^s}\right)_T$	Beginning of first micro step only

- **Initialization:** The values of the growth stage variables are updated with the values of the nucleation stage. The phase diagram parameters are also computed corresponding to these values. Here we distinguish the phase diagram variables into two sets as shown in Table 3.2. The first set of parameters are computed corresponding to the interfacial liquid composition while the second set of parameters are computed corresponding to the average composition of the phase and temperature. This has been done with the aim to avoid unrealistically large computation times. This approach might introduce very small errors at the expense of reducing the computation cost.

- **Computation of morphological parameters:** The grain radius, the interfacial area density and the diffusion length are computed from the various co-relations mentioned in section 2.6.2.2

- **Iteration:** We have two iteration loops as shown in Fig. 3.3. The inner iteration loop corresponds to variable 'j' and the outer iteration loop corresponds to variable 'n'.

   - **Inner iteration loop (j):** The inner iteration loop is used to solve the Eqns. 3.37, 3.38 and 3.39. Values corresponding to parameters with index 'j+1' at time $t + \delta t$ are obtained.

$$\delta\langle h\rangle = A + B + C \quad (3.37)$$

$$A = -\left(\frac{^{\mathbf{v+1}}g_{\mathrm{s}}^{\mathrm{tr}} - {}^{\mathbf{t}}g_{\mathrm{s}}^{\mathrm{tr}}}{n_{\mathrm{mic}}} + \frac{^{\mathbf{t+\Delta t}}\Theta_s}{\rho} + \frac{^{\mathbf{j+1}}\Gamma_{\mathrm{s/l}}\delta t}{\rho}\right)\left({}^{\mathbf{j}}\langle h_{\mathrm{l}}\rangle^{\mathrm{l}} - {}^{\mathbf{j}}\langle h_{\mathrm{s}}\rangle^{\mathrm{s}}\right)$$

$$B = \sum_i \left[{}^{\mathbf{t}}g_{\mathrm{s}}\left(\frac{\partial\langle h_{\mathrm{s}}\rangle^{\mathrm{s}}}{\partial\langle c_{\mathrm{s}}^i\rangle^{\mathrm{s}}}\right)_T \left({}^{\mathbf{n}}\langle c_{\mathrm{s}}^i\rangle^{\mathrm{s}} - {}^{\mathbf{t}}\langle c_{\mathrm{s}}^i\rangle^{\mathrm{s}}\right) + \left(1 - {}^{\mathbf{t}}g_{\mathrm{s}}\right)\left(\frac{\partial\langle h_{\mathrm{l}}\rangle^{\mathrm{l}}}{\partial\langle c_{\mathrm{l}}^i\rangle^{\mathrm{l}}}\right)_T \left({}^{\mathbf{n}}\langle c_{\mathrm{l}}^i\rangle^{\mathrm{l}} - {}^{\mathbf{t}}\langle c_{\mathrm{l}}^i\rangle^{\mathrm{l}}\right) \right]$$

$$C = \left({}^{\mathbf{j+1}}T - {}^{\mathbf{t}}T\right)\left[\left(1 - {}^{\mathbf{t}}g_{\mathrm{s}}\right)\left(\frac{\partial\langle h_{\mathrm{l}}\rangle^{\mathrm{l}}}{\partial T}\right)_{\langle c_{\mathrm{l}}^i\rangle^{\mathrm{l}}} + {}^{\mathbf{t}}g_{\mathrm{s}}\left(\frac{\partial\langle h_{\mathrm{s}}\rangle^{\mathrm{s}}}{\partial T}\right)_{\langle c_{\mathrm{s}}^i\rangle^{\mathrm{s}}} \right]$$

$${}^{\mathbf{j}}c_{\mathrm{l}}^{*i}\left(k_p^i - 1\right)\frac{^{\mathbf{j+1}}\Gamma_{\mathrm{s/l}}}{\rho} + {}^{\mathbf{j+1}}c_{\mathrm{l}}^{*i}\left(\frac{S_v^{\mathrm{s}}D_{\mathrm{l}}^i}{\delta_{\mathrm{l}}^i} + k_p^i\frac{S_v D_{\mathrm{s}}^i}{\delta_{\mathrm{s}}^i}\right) = {}^{\mathbf{n}}\langle c_{\mathrm{l}}^i\rangle^{\mathrm{l}}\frac{S_v^{\mathrm{s}}D_{\mathrm{l}}^i}{\delta_{\mathrm{l}}^i} + {}^{\mathbf{n}}\langle c_{\mathrm{s}}^i\rangle^{\mathrm{s}}\frac{S_v^{\mathrm{s}}D_{\mathrm{s}}^i}{\delta_{\mathrm{s}}^i}$$

$$(3.38)$$

$$^{\mathbf{j+1}}T - {}^{\mathbf{t}}T = \sum_i m_l^i({}^{\mathbf{j+1}}c_{\mathrm{l}}^{*i} - {}^{\mathbf{t}}c_{\mathrm{l}}^{*i}) \tag{3.39}$$

Eqn. 3.38 is non-linear as the left most term is the product of the unknowns $^{\mathbf{t+\delta t}}\Gamma_{\mathrm{s/l}}$ and $^{\mathbf{t+\delta t}}c_{\mathrm{l}}^{*i}$ which makes the equation non-linear. The non-linear equation is linearized by using the value of c_{l}^{*i} at the previous iteration 'j'. These three equations in essence are similar to the eqns. used in SOLD® except for the fact that variable thermodynamic parameters are now introduced into the model. However, a key difference lies in Eqn. 3.39. Eqn. 3.39 links the interfacial concentration at time t and $t+\delta t$ unlike in SOLID® where the temperature $^{\mathbf{t+\delta t}}T$ is linked directly to the interfacial concentration $^{\mathbf{t+\delta t}}c_{\mathrm{l}}^{*i}$ and there is not requirement for $^{\mathbf{t}}c_{\mathrm{l}}^{*i}$. The requirement for $^{\mathbf{t}}c_{\mathrm{l}}^{*i}$ poses a problem.

During primary solidification, the volume element at time t could exist in two states :

- Fully liquid
- Primary solidification

The interfacial composition is available when the volume element is at time t. However, no such information is available for a fully liquid state at temperature $^{\mathbf{t}}T$ at time t. For a binary alloy, there exists a direct correlation between the temperature and the interfacial concentration, whereas for a multi-component alloy, there is no unique solution. Fig. 3.4 shows the isothermal lines on the liquidus surface for primary solidification of the ferrite phase (δ) in an Fe-C-Cr alloy obtained using Thermo-Calc® (TCFE9 database). For a ternary alloy, all the points on a line correspond to the same temperature. Thus, a special treatment is required for the first micro time-step.
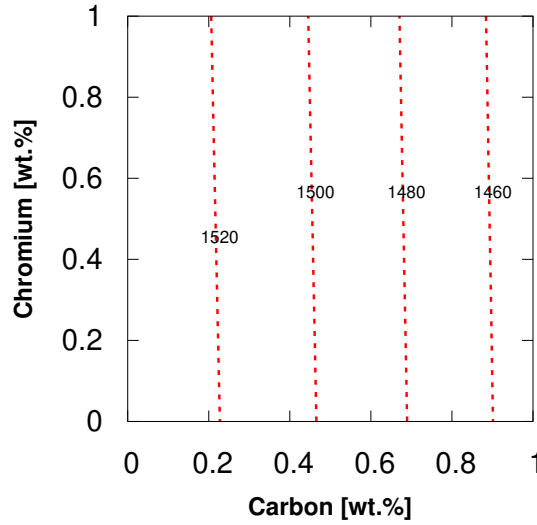
Figure 3.4 – Isothermal contours of the liquidus surface for primary solidification of δ ferrite for Fe-C-Cr alloy

Eqn. 3.39 imposes two prerequisites on the combination of temperature (^{t}T) and interfacial composition $^{t}c_{l}^{*i}$. First, they should lie on the liquidus surface. Second, the interfacial compositions $^{t}c_{l}^{*i}$ and $^{t+\delta t}c_{l}^{*i}$ are close such that the liquidus slope obtained using $^{t}c_{l}^{*i}$ does not introduce significant error. Thus, for the first micro time-step, Eqn. 3.39 is modified to

$$\implies {}^{j+1}T - T^{*}\left({}^{v+1}[\langle c_{l}^{i}\rangle^{l}]^{tr}\right) = \sum_{i} m_{l}^{i}({}^{j+1}c_{l}^{*i} - {}^{v+1}[\langle c_{l}^{i}\rangle^{l}]^{tr}) \tag{3.40}$$

where T^{*} is the liquidus temperature for the average liquid composition after the transport stage $\left({}^{v+1}[\langle c_{l}^{i}\rangle^{l}]^{tr}\right)$. The liquidus slope is calculated accordingly. This approximation could introduce error if the liquid at time t is highly undercooled. The magnitude of this error depends on the variation of liquidus slope as a function of composition. However, in the current work, this effect has not been further explored. The convergence criteria for Γ_{s}, c_{l}^{*i} are as follows:

$$\left|\frac{{}^{j+1}\Gamma_{s} - {}^{j}\Gamma_{s}}{{}^{j+1}\Gamma_{s}}\right| < 10^{-9}$$

$$\left|\frac{{}^{j+1}c_{l}^{*i} - {}^{j}c_{l}^{*i}}{{}^{j+1}c_{l}^{*i}}\right| < 10^{-9}$$

OR

$$\mathbf{j + 1} >= \mathbf{j_{max}}$$

– **Outer iteration loop (n):** Once the converged values of Γ_{s}, c_{l}^{*i} and T are obtained (further referred to as $^{n+1}c_{l}^{*i}$, $^{n+1}\Gamma_{s/l}$, ^{n+1}T), g_{s}, $\langle c_{l}^{i}\rangle^{l}$ and $\langle c_{s}^{i}\rangle^{s}$ are solved for, corresponding to parameters with index 'n+1' at time $t + \delta t$.

$$^{n+1}g_{s} = {}^{t}g_{s} + \frac{^{n+1}\Gamma_{s/l}}{\rho}\delta t \tag{3.41}$$

$$\frac{\left(^{\mathbf{n+1}}g_{\mathrm{s}}\,^{\mathbf{n+1}}\langle c_{\mathrm{s}}^{i}\rangle^{\mathrm{s}}\right) - \left(^{\mathbf{t}}g_{\mathrm{s}}\,^{\mathbf{t}}\langle c_{\mathrm{s}}^{i}\rangle^{\mathrm{s}}\right)}{\delta t} = \frac{^{\mathbf{n+1}}\Gamma_{\mathrm{s/l}}k_{p}^{i\,\mathbf{n+1}}c_{1}^{*i}}{\rho} + \frac{S_{v}^{\mathrm{s}}D_{\mathrm{s}}^{i}}{\delta_{\mathrm{s}}^{i}}\left(k_{p}^{i\,\mathbf{n+1}}c_{1}^{*i} - {}^{\mathbf{n}}\langle c_{\mathrm{s}}^{i}\rangle^{\mathrm{s}}\right)$$

(3.42)

$$\frac{\left(^{\mathbf{n+1}}g_{\mathrm{l}}\,^{\mathbf{n+1}}\langle c_{1}^{i}\rangle^{\mathrm{l}}\right) - \left(^{\mathbf{t}}g_{\mathrm{l}}\,^{\mathbf{t}}\langle c_{1}^{i}\rangle^{\mathrm{l}}\right)}{\delta t} = -\frac{^{\mathbf{n+1}}\Gamma_{\mathrm{s/l}}\,^{\mathbf{n+1}}c_{1}^{*i}}{\rho} + \frac{S_{v}^{\mathrm{s}}D_{\mathrm{l}}^{i}}{\delta_{\mathrm{l}}^{i}}\left(^{\mathbf{n+1}}c_{1}^{*i} - {}^{\mathbf{n}}\langle c_{1}^{i}\rangle^{\mathrm{l}}\right)$$

(3.43)

The convergence criteria for $\langle c_{\mathrm{s}}\rangle^{\mathrm{s}}$, $\langle c_{1}\rangle^{\mathrm{l}}$ are as follows:

$$\left|\frac{^{\mathbf{n+1}}[\langle c_{\mathrm{s}}\rangle^{\mathrm{s}}] - {}^{\mathbf{n}}[\langle c_{\mathrm{s}}\rangle^{\mathrm{s}}]}{^{\mathbf{n+1}}[\langle c_{\mathrm{s}}\rangle^{\mathrm{s}}]}\right| < 10^{-6}$$

$$\left|\frac{^{\mathbf{n+1}}[\langle c_{1}\rangle^{\mathrm{l}}] - {}^{\mathbf{n}}[\langle c_{1}\rangle^{\mathrm{l}}]}{^{\mathbf{n+1}}[\langle c_{1}\rangle^{\mathrm{l}}]}\right| < 10^{-6}$$

OR

$$\mathbf{n+1} >= n_{max}$$

3.4.3.1   Modifications to the dendrite tip growth model

The microscopic growth model described above is applicable for the two phase globular as well as the three phase dendritic model. However, the model describing the kinetics of the dendrite tip growth needs to be modified. The dendrite tip growth model as discussed in the previous chapter links the total undercooling (ΔT) to the thermal undercooling (ΔT_t) and the solutal undercooling (ΔT_c) (curvature undercooling is neglected). The total undercooling is given by

$$\Delta T = T^{\infty} - T(\langle c_{1}^{i}\rangle^{\mathrm{e}})$$

(3.44)

where T^{∞} is the far field temperature and $T(\langle c_{1}^{i}\rangle^{\mathrm{e}})$ is the liquidus temperature for the far-field liquid with composition $\langle c_{1}^{i}\rangle^{\mathrm{e}}$ and is obtained using CALPHAD data. By assuming a linearized phase diagram, the solutal undercooling ΔT_c is computed by linking the liquidus slope to the composition difference between the tip and the far field and is given by

$$\Delta T_c = -\sum_{i} m_{1}^{i}\langle c_{1}^{i}\rangle^{\mathrm{e}}\left[1 - \frac{1}{1 - \left(1 - k_{p}^{i}\right)\Omega_{c}^{i}}\right]$$

(3.45)

where the liquidus slope, m_{1}^{i}, and the partition coefficient, k_{p}^{i}, are computed for the far-field composition $\langle c_{1}^{i}\rangle^{\mathrm{e}}$. Thus, for the Eqns. 3.44 and 3.45 to be consistent, we need to calculate an artificial pure metal temperature T_{f}' such that

$$T_{f}' = T(\langle c_{1}^{i}\rangle^{\mathrm{e}}) - \sum_{i} m_{1}^{i}\langle c_{1}^{i}\rangle^{\mathrm{e}}$$

(3.46)

This approach to account for variable phase diagram parameters can be termed as a 'crude' approach. The development of the dendrite tip growth kinetics model coupled with thermodynamic equilibrium calculation

is a work in progress in CEMEF, Sophia Antipolis, France. This development is based on the theory provided by Hunzinker [138]. Implementation of the proposed approach forms a part of the future scope of the work.

3.4.3.2 Approach µSOLID

During the course of the present work, a new resolution algorithm was proposed and tested. In the 'Approach SOLID®', the contribution of the transport and nucleation stage was used as the initial conditions for the growth model. In the new approach, further referred to as 'Approach µSOLID®', the contribution of the transport and nucleation stage was not used as the initial condition for the growth model. The contribution of the transport stage is divided over the 'n' micro time-steps and is added at each micro time-step. The nucleation stage occurs in conjunction with the growth model and uses micro time-steps. Fig. 3.5 shows a schematic representation of the two resolution algorithms.

Approach SOLID®

Transport
+
Nucleation

Variation over each micro time-step

$$\delta \langle h \rangle = \frac{\Delta h}{n_{\mathrm{mic}}}$$
$$\delta g_{\mathrm{s}} = \frac{\Delta g_{\mathrm{s}}^{\mathrm{tr}} + \Delta g_{\mathrm{s}}^{\mathrm{nuc}}}{n_{\mathrm{mic}}} + \delta g_{\mathrm{s}}^{\mathrm{gr}}$$
$$\delta \langle c_{\mathrm{l}}^{i} \rangle^{\mathrm{l}} = \delta \langle c_{\mathrm{l}}^{i} \rangle^{\mathrm{l,gr}}$$
$$\delta \langle c_{\mathrm{s}}^{i} \rangle^{\mathrm{s}} = \delta \langle c_{\mathrm{s}}^{i} \rangle^{\mathrm{s,gr}}$$

N (constant) or 0 (if remelting)

(a)

Approach µSOLID®

Transport

Variation over each micro time-step

$$\delta \langle h \rangle = \frac{\Delta h}{n_{\mathrm{mic}}}$$
$$\delta g_{\mathrm{s}} = \frac{\Delta g_{\mathrm{s}}^{\mathrm{tr}}}{n_{\mathrm{mic}}} + \delta g_{\mathrm{s}}^{\mathrm{nuc}} + \delta g_{\mathrm{s}}^{\mathrm{gr}}$$
$$\delta \langle c_{\mathrm{l}}^{i} \rangle^{\mathrm{l}} = \frac{\Delta \langle c_{\mathrm{l}}^{i} \rangle^{\mathrm{l,tr}}}{n_{\mathrm{mic}}} + \delta \langle c_{\mathrm{l}}^{i} \rangle^{\mathrm{l,nuc}} + \delta \langle c_{\mathrm{l}}^{i} \rangle^{\mathrm{l,gr}}$$
$$\delta \langle c_{\mathrm{s}}^{i} \rangle^{\mathrm{s}} = \frac{\Delta \langle c_{\mathrm{s}}^{i} \rangle^{\mathrm{s,tr}}}{n_{\mathrm{mic}}} + \delta \langle c_{\mathrm{s}}^{i} \rangle^{\mathrm{s,nuc}} + \delta \langle c_{\mathrm{s}}^{i} \rangle^{\mathrm{s,gr}}$$
$$\delta N = \frac{\Delta N^{\mathrm{tr}}}{n_{\mathrm{mic}}} + \delta N^{\mathrm{nuc}} + \delta N^{\mathrm{gr}}$$

(b)
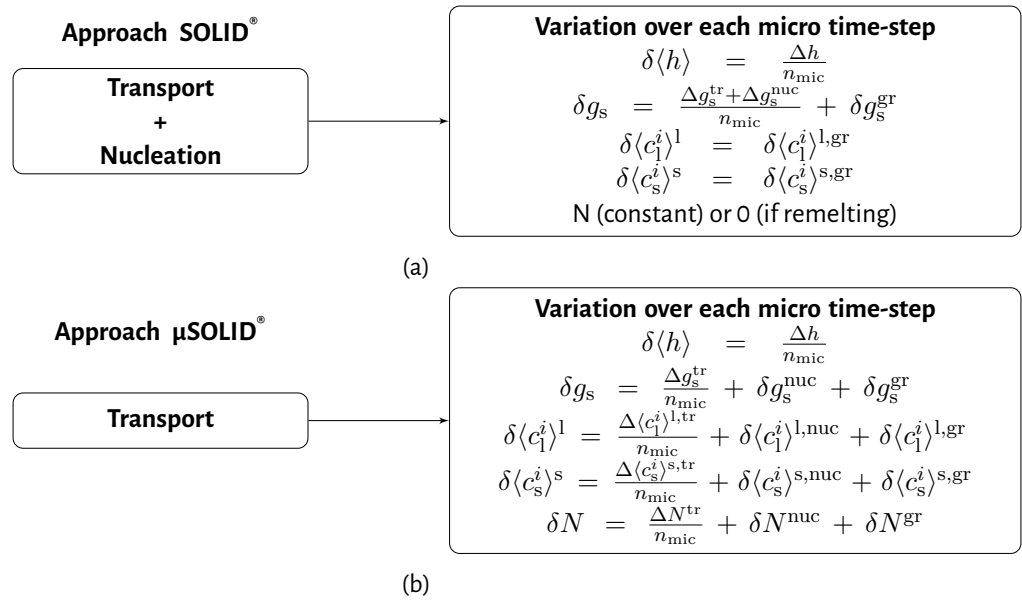
Figure 3.5 – Schematic representation of the resolution algorithm a) Approach SOLID® b) Approach µSOLID®

The enthalpy balance equation remains the same except that δg_{l} is given by

$$\delta g_{\mathrm{l}} = -\left(\frac{^{\mathbf{v+1}} g_{\mathrm{s}}^{\mathrm{tr}} - {}^{\mathbf{t}} g_{\mathrm{s}}^{\mathrm{tr}}}{n} + \frac{^{\mathbf{t+\Delta t}} \Theta_{s}}{\rho} + \frac{^{\mathbf{t+\delta t}} \Gamma_{\mathrm{s/l}} \delta t}{\rho} \right) \tag{3.47}$$

such that the nucleation stage contribution is not divided by n micro time-steps. While nucleation is assumed to be an instantaneous phenomena, its effect on the enthalpy balance is divided over the micro time-steps. This effectively corresponds to nucleating $\frac{\Theta_{s}/\rho}{n}$ solid mass continuously over the n micro time-steps for the same grain density N_{g}. This modification does not have a significant impact on the result of the growth model, only the growth kinetics is modified slightly.

'Approach µSOLID' is computationally more expensive as compared to 'Approach SOLID'. This is due to the fact that after each micro time-step, (assuming no nucleation occurs) addition of the contribution of the transport stage results in the solid-liquid interface being out of equilibrium. Whereas in 'Approach SOLID', it is only the first iteration in which the solid-liquid interface is out of equilibrium. Thus, while 'Approach SOLID' might require more iterations to converge for the first micro time-step, it requires less iterations for the subsequent

micro time-steps. Further work needs to be done to understand the implications of the two schemes on the final results and is a work in progress. In the present work, we mostly focus on 'Approach SOLID' while also presenting the results of 'Approach μSOLID' on a validation case. This approach is also being extended to the Columnar to Equiaxed Transition (CET) model.

3.4.4   Modification to microscopic growth model for CET (columnar to equiaxed transition)

As mentioned in the previous chapter, the implementation of the CET model has been presented in Leriche [123]. To account for the variable phase diagram parameters, it is only the microscopic growth model that is modified while the columnar front tracking algorithm is unmodified. The basis of the microscopic growth model for CET is on similar lines as the model for equiaxed grains. However, due to presence of six phases (3 phases for the columnar and 3 phases for the equiaxed region), there are more equations which correspond to:

 – Separate interfacial solute balance for the columnar and equiaxed region

 – Separate enthalpy balance for the columnar and equiaxed region

 – Separate interfacial equilibrium relationship for the columnar and equiaxed region

 – Total enthalpy balance

To maintain the flow of the chapter, the model is presented in Appendix A.

3.4.5   Solidification dynamics

$t+\delta t$ \\ t	L	L+S	QE	S
L	1	2	3	4
L+S	5	6	7	8
QE	~~9~~	~~10~~	11	12
S	~~13~~	~~14~~	~~15~~	16

Table 3.3 – Transformation dynamics of the volume element

A solidifying control volume element can encounter various phase transformation dynamics. At the beginning of the time step (t), the control volume element can be in one of the possible four states: fully liquid (L) (state=1), mushy with the presence of primary phase (L+S) (state=2), quasi-eutectic (QE) (state=3) and fully solid (S) (state=4). Quasi-eutectic solidification corresponds to the state of the system towards the end of solidification. No solute partitioning occurs during this quasi-eutectic solidification. This is a special treatment to model the end of solidification. The solidification path is cut off at a predefined temperature T_{sol0}, after which the rest of the solidification proceeds at constant temperature T_{sol0} until the fully solid (S) (state=4) is
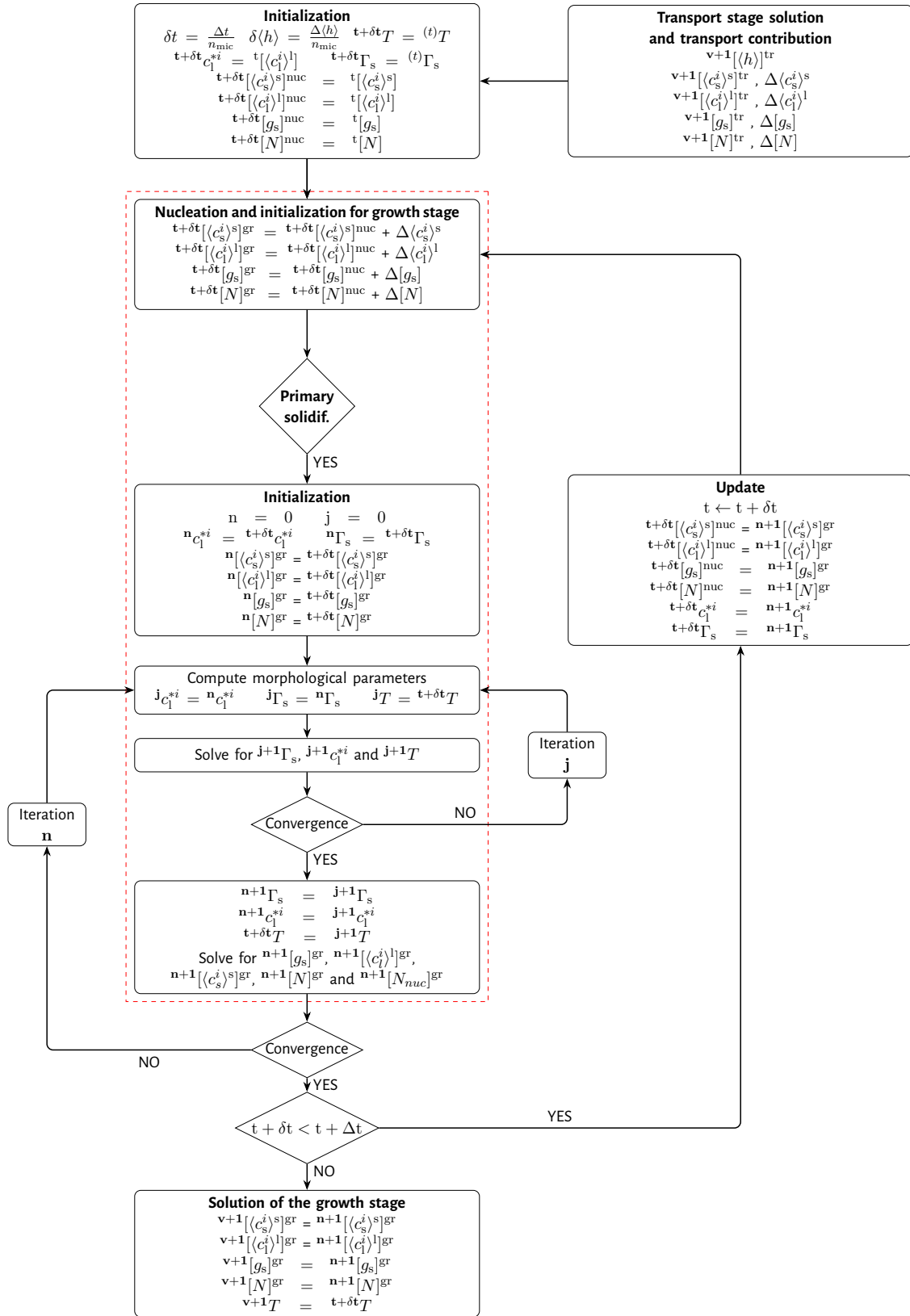
Figure 3.6 – Resolution algorithm for primary solidification - Approach μSOLID®
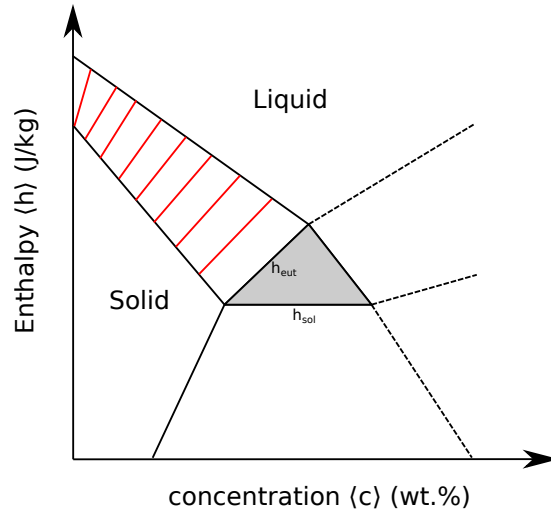
Figure 3.7 – Enthalpy-concentration phase diagram for a binary alloy

reached. For a binary system which has a constant T_{eut}, T_{sol0} ie equal to T_{eut}. However, for multicomponent systems, T_{eut} is not constant. Hence, T_{sol0} for such cases are obtained through regression correlations found in literature. At time $(t+\delta t)$, the control volume element can be in one of the above-mentioned four states. Thus, there are 16 possible cases which are shown in table 3.3. Transitions highlighted in red are not accounted for in the current algorithm. These transitions correspond to remelting during quasi-eutectic solidification and after complete solidification. We assume that these transitions are unlikely to be encountered

Modeling these possible cases requires determination of the system state at time t. The system states are determined by employing conditions imposed on the liquid phase fraction in conjunction with an average enthalpy based criteria. Fig. 3.7 shows the enthalpy-concentration diagram in the primary solidification domain for a binary alloy. The red lines highlight the isotherms in the (L+S) domain. The gray area corresponds to the isothermal domain at temperature T_{sol0}. h_{sol} and h_{eut} are calculated using the following formulation:

$$h_{\mathrm{sol}} = h_{\mathrm{sol}}(T_{\mathrm{sol0}}, \langle c \rangle) \tag{3.48}$$

$$h_{\mathrm{eut}} = g_{\mathrm{s}} h_{\mathrm{sol}}(T_{\mathrm{sol0}}, \langle c_{\mathrm{s}} \rangle^{\mathrm{s}}) + g_{\mathrm{l}} h_{\mathrm{liq}}(T_{\mathrm{sol0}}, \langle c_{\mathrm{l}} \rangle^{\mathrm{l}}) \tag{3.49}$$

where h_{sol} and h_{liq} are obtained from Thermo-Calc®. The conditions for determining the system states are shown in Fig. 3.8. Presence of solid grains is used to distinguish the pure liquid domain from a domain which undergoes primary or quasi-eutectic solidification.

3.5   CALPHAD method

For most multicomponent alloys, phase diagrams are not available and the usual approach is to deduce the partition coefficients and liquidus slopes for each solute from information on the binary alloys. This approach leaves out the various interactions between different alloying elements. CALPHAD (CALculation of PHAse Diagrams) is a robust approach through which we are able to get multicomponent data which allows for the various interactions between the alloying elements. The strength of the CALPHAD method is that data for binary systems can be used to derive ternary system data which can be further used to build up databases for
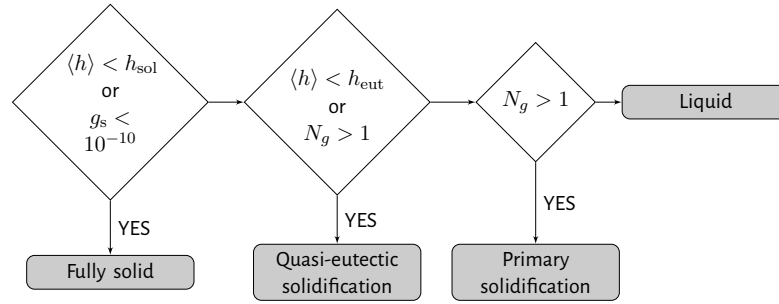
Figure 3.8 – Algorithm for determination of the solidification state

multi-component systems. This approach limits the experiments to be carried out on a multicomponent alloy. Calculating the phase diagram requires the computation of minima of a thermodynamic potential. The potential used in CALPHAD is the Gibbs free energy (G). Thermodynamic databases give a parametric description of the Gibbs free energy for all phases of the considered alloy system as a function of temperature, composition and pressure. The parametric description depends on the Gibbs free energy model that accounts for crystal structures of the individual phases. The phases concerned during solidification are considered to be substitutional solution phases. For a substitutional solution phase, the total Gibbs energy G^ϕ of a phase is

$$G^\phi = {}^{\mathrm{ref}}G^\phi + {}^{\mathrm{ideal}}G^\phi + {}^{\mathrm{ex}}G^\phi + {}^{\mathrm{mag}}G^\phi \tag{3.50}$$

where ${}^{\mathrm{ref}}G^\phi$, ${}^{\mathrm{ideal}}G^\phi$, ${}^{\mathrm{ex}}G^\phi$ and ${}^{\mathrm{mag}}G^\phi$ represent the reference, ideal mixing, excess and the magnetic contribution. The reference term corresponds to a simple arithmetic mixture of the Gibbs energy of the constituent components

$$
{}^{\mathrm{ref}}G^\phi = \sum_{i=1}^{n} x_i G_i^o(T) \tag{3.51}
$$

where the temperature dependence of $G_i^o(T)$ is formulated as a power series of T

$$
G_i^o(T) = a + bT^{-1} + cT\ln(T) + \sum_i d_i T^i \tag{3.52}
$$

The ideal mixing term corresponds to the entropy of mixing for an ideal solution

$$
{}^{\mathrm{ideal}}G^\phi = RT \sum_{i=1}^{n} x_i \ln(x_i) \tag{3.53}
$$

and the excess term corresponds to deviation from ideal mixing. This is due to various interactions between the constituent components. The excess term is represented as (for a binary alloy)

$$
{}^{\mathrm{ex}}G^\phi = \sum_{i=1}^{n-1} \sum_{j=i+1}^{n} x_i^\phi x_j^\phi L_{ij}^\phi \tag{3.54}
$$

where L^ϕ is the interaction parameter. Higher the number of constituent components, higher the number of terms in the excess contribution. The magnetic contribution is described by

$$
{}^{\mathrm{mag}}G^\phi = RT\ln\left(\beta^\phi + 1\right) \cdot f(\tau) \tag{3.55}
$$

where β^ϕ is a composition dependent parameter related to the magnetic entropy. Using this formulation of the total Gibbs energy, various thermodynamic functions can be obtained. Some of the thermodynamic functions of interest are enthalpy (h) and specific heat capacity (C_p) of a phase, which are given by:

$$h(T) = G(T) - T \left(\frac{\partial G(T)}{\partial T} \right)_P \tag{3.56}$$

$$h(T) = -T \left(\frac{\partial^2 G(T)}{\partial T^2} \right)_P \tag{3.57}$$

3.6   Coupling microsegregation model with CALPHAD data

In ternary and higher order systems, the phase diagram parameters are highly dependent on the temperature, composition and the solid phase. This has resulted in coupling the microsegregation models with CALPHAD tools. Yan *et al.* [139] highlighted the importance of reliable phase diagram data in validating the microsegregation model for Al - 4.5 wt.% Cu system. They concluded that an uncertainty of 0.15% makes an appreciable difference in the microsegregation calculated by the model. They obtained the partition coefficients for the system via the TQ-Interface® which is provided by Thermo-Calc®. Similar coupling with PANDAT® software was tested on Al-Cu-Mg-Si quaternary alloy by Yan *et al.* [140]. Such multicomponent solidification simulation with "real" phase diagram data is of great industrial interest. However, the complexity of performing such simulations stems from the demand to have easy and quick access to the phase diagram information. Jacot and Rappaz [141] have highlighted the two approaches used to access thermodynamic data through CALPHAD software:

- **Direct coupling:** Various softwares provide an interface through which thermodynamic data can be imported into the solidification framework. Thermo-Calc® provides an interface called 'TQ-Interface' which uses specific libraries in C or Fortran. Chen *et al.* [142] have used TQ-Interface to perform microsegregation simulations which accounts for back diffusion of carbon (SCHEIC module of Thermo-Calc® - paraequilibrium solidification model with complete interstitial and negligible substitutional solute back diffusion) as well as to develop a phase field simulation software MICRESS® (MICRostructural Evolution Simulation Software). Some other works which have directly coupled the model with TQ-Interface are Jacot and Rappaz [141], Zhang *et al.* [143] etc. As highlighted by Jacot and Rappaz [141], while direct coupling is easy to implement, it is computationally intensive and exposed to robustness issues.

- **Tabular method:** Another approach to couple the simulations with CALPHAD data is the tabular approach. Within this approach, Thermo-Calc® along with the appropriate thermodynamic databases are used to perform phase equilibrium calculations which are employed to tabulate the phase diagram information. The information tabulated depends on the solidification simulation. Doré *et al.* [54] and Thuinet and Combeau [114] employed the tabular approach to perform microsegregation simulations. For the primary phase in a ternary system, the mapping file stores the data for the liquidus surface as shown in Table 3.4.

  These values are stored for all the elements in a certain range using a typical grid spacing (Δw_i) as shown in Fig. 3.9. These data files are used as input to the microsegregation model. At each time

c_1^{*1}	...	c_1^{*i}	T	k_p^1	...	k_p^i	m_1^1	...	m_1^i
.	.	.	.	.	.	.	.	.	.
.	.	.	.	.	.	.	.	.	.
.	.	.	.	.	.	.	.	.	.

Table 3.4 – Mapping file used by Doré *et al.* [54]
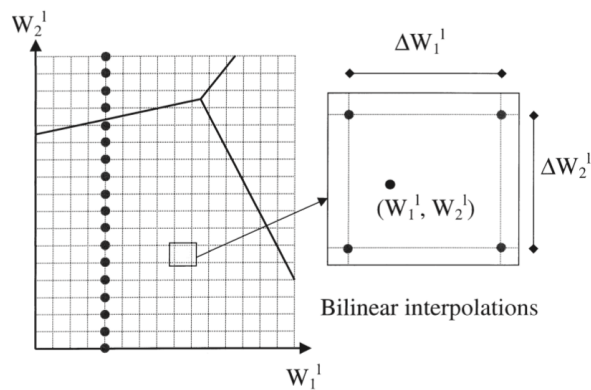
Figure 3.9 – Mapping of the liquidus surface [54]

step, the thermodynamic data corresponding to the values (w_1^1, w_2^1), are calculated using a bilinear interpolation. The solidification path ends at the eutectic point. Thus, mapping of the liquidus of the eutectic phase is also made. Du *et al.* [144] also used the same approach to simulate the macrosegregation during direct chill casting of multicomponent aluminium alloys. However, the mapping file stored the average liquid composition ($\langle c_1^i \rangle^1$) and the solid fraction (g_s) as a function of the average composition ($\langle c \rangle$) and temperature (T). The mapping file used by Saad *et al.* [145] is similar to that of Du *et al.* [144] along with additional information about the intrinsic phase enthalpies ($\langle h_\phi \rangle^\phi$). Du *et al.* [144] highlight the limitations posed by quinary and higher component number alloy systems on the size of the mapping file. They show that for quinary alloys, the size of the mapping file used by them could reach to a size of 100 GB. While this problem could be overcome by optimizations such as employing non-uniform mapping steps, performing bilinear interpolation on-line could still be computationally expensive. With these limitations, we propose to perform regression analysis on the mapping file data. Artificial neural networks (ANN) have been used to perform regression in the current work. These are algorithms that come under the paradigm of Machine Learning (ML). ANN offers the advantage of implicitly detecting complex non-linear relationships between the dependent and independent variables. This is critical as the mapping file used in the current work includes a wide variety of dependent variables. The mapping file used in the current model is shown in Table. 3.6 along with the mapping of the liquidus surface data in Table 3.4. Using these tables, various regression functions can be generated as shown in Table. 3.7.

The two kinds of file referred to as 'Phase data file' and 'Interface equilibrium data file' corresponds to data in Table. 3.6 and Table. 3.4 respectively. Two 'Phase data file' exist, one for liquid and the primary solid phase and one 'Interface equilibrium data file' exists for the liquid/primary solid equi-

$\langle c^1 \rangle$	...	$\langle c^i \rangle$	T	g_ϕ	$\langle c_1^1 \rangle^1$	...	$\langle c_1^i \rangle^1$
.	.	.	.	.	.	.	.
.	.	.	.	.	.	.	.
.	.	.	.	.	.	.	.

Table 3.5 – Mapping file used by Du *et al.* [144]

$\langle c_\phi^1 \rangle^\phi$	...	$\langle c_\phi^i \rangle^\phi$	T	h_ϕ	$\left(\dfrac{\partial \langle h_\phi \rangle^\phi}{\partial T} \right)_{\langle c \rangle^\phi}$	$\left(\dfrac{\partial \langle h_\phi \rangle^\phi}{\partial \langle c^1 \rangle} \right)_{T, \langle c^{j \neq 1} \rangle}$	...	$\left(\dfrac{\partial \langle h_\phi^\phi \rangle}{\partial \langle c^i \rangle} \right)_{T, \langle c^{j \neq i} \rangle}$
.	.	.	.	.	.	.	.	.
.	.	.	.	.	.	.	.	.
.	.	.	.	.	.	.	.	.

Table 3.6 – Phase data file ($\phi = \delta$ or γ or liquid)

Table 3.7 – Thermodynamic functions obtained from neural network regression

Inputs	Outputs	Description	File type
$T, \langle c_\phi^1 \rangle^\phi ... \langle c_\phi^i \rangle^\phi$	$\langle h_\phi \rangle^\phi$	Enthalpy of phase	Phase data file
$T, \langle c_\phi^1 \rangle^\phi ... \langle c_\phi^i \rangle^\phi$	$\left(\dfrac{\partial \langle h_\phi \rangle^\phi}{\partial T} \right)_{\langle c_\phi^i \rangle^\phi}$	Specific heat capacity of phase	Phase data file
$T, \langle c_\phi^1 \rangle^\phi ... \langle c_\phi^i \rangle^\phi$	$\left(\dfrac{\partial \langle h_\phi \rangle^\phi}{\partial \langle c_\phi^i \rangle} \right)_{T, \langle c_\phi^{j \neq i} \rangle^\phi}$	Composition effect on phase enthalpy	Phase data file
$\langle h_1 \rangle^1, \langle c_1^1 \rangle^1 ... \langle c_1^i \rangle^1$	T_1	Temperature of liquid phase	Phase data file
$\langle h_s \rangle^s, \langle c_s^1 \rangle^s ... \langle c_s^i \rangle^s$	T_s	Temperature of solid phase	Phase data file
$c_1^{*1} ... c_1^{*i}$	T	Interfacial temperature	Interface equlib. data file
$c_1^{*1} ... c_1^{*i}$	$k_p^1 ... k_p^i$	Partition coefficients	Interface equlib. data file
$c_1^{*1} ... c_1^{*i}$	$m_1^1 ... m_1^i$	Liquidus slope	Interface equlib. data file

librium. The variation of various interfacial equilibrium parameters for Fe-C-Cr alloy with primary δ ferrite phase is shown in Fig. 3.10. It can be seen that for a ternary system itself, the surface of the partition coefficient and the liquid slope maps can be quite complex, hence the application of ANN. In the next section, we briefly introduce ANN.
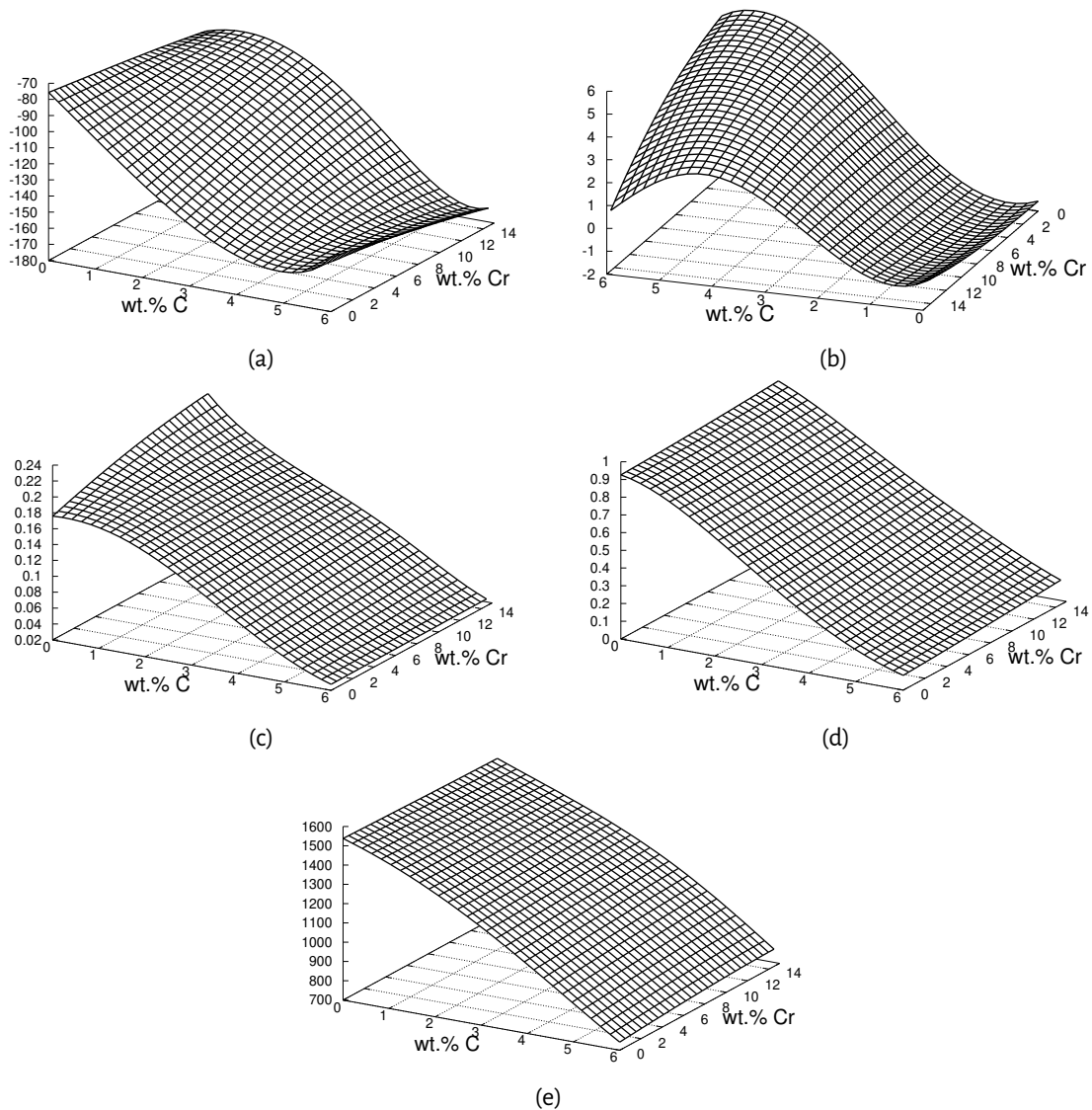
Figure 3.10 – Interfacial phase diagram parameters: a) m_l for carbon b) m_l for chromium c) k_p for carbon d) k_p for chromium and e) liquidus temperature for Fe-C-Cr system with liquid and δ-ferrite as obtained from Thermo-Calc®

3.7 Artificial Neural network (ANN)

ANN models are computing paradigms that mimic the functioning of the biological brain. These modeling techniques are useful where the relationships between inputs and the outputs are not sufficiently known. ANN has a computational system called node (artificial neuron) which is similar to the neuron in the brain and has been around for more than half a century since McCulloch and Pitts [146] first mentioned it. Each of these nodes acts like a microprocessor. The nodes are interconnected to each other in layers forming an interconnected network to provide an output. This interconnected network mimics a non-linear regression model capable of analyzing the patterns in the inputs and the target output data provided to the model. ANN has been used quite commonly in the field of mechanical and materials engineering. ANN are shown to have performed better than other regression counterparts based on the accuracy.

Haghdadi *et al.* [147] developed an ANN model to predict the high temperature flow of A356 aluminium al-
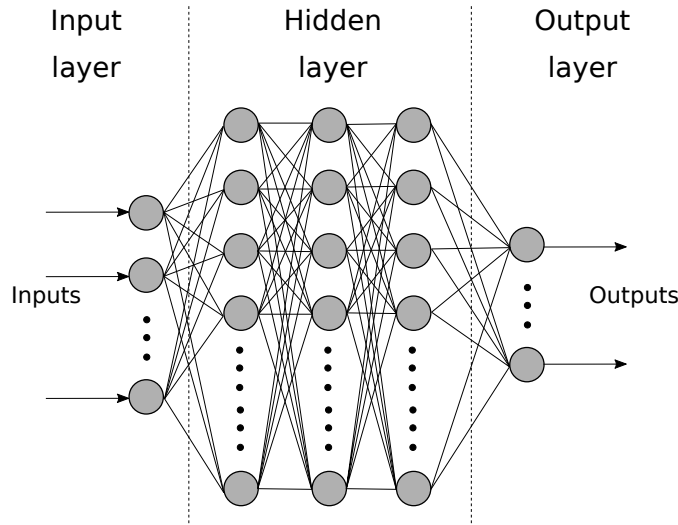
Figure 3.11 – Schematic representation of a multilayer perceptron (MLP) neural network

loy. The factors considered for the model were temperature, strain and strain rate. The results suggested ANN as the statistically efficient and robust tool for property design . Han *et al.* [148] developed an ANN model to predict the high temperature flow stress of 904L austenitic stainless steel in a cast condition . Krajewski and Nowacki [149] developed an ANN model to correlate the alloying element composition, transition temperature and other microstructural features on the tensile strength based on the experimentally validated data of dual phase steels. All of the above mentioned work use Multi-Layer Perceptron (MLP) which is the most basic ANN architecture. MLP's are feed forward neural networks with at least three layers (input, one hidden and one output) of any number of neurons along with an activation function. In the present work, MLP based ANN has been used to model the various thermodynamic correlations that are required in the solidification model.

3.7.1   Multi-layer perceptron (MLP)

The MLP model is composed of one or multiple neurons (or nodes) which are distributed in an input layer, one or more hidden layers, and an output layer. Each neuron processes its inputs (in a non linear manner) and generates an output value that is transmitted to the neurons in the subsequent layer. The neurons in their respective layers are arranged in a feedforward manner. Feedback connections are not allowed. Fig. 3.11 shows a schematic representation of a multi-layer perceptron (MLP) neural network. For a given a set of input data, $(x_1, , x_2, ..., x_n)$ where $x_i \in \mathbf{R}^n$, for m_1 number of neurons in the next layer, m_1 linear combinations are performed such that

$$a_j = \sum_{i=1}^{n} w_{ji}^{(1)} x_i + w_{j0}^{(1)} \tag{3.58}$$

where $j = 1, ..., m_1$ and the superscript (1) indicates the layer to which the parameters belong to, in this case the first. The parameter w_{ji} is referred to as the weights and w_{j0} as the bias. The quantities a_j are known as activations. The neuron output value for each of these functions are transformed using a nonlinear function $h(.)$. These activation functions make it possible for the model to capture the non-linear relationship between the input and output variables. Various activation functions exist in literature. The most commonly used activation functions have been shown in Fig. 3.12a. The output of the activation function gives $z_j = h(a_j)$ and is

referred to as 'hidden units'. These values are again linearly combined to the output unit activation

$$a_k = \sum_{j=0}^{m_1} w_{kj}^{(2)} z_j + w_{k0}^{(2)} \tag{3.59}$$

where $k = 1, ..., m_2$ is the total number of outputs and corresponds to the number of nodes in the next layer. This transformation can be performed multiple times depending on the number of hidden layers in the MLP-ANN. For a single hidden layer MLP-ANN, the complete transformation is given by

$$y_k(\mathbf{x}, \mathbf{w}) = \sum_{j=0}^{m_1} w_{kj}^{(2)} h \left(\sum_{i=1}^{n} w_{ji}^{(1)} x_i + w_{j0}^{(1)} \right) + w_{k0}^{(2)} \tag{3.60}$$

where the set of all the weight and bias matrices have been grouped together into a vector $\mathbf{w}$. Thus, the neural network is simply a nonlinear function from a set of input variables $\{x_i\}$ to a set of output variables $\{y_k\}$ controlled by a vector $\mathbf{w}$ of adjustable parameters.
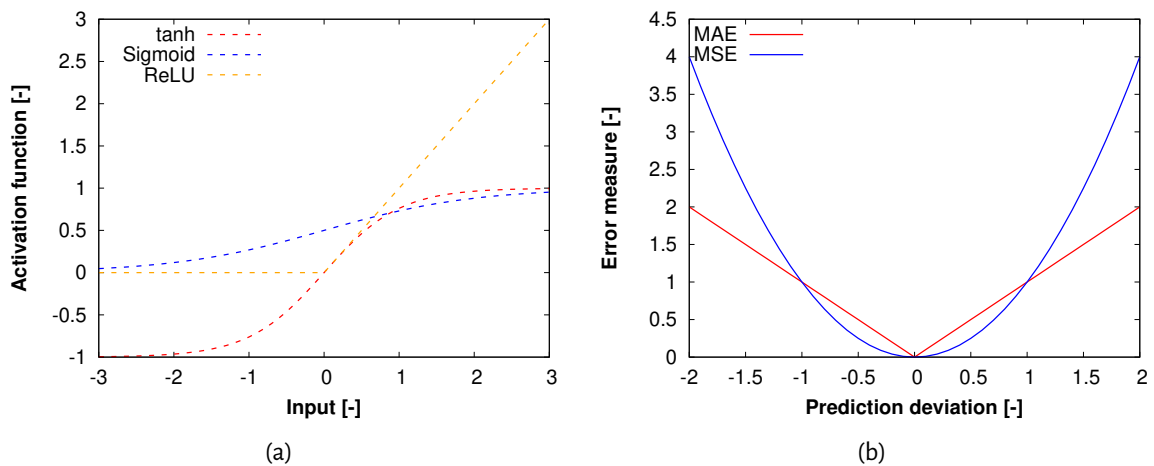
Figure 3.12 – a) Examples of commonly used activation functions. Shown here are the tanh function (dashed red line), sigmoid function (dashed blue line) and ReLU function (dashed orange line) b) Comparison between the mean absolute error (MAE) and mean squared error (MSE) loss function

3.7.1.0.1 Training: This section briefly covers the training procedure of the neural network. The neural networks are trained in a data-driven manner. The main steps in the training procedure are as follows:

– **Initialization:** The weights and the biases of the neural network are initialized randomly and an iteration loop is started

– **Prediction:** The input variables in the test data are given as inputs to the neural network for which the output variables are predicted using the mathematical formulation described above

– **Score calculation:** The outputs predicted by the neural network are compared to the actual output values available in the test data. The performance of the neural network is measured using a 'loss function'. The 'loss function' is a function to compute the performance of the neural network. It is a kind of a penalty imposed for the error introduced due to wrong prediction of the neural network. It is used as the objective function for the optimization of the weights and biases of the neural network. The common 'loss function' used in neural networks are mean squared error (MSE) and the

mean absolute error (MAE). Fig. 3.12b shows the comparison between MAE and MSE. MAE penalizes the neural network more severely as compared to MSE when the prediction deviation is small. When the prediction deviations are greater than 1, MSE penalizes the network more severely. Thus, MSE penalizes predictions that are very far off from the actual value, thus leading to a network with less pronounced outliers. In the present work, MSE is chose as the 'loss function' which is given by

$$J_{\mathrm{MSE}} = \frac{1}{n} \sum_{i=1}^{n} (t_i - o_i)^2 \tag{3.61}$$

where J_{MSE} is the value of the loss function, n is the number of test data, t_i is the target value of the data instance i and o_i is the value predicted by the neural network for the instance i. MSE is also used to quantify the final accuracy of the neural network.

– **Optimization:** The value of the 'loss function' is the function of the weights and the biases of the neural network. Thus, changing the values of these weights and biases results in the change in the value of the 'loss function'. The process of adjusting these weights and biases is called optimization. A general optimization algorithm (gradient descent) is represented by:

  – **Initialization:** The algorithm is given an initial guess value $\mathbf{w^0}$ along with parameters such as convergence criteria val and a maximum number of iterations n_{iter}. An iteration loop begins

  – **Diffrentiation:** Values of the objective function $\{y^k\}$ are calculated using the input data and $\mathbf{w^k}$ where k is the iteration variable. Further, gradient of the objective function is calculated at point $\mathbf{w^k}$ using numerical differentiation.

  – **Update:** Based on the values of the gradient calculated in the previous step along with a pre-defined update scheme, the set of inputs is updated

  $$\mathbf{w^{k+1}} = \mathbf{w^k} - \alpha \nabla \mathbf{w^k} \tag{3.62}$$

  where α is update step size and is referred to as 'learning rate'.

  – **Convergence:** The convergence of $\mathbf{w^{k+1}}$ is checked. If the convergence criteria is met, the iteration is stopped, else it is stopped when n_{iter} is reached.

The performance of the MLP-ANN depends on various parameters. Some of the parameters are the network topology, the activation function and data management. This is not an exhaustive list of all the parameters but the parameters which were considered in this work.

– **Network topology:** The design of the network topology of the hidden layers is critical in deciding the efficiency of the model. The overfitting or underfitting of the model is controlled by the topology of the nodes and the layers. However, it has been proven that in most function approximation problems such as the present one, one hidden layer is sufficient to approximate continuous functions. However, two or more hidden layers may be necessary for learning functions with discontinuities [150]

– **Activation function:** As mentioned earlier, there are various activation functions mentioned in the literature with the most popular ones being the sigmoid, tanh and various versions of the ReLU function. ReLU and its derivatives are highly popular among deep neural networks. This is due to the fact
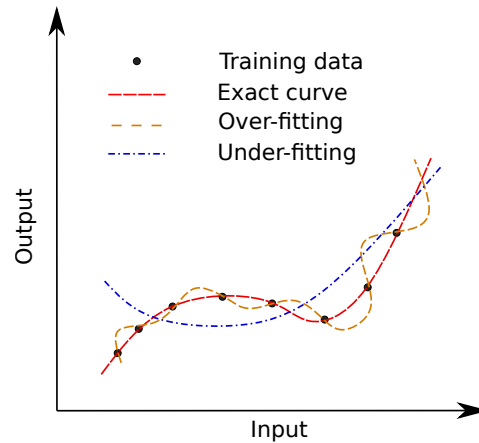
Figure 3.13 – Illustration of an over-fitted and an under-fitted curve. The under-fitted curve can result from neural network having too few neurons or short training time and vice versa for the over-fitted curve

that the value of the ReLU function for an input less than 0 is 0. This results in less nodes being activated for an input and results in reduction in computational power. However, as the derivative of the ReLU function is 0 for values less than 0, the weights and the bias matrix are never updated during the training of the neural network and the neural network does not learn. This problem is referred to as the 'dying ReLU' problem. Thus, using ReLU functions requires a higher number of nodes (this is not a generic statement but was observed during the course of the present work). As the main purpose of the current work was to use a neural network with the least amount of nodes, the tanh function was chosen as the main activation function. Further, some of the literature mentioned in the above section which focused on the applications of the shallow neural network in the mechanical and materials domain, we persisted with tanh function as well. Performance of the various activation functions is beyond the scope of the present work.

— **Data processing:** Data processing is the foundation of ANN. Proper data management is the difference between an average and a good neural network. In order to properly train, evaluate, and choose between different neural network alternatives, it is important to divide the total data set into two subsets: the training set and the testing set.

  — **Training set:** The training set is the part of the original data set which is used to train the neural network. It is critical that the training set is representative of the entire data set. Non-representative data sets result in the network developing bias towards certain parts of the original data set.

  — **Testing set:** This data set is used to evaluate the performance of the MLP-ANN. The test set is used once the network has been trained on the training set. Generally, a poor scoring network on both the training and testing set results in underfitting of the training set. If a network performs well for the training set but poorly for the testing set points to overfitting of the network.

The rule of thumb is to divide the training and testing set with a ratio of 4:1. To further improve the performance of the neural network, 'cross-validation' technique is used.

  — **Cross validation:** Cross-validation is a machine learning approach used to improve the
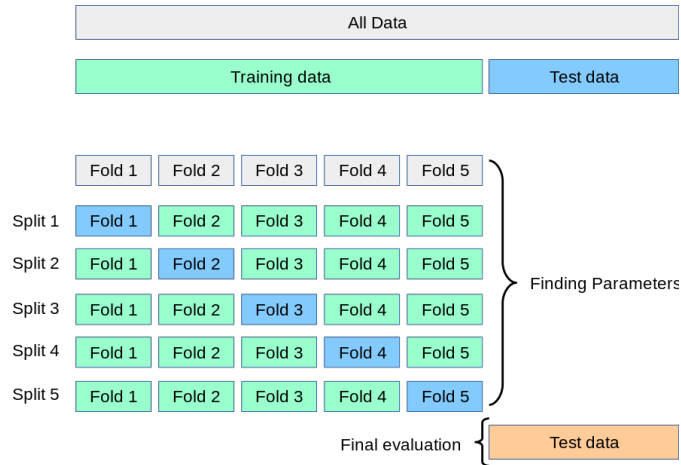
Figure 3.14 – Schematic representation of cross-validation technique [151]

quality of a neural network. While dividing the dataset into 'train data' and 'test data' prevents over-fitting, there is still a risk of over-fitting if the partitioning of the dataset is not performed well. A solution to this problem is a procedure called 'cross-validation'. Within the framework of scikit-learn®, the 'k-fold' cross validation technique has been used. In this approach, the 'train data' is roughly divided into k equal sized sets as shown in Fig. 3.14 such that each set is used exactly once as the 'test data'. The procedure for each of the 'k folds' is as follows:

- Model is trained using $k-1$ of the folds as 'train data'
- The remaining fold is used as a 'test data' to compute the performance of the neural network

The final measurement of the performance of the neural network is the average of all the trials. This approach is computationally expensive but produces higher accuracy neural networks. When applied to several neural networks with various sets of free parameter values such as number of hidden nodes, number of hidden layers, backpropagation learning rate etc, the results of cross validation can be used to select the best set of parameter values.

Most of the time, the input and output contain data which differ in magnitudes. E.g., in the present work, while the composition and partition coefficients are of the same order of magnitude, the enthalpy is usually 5-6 orders of magnitude larger. This causes issues during optimization of the neural network. To solve this issue, the data should be either re-scaled, standardized or normalized. In the present work, we use the mean normalization approach which is given by

$$x^{'} = \frac{x - \text{avg.}(x)}{\text{max.}(x) - \text{min.}(x)} \qquad (3.63)$$

where avg., max. and min. are the average, minimum and maximum of the dataset.

3.8 Application of MLP-ANN to CALPHAD data

The regression functions for all the thermodynamic functions required for the solidification model were generated using MLPRegressor [152]. As mentioned earlier, the number of hidden layers was currently limited to 1. In order to illustrate the use of MLP-ANN, regression functions were generated for the Fe-C-Cr system for a composition range given in Table 3.8. Fig. 3.15 produces a qualitative validation of the regression function for the slope of liquidus slope of carbon. The liquidus slope is chosen here as it is more complex when compared to other interfacial phase diagram parameter maps. The number of nodes in the hidden layer was currently set to 5. It can be seen that the regression function does not reproduce the curve accurately in high carbon range as well as low carbon-high chromium range. The MSE of the regression function is 8×10^{-4} which is on the higher side.

Table 3.8 – Composition range of Fe-C-Cr alloy

Elements	wt.%
C	0.001-6.0
Cr	0.001-15.0
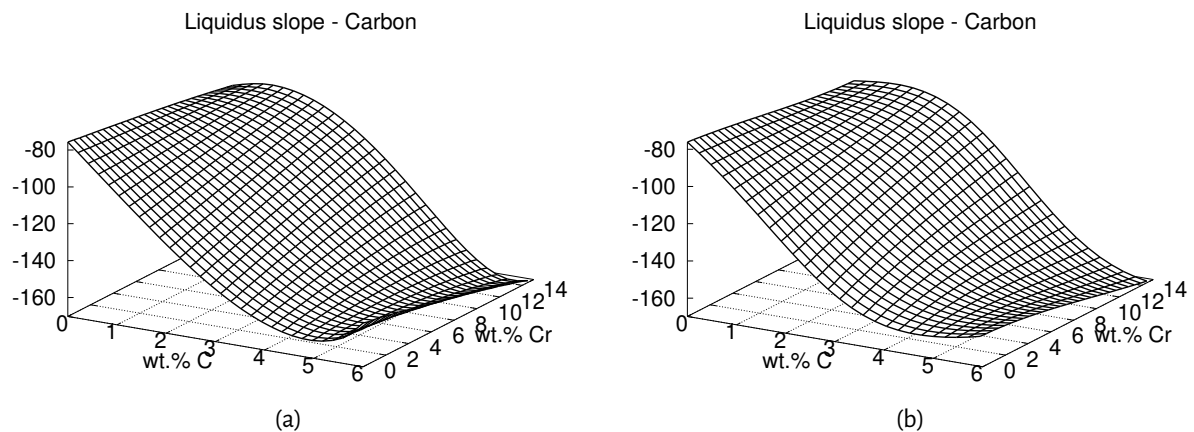
Figure 3.15 – Variation of liquidus slope of carbon in a ternary Fe-C-Cr alloy a) actual data b) MLPRegressor output

Fig. 3.16 shows the $\frac{Y_{\text{pred}}}{Y_{\text{val}}}$ (Y_{pred} is the value predicted by the regression function and Y_{val} is the actual value) for the liquidus slope of carbon and chromium for 300 random data points. It can be seen that the liquidus slope predicted for chromium has a higher accuracy than that for carbon. The points with high errors are most likely to correspond to the region of high carbon or low carbon-high chromium domain. These composition domains are most likely beyond the range of composition encountered during solidification as will be seen in the simulation results of industrial ingots in next chapter as well as sulphur print of 65t steel ingot [1]. Thus, we can safely reduce the composition range of the mapping files so as to increase the performance of the neural network while keeping the same number of nodes in the hidden layer. This also highlights the fact that while a generic regression function can be generated, a prior understanding of the system results in an efficient regression function.

(a)   (b)
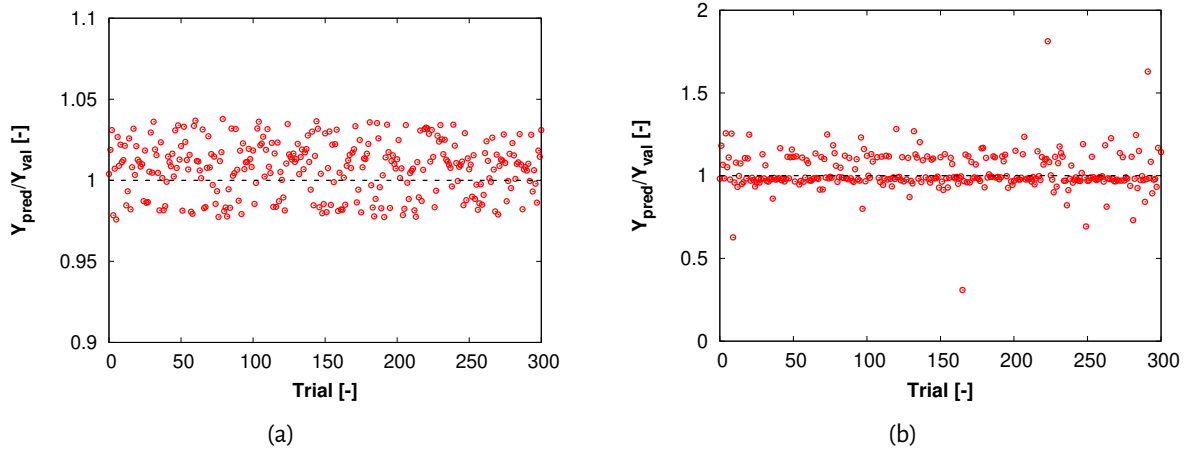
Figure 3.16 – Ratio of predicted value Y_{pred} and actual value Y_{val} for the liquidus slope of a) carbon and b) chromium for the composition range in Table 3.8

(a)   (b)
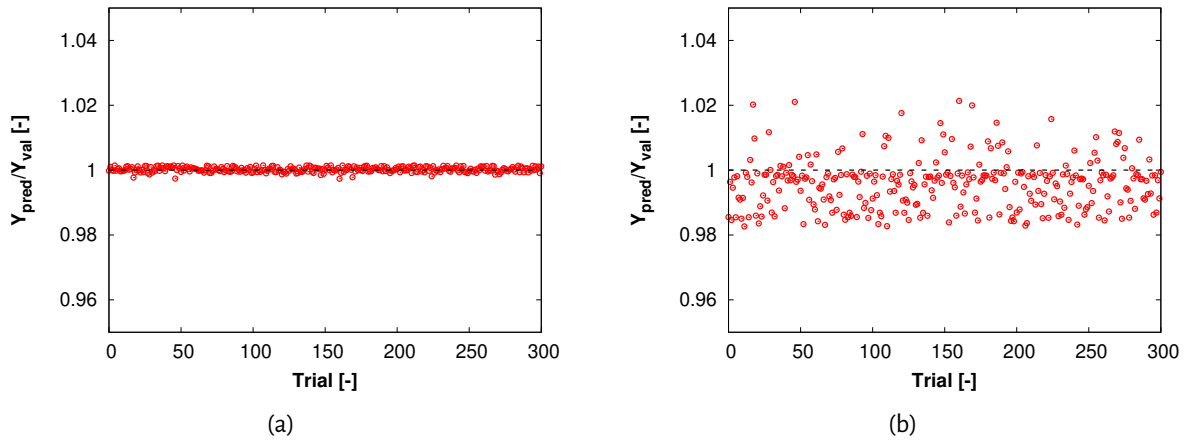
Figure 3.17 – Ratio of predicted value Y_{pred} and actual value Y_{val} for the liquidus slope of a) carbon and b) chromium for the composition range in Table 3.9

Table 3.9 – Modified composition range of Fe-C-Cr alloy

Elements	wt.%
C	0.001-1.5
Cr	0.001-1.5

New regression functions are generated using a limited composition range as shown in Table 3.9. The MSE for the new regression function for the liquidus slope is 1.5×10^{-6}. Fig. 3.17 shows that the new regression function performs much better. While Fig. 3.17 shows the value of $\frac{Y_{pred}}{Y_{val}}$ for 300 random data points, Fig. 3.18 shows the map of $\frac{Y_{pred}}{Y_{val}}$ over the whole composition domain. The surface of the $\frac{Y_{pred}}{Y_{val}}$ map has been observed to depend on the number of nodes in the hidden layer. The new regression function has 5 nodes in the hidden layer. The various matrices and data employed to compute the liquidus slope are listed below to demonstrate the output of ANN-MLP which are subsequently used in the solidification model. Table C.1 lists the MSE for all the regression functions used and also highlights that R^2 is not the correct metric to quantify the performance

$$m_l \text{ (carbon) } Y_{pred}/Y_{val} \qquad\qquad m_l \text{ (chromium) } Y_{pred}/Y_{val}$$

(a) (b)
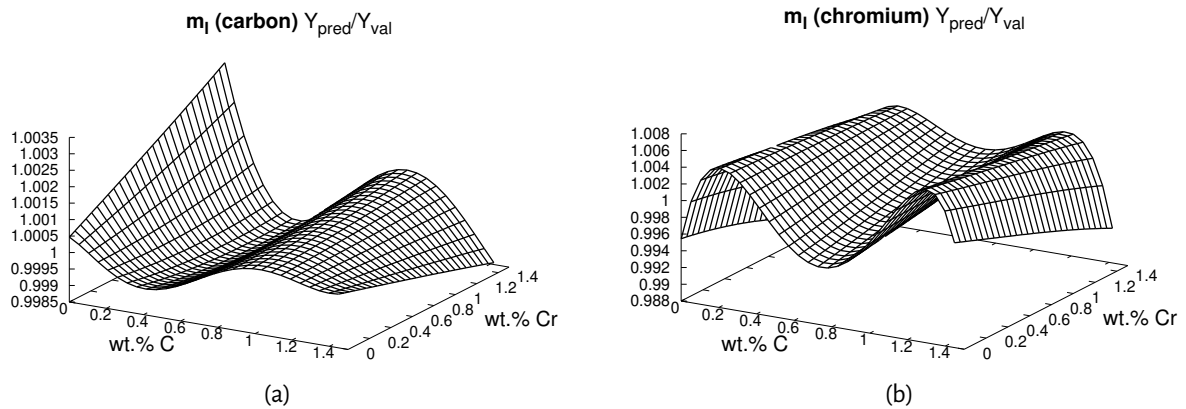
Figure 3.18 – Variation of error in liquidus slope of a) carbon and b) chromium in a ternary Fe-C-Cr alloy

of the regression functions.

$$X(max,min,mean) = \begin{pmatrix} 1.5 & 0.0001 & 0.75407611 \\ 1.5 & 0.0001 & 0.74259851 \end{pmatrix} \quad Y(max,min,mean) = \begin{pmatrix} -75.69369 & -110.9166 & -93.17412632 \\ -1.003559 & -1.789171 & -1.57949981 \end{pmatrix}$$

$$\text{Weight and bias matrix } W_1 = \begin{bmatrix} -0.23293439 & -0.14388315 \\ -1.43281521 & -0.14388315 \\ -1.26083987 & 0.06065979 \\ 0.18005745 & -0.20018612 \\ -0.31146483 & -0.00397241 \\ -0.24020179 & 0.09039775 \end{bmatrix} \quad b_1 = \begin{bmatrix} 0.20321721 \\ -0.94004447 \\ 0.63762646 \\ -0.25646379 \\ 0.117405 \\ 0.18884751 \end{bmatrix}$$

$$W_2 = \begin{bmatrix} 0.09982524 & 0.49237543 & 0.59243352 & -0.03777544 & 0.16175804 & 0.1252996 \\ 0.55768558 & 1.29609786 & -2.54637381 & -0.63247526 & 0.52635706 & 0.62399609 \end{bmatrix} \quad b_2 = \begin{bmatrix} -0.04277337 \\ 1.7420046 \end{bmatrix}$$

To summarize the overall scheme of the solidification model, we first generate the mapping files for the desired primary solid and the liquid phase for the alloy system. This data is used by the MLP-ANN to generate the various regression functions described earlier. Subsequently, these regression functions are imported into the solidification model and used. Fig. 3.19 shows the schematic work-flow.
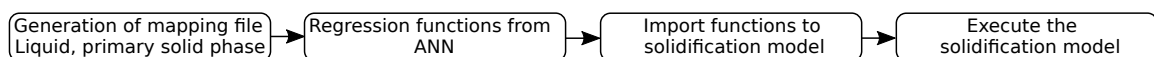
Figure 3.19 – Work-flow of the solidification model coupled with ANN-MLP

3.9 Model validation

In the present section, validation of the new growth model will be presented for cases without solid and liquid transport. As the validation case for solid and liquid transport, the Hebditch-Hunt benchmark case forms an integral part of discussion in the next chapter as well, we will present the case description, validation and the

(a)   (b)

(c)   (d)
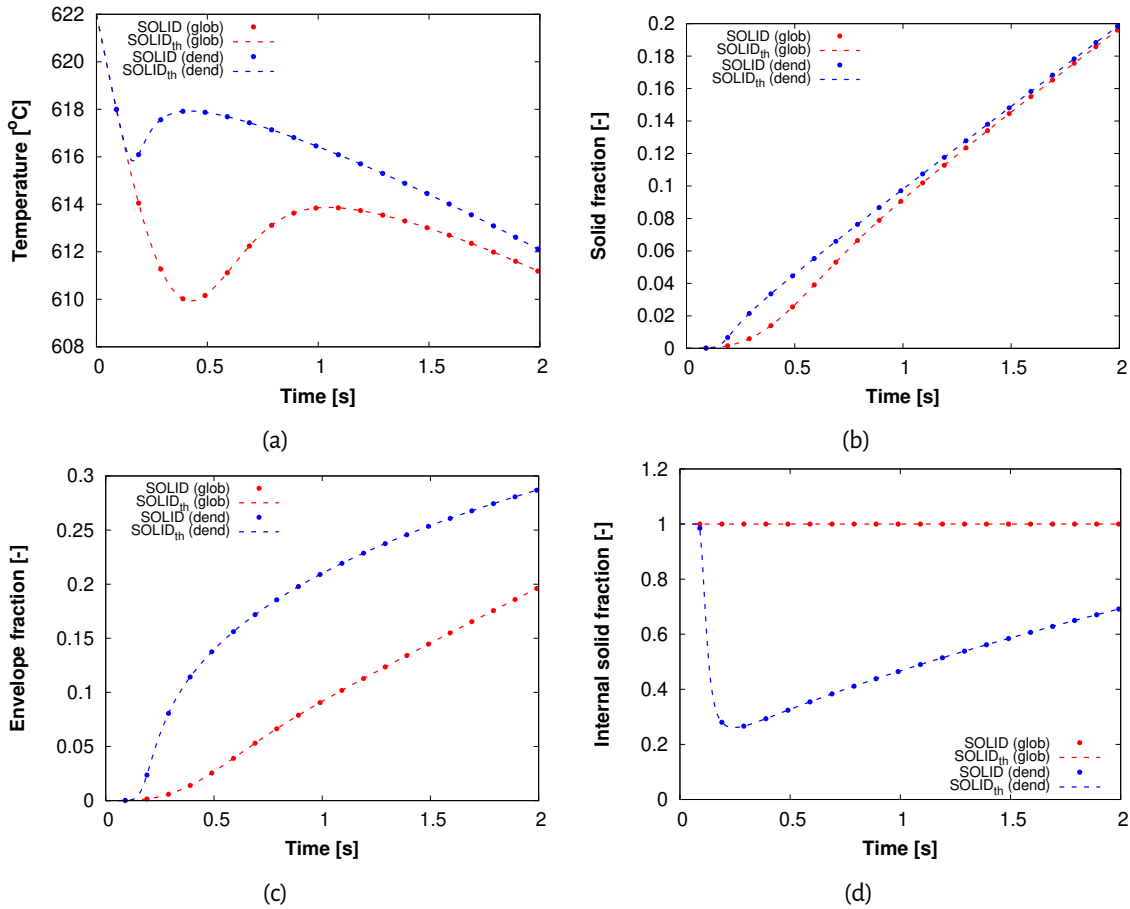
Figure 3.20 – Time evolution of parameters a) temperature b) solid fraction c) envelope fraction and c) internal solid fraction for R_f=0.1mm for SOLID® and SOLID®$_{th}$ models for the globular (glob) and dendritic (dend) model

results in the next chapter.

3.9.1   Equiaxed grain growth model

3.9.1.1   Without CALPHAD coupling

The validation of the new growth model is performed by simulating a pure thermal solidification for a test case proposed by Bedel [122]. The test case consists of solidification of unary control volume of pure liquid with composition Al-5 wt.% Si cooling at a constant rate of 45 K/s. Nucleation occurs at a the liquidus temperature with no undercooling. The simulations are performed for three grain sizes: 0.1 mm, 1 mm and 10 mm for which the nuclei grain densities are calculated accordingly. Simulations are performed with different growth models: the two phase globular model and the three phase dendritic model. The thermophysical and simulation parameters used for the simulation are given in Table B.1 and B.2.

Fig. 3.20 shows the temporal evolution of various parameters in the time interval of 0-2 s. It can be seen that the new growth model (SOLID®$_{th}$) retrieves the result of the SOLID®, thus validating the implementation of SOLID®$_{th}$. The models are able to depict the recalescence which is a consequence of the limited solute diffusion in the liquid and the solid phase. The end of recalescence corresponds to the solutal impingement due to the presence of other grains. The three phase dendritic model predicts a faster recalescence with respect to the two phase globular model due to the higher growth rate of the solid phase. This is due to the higher
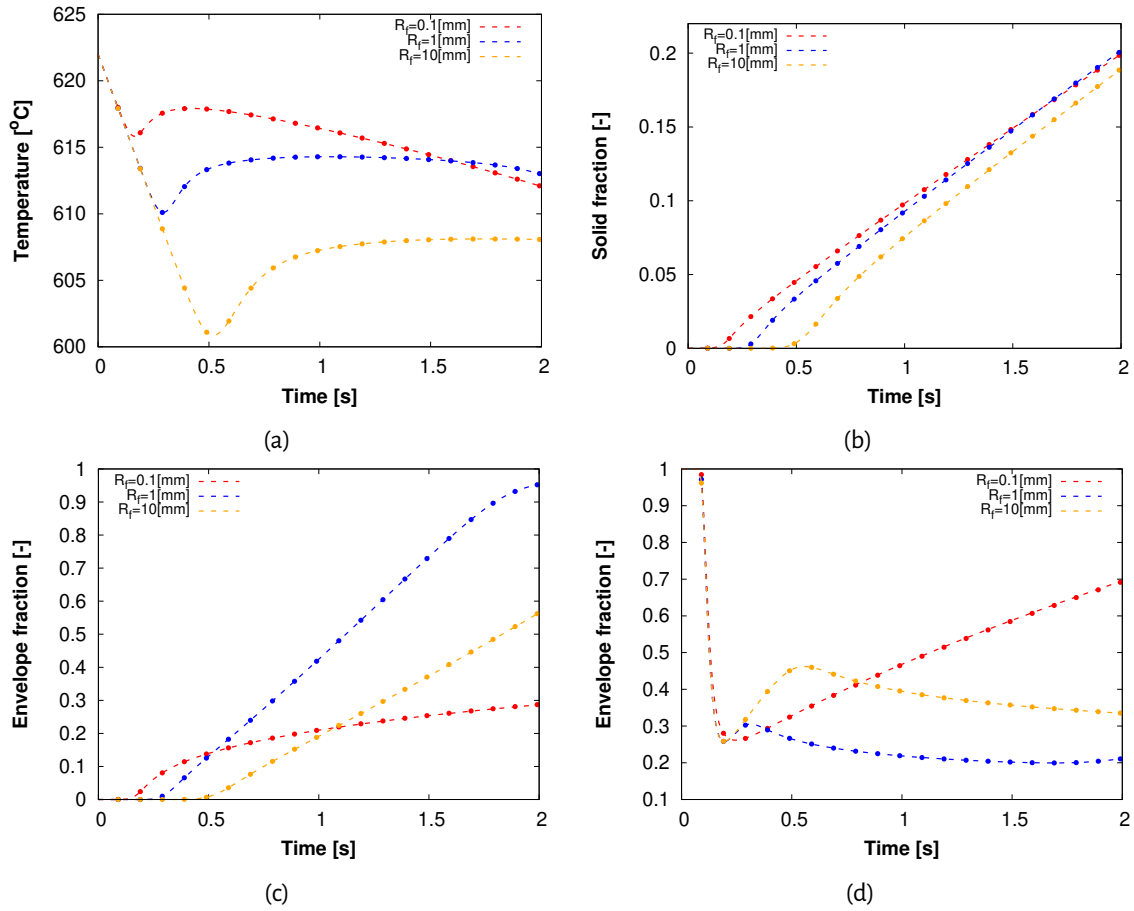
Figure 3.21 – Time evolution of parameters a) temperature b) solid fraction c) envelope fraction and c) internal solid fraction for SOLID®(·) and SOLID®$_{th}$(–) models

supersaturation in the dendritic model as the envelope grows much faster as compared to the solid grain. The three phase dendritic model also allows for better description of the grain morphology as shown in Fig. 3.20d, especially in cases with low grain density where the solid grains develop a dendritic morphology. Fig. 3.21 compares the effect of the grain density on the temporal evolution of various parameters for the dendritic model. Higher grain density results in a higher increase in the solid fraction, thus a faster beginning of the recalescence as compared to the case with less grain density. Higher grain density also results in a faster solutal impingement effect and a sharper recalescence as compared to the low grain density case.

3.9.1.2 With CALPHAD coupling

To validate the coupling of the solidification model with CALPHAD data through MLP-ANN regression, we employ the Al-Si alloy with the same composition and thermophysical properties as described earlier. Thermo-Calc® data was tabulated for the Al-Si system using the ALDEMO database and was used to generate regression functions. Fig. 3.22a shows a comparison of the phase diagram obtained from Thermo-Calc® with respect to the linear phase diagram assumed in the previous case. We observe that while the melting temperature of the pure Al metal is the same, the liquidus and solidus differ as a result of the liquidus slope (m_l^i) and partition coefficient (k_p^i) used. 577 °C is the eutectic temperature. Scheil solidification simulations were performed by setting $D_l^{Si} = 10^{-6}$ m²/s and $D_s^{Si} = 10^{-13}$ m²/s in the solidification model. Fig. 3.22b shows the scheil

(a)   (b)
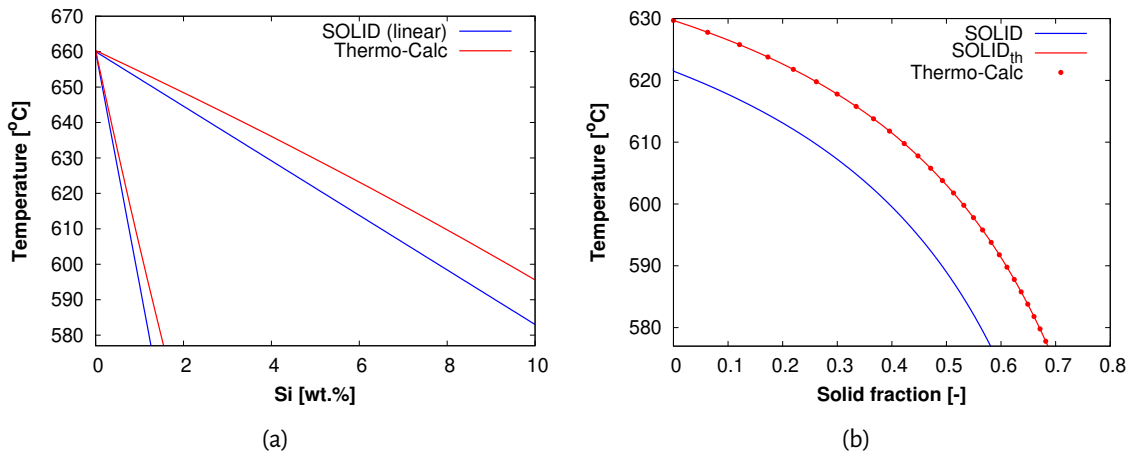
Figure 3.22 – a) Al-Si phase diagram obtained from Thermo-Calc® and b)Scheil solidification of Al-5 wt.% Si alloy using Thermo-Calc®, SOLID® and SOLID®$_{th}$

solidification path for the alloy obtained from Thermo-Calc®, SOLID® and SOLID®$_{th}$. SOLID®$_{th}$ retrieves the results of Thermo-Calc®, thus validating the implementation of Thermo-Calc®data in the new model (similar comparisons have been performed for Sn-Pb and Fe-C-Cr alloy in Sections 5.1.1 and 5.2.3 respectively). While the results of SOLID®can be improved by modifying T_f, m_1^i and k_p^i such that the linearized phase diagram approaches the phase diagram of Thermo-Calc®, this approach is not possible for open system where the nominal composition changes with time, thus highlighting the importance of the new implementation of the microscopic growth model.

3.9.2   Columnar grain growth model
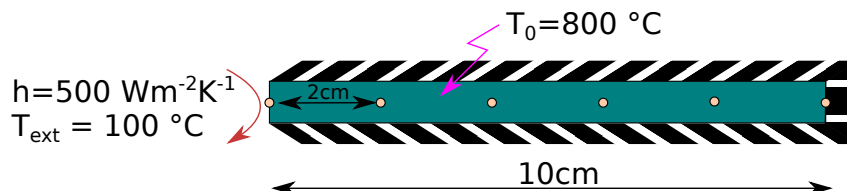
Figure 3.23 – Schematic representation of the simulation case

The columnar front tracking algorithm implemented in SOLID®has been already validated [123]. However, the new microscopic growth model implemented has to be validated. The new microscopic growth model has been validated on a 1D directional solidification case. In this case, the columnar front tracking algorithm is employed along with the macroscopic energy transport model and the microscopic growth model which considers only the presence of columnar grains. Liquid convection and nucleation and growth of equiaxed grains are neglected. The solidification domain is the rectangular area shown in Fig. 3.23 which is 10 cm long and 1 mm thick. It is cooled on the left side (h_{ext}=500 W/m^{2}K and T_{ext}=100 ^{o}C). The other sides are adiabatic. Six sensors are placed inside the domain: two at the ends and four spaced 20mm apart. Table B.3 and B.4 list the thermophysical and simulation parameters.

Fig. 3.24a and 3.24b show the temporal evolution of temperature and solid fraction for the different sensors. We only compare the results of SOLID® with the SOLID®$_{th}$. The results of the SOLID®$_{th}$ correspond quite well to the results from SOLID®, thus validating the implementation of the new model. Readers are referred to

the Leriche [123] for comparison of the SOLID® results with front tracking algorithm [153] and Cellular-automata finite element (CAFE) model [154]. The liquidus temperature of the alloy is 618 °C. Fig. 3.24a shows a rapid cooling in the earlier stages which corresponds to the liquid cooling. Subsequently, solidification is accompanied by the release of latent heat resulting in a slower cooling. Faster cooling resumes after complete solidification at the eutectic temperature. Fig. 3.22b shows the evolution of the solid fraction for various points. Advancement of the columnar front requires a positive temperature gradient ΔT ahead of the columnar front. For example, a ΔT of 5 °C is required for the last sensor. Subsequent solidification occurs which is accompanied with an increase of 0.12 in the solid phase fraction.

3.10 Summary

In this chapter, we present a unique approach to couple the solidification model with CALPHAD data. CALPHAD data is employed in the microscopic growth model as well as the macroscopic heat transfer model. The macroscopic heat transfer model is not modified. However, the microscopic growth model requires modification to be coupled with CALPHAD data. Our overall contributions can be encapsulated as follows:

– Consistent implementation of the microscopic growth model (for the two phase globular and three phase dendritic equiaxed solidification model) within the framework of the splitting scheme [53].

– To identify the various thermodynamic functions required for coupling the solidification model with CALPHAD data.

– Use of ANN-MLP to produce regression relationships for the various thermodynamic functions used in the solidification model.

– Extending the new implementation of the microscopic growth model to the six phase model which accounts for columnar and equiaxed grains and is used to model Columnar to Equiaxed Transition (CET).

Other than these primary contributions, we also proposed a new time integration scheme: μSOLID. The new scheme is used to couple the microscopic growth model with the macroscopic model within the splitting scheme [53] framework. The above mentioned implementations are validated. The new implementation of the equiaxed solidification model is validated for globular and dendritic solidification of Al-5 wt.% Si alloy. Similarly, the new implementation of the columnar solidification model is validated for Al-7 wt.% Si alloy. The coupling of the solidification model (neglecting macrosegregation) with CALPHAD data is validated by comparing the Scheil solidification results from Thermo-Calc® for Al-5 wt.% Si alloy with SOLID®th results.

(a)

(b)
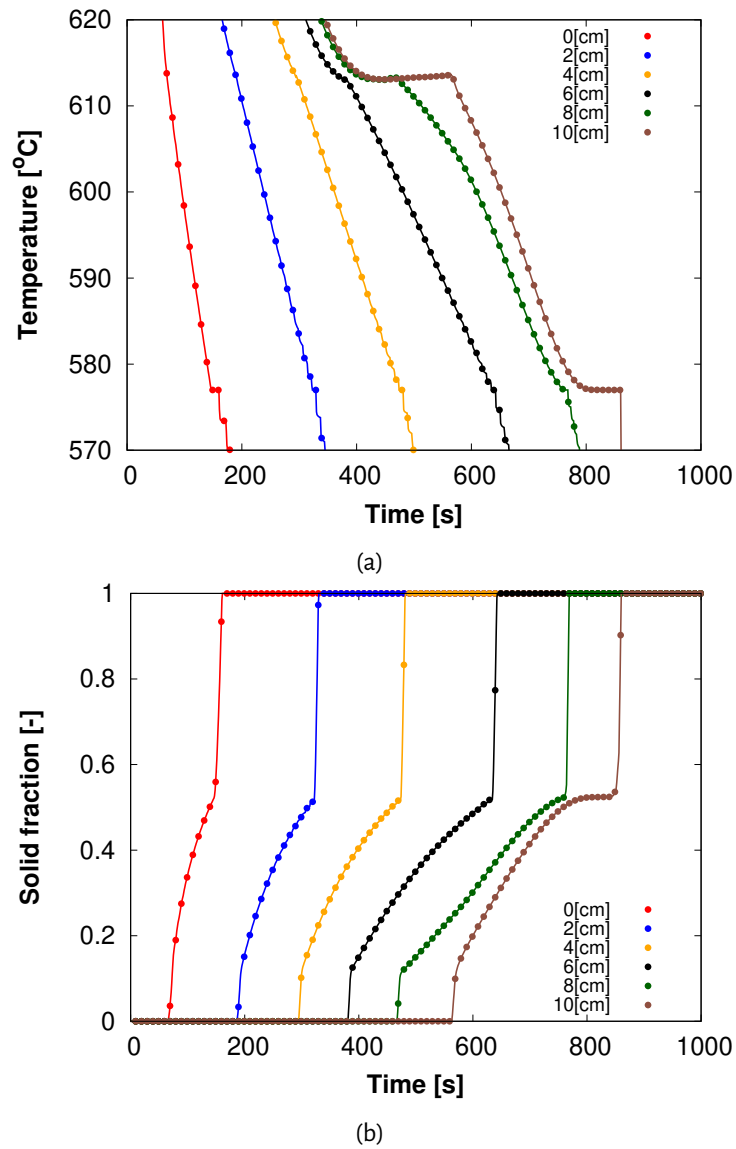
Figure 3.24 – Temporal evolution of a) temperature and b) solid fraction for various sensors positioned in the domain

Chapter 4 : Solutal boundary layer thickness in the liquid phase

Solutal boundary layer thickness for equiaxed globular solidification in multicomponent alloys

S. Sachi[a], G. Guillemot[b], M. Založnik[a], Ch.-A. Gandin[b] and H. Combeau[a,*]

[a] *Université de Lorraine, CNRS, IJL, F-54000 Nancy, France*

[b] *Mines ParisTech, CEMEF UMR CNRS 7635, F-06904 Sophia Antipolis, France*

ARTICLE INFO

ABSTRACT

Volume average based solidification models are employed extensively to simulate solidification of large ingots. These models rely on accurate representatation of the microstructural phenomena, such as the solute profile in the liquid phase. We present an improved approximation for the solutal boundary layer thickness in the liquid phase. The approximation is based on stagnant film model (SFM) which accounts liquid convection, in addition to the movement of solid/liquid interface. The proposed model is validated for pure diffusion cases and is compared to existing models. The effect of convection on the solutal boundary layer thickness is further explored.

1. Introduction

Solidification of metallic alloys is complex and a time-consuming process. It encompasses various phenomena occurring over various length scales ranging from microscopic (grain nucleation and growth) to macroscopic (heat, mass and solute transfer). This results in generation of macrosegregation which are chemical heterogeneities at the length scale of the product. These segregation patterns determine the structure and properties of the cast product. Computation of macrosegregation through multi-phase multi-scale solidification model requires a model relating the specific enthalpy and the local average solute concentration to temperature, solid fraction and the solute concentrations in the solid and liquid phase i.e. microsegregation model. Various microsegregation models have been developed which include analytical approaches as well as numerical models. Initial analytical models assume complete mixing in the liquid phase and large diffusion or no diffusion in the solid phase corresponding to the lever rule (LR) and Gulliver-Scheil (GS) approximations [1]. Subsequently, analytical models considering finite diffusion in solid have been proposed [2, 3]. which were further extended to equiaxed solidification with finite diffusion in liquid and solid phases [4, 5]. Complete numerical approaches are also available [6, 7, 8]. Analytical microsegregation models are preferred when coupling with volume averaging based solidification model as they are computationally cheap and time effecient when compared to numerical models.

Analytical models rely on accurate representation of microstructural phenomena such as the grain morphology and solute profile in the phases. Estimation of grain morphology for globular equiaxed grains is straight forward. However, the solute profile in the phases which determines the solute flux and eventually the velocity of the s/l interface velocity requires the computation of the solute composition gradients at the s/l interface. These composition gradients are approximated by defining a characteristic diffusion length δ. Accurate representation of grain morphology and solute profile in the phases allow for description of solidification kinetics which account for competition between nucleation and growth. This competition is critical as it determines: (i) number of grains which nucleate (ii) undercooling achieved during solidification. Macroscopic motion is strongly dependent on these parameters, thus affecting macrosegregation. grain number density in liquid influences the hydrodynamic properties of the slurry liquid as well as porous mush which determines the dynamics of the flow. Undercooling affects the thermal and solutal gradients which is the driving force for thermo-solutal convection in liquid.

Faster diffusion in liquid when compared to solid, coupled with the effect of moving s/l interface and convection in liquid makes an accurate description of the composition profile and eventually the diffusion length in liquid difficult. Most of the analytical models present in the literature do not account for these phenomena, specially liquid convection even though most of the solidification processes are significantly affected by it. The purpose of this paper is to propose a new analytical model for liquid diffusion length in multicomponent alloys which accounts for liquid convection and s/l interface motion. In the first part of this work, we compare results from equiaxed solidification model using various analytical expression for liquid diffusion length with a numerical model for a pure diffusive case. Subsequently, we propose a new liquid diffusion length model in the case of globular growth and demonstrate the importance of accouting for liquid convection and s/l interface motion. Such a diffusion length model can be applied to dendritic grain growth model but is not considered in this paper.

2. Modeling of diffusion length in volume averaged models

Locally, the growth rate of a solid grain is the velocity of the solid-liquid interface, v_i, and it depends on the difference of the solute diffusion fluxes on the solid and the liquid side of the interface, as well as on the conditions at the interface. The interface solute balance gives the interface growth velocity, v_i,

$$\left(c_l^* - c_s^*\right) v_i = -D_l \left.\frac{\partial c_l}{\partial n}\right|_i + D_s \left.\frac{\partial c_s}{\partial n}\right|_i ,$$ (1)

where D_ϕ, c_ϕ^*, and c_ϕ are the diffusion coeffecient, interfacial concentration and the concentration of phase ϕ, respectively, and $\partial/\partial n|_i$ is the gradient at the interface in the direction normal to the interface. In volume-averaged models local variations of interface velocity, concentration, etc., are not described, only quantities averaged over a representative elementary volume (REV) are considered. For equiaxed globular growth such an REV contains a population of grains. The averaged overall growth rate of all the interfaces in an REV of volume V_0 is expressed as a variation of the solid fraction, g_s, within the REV:

$$\frac{1}{V_0} \int_{A_s} v_i \, dA = \frac{\partial g_s}{\partial t} ,$$ (2)

where A_s is the solid-liquid interface surface. To average the interface balance (Eq. (1)) we need to express the average solute fluxes at the interface. This is usually done by modeling the average gradient at the interface as the difference between the interface concentration, c_ϕ^* and the REV average concentration, $\langle c_\phi \rangle^\phi$, divided by a diffusion length, δ_ϕ.

$$\frac{1}{V_0} \int_{A_k} D_\phi \left.\frac{\partial c_\phi}{\partial n}\right|_i \, dA = S_v D_\phi \frac{c_\phi^* - \langle c_\phi \rangle^k}{\delta_\phi}$$ (3)

Further, a specific surface area of the solid liquid interface, S_v, is introduced that takes into account the grain shape and the size. This model of the diffusion flux at the interface reflects the fact that in averaged models the only information on the far-field concentration that is intrinsically available is the average concentration of a phase. This is a simplification and the definition of the average diffusion length, δ_ϕ, must account for this image:

$$\delta_\phi = S_v D_\phi \left(c_\phi^* - \langle c_\phi \rangle^k\right) \left[\frac{1}{V_0} \int_{A_k} D_\phi \left.\frac{\partial c_\phi}{\partial n}\right|_i \, dA\right]^{-1}$$ (4)

The volume-averaged interface balance can be written as

$$(1 - k)c_l^* \frac{\partial g_s}{\partial t} = S_v D_l \frac{c_l^* - \langle c_l \rangle^l}{\delta_l} + S_v D_s \frac{c_s^* - \langle c_s \rangle^s}{\delta_s}$$ (5)

Together with thermodynamic relations that give the equilibrium state at the interface (c_l^* and c_s^*) and with solute balances for each phase that give the average concentrations ($\langle c_l \rangle^l$ and $\langle c_s \rangle^s$) these equations give the growth rate of the solid, $\partial g_s / \partial t$.

Because they determine the growth rate of the solid, the constitutive relations for diffusion length are key ingredients of volume-averaged solidification models. The liquid diffusion length, δ_ϕ, is also of particular importance for the quantification of the constitutional undercooling in the liquid and thus a key element for the description of the coupling with nucleation and for structural transitions, such as the columnar-to-equiaxed transition.

To model the effective averaged quantities δ_ϕ and S_v the conception of an average grain is often used. We image the average grain as a single grain growing in a confinement that corresponds to the volume N_v^{-1}, where N_v is the population density of the grains in the REV, i.e., the number of grains per unit volume. For globular solidification a convenient image of an average grain is a spherical grain growing in a sphere of radius $R_f = (3/(4\pi N_v))^{-1/3}$, as shown in Fig. 1. Zero flux conditions on the outer sphere imply a periodic arrangement, however the geometry is simplified to spherical in order to allow for the assumption of spherical symmetry. Local thermodynamic equilibrium is assumed at the solid-liquid interface.

3. Models for purely diffusive growth

3.1. Overview of model formulations

In literature, various models have been proposed to model the liquid diffusion length for a growing spherical grain in pure diffusive growth and an overview of these models is provided in Table 1. All these models assume that the grain grows axisymmetrically within a spherical confinement. However, they vary on the assumptions with regards to the description of the grain confinement and on some other aspects of the physical phenomena involved. In Table 1, $\delta_v = D_l / v_i$ and Pe$=R_f v_l / D_l$ (flow Péclet number).

Table 1
Liquid diffusion length models for spherical grain/envelope for pure diffusion

Reference	Expression for δ_l
Fixed interface models	
Ni & Beckermann [9]	R^*
Wu & Ludwig [10]	
Wu et al. [11]	$R^* \left(1 - \frac{R^*}{R_f} \right)$
Mobile interface models	
Wu & Ludwig [12]	$\min\left(\delta_v, R^*, R_f - R^* \right)$
Wang & Beckermann [5]	$\frac{R_f}{Pe} \left\{ 1 - 3 \left(\frac{R_f}{R^*} \right)^3 \exp\left(-Pe \frac{R^*}{R_f} \right) \int_{R^*/R_f}^1 \left[x^2 \exp\left(\frac{Pe(R^*/R_f)^2}{x} \right) \right] dx \right\}$
Martorano et al. [13]	$\frac{R^{*2}}{(R_f^3 - R^{*3})} \left\{ \exp\left(-\frac{R_f - R^*}{\delta_v} \right) \left(\delta_v^2 + R_f \delta_v - R_f^2 \right) - \left(\delta_v^2 + R^* \delta_v - \frac{R_f^3}{R} \right) + \frac{R_f^3}{\delta_v} \exp\left(\frac{R^*}{\delta_v} \right) \left[E_1 \left(\frac{R_f}{\delta_v} \right) - E_1 \left(\frac{R^*}{\delta_v} \right) \right] \right\}$
Tveito et al. [14, 15]	$\left\{ \frac{1}{R^*} + \frac{\frac{R_f^2 - R^{*2}}{2\delta_v}}{\frac{R_f^2 - R^{*2}}{2} - \delta_v \left(R^* + \delta_v - (R_f + \delta_v) \exp\left(-\frac{R_f - R^*}{\delta_v} \right) \right)} \right\}^{-1}$
Guillemot & Gandin [16]	Post computation from an analytical solution for liquid solute profile

The diffusion length models can be classfied into two categories: i) *fixed interface* models and ii) *mobile interface* models. These models assume the composition profile normal to the s/l interface to be quasi-steady as the solutal Péclet numbers encountered during most solidification processes are small. In the *fixed interface* models, interface motion is neglected. They are therefore expected to be applicable only in situations with slow interface
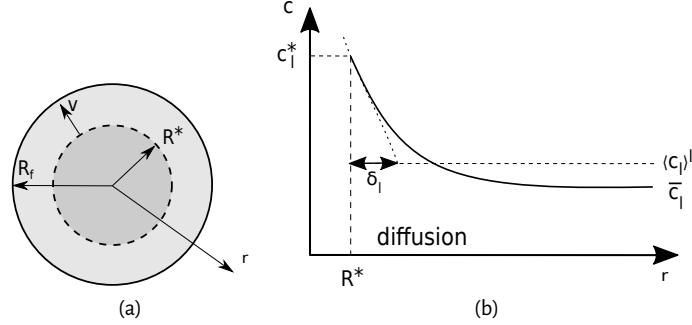
Figure 1: Schematic representation of solute profile in the extragranular liquid for pure diffusion

motion, i.e., at very low Péclet numbers. The diffusion length correlation used by Ni & Beckermann [9] and Wu & Ludwig [10], $\delta_l = R^*$, corresponds to the diffusive steady state growth of a spherical crystal in an infinite melt. Thus, the model does not account for solutal confinement, i.e. impingement of the solutal fields due to presence of neighbouring grains. Wu *et al.* [11] modified the relation to account for solutal impingement as the grain radius approaches the final radius, R_f. In other words, the system that these constitutive laws are approximating is given by the following diffusion equation and boundary conditions:

$$0 = \frac{D_l}{r^2} \frac{\partial}{\partial r} \left[r^2 \frac{\partial c_l}{\partial r} \right] \text{ with } \begin{cases} c_l(R^*) = c_l^* \\ c_l(\infty) = c_0 \quad\quad \text{Ni \& Beckermann [9] and Wu \& Ludwig [10]} \\ c_l(R_f) = \langle c_l \rangle^l \quad \text{Wu \textit{et al.}[11]} \end{cases} \tag{6}$$

Wu & Ludwig [12] also have used a hybrid diffusion length correlation which limits the diffusion length to $\left(R_f - R^* \right)$ towards the later stages of solidification. These liquid diffusion length models do not impose any condition on the solute mass conservation, which can result in issues in simulating the end of solidification. The solute balance in the liquid phase, neglecting diffusion in the solid phase is

$$g_l \frac{\partial \langle c_l \rangle^l}{\partial t} = \left(c_l^* - \langle c_l \rangle^l \right) \left[\frac{\partial g_l}{\partial t} + \frac{D_l S_v}{\delta_l} \right] = \left(c_l^* - \langle c_l \rangle^l \right) \left[-S_v v_i + \frac{D_l S_v}{\delta_l} \right] \tag{7}$$

Imposing the condition $\dfrac{\partial \langle c_l \rangle^l}{\partial t} > 0$ leads to $\left(\delta_l < D/v_i \right)$. This conditions poses an upper limit on all *fixed interface* diffusion length models. Not limiting the liquid diffusion length results in the solute depletion of the extragranular liquid for an alloy with $k < 1$. However, as mentioned by Wang and Beckermann [17], this relationship should not be considered as a correlation for liquid diffusion length as the assumptions on which the expression is based may not be generally valid. Further, as no liquid enrichment occurs, correction procedure are required to simulate the end of solidification.

The second class of models referred to as *mobile interface* considers a moving s/l interface with a finite growth velocity v_i. The models of Wang & Beckermann [5], Martorano *et al.* [13] and Tveito *et al.* [14,15] solve the diffusion equation in spherical symmetry, assuming quasi-steady state in the moving coordinate system fixed to the solid surface. The diffusion equation and the conditions imposed in all moving interface models are

$$-v_i \frac{\partial c_l}{\partial r} = \frac{D_l}{r^2} \frac{\partial}{\partial r} \left[r^2 \frac{\partial c_l}{\partial r} \right] \text{ with } \begin{cases} c_l(R^*) = c_l^* \\ \langle c_l \rangle^l = \frac{1}{\frac{4}{3}\pi \left(R_f^3 - R^{*3} \right)} \int_{R^*}^{R_f} c_l(r) 4\pi r^2 \, dr \end{cases} \tag{8}$$
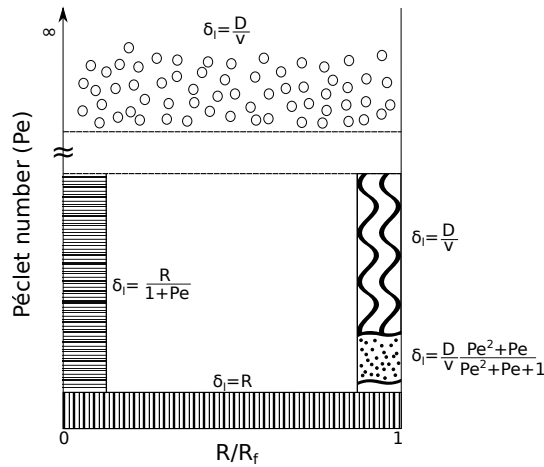
Figure 2: Schematic representation of the liquid diffusion length obtained from the model of Tveito *et al.* [14, 15] for various limiting cases.

Modification of $\langle c_l \rangle^l$ during solidification accounts for the solutal impingement effect. The three models differ in the assumptions, however, which results in different relations for diffusion length. Wang & Beckermann [5] is originally proposed for dendritic equiaxed grains. However, the dendritic grain along with the intra-granular liquid is formulated as a growing spherical envelope, due to which the resulting diffusion length expression is also applicable to globular grains. They assume that in the reference frame of the moving interface, the liquid moves at a radial velocity $-v(r)$, whose distribution is given by

$$v(r) = -v_i \left(\frac{R^*}{r} \right)^2 \tag{9}$$

Tveito *et al.* [14, 15] hypothesize that the evolution of composition with time in the reference frame of the moving interface is proportional to velocity, v_i, and to the deviation from equilibrium, $\left(c_l - \langle c_l \rangle^l \right)$. Martorano *et al.* [13] make no further simplifying assumptions.

All of these models inherently satisfy the condition $\left(\delta_l < D_l / v_i \right)$ and this is also shown in Fig. 2 which highlights the liquid diffusion length obtained from the model of Tveito *et al.* [14, 15] for various limiting cases. For very low Péclet numbers, the liquid diffusion length always approaches the grain radius R^*. As the Péclet number increases, for low solid fraction, the liquid diffusion length roughly decreases to $\frac{R^*}{1+Pe}$. For high solid fractions and high Péclet number, the liquid diffusion length approaches D_l / v_i. Guillemot and Gandin [16] proposed a steady state analytical solution for isothermal 1D growth of s/l interface in an undercooled melt controlled by multicomponent diffusion in liquid phase. The model was extended to simulate equiaxed globular solidification by incorporating a far field composition $\bar{c}_l$ such that the second condition in Eq. 8 is satisfied. This approach was validated by 1D Landau transform based numerical simulations. The analytical solution for the composition profile in the liquid phase can be used to compute the liquid diffusion length. The model of Tveito *et al.* [14, 15] is the only model that accounts for liquid convection by using a stagnant film model which will be discussed later in this article. Table 2 highlights the primary phenomena accounted for by the various liquid diffusion length models as well as the name used later in the article to refer to the models.

4. Comparison of models

The globular equiaxed growth model has been applied to simulate the solidification of a ternary Fe-1 wt.% C -10 wt.% Cr alloy. The simulations are performed with the various correlations for the liquid diffusion length and

Table 2
Phenomena captured by different liquid diffusion length models for spherical grains

Reference	s/l interface movement	Grain interaction	Name
Ni & Beckermann [9]	✗	✗	Ni1991
Wang & Beckermann [5]	✓	✓	Wang1993
Martorano *et al.* [13]	✓	✓	Martorano2003
Wu *et al.* [11]	✗	✓	Wu2013
Tveito *et al.* [14, 15]	✓	✓	Tveito2012
Guillemot & Gandin [16]	✓	✓	Guillemot2015
Wu *et al.* [12]	✗	✓	Wu2019

compared with the results from Guillemot2015. As the Guillemot2015 approach has already been validated with numerical simulations, comparing the solidification results with numerical models such as Thuinet and Combeau [8] is deemed unnecessary. The phase diagram is linearized. Constant values for the liquidus slope $m_l^i = \partial T_l / \partial c_l^{*i}$ and partition coefficient k^i are proposed for each solute species i. These values are listed in Table 3 and are obtained from Thermo-Calc® (TCFE8 databse) at the liquidus temperature of the alloy. Simulation parameters for the solidification simulation are given in Table 4. Two sets of grain densities are used so as to study a wider domain of solidification conditions. For lower grain densities, R_f is higher. In such cases, the growth rate is higher due to lower enrichment of the liquid and the interaction between grains occur at a later stage of solidification. Higher grain number density results in lower growth rate. Sufficiently small values for the diffusion coefficients in the solid phase are imposed such that diffusion in solid phase is negligible as the Guillemot & Gandin [16] model does not account for diffusion in the solid phase.

Table 3
Thermophysical properties of Fe-1 wt.% C - 10 wt.% Cr alloy

Property	Symbol	Units	Value
Partition coeff. (C)	k_p	-	0.39
Partition coeff. (Cr)	k_p	-	0.75
Liquidus slope (C)	m_l	Kwt.%$^{-1}$	−65.0
Liquidus slope (Cr)	m_l	K/wt.%$^{-1}$	−2.0
Solid diffusion coeff. (C)	D_s	m^{2}s^{-1}	1×10^{-13}
Liquid diffusion coeff. (C)	D_l	m^{2}s^{-1}	3×10^{-8}
Solid diffusion coeff. (Cr)	D_s	m^{2}s^{-1}	1×10^{-13}
Liquid diffusion coeff. (Cr)	D_l	m^{2}s^{-1}	3×10^{-9}
Melting point of pure substance	T_f	°C	1527
Liquid density	ρ_l	kgm^{-3}	7600
Latent heat	L_f	Jkg^{-1}	2.5×10^5
Specific heat capacity	C_p	Jkg^{-1}K^{-1}	700

High grain number density

The final grain number density of $R_f = 1.3365 \times 10^{-4}$ m corresponds to equiaxed grain number density of 10^{11} [m^{-3}]. The liquidus and solidus temperature of this alloy is 1442°C and 1333.7°C with a solidification temperature range of 108.3°C. The temperature evolution is the result of energy balance between the latent heat released due to growth of the globular grains and the heat extracted from the system, the difference is directly linked to the s/l interface velocity and hence to the diffusion length. The difference in the recalescence behaviour shown

Table 4
Simulation parameters

Parameters	Symbol	Units	Value
Final grain size - Case A	R_{f}	m	1.3365×10^{-4}
Final grain size - Case B	R_{f}	m	6.2035×10^{-4}
Solidification end temperature - Fe-1 wt.% C - 10 wt.% Cr	T_{sol}	°C	1250
Time step	Δt	s	1×10^{-3}
Nucleation radius	R_0	m	0.5×10^{-6}
Nucleation undercooling	ΔT_{nuc}	°C	1×10^{-3}
Heat extraction rate	$\dot{H}$	Js^{-1}kg^{-1}	11666.67

in Fig.3 is a direct consequence of the liquid diffusion lengths obtained from various models as presented in Fig. 4. The red curve corresponds to the Guillemot2015 solution which is the reference solution. It should be pointed out that the results shown correspond to the early stages of solidification up to a point after recalescence as this is where the solidification path departs appreciably from the standard Scheil solidification. All the models predict a liquid diffusion length equal to R^* during the early stages of solidification in concurrence with Fig. 2. However, as the Péclet number increases, the results from *mobile interface* and *fixed interface* differ. The *mobile interface* models describe the liquid diffusion length quite close to the Guillemot2015 solution. These models slightly over-predict the liquid diffusion length as transient effects are not accounted for. Martorano2003 produces the closest result to reference solution and this is attributed to the fact that Martorano2003 do not make simplifying assumptions and the solute profile obtained from the solution of the diffusion equation is the most accurate for a quasi steady state. The *fixed interface* models introduce significant error as they do not account for the interface motion which results in the over-prediction of the liquid diffusion length and slower solidification kinetics. As solidification progresses, the solutal impingement effect results in the deviation of the liquid diffusion length from R^* for Wu2013. However, Ni1993 and Wu2019 continue with R^* until the system size effect is enforced which causes the sudden transition from R^* to $R_{\mathrm{f}} - R^*$ for Wu2019.
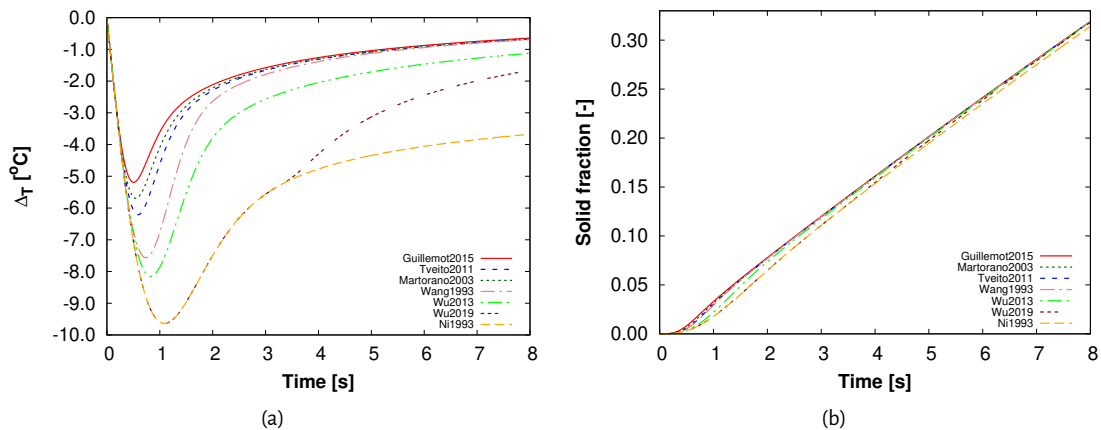
Figure 3: Evolution of (a) undercooling and (b) solid fraction with time

The *fixed interface* models predict the same liquid diffusion lengths for carbon and chromium unlike the *mobile interface* models which take into account the effect of diffusivity of the elements on their respective liquid diffusion lenghts. For a multicomponent alloy, accounting for different diffusivities of the solute elements is critical as the interface motion is controlled by the diffusion of the slower solute element. In the present case, the interface
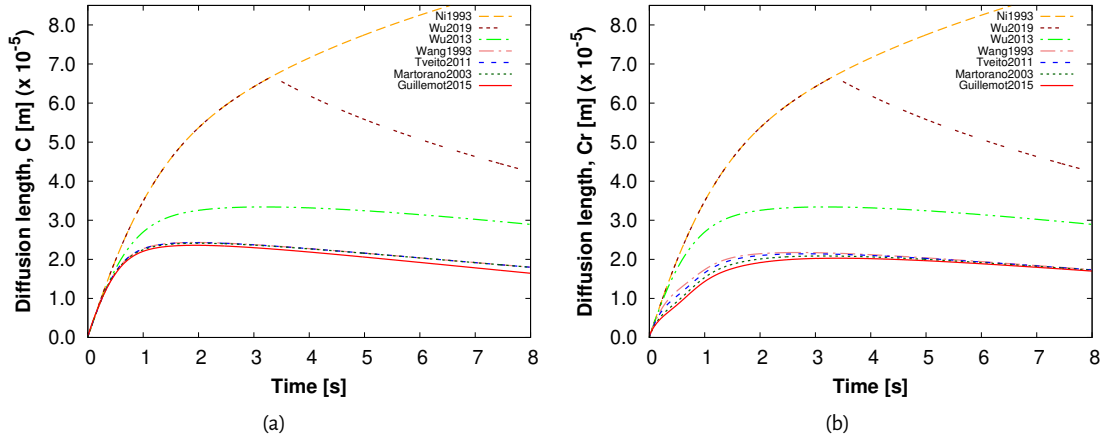
Figure 4: Evolution of liquid diffusion length for (a) carbon and (b) chromium with time
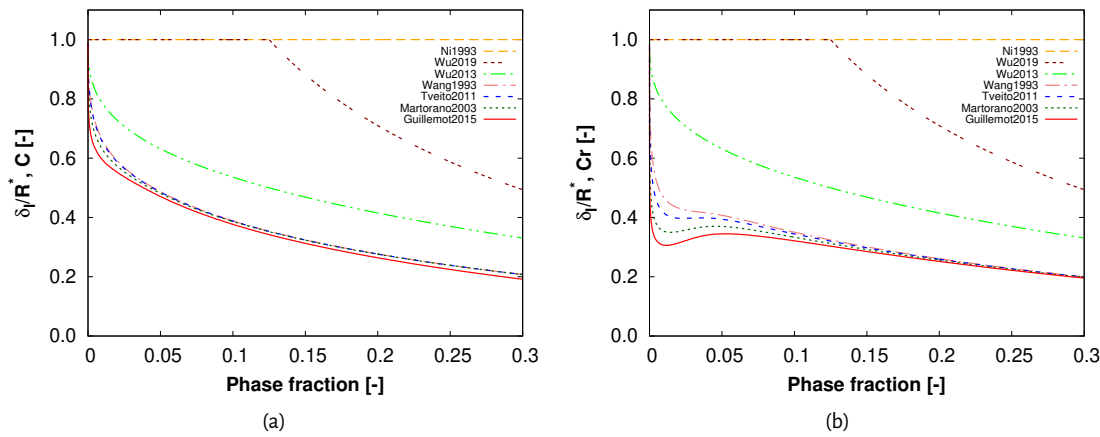
Figure 5: Evolution of δ_l / R^* as solidificaton progresses

motion is controlled by the diffusion of chromiun whose liquid diffusivity is an order lower that that of carbon and can be observed in fig. 5. Lower the value of δ_l / R^*, higher is the impact of the solutal advection and diffusion, solutal impingement or system size effect. For the diffusion length models of Ni1993 and Wu2019, during the early stages of solidification, the $\delta_l / R^* = 1$. There is no system size effect or solutal impingement effect as R^* corresponds to solid sphere growing in an infinite melt with the far field composition fixed at c_0. The diffusion length for Wu2019 changes from R^* to $R_f - R^*$ which causes the sudden transition as the system size effect is enforced. The system size effect and the solute impingement results in a monotonic decrease in δ_l / R^* for Wu2013 and the slope of the curve is given by $-1/3 g_s^{2/3}$. As the *mobile interface* models account for solutal advection, the behaviour of the δ_l / R^* varies for the two solute elements due to difference in Péclet numbers. Higher the Péclet number, lower is the δ_l / R^* as δ_l roughly corresponds to $\frac{R^*}{1+\text{Pe}}$ during this regime as shown in Fig. 2. Higher value of Péclet number for chromium results in lower value of δ_l / R^* compared to carbon during early stages of solidification. In the present solidification model, the end of recalescence corresponds to the beginning of solutal impingement. For a multicomponent system, it is the faster diffusing element for which the solute layer reaches the grain limit R_f at the end of recalescence. Fig. 6 shows the normalized (c_l / c_0) solute profile in the liquid after
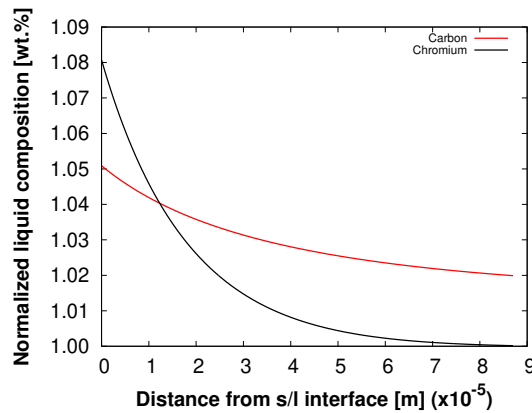
Figure 6: Solute profile in the extragranular liquid for (a) carbon and (b) chromium at the end of recalescence

recalescence when solutal impingement effect comes into effect for carbon. This results in the monotonic decrease in δ_l/R^* of carbon as opposed to chromium where the reduction in solutal advection due to reduction in s/l interface velocity results in increase of δ_l/R^* before the solutal impingement effect is enforced.
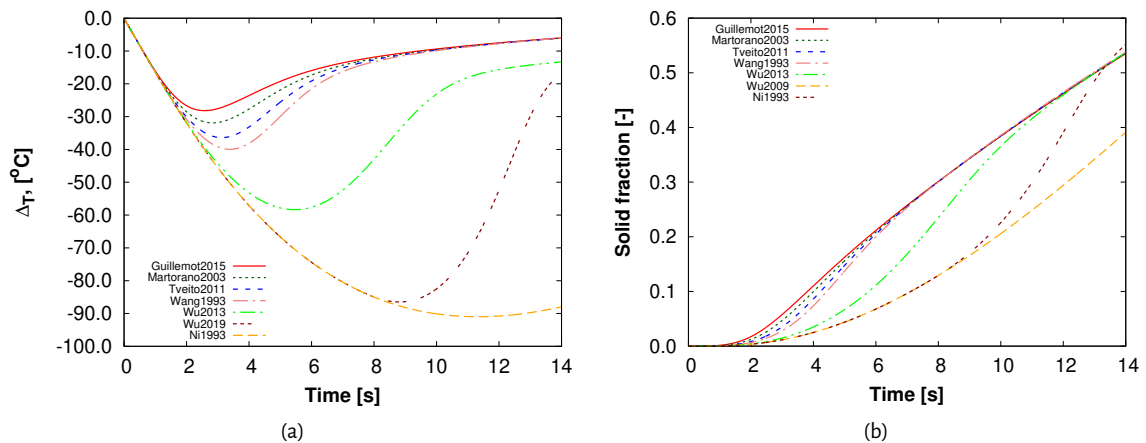
Figure 7: Evolution of (a) undercooling and (b) solid fraction with time

Low grain number density

In the second case, the final grain number density of $R_f =$ of 6.2035×10^{-4} m corresponds to equiaxed grain number density of 10^9 [m^{-3}]. The s/l interface velocity is higher when compared to a high grain number density case, which results in a larger R^*, hence a larger liquid diffusion length during the early stages of solidification. Thus, the slower solidification kinetics results in extraction of more sensible heat and less latent heat causing a larger undercooling as shown in Fig. 7a. Similar to the previous results, the *mobile interface* models perform better when compared to *fixed interface* models as shown in Fig. 8. However, the relative error increases as the Fourier number is decreased. The undercooling for *mobile interface* models vary in the range of 30-40 ºC and 60-90 ºC for *fixed interface* models during recalescence. These high values of undercooling result in significant deviation of the solidification kinetics from Guillemot2015 as shown in Fig. 7b. Fig. 8a and 8b show the liquid diffusion lengths for carbon and chromium respectively. The liquid diffusion length of carbon behaves on similar lines as for the
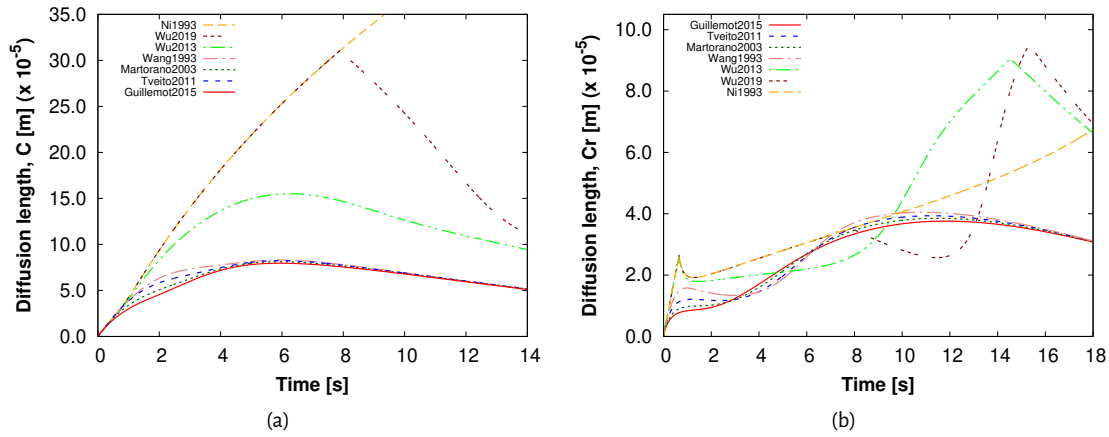
Figure 8: Evolution of liquid diffusion length for (a) carbon and (b) chromium with time
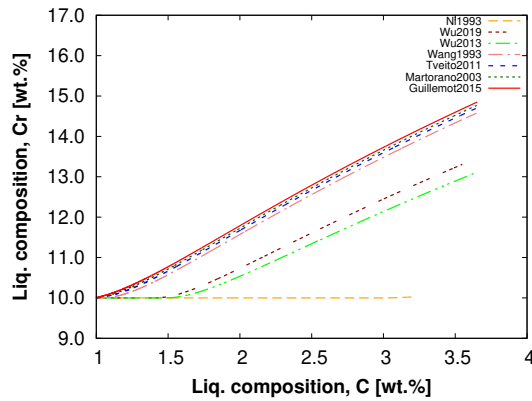
Figure 9: Liquid composition evolution as solidification progresses

case with higher Fourier number. However, for chromium, the difference between the liquid diffusion lengths obtained from *mobile interface* and *fixed interface* have significant difference in their behaviour. The liquid diffusion length for chromium obtained from *mobile interface* models are close to the reference solution of Guillemot2015. The *fixed interface* models predict a diffusion length closer to R^* at very low values of solid fraction which does not satisfy the solute mass conservation for chromium. In accordance with Eq. 7, the liquid diffusion length switches over to D_l/v and steady state is reached with respect to chromium ($\Omega = 1$). Fig. 9 shows the solidification path for the alloy. No chromium segregation occurs for the *fixed interface* models until the system size effect is enforced on Wu2013 and Wu2019.

The solidification cases demonstrated above show the various limitations of the *fixed interface* models. The *mobile interface* model of Martorano2005 predict the diffusion length closest to the reference solution of Guillemot2015 in all the cases. Hence, it is the ideal diffusion length model to be used for various solidification models. However, the model is limited to pure diffusion which limits its applicability. Thus, we propose a modification to Martorano2005 to account for liquid convection. Stagnant film model is used on similar lines as used for Tveito2011 and will be discussed in the next section.

Conclusion

We can conclude that the fixed interface models are not suitable for the quantification of the diffusion length and of the solidification rate in realistic conditions (in terms of grain number density, cooling rate and material properties). *Mobile interface* models provide a fairly accurate quantification of the diffusion length and of the solidification path. Nevertheless, significant differences appear in the predicted constitutional undercooling during and just after recalescence. Generally, the models tend to overestimate the undercooling. This can significantly affect the coupling of growth models with nucleation, as well as the description of structural transitions, such as globular to dendritic transition and columnar to equiaxed transition.

5. Models with convection in the liquid

5.1. Overview of model formulations

The solute boundary layer is significantly affected by liquid convection. Liquid convection results in smaller diffusion length and intensification of the diffusive flux, thus promoting enrichment of the liquid phase. Wang *et al.* [17] introduced a flow Péclet number into the diffusion length model. The models of Ni & Beckermann [9], Appolaire *et al.* [18] and Wang *et al.*(2019) [19] account for the effect of convection via a Sherwood number (Sh) which has to be chosen from experimental data. An empirical relationship for Sherwood expression as defined by Rowe and Claxton [20] which accounts for the effect of fluid flow over a sphere of fixed size is

$$\mathrm{Sh} = \mathrm{Sh}_{\mathrm{diff}} + \mathrm{Sh}_{\mathrm{conv}} = \frac{2}{1 - g_{\mathrm{s}}^{1/3}} + \frac{2}{3(1 - g_{\mathrm{s}})}\mathrm{Sc}^{\mathrm{a}}\mathrm{Re}^{\mathrm{b}} \tag{10}$$

$$\mathrm{Sc} = \frac{\nu}{D_{\mathrm{l}}}, \qquad \mathrm{Re} = \frac{g_{\mathrm{l}}(2R^*)\left|\left\langle \vec{v}_{\mathrm{l}} \right\rangle^{\mathrm{l}} - \left\langle \vec{v}_{\mathrm{s}} \right\rangle^{\mathrm{s}}\right|}{\nu} \tag{11}$$

$$a = \frac{1}{3}, \qquad b = \frac{2\mathrm{Re}^{0.28} + 4.65}{3\left(\mathrm{Re}^{0.28} + 4.65\right)} \tag{12}$$

where Sc is the Schmidt number, Re is the Reynolds number, ν is the kinematic viscosity, $\left\langle \vec{v}_{\mathrm{l}} \right\rangle^{\mathrm{l}}$ and $\left\langle \vec{v}_{\mathrm{s}} \right\rangle^{\mathrm{s}}$ is the intrinsic velocity of the solid and liquid phase respectively, a and b experimentally determined coefficients. The diffusion length around a growing sphere with a quasi steady solute profile is linked to the Sherwood number by

$$\delta_{\mathrm{l}} = 2R^*/\mathrm{Sh} \tag{13}$$

In the absence of convection (i.e., Re=0), Sherwood number $\rightarrow$ 2 and the diffusion length tends to R^*.

The diffusion length models accounting for liquid convection have been listed in Table 5. Most of them are *fixed interface* model that have been corrected for convection. Furthermore, the model of Appolaire *et al.* [18] is formulated for a single grain and does not account for solutal interactions. The only moving interface model with convection is the one by Tveito *et al.* [14, 15]. It employs the concept of a stagnant film, which will be detailed in the next section and used in a new stagnant-film model formulation.

5.2. New stagnant-film model

The comparison of diffusive models in Section 4 has shown the various limitations of the *fixed interface* models. The *mobile interface* model of Martorano2005 predict the diffusion length closest to the reference solution of Guillemot2015 in all the cases. Hence, it is the ideal diffusion length model to be used for various solidification models. However, the model is limited to pure diffusion which limits its applicability. Thus, we propose a modification to Martorano2005 to account for liquid convection. The stagnant film model is introduced on similar lines as used in Tveito2011 and will be discussed in this section.

Table 5
Liquid diffusion length models for spherical grain/envelope

Reference	Expression for δ_l	Name
Fixed interface models		
Ni & Beckermann [21]	$R^* \left[\dfrac{1}{1-g_s^{1/3}} + \dfrac{Sc^{1/3}Re^a}{3g_l} \right]^{-1} \quad a = \dfrac{2Re^{0.28}+4.65}{3(Re^{0.28}+4.65)}$	Ni1993
Wang & Beckermann [17]	$\dfrac{2R}{2+0.865\left(\frac{C}{g_l}\right)^{1/3}Pe^{i\,1/3}} \quad C = \dfrac{2+\frac{4}{3}(g_s)^{5/3}}{2-3g_s^{1/3}+3g_s^{5/3}-2g_s^2}$	Wang1996
Appolaire *et al.* [18]	$\mathbf{min}\left(\delta_v^i, \dfrac{2R^*}{Sh}\right) \; Sh = 2 + 0.6Sc^{1/3}Re^{1/2}$	Appolaire2008
Wang *et al.*(2019) [19]	$\mathbf{min}\left[R^*\left[\dfrac{1}{1-(g_s)^{1/3}} + \dfrac{Sc^{1/3}Re^a}{3g_l} \right]^{-1}, \delta_v^i \right] \quad a = \dfrac{2Re^{0.28}+4.65}{3(Re^{0.28}+4.65)}$	Wang2019
Mobile interface models		
Tveito *et al.* [14, 15]	$\delta_v^i\left[\dfrac{\delta_v^i}{R^*} - \dfrac{f(R^*,\Delta)+g(R_f,R^*,\Delta)}{\delta_v^i[R^*+\delta_v^i-(R^*+\Delta+\delta_v^i)e^{-\Delta/\delta_v^i}]-f(R^*,\Delta)+(e^{-\Delta/\delta_v^i}-1)g(R_f,R^*,\Delta)} \right]^{-1}$	Tveito2011
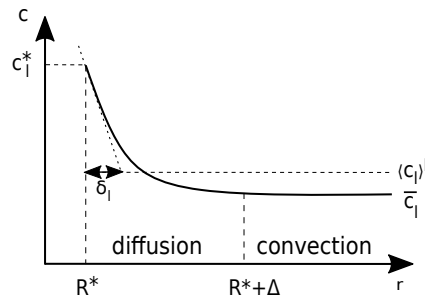
Figure 10: Schematic representation of solute profile in the extragranular liquid for diffusion with convection

The analytical solution proposed by Martorano *et al.* [13] is derived by considering the system shown in Fig. 1a. The domain consist of a spherical unit cell of radius R_f. The solid is as the center of the domain with an instantaneous radius of R^* and is growing with an outward velocity of v. The diffusion in the extragranular liquid between R^* and R_f for an element i is governed by the diffusion equation in spherical co-ordinate:

$$\frac{\partial c_l}{\partial t} = \frac{D_l}{r^2}\frac{\partial}{\partial r}\left[r^2 \frac{\partial c_l}{\partial r} \right] \tag{14}$$

where c_l is the local solute concentration and r is the radial coordinate. The solution of the above equation is:

$$c_l(r) = B - A\left(\frac{\exp\left(-\frac{rv}{D_l^i}\right)}{\left(\frac{rv}{D_l^i}\right)} - E_1\left(\frac{rv}{D_l^i}\right) \right) \tag{15}$$

where A and B are constants that depend on the boundary conditions. The liquid diffusion length to account for convection is formulated using stagnant film model [22] where the extragranular liquid is separated into two regions as shown in Fig.10a. The solute transfer in the stagnant film region close to the s/l interface ($r = R^*$) is assumed to be controlled by diffusion and is defined by a thickness Δ. Convection dominates beyond this point

and the extragranular liquid composition is assumed to be homogenenous. The conditions imposed are given in Eq. 8 along with the additional boundary condition

$$c_1 = \bar{c}_1 \quad \text{at} \quad r = \left(R^* + \Delta \right) \tag{16}$$

For the solute profile given by Eq. 15, the new expression for the diffusion length is

$$\delta_1 = \frac{R^{*2}\exp\left(\frac{R^*}{\delta_v}\right)\mathbf{C}}{\delta_v} \tag{17}$$

where $\mathbf{C}$ is

$$\mathbf{C} = \left(\frac{\exp\left(-\frac{R^*}{\delta_v}\right)}{\left(\frac{R^*}{\delta_v}\right)} - \mathrm{E}_1\left(\frac{R^*}{\delta_v}\right) \right) - \frac{\left(R_f^3 - R_c^3\right)}{\left(R_f^3 - R^{*3}\right)}\left[\left(\frac{\exp\left(-\frac{R_c}{\delta_v}\right)}{\left(\frac{R_c}{\delta_v}\right)} - \mathrm{E}_1\left(\frac{R_c}{\delta_v}\right) \right)\right] - \frac{\delta_v^3}{\left(R_f^3 - R^{*3}\right)}$$

$$\left[\left[\exp\left(-\frac{R_c}{\delta_v}\right)\left(\left(\frac{R_c}{\delta_v}\right)^2 - \frac{R_c}{\delta_v} - 1\right) - \left(\frac{R_c}{\delta_v}\right)^3\mathrm{E}_1\left(\frac{R_c}{\delta_v}\right)\right] - \left[\exp\left(-\frac{R^*}{\delta_v}\right)\left(\left(\frac{R^*}{\delta_v}\right)^2 - \frac{R^*}{\delta_v} - 1\right) - \left(\frac{R^*}{\delta_v}\right)^3\mathrm{E}_1\left(\frac{R^*}{\delta_v}\right)\right]\right]$$
$$\tag{18}$$

and $R_c = (R^* + \Delta)$. An in-detailed derivation of the diffusion length expression can be found in the appendix. Using Eq. 6 and imposing the boundary condition $c_1(R_c) = \bar{c}$, we get we get

$$\delta_1 = R^* \left[1 - \frac{R^*}{R^* + \Delta} \right] \tag{19}$$

Substituting Eq. 13 into 19, the expression for the stagnant film thickness is

$$\Delta = R^* \left[\frac{\frac{2}{\mathrm{Sh}}}{1 - \frac{2}{\mathrm{Sh}}} \right] , \tag{20}$$

where the Sherwood number is given by Eqs. (10–12).

6. Comparison of models with convection

The modified Martorano model will be compared to other liquid diffusion length models accounting for convection. The simulation setup is the case B for Fe-1 wt.% C -10 wt.% Cr alloy. A velocity difference between solid and liquid, $\left(\left|\langle \vec{v}_1 \rangle^1 - \langle \vec{v}_s \rangle^s\right|\right)$, of 0.5mm/s is imposed corresponding to a weak liquid flow around the solid grains. As the model of Guillemot and Gandin [16] currently does not accout for liquid convection, there is no reference solution. However, as the relative velocity between the solid and liquid phase is small, the result is expected to be closer to the solution for pure diffusive case.

Fig. 11a shows the undercooling obtained from various liquid diffusion length models. The modified Martorano model predicts a lower undercooling as liquid convection is introduced when compared to the result for the pure diffusive case from the same model. This is a direct consequence of the lower liquid diffusion length obtained for carbon and chromium as shown in Fig. 12. The modified Martorano model perfoms much better when compared to other liquid diffusion length models which account for liquid convection. The model of Appolaire2008 predicts a much larger undercooling and can be attributed to the Sherwood number approximation used. Similar to case B for Fe-1 wt.% C -10 wt.% Cr alloy for the pure diffusion case, the fixed interface models predict a liquid diffusion length given by D_1/v_i for chromium after the initial stages of solidification. This results in no segregation in chromium for the *fixed interface* models.
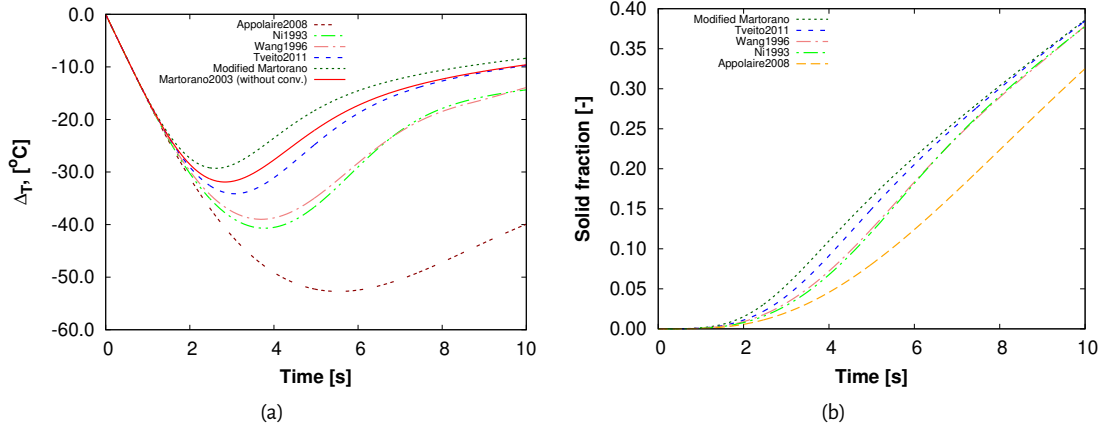
Figure 11: Evolution of (a) undercooling and (b) solid fraction with time. $\left(\left| \langle \vec{v}_l \rangle^l - \langle \vec{v}_s \rangle^s \right| \right) = 0.5$ mm/s.
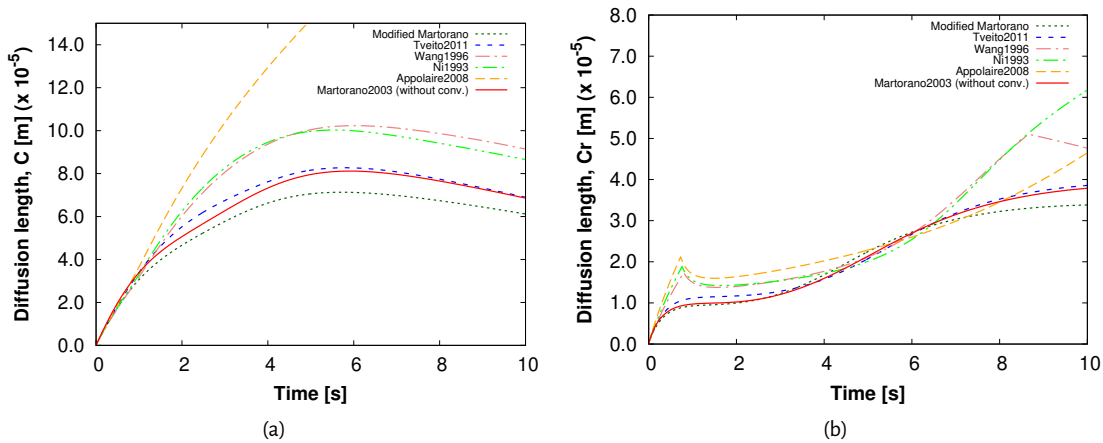
Figure 12: Evolution of liquid diffusion length for (a) carbon and (b) chromium with time. $\left(\left| \langle \vec{v}_l \rangle^l - \langle \vec{v}_s \rangle^s \right| \right) = 0.5$ mm/s.

7. Conclusion

In order to accurately describe the liquid diffusion on microscopic level, an accurate apporximation of the diffusion length is required. Various analytical liquid diffusion length models available in literature have been presented. These models are based on various assumptions which limit their application to a wide range of solidification conditions. The models are studied and their results have been compared against the exact solution for two case of pure diffusion. The study shows that the diffusion length model impact the undercooling and the solutal enrichment of the liquid phase. Accouting for the movement of the solid-liquid interface is critical. The diffusion length model proposed by Martorano *et al.* [13] produces results closest to the exact solution. However, the model is applicable only for pure diffusion case. Thus, the model is extended to account for liquid convection by using the stagnant film model [22]. This extension allows for employing the Martorano *et al.* [13] with volume-average based solidification models which are used to simulate solidification of large ingots, where liquid convection plays a crucial role.

Appendix

A. Description of variables used in the diffusion length expressions

$$\delta_v^i = D_1^i / v \qquad\qquad \mathrm{Pe}^i = R_f / \delta_v^i \qquad\qquad \mathrm{Re} = \frac{\rho u (2R^*) g_1}{\mu}$$

$$f\left(R^*, \Delta\right) = \frac{(R^* + \Delta)^2 - R^{*2}}{2} \qquad g\left(R_f, R^*, \Delta\right) = \frac{R_f^3 - (R^* + \Delta)^3}{3\left(R^* + \Delta\right)} \qquad \Delta = \min\left[\left(R_f - R^*\right), \frac{2R^*}{\mathrm{Sh}_{\mathrm{conv}}^i}\right]$$

· Pe - Peclet number

· Re - Reynolds number

B. Application of stagnant film model to the diffusion length expression of Martorano *et al.* [13]

The domain consist of a spherical unit cell of radius R_f. The solid is as the center of the domain with an instantaneous radius of R^* and is growing with an outward velocity of v. The diffusion in the extragranular liquid between R^* and R_f for an element i is governed by the solute conservation equation:

$$\frac{\partial c_1}{\partial t} = \frac{D_1^i}{r^2} \frac{\partial}{\partial r}\left[r^2 \frac{\partial c_1}{\partial r}\right] \tag{21}$$

where c_1 is the local solute concentration and r is the radial coordinate.

The solution of the above equation can be given by:

$$c_1(r) = B - A\left(\frac{\exp\left(-\frac{rv}{D_1^i}\right)}{\left(\frac{rv}{D_1^i}\right)} - \mathrm{E}_1\left(\frac{rv}{D_1^i}\right)\right) \tag{22}$$

where E_1 is the exponential integral function defined by,

$$\mathrm{E}_1 = \int_x^\infty \frac{\exp(-t)}{t}\, \mathrm{dt}. \tag{23}$$

For the configuration shown in Fig. 10, the boundary conditions are as follows:

$$c_1^* = B - A\left(\frac{\exp\left(-\frac{R^* v}{D_1^i}\right)}{\left(\frac{R^* v}{D_1^i}\right)} - \mathrm{E}_1\left(\frac{R^* v}{D_1^i}\right)\right) \tag{24}$$

$$\bar{c}_1 = B - A\left(\frac{\exp\left(-\frac{(R^* + \Delta)v}{D_1^i}\right)}{\left(\frac{(R^* + \Delta)v}{D_1^i}\right)} - \mathrm{E}_1\left(\frac{(R^* + \Delta)v}{D_1^i}\right)\right) \tag{25}$$

For the sake of clarity, $(R^* + \Delta)$ will be referred to as R_c and (D_1^i/v) as δ_v. The final condition states the conservation of mass in the liquid phase:

$$\frac{4\pi(R_f^3 - R^{*3})\langle c_1\rangle^l}{3} = \int_{R^*}^{R_c} c_1(4\pi r^2).dr + \int_{R_c}^{R_f} \bar{c}_1(4\pi r^2).dr \tag{26}$$

Subtracting Eqn. 25 from Eqn. 24, we obtain:

$$\bar{c}_l = c_l^* - A\left[\left[\frac{\exp\left(-\frac{R_c}{\delta_v}\right)}{\left(\frac{R_c}{\delta_v}\right)} - E_1\left(\frac{R_c}{\delta_v}\right)\right] - \left[\frac{\exp\left(-\frac{R^*}{\delta_v}\right)}{\left(\frac{R^*}{\delta_v}\right)} - E_1\left(\frac{R^*}{\delta_v}\right)\right]\right] \tag{27}$$

Integrating the first part on the R.H.S of Eqn. 26,

$$\int_{R^*}^{R_c} c_1(4\pi r^2).dr = 4\pi \int_{R^*}^{R_c}\left[B - A\left(\frac{\exp\left(-\frac{r}{\delta_v}\right)}{\left(\frac{r}{\delta_v}\right)} - E_1\left(\frac{r}{\delta_v}\right)\right)\right](r^2).dr$$

$$= \frac{4\pi}{3}\left(R_c^3 - R^{*3}\right)\left[c_1^* + A\left(\frac{\exp\left(-\frac{R^*}{\delta_v}\right)}{\left(\frac{R^*}{\delta_v}\right)} - E_1\left(\frac{R^*}{\delta_v}\right)\right)\right] - 4\pi A\int_{R^*}^{R_c}\left(\frac{\exp\left(-\frac{r}{\delta_v}\right)}{\left(\frac{r}{\delta_v}\right)} - E_1\left(\frac{r}{\delta_v}\right)\right)(r^2).dr \tag{28}$$

Further. integrating the second term on the R.H.S, we introduce a change of variable

$$r = \delta_v u \implies dr = \delta_v du \tag{29}$$

$$4\pi A\int_{R^*}^{R_c}\left(\frac{\exp\left(-\frac{r}{\delta_v}\right)}{\left(\frac{r}{\delta_v}\right)} - E_1\left(\frac{r}{\delta_v}\right)\right)(r^2).dr = 4\pi\delta_v^3 A\int_{\frac{R^*}{\delta_v}}^{\frac{R_c}{\delta_v}}\left(\frac{\exp(-u)}{(u)} - E_1(u)\right)(u^2).du \tag{30}$$

$$\int\left(\frac{\exp(-u)}{(u)} - E_1(u)\right)(u^2).du = -u\exp(-u) - \exp(-u) - \frac{u^3}{3}E_1(u) + \frac{u^2}{3}\exp(-u) + \frac{2u}{3}\exp(-u) + \frac{2}{3}\exp(-u)$$

$$= \exp(-u)\left(\frac{u^2}{3} - \frac{u}{3} - \frac{1}{3}\right) - \frac{u^3}{3}E_1(u) \tag{31}$$

Using Eqn. 31 in Eqn. 30, we obtain:

$$4\pi\delta_v^3 A\left[\exp(-u)\left(\frac{u^2}{3} - \frac{u}{3} - \frac{1}{3}\right) - \frac{u^3}{3}E_1(u)\right]_{\frac{R^*}{\delta_v}}^{\frac{R_c}{\delta_v}} = \frac{4\pi\delta_v^3 A}{3}\left[\exp(-u)\left(u^2 - u - 1\right) - u^3 E_1(u)\right]_{\frac{R^*}{\delta_v}}^{\frac{R_c}{\delta_v}}$$

$$= \frac{4\pi\delta_v^3 A}{3}\left[\left[\exp\left(-\frac{R_c}{\delta_v}\right)\left(\left(\frac{R_c}{\delta_v}\right)^2 - \frac{R_c}{\delta_v} - 1\right) - \left(\frac{R_c}{\delta_v}\right)^3 E_1\left(\frac{R_c}{\delta_v}\right)\right] - \left[\exp\left(-\frac{R^*}{\delta_v}\right)\left(\left(\frac{R^*}{\delta_v}\right)^2 - \frac{R^*}{\delta_v} - 1\right) - \left(\frac{R^*}{\delta_v}\right)^3 E_1\left(\frac{R^*}{\delta_v}\right)\right]\right] \tag{32}$$

Hence, we can write:

$$\int_{R^*}^{R_c} c_1(4\pi r^2).dr = \frac{4\pi}{3}\left(R_c^3 - R^{*3}\right)\left[c_1^* + A\left(\frac{\exp\left(-\frac{R^*}{\delta_v}\right)}{\left(\frac{R^*}{\delta_v}\right)} - \mathrm{E}_1\left(\frac{R^*}{\delta_v}\right)\right)\right] -$$

$$\frac{4\pi\delta_v^3 A}{3}\left[\left[\exp\left(-\frac{R_c}{\delta_v}\right)\left(\left(\frac{R_c}{\delta_v}\right)^2 - \frac{R_c}{\delta_v} - 1\right) - \left(\frac{R_c}{\delta_v}\right)^3 \mathrm{E}_1\left(\frac{R_c}{\delta_v}\right)\right] - \left[\exp\left(-\frac{R^*}{\delta_v}\right)\left(\left(\frac{R^*}{\delta_v}\right)^2 - \frac{R^*}{\delta_v} - 1\right) - \left(\frac{R^*}{\delta_v}\right)^3 \mathrm{E}_1\left(\frac{R^*}{\delta_v}\right)\right]\right]$$

(33)

$$\int_{R_c}^{R_f} \bar{c}_1(4\pi r^2).dr = \frac{4\pi}{3}\left(R_f^3 - R_c^3\right)\left[c_l^* - A\left[\left(\frac{\exp\left(-\frac{R_c}{\delta_v}\right)}{\left(\frac{R_c}{\delta_v}\right)} - \mathrm{E}_1\left(\frac{R_c}{\delta_v}\right)\right) - \left(\frac{\exp\left(-\frac{R^*}{\delta_v}\right)}{\left(\frac{R^*}{\delta_v}\right)} - \mathrm{E}_1\left(\frac{R^*}{\delta_v}\right)\right)\right]\right]$$

(34)

Eqn. 26 is written as:

$$\frac{4\pi(R_f^3 - R^{*3})\langle c_1\rangle^l}{3} = \frac{4\pi}{3}\left(R_c^3 - R^{*3}\right)\left[c_1^* + A\left(\frac{\exp\left(-\frac{R^*}{\delta_v}\right)}{\left(\frac{R^*}{\delta_v}\right)} - \mathrm{E}_1\left(\frac{R^*}{\delta_v}\right)\right)\right] -$$

$$\frac{4\pi\delta_v^3 A}{3}\left[\left[\exp\left(-\frac{R_c}{\delta_v}\right)\left(\left(\frac{R_c}{\delta_v}\right)^2 - \frac{R_c}{\delta_v} - 1\right) - \left(\frac{R_c}{\delta_v}\right)^3 \mathrm{E}_1\left(\frac{R_c}{\delta_v}\right)\right] - \left[\exp\left(-\frac{R^*}{\delta_v}\right)\left(\left(\frac{R^*}{\delta_v}\right)^2 - \frac{R^*}{\delta_v} - 1\right) - \left(\frac{R^*}{\delta_v}\right)^3 \mathrm{E}_1\left(\frac{R^*}{\delta_v}\right)\right]\right]$$

$$+\frac{4\pi}{3}\left(R_f^3 - R_c^3\right)\left[c_l^* - A\left[\left(\frac{\exp\left(-\frac{R_c}{\delta_v}\right)}{\left(\frac{R_c}{\delta_v}\right)} - \mathrm{E}_1\left(\frac{R_c}{\delta_v}\right)\right) - \left(\frac{\exp\left(-\frac{R^*}{\delta_v}\right)}{\left(\frac{R^*}{\delta_v}\right)} - \mathrm{E}_1\left(\frac{R^*}{\delta_v}\right)\right)\right]\right]$$

$$\implies \frac{\langle c_1\rangle^l - c_l^*}{A} = \mathbf{C} = \frac{\left(R_c^3 - R^{*3}\right)}{\left(R_f^3 - R^{*3}\right)}\left(\frac{\exp\left(-\frac{R^*}{\delta_v}\right)}{\left(\frac{R^*}{\delta_v}\right)} - \mathrm{E}_1\left(\frac{R^*}{\delta_v}\right)\right) - \frac{\left(R_f^3 - R_c^3\right)}{\left(R_f^3 - R^{*3}\right)}\left[\left(\frac{\exp\left(-\frac{R_c}{\delta_v}\right)}{\left(\frac{R_c}{\delta_v}\right)} - \mathrm{E}_1\left(\frac{R_c}{\delta_v}\right)\right) - \left(\frac{\exp\left(-\frac{R^*}{\delta_v}\right)}{\left(\frac{R^*}{\delta_v}\right)} - \mathrm{E}_1\left(\frac{R^*}{\delta_v}\right)\right)\right]$$

$$-\frac{\delta_v^3}{\left(R_f^3 - R^{*3}\right)}\left[\left[\exp\left(-\frac{R_c}{\delta_v}\right)\left(\left(\frac{R_c}{\delta_v}\right)^2 - \frac{R_c}{\delta_v} - 1\right) - \left(\frac{R_c}{\delta_v}\right)^3 \mathrm{E}_1\left(\frac{R_c}{\delta_v}\right)\right] - \left[\exp\left(-\frac{R^*}{\delta_v}\right)\left(\left(\frac{R^*}{\delta_v}\right)^2 - \frac{R^*}{\delta_v} - 1\right) - \left(\frac{R^*}{\delta_v}\right)^3 \mathrm{E}_1\left(\frac{R^*}{\delta_v}\right)\right]\right]$$

(35)

$$\implies \frac{\langle c_1\rangle^l - c_l^*}{A} = \mathbf{C} = \left(\frac{\exp\left(-\frac{R^*}{\delta_v}\right)}{\left(\frac{R^*}{\delta_v}\right)} - \mathrm{E}_1\left(\frac{R^*}{\delta_v}\right)\right) - \frac{\left(R_f^3 - R_c^3\right)}{\left(R_f^3 - R^{*3}\right)}\left[\left(\frac{\exp\left(-\frac{R_c}{\delta_v}\right)}{\left(\frac{R_c}{\delta_v}\right)} - \mathrm{E}_1\left(\frac{R_c}{\delta_v}\right)\right)\right]$$

$$-\frac{\delta_v^3}{\left(R_f^3 - R^{*3}\right)}\left[\left[\exp\left(-\frac{R_c}{\delta_v}\right)\left(\left(\frac{R_c}{\delta_v}\right)^2 - \frac{R_c}{\delta_v} - 1\right) - \left(\frac{R_c}{\delta_v}\right)^3 \mathrm{E}_1\left(\frac{R_c}{\delta_v}\right)\right] - \left[\exp\left(-\frac{R^*}{\delta_v}\right)\left(\left(\frac{R^*}{\delta_v}\right)^2 - \frac{R^*}{\delta_v} - 1\right) - \left(\frac{R^*}{\delta_v}\right)^3 \mathrm{E}_1\left(\frac{R^*}{\delta_v}\right)\right]\right]$$

(36)

The diffusion length at $r = R^*$ is given by:

$$\delta_l = \frac{\left(\langle c_1\rangle^l - c_l^*\right)R^{*2}\exp\left(\frac{R^*}{\delta_v}\right)}{A\delta_v} = \frac{R^{*2}\exp\left(\frac{R^*}{\delta_v}\right)\mathbf{C}}{\delta_v}$$

(37)

References

[1] W. Kurz and David J. Fisher. Fundamentals of solidification. 1989.

[2] H. D. Brody and M. C. Flemings. *Transaction of the Metallurgical Society of AIME*, 236:615–624, 1966.

[3] S. Kobayashi. Solute redistribution during solidification with diffusion in solid phase: a theoretical analysis. *Journal of crystal growth*, 88(1):87–96, 1988.

[4] M. Rappaz and P. Thévoz. Solute diffusion model for equiaxed dendritic growth: Analytical solution. *Acta Metallurgica*, 35(12):2929–2933, 1987.

[5] C. Y. Wang and C. Beckermann. A multiphase solute diffusion model for dendritic alloy solidification. *Metallurgical and Materials Transactions A*, 24(12):2787–2802, 1993.

[6] X. Doré, H. Combeau, and M. Rappaz. Modelling of microsegregation in ternary alloys: Application to the solidification of al–mg–si. *Acta Materialia*, 48(15):3951–3962, 2000.

[7] Annika Borgenstam, Lars Höglund, John Ågren, and Anders Engström. Dictra, a tool for simulation of diffusional transformations in alloys. *Journal of phase equilibria*, 21(3):269–280, 2000.

[8] L. Thuinet and H. Combeau. A new model of microsegregation for macrosegregation computation in multicomponent steels. part i: theoretical formulation and algorithm. *Computational materials science*, 45(2):294–304, 2009.

[9] C. Ni, J. and Beckermann. A volume-averaged two-phase model for transport phenomena during solidification. *Metallurgical Transactions B*, 22(3):349, 1991.

[10] M. Wu and A. Ludwig. Modeling equiaxed solidification with melt convection and grain sedimentation—i: Model description. *Acta Materialia*, 57(19):5621–5631, 2009.

[11] M. Wu, J. Li, A. Ludwig, and A. Kharicha. Modeling diffusion-governed solidification of ternary alloys–part 1: Coupling solidification kinetics with thermodynamics. *Computational materials science*, 79:830–840, 2013.

[12] Menghuai Wu, Andreas Ludwig, and Abdellah Kharicha. Volume-averaged modeling of multiphase flow phenomena during alloy solidification. *Metals*, 9(2):229, 2019.

[13] M. A. Martorano, C. Beckermann, and C.-A. Gandin. A solutal interaction mechanism for the columnar-to-equiaxed transition in alloy solidification. *Metallurgical and Materials Transactions A*, 34(8):1657–1674, 2003.

[14] KO Tveito, M Bedel, Miha Založnik, H Combeau, and M M'Hamdi. The effect of finite microscopic liquid solute diffusion on macrosegregation formation. In *IOP Conference Series: Materials Science and Engineering*, volume 27, page 012040. IOP Publishing, 2012.

[15] Marie Bedel. *Étude de la formation des structures de solidification et des macroségrégations en coulée semi-continue d'aluminium*. PhD thesis, 2014. Thèse de doctorat dirigée par Combeau, Hervé et Založnik, Miha Sciences des matériaux Université de Lorraine 2014.

[16] G. Guillemot and C.-A. Gandin. Analytical model for equiaxed globular solidification in multicomponent alloys. *Acta Materialia*, 97:419–434, 2015.

[17] C.Y. Wang and C. Beckermann. Equiaxed dendritic solidification with convection: Part i. multiscale/multiphase modeling. *Metallurgical and materials transactions A*, 27(9):2754–2764, 1996.

[18] B. Appolaire, H. Combeau, and G. Lesoult. Modeling of equiaxed growth in multicomponent alloys accounting for convection and for the globular/dendritic morphological transition. *Materials Science and Engineering: A*, 487(1-2):33–45, 2008.

[19] Tao Wang, Sergey Semenov, Engang Wang, Yves Delannoy, Yves Fautrelle, and Olga Budenkova. Effect of diffusion length in modeling of equiaxed dendritic solidification under buoyancy flow in a configuration of hebditch–hunt experiment. *Metallurgical and Materials Transactions B*, 50(6):3039–3054, 2019.

[20] P. N. Rowe and K. T. Claxton. *Trans. Instn Chem. Engrs*, 43:321–333, 1965.

[21] J. Ni and C. Beckermann. Modeling of globulitic alloy solidification with convection. *Journal of Materials Processing and Manufacturing Science*, 2:217–231, 1993.

[22] B. Cantor and A. Vogel. Dendritic solidification and fluid flow. *Journal of Crystal Growth*, 41(1):109–123, 1977.

Chapter 5 :   Validation and industrial application

Contents

Manufacturing of ingots is an industrial process which is expensive and time consuming. Their microstructure and segregation characteristics are of great concern to the manufacturers as they affect the final performace of the product. Numerical simulation is the primary tool that is used to predict the structure and segregation of cast ingots and further optimize the process by revealing the possible mechanisms that lead to formation of defects. The main phenomena responsible for the formation of segregation in ingot casting have been identified long years ago and are governed by: i) melt flow induced by thermo-solutal natural convection, shrinkage and forced convection ii) transport of solute-lean free floating equiaxed grains. Several models have been developed which try to account for the afore mentioned phenomena and simulate solidification of large ingots, one of them being SOLID®. While the model allows for some insight into the origin of microstructure and segregation that form within an ingot, the simulations are very sensitive to the *numerical parameters* as well as to the *constitutive models* used in the simulations. As presented in the earlier chapters, modifications correponding to the *numerical parameters* (phase diagram parameters) and *constitutive model* (liquid diffusion length) have been implemented in SOLID® and is further referred to as SOLID®$_{th}$.

The main focus of this chapter is the application of SOLID®$_{th}$ to simulate solidification of industrial ingot. However, before the model is applied to industrial ingots, the model is applied to a benchmark solidification experiment. Benchmark solidification experiments are specially designed and are usually conducted in a simple geometry with simplified boundary conditions. Low melting point alloys are used which facilitate in-situ temperature measurement. Further, quantitative data such as the distribution of temperature and solute elements serve as reference for the numerical simulations and can be used to validate the model. Over the course of discussion, pertaining to the solidification with SOLID®$_{th}$, various simulations have been performed with different set of parameters. The simulation desciption along with its 'case name' in the following discussion is provided in Table 5.1. The name of the simulation cases are in bold to avoid confusion with the model name. Simulation results with SOLID® will be presented only to validate the implementation of SOLID®$_{th}$ in the case of liquid convection and moving grains (as SOLID®$_{th}$ has already been validated for a control volume solidification in Chapter 3).

Table 5.1 – Description for simulation cases

Case name	Description
SOLID®	Original model
SOLID®$_{th}$ - var	SOLID®$_{th}$ with variable phase diagram parameters
SOLID®$_{th}$ - const	SOLID®$_{th}$ with all phase diagram parameters constant
SOLID®$_{th}$ - ip	SOLID®$_{th}$ with only the interfacial phase diagram parameters (partition coeff, liquidus temperature and liquidus slope) variable. The phase enthalpies are modeled with constant C_p and L_f
SOLID®$_{th}$ - const mod	SOLID®$_{th}$ with all phase diagram parameters constant. The partition coefficient and liquidus slope are modified
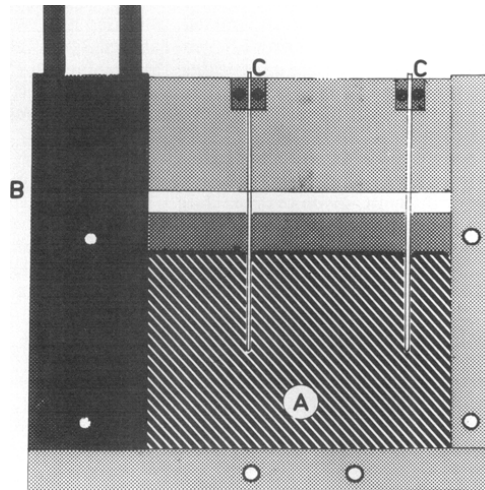
Figure 5.1 – Hebditch-Hunt solidification setup [155]

(a)   (b)
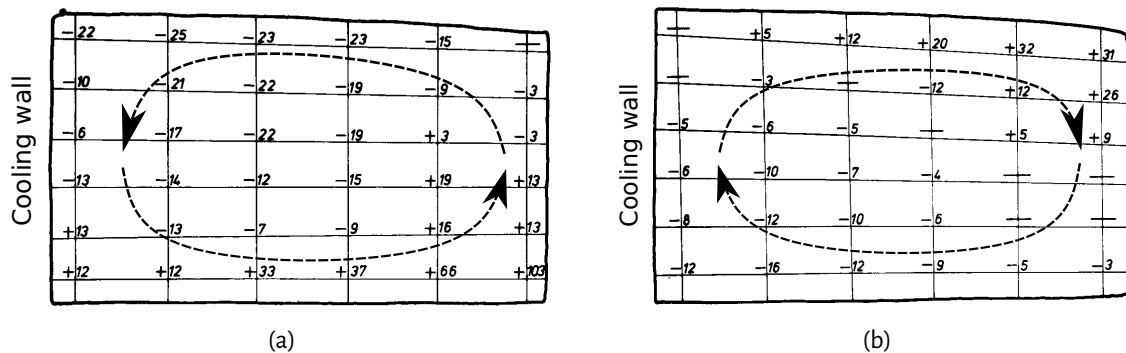
Figure 5.2 – Segregation maps reported by Hebditch-Hunt [155] for a) Sn- 5 wt.% Pb and b) Pb- 48 wt.% Sn [155]

5.1 Hebditch-Hunt benchmark simulation

One of the most influential benchmark experiment was performed by Hebditch and Hunt [155]. Pb-Sn alloys were solidified in a thin section mold with inner dimension of 100 mm x 60 mm x 10 mm, and is shown in Fig. 5.1 where 'A' is the alloy, 'B' is the chill block and 'C' are the thermocouples. All the sides are completely thermally insulated, except for the one narrow side face from which the ingot is cooled. Concentration distribution at different stages were analyzed along with the presentation of the solidified macrostructure. The Hebditch-Hunt experiment illustrates the importance of thermo-solutal convection on the formation of macrosegregation. It is verified that columnar grains are mostly present except at the end of solidification. Thus, any segregation due to settling of equiaxed grains can be neglected and it can be safely concluded that macrosegregation is entirely caused due to liquid convection. The segregation of solute changes the liquid composition which modifies the liquid density which induces solutal convection. Fig. 5.2 shows the segregation maps for Sn-Pb alloys. In the first case of Sn- 5 wt.% Pb (Fig. 5.2a), rejection of Pb in the mushy zone on the left of the cavity results in an increase in the local liquid density. This drives an counterclockwise liquid current which is also reinforced with the thermal contribution. In the case of Pb- 48 wt.% Sn (Fig. 5.2b), the tin that is rejected in the mushy zone reduces the liquid density which counteracts the thermal contribution, resulting in a clockwise current.

In order to validate the implementation of coupling the microscopic growth model with the macroscopic

Table 5.2 – Phase diagram parameters for Sn - 5 wt.% Pb alloy

Property	Symbol	Units	Value
Partition coeff. (Pb)	k_p^i	-	0.0656
Liquidus slope (Pb)	m_l^i	K(wt.%)$^{-1}$	-1.286
Latent heat	L_f	Jkg^{-1}	61000
Specific heat capacity	C_p	Jkg^{-1}K^{-1}	260
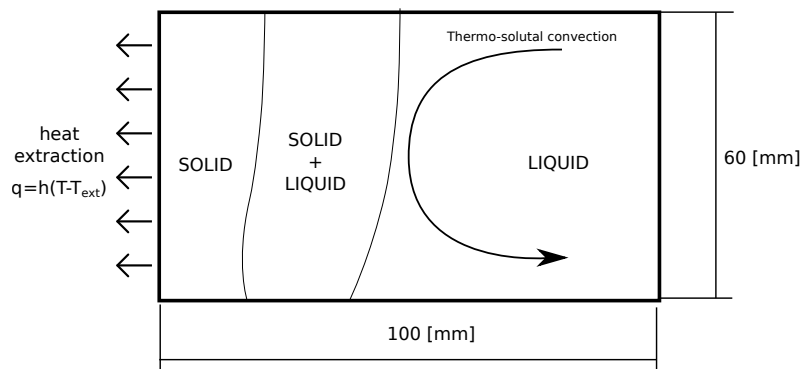
Figure 5.3 – Schematic of the 2D solidification domain in the Hebditch-Hunt case (Sn - 5 wt.% Pb alloy) with the chill heat transfer parameters: h=300 Wm^{-2}K^{-1} and T$_{ext}$= 25 ^{o}C

model, Hebditch-Hunt benchmark case for Sn- 5 wt.% Pb is considered. It has been used to validate various solidification models [156, 98, 135, 134]. Most of these simulations have obtained similar segregation pattern as observed in experimental observations. These simulations also predict the formation of segregation channels in the mushy zone. It is believed that these channels have a strong impact on the final macrosegregation pattern as the enriched intra-granular liquid can flow into the bulk through these channels. Fig. 5.3 is a schematic illustration of the solidification domain with the boundary condition applied to left wall. The thermo-physical properties used to perform the simulations are reported in B.6. The domain is discretized with rectangular shaped cells of 1.25 mm x 2 mm (80×60). The other simulation parameters are given in Table B.7. The time step used for the simulations is 1.5×10^{-3} s with 10 micro time-steps. The phase diagram parameters have been separately listed in Table 5.2 as they are a major part of the discussions in the following sections. The values of the parameters listed in Table 5.2 are the 'classical values' used in literature [157, 158, 102, 134] to perform simulations for the Hebditch-Hunt benchmark case. The 'classical value' for the partition coefficient corresponds to the value of partition coefficient close to the eutectic composition and the 'classical value' for the liquidus slope corresponds to the value of liquidus slope which best approximates the actual liquidus surface. Before presenting the results of the Hebditch-Hunt simulation, control volume Scheil solidification simulations were performed. This simulation helps to understand the impact of variable interfacial phase diagram parameters, neglecting the impact of macrosegregation which can complicate the analysis of the final results.
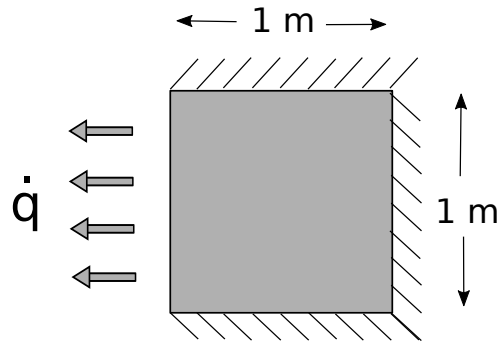
Figure 5.4 – Schematic of the system dimension and boundary condition of the control volume test case

(a)

(b)

(c)
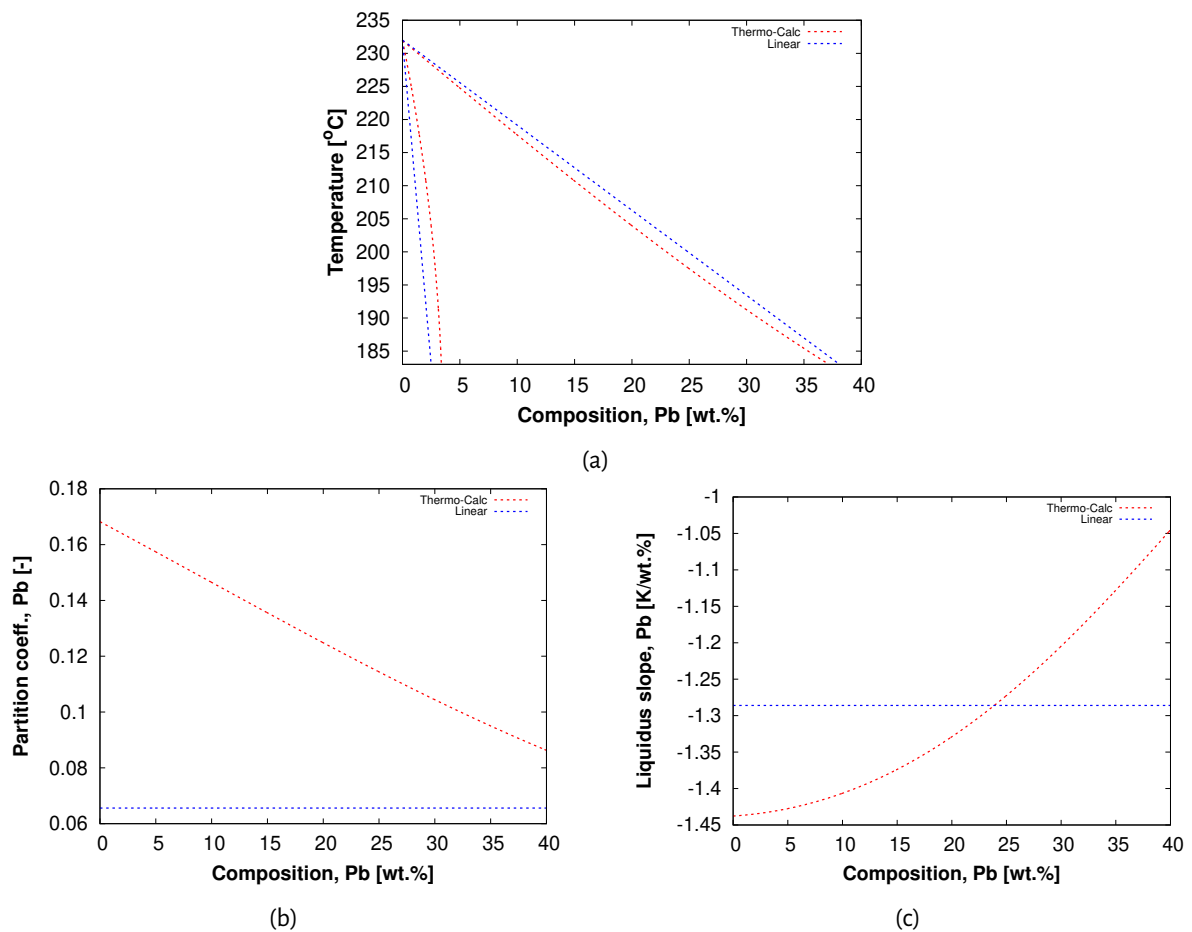
Figure 5.5 – a) Sn-Pb phase diagram obtained from Thermo-Calc® as well as the linearized Sn-Pb phase diagram for the hypo-eutectic domain (Table 5.2). Variation of b) partition coefficient and c) liquidus slope as a function of Pb composition

5.1.1 Control volume solidification

Preliminary solidification simulations were performed for a closed control volume under the conditions of linear decreasing enthalpy. Fig. 5.4 shows the system dimension and the boundary condition used for the control volume test case. Scheil solidification is assumed for the alloy and is imposed by using a high diffusion coefficient for Pb in the liquid phase (10^{-6} m^{2}s^{-1}) and a low value in the solid phase (10^{-13} m^{2}s^{-1}). Results are shown for three simulations cases:

– Thermo-Calc® using the NIST-solder database

– **SOLID®$_{th}$ - var**: simulations coupled to the phase diagram parameter using ANN-MLP

– **SOLID®$_{th}$ - const**: simulations assuming constant phase diagram parameters (Table 5.2)

Primary solidification is assumed to finish at 183 °C (T_{sol0}) for SOLID®$_{th}$. Thermo-Calc® calculates the eutectic temperature to be 182.24 °C. Fig. 5.5a shows the phase diagram obtained from Thermo-Calc® as well as the linear phase diagram obtained using constant phase diagram parameters reported in Table 5.2 and is shown in Fig. 5.5b and Fig. 5.5c. Data from Thermo-Calc® was generated according to the parameters given in Table C.2. The required thermodynamic regression functions were obtained using ANN-MLP (as discussed in chapter 3) and Table C.3 lists the accuracy of the regression relationships obtained.

(a)

(b)

(c)
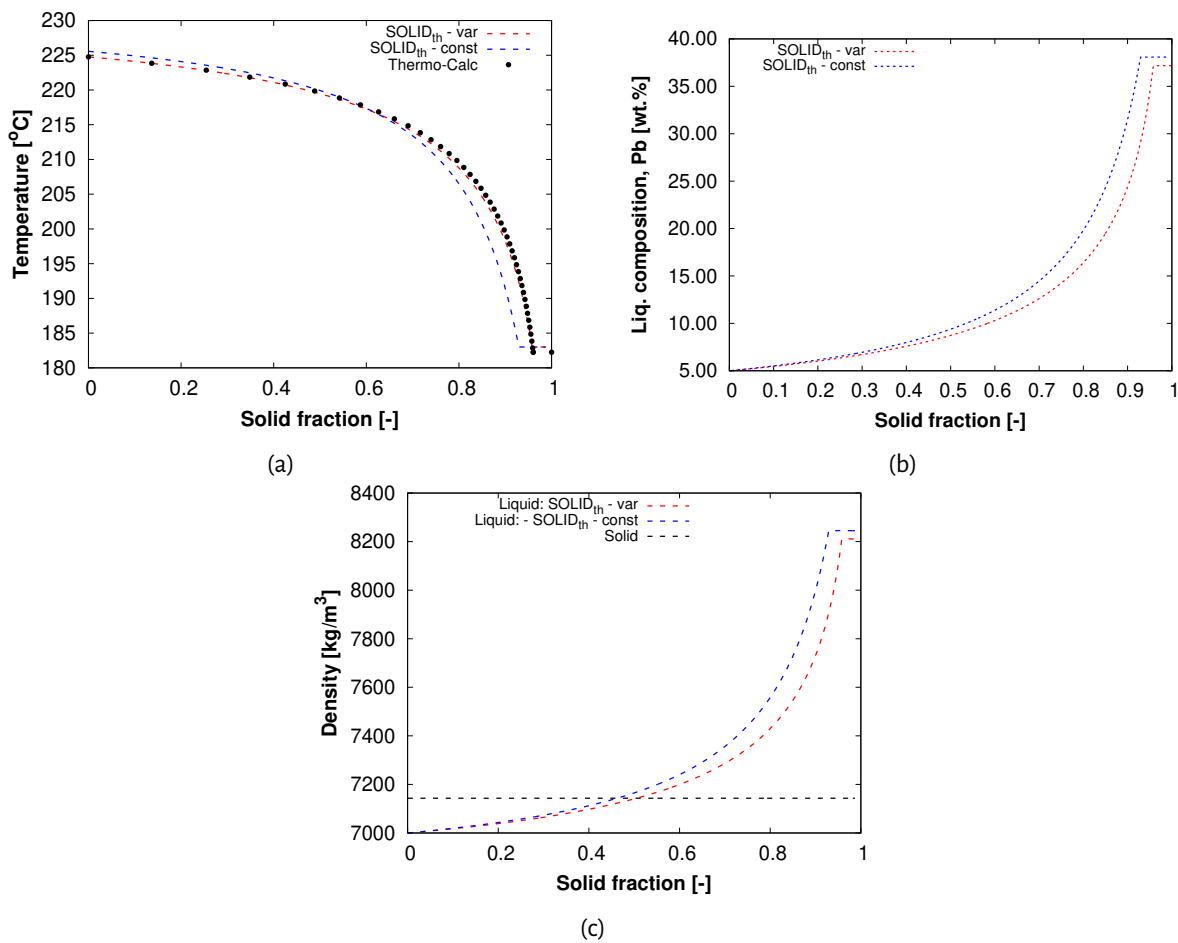
Figure 5.6 – a) Comparison of Scheil solidification of Sn-Pb alloy for **SOLID®$_{th}$ - var**, **SOLID®$_{th}$ - const** and Thermo-Calc®. along with the b) liquid composition and c) density evolution

The liquidus temperature obtained in Thermo-Calc® is lower than the values obtained with the linearized phase diagram. This results in solidification of Sn - 5 wt.% Pb alloy beginning at a temperature of 224.75 °C for Thermo-Calc® and **SOLID®$_{th}$ - var**, as compared to 225.56 °C for **SOLID®$_{th}$ - const** and is shown in Fig.5.6a. As solidification progresses, larger microsegregation is observed for **SOLID®$_{th}$ - const** as compared to **SOLID®$_{th}$ - var** (Fig. 5.6b), and which can be attributed to the lower values of partition coefficient. This, coupled with the high values of liquidus slope used for most of the solidification domain for **SOLID®$_{th}$ - const**, results in a faster reduction in temperature as solidification progresses when compared to the other models. The re-

(a)

(b)
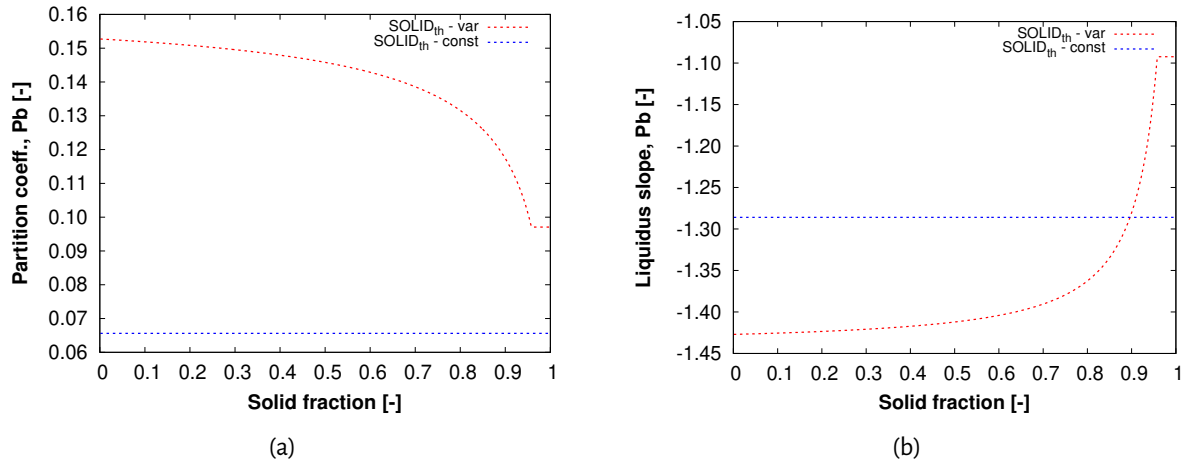
Figure 5.7 – Evolution of a) partition coeff. and b) liquidus slope during Scheil solidification of Sn- 5 wt.% Pb alloy

(a)

(b)
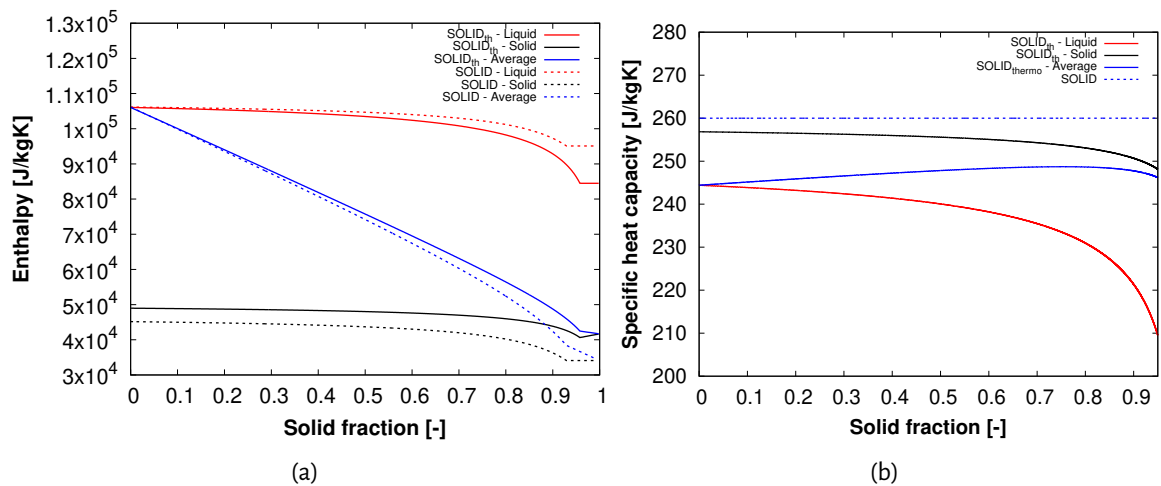
Figure 5.8 – Evolution of a) phase and average enthalpy and b) specific heat capacity obtained from SOLID$^{®}_{th}$ and SOLID$^{®}$ during Scheil solidification

sults for **SOLID$^{®}_{th}$ - var** reproduce the results of Thermo-Calc$^{®}$, however, there are slight variations in the later part of solidification (in between solid fraction 0.65-0.85). This slight variation could not be attributed to any specific issues. As T_{sol0} is reached, solidification progresses at a constant temperature (referred to as quasi-eutectic solidification in the Chapter 3). For the present case, T_{sol0} is equal to the eutectic temperature T_{eut}. For **SOLID$^{®}_{th}$ - const**, 0.07 solid fraction of eutectic phase is predicted as compared to ≈ 0.04 for **SOLID$^{®}_{th}$ - var** and Thermo-Calc$^{®}$, an over-prediction by 75%. The amount of eutectic phase determines the post-processing of cast ingots. Hence, it is critical to accuratelty predict the eutectic phase fraction. Fig. 5.7 shows the variation of the partition coefficient and liquidus slope during Scheil solidification. There is significant variation in partition coefficient and the liquidus slope over the course of Scheil solidification, highlighting the importance of coupling the solidification simulations with phase diagram data.

Fig. 5.8a shows the evolution of the phase enthalpy and average enthalpy during primary solidification for **SOLID$^{®}_{th}$ - var** and **SOLID$^{®}_{th}$ - const**. The reference state for the enthalpy values are defined such that the enthalpy of the liquid phase at $g_s = 0$ is identical in both the data sets. The difference between the liquid and solid phase enthalpy obtained for **SOLID$^{®}_{th}$ - const** is higher on account of the larger latent heat value used.

The phase enthalpy remains constant for **SOLID**®**th - const** during quasi-eutectic solidification. However, for **SOLID**®**th - var**, while the temperature is constant, the composition of the solid phase increases which results in an increase in the solid phase enthalpy. This increase in solid phase enthalpy is the result of the assumption in regards to the modeling the end of solidification. Eutectic solid composition is fixed and hence its enthalpy. However, in the present model, we assume solidification to proceed without partitioning which modifies the solid composition, and hence its enthalpy. Improving the modeling of end of solidification forms the future scope of this work. Further, the specific heat capacity of solid phase is higher than the liquid phase, both of which decrease as solidification progresses for **SOLID**®**th - var** (Fig. 5.8b).
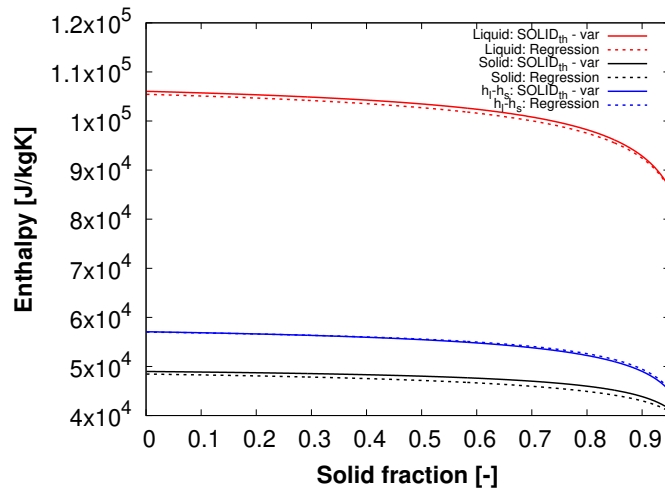
Figure 5.9 – Comparison of interfacial liquid and solid enthalpies and their difference with the regression relationsips for the same provided by Poirier and Nandapurkar [159]

Poirier and Nandapurkar [159] used earlier published co-relations for phase enthalpies and proposed regression relationships for the enthalpy of the interfacial liquid and solid BCT phases as a function of the interfacial liquid Sn composition $\left(c_{\mathrm{l}}^{*,\mathrm{Sn}}\right)$ as given below:

$$h_{\mathrm{l}} = 8.912 + 1.8860 c_{\mathrm{l}}^{*,\mathrm{Sn}} - 0.012432 \left(c_{\mathrm{l}}^{*,\mathrm{Sn}}\right)^2 + 1.5128 \times 10^{-6} \left(c_{\mathrm{l}}^{*,\mathrm{Sn}}\right)^3 + 3.4702 \times 10^{-7} \left(c_{\mathrm{l}}^{*,\mathrm{Sn}}\right)^4 \quad (5.1)$$

$$h_{\mathrm{s}} = -8.8565 + 1.6770 c_{\mathrm{l}}^{*,\mathrm{Sn}} - 0.020155 \left(c_{\mathrm{l}}^{*,\mathrm{Sn}}\right)^2 + 9.3179 \times 10^{-5} \left(c_{\mathrm{l}}^{*,\mathrm{Sn}}\right)^3 \quad (5.2)$$

$$h_{\mathrm{l}} - h_{\mathrm{s}} = 3.949 + 0.91623 c_{\mathrm{l}}^{*,\mathrm{Sn}} - 5.6966 \times 10^{-3} \left(c_{\mathrm{l}}^{*,\mathrm{Sn}}\right)^2 + 2.03078 \times 10^{-5} \left(c_{\mathrm{l}}^{*,\mathrm{Sn}}\right)^3 \quad (5.3)$$

Fig. 5.9 shows a comparison of the interfacial liquid and solid enthalpies along with the difference between the two obtained for the same Scheil solidification profile. For the case of **SOLID**®**th - var**, the values for the phase enthalpies are obtained through ANN-MLP. Whereas, in the second case, the regression relationships are used. The values obtained from the model are in good accordance with the regression relationships, thus, further validating the new implementations in SOLID®th. The value for $h_{\mathrm{l}} - h_{\mathrm{s}}$ varies in the range of ≈ 57000 Jkg^{-1}K^{-1} in the earlier stages of solidification to ≈ 44000 Jkg^{-1}K^{-1} as solidification finishes, which is lower than the latent heat value used for **SOLID**®**th - const** (61000 Jkg^{-1}K^{-1}). Miettinen [160] stated that the latent heat can

be approximated using the following relationship:

$$L_f = h\left(T_{\text{liq}}\right) - h\left(T_{\text{sol}}\right) - \int_{T_{\text{sol}}}^{T_{\text{liq}}} C_p \mathrm{d}T \tag{5.4}$$

where T_{liq} and T_{sol} are the liquidus and solidus temperature respectively. C_p is defined as:

$$C_p = g_{\text{s}} C_{p,\text{s}} + g_{\text{l}} C_{p,\text{l}} \tag{5.5}$$

This description of latent heat is consistent with the definition of L_f described in SOLID® as well as other models which assume constant L_f and C_p to be constant and equal for both the phases. Using the values of $h\left(T_{\text{liq}}\right)$ and $h\left(T_{\text{sol}}\right)$ from Fig. 5.8a and an average value of C_p from Fig. 5.8b, the latent heat value is found to be $\approx$ 54000 Jkg^{-1}K^{-1} which is around 11.5% lower than the current used value of 61000 Jkg^{-1}K^{-1}. In the following section, simulations have not been discussed with the calculated value of 54000 Jkg^{-1}, it is proposed as an improved value of latent heat for the future simulations of Hebditch-Hunt benchmark case.

5.1.2 Hebditch-Hunt case: fixed solid phase (HH-fix)

To simulate the growth of the columnar grains in the Hebditch-Hunt test case, the solid is assumed to be fixed and is modeled by setting the parameter $g_{\text{env}}^{pack} = 0.0$. The simulation was performed with SOLID®$_{\text{th}}$ assuming all phase diagram to be constant (**SOLID®$_{\text{th}}$ - const**). Fig. 5.10 - Fig. 5.12 show the distribution of average composition, temperature, solid fraction and intrinsic liquid velocity at 20 s, 200 s and 700 s respectively. Cooling starts on the left surface and solid grains nucleate as soon as the nucleation undercooling criteria is satisfied. During solidification, the rejection of solute from the solid to the liquid phase results in enrichment of the liquid, making it heavier in accordance with Fig. 5.6c. This induces a downward liquid convection as shown in Fig. 5.10d, henceforth referred to as 'counterclockwise' flow. The average composition in Fig. 5.10a shows that while a large part of the cavity remains at the initial composition, the counterclockwise flow transports the enriched liquid, resulting in an increase in the average Pb composition near the base of the cavity. The heat is extracted by conduction through the solid fixed layer near the cooled wall.

As solidification progresses, the global solidification front advances from left to right. By 200 s, considerable solid phase has formed and the bulk liquid composition has increased beyond the nominal composition of 5 wt.% Pb. The counterclockwise flow enriches the bottom region of the cavity (Fig. 5.11a) which reduces the liquidus temperature and delays solidification. Formation of channel segregates of low intensity is observed and is due to the solute rich liquid which flows towards the bottom of the cavity in the mushy zone by the counterclockwise thermo-solutal convection. The nature of these channel segregates does not change during the course of solidification. The counterclockwise flow also bends the temperature field in the same direction as seen in Fig. 5.11b. By 700 s, continued downward movement of the enriched liquid results in a segregated channel confined at the bottom of the cavity which extends over the entire length of the cavity. Whereas in the inner part of the cavity, more channel segregates have formed. The orientation and the number of the segregated channels is strongly influenced by the parameters used in the permeability model for the description of the mushy zone.

Fig. 5.13 shows the final Pb segregation map. The general segregation trend is in accordance with the experimental observations. The final Pb segregation maps obtained are compared with the experimental results of the Hebditch-Hunt benchmark case and is shown in Fig. 5.14. In these figures, the relative variation of composition ($\Delta\langle c \rangle / c_0$) of Pb are plotted as a function of distance to the chill for four heights: 0.5, 2.5, 3.5 and

HH-fix: 20 s

(a) Average composition wt.%

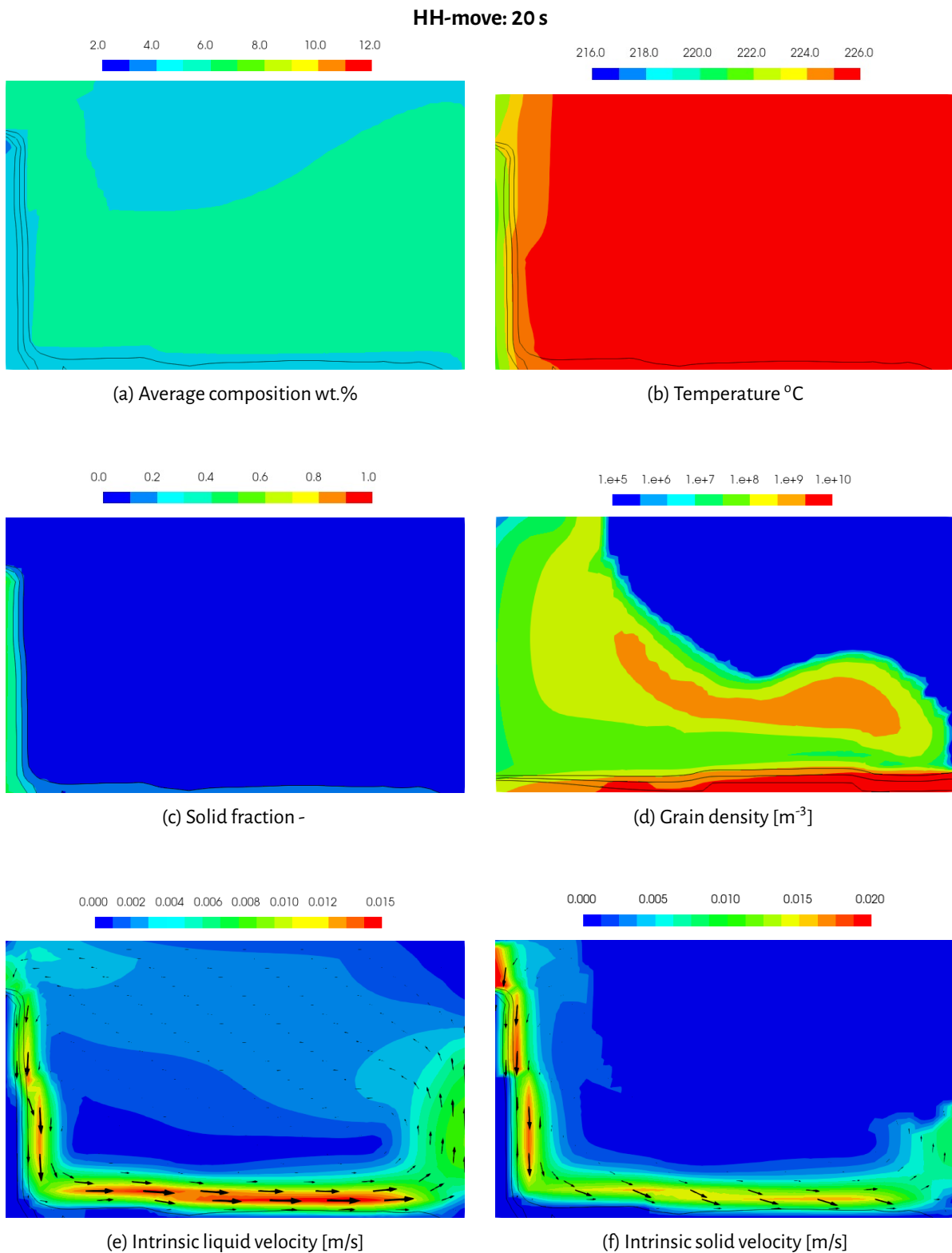(b) Temperature °C

(c) Solid fraction -

(d) Intrinsic liquid velocity [m/s]
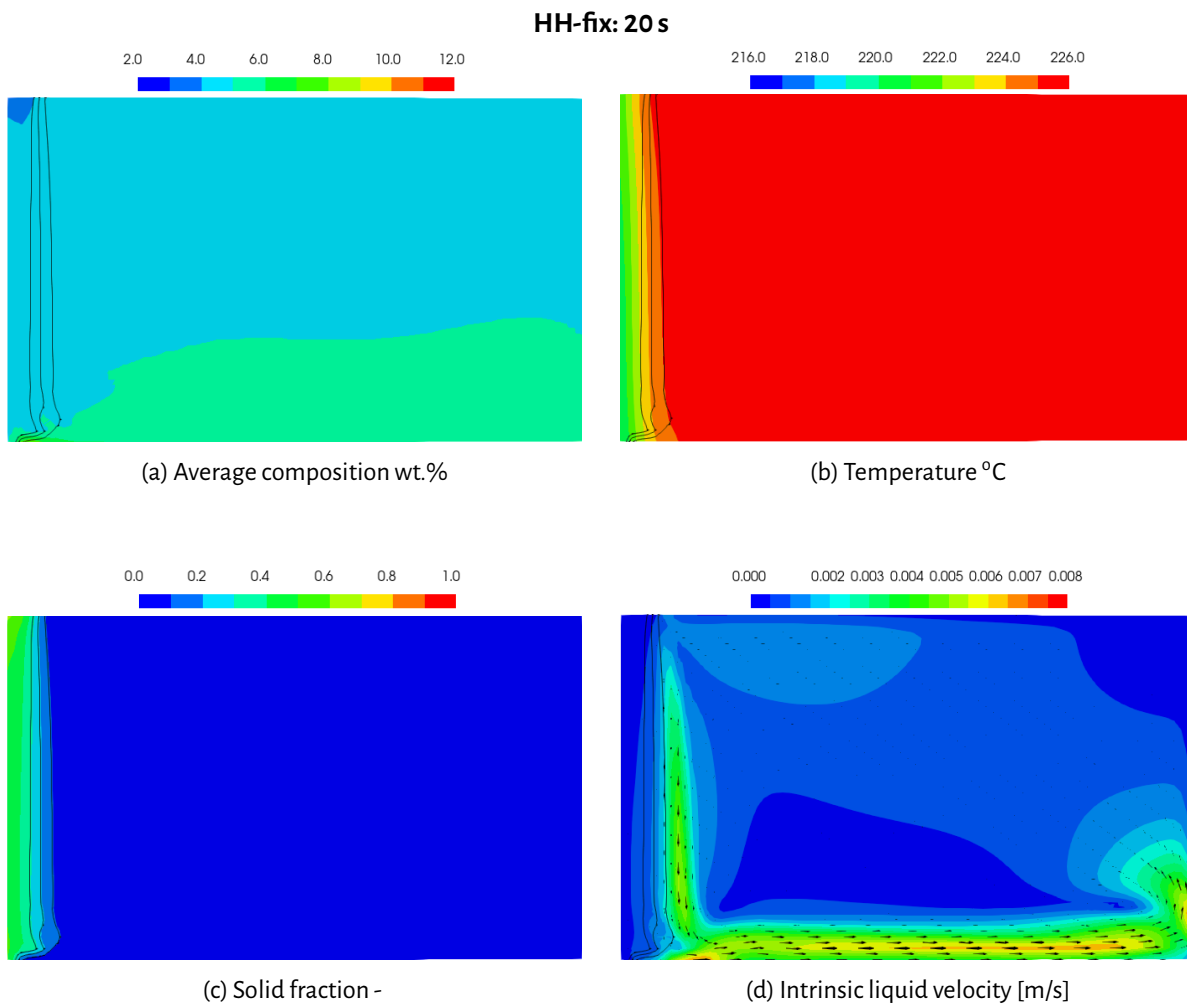
Figure 5.10 – Profiles for: a) liquid composition b) temperature c) solid fraction and d) intrinsic liquid velocity for **SOLID**®$_{th}$ **- const** at 20 s. The black iso-lines represent the solid fraction at 0.1, 0.2 and 0.3. Alloy: Sn - 5 wt.% Pb

Table 5.3 – HH-fix: Computational time

Simulation case	Computational time [h]
SOLID®	≈ 73
SOLID®$_{th}$ **- const**	≈ 76

HH-fix: 200 s

(a) Average composition wt.%

(b) Temperature °C

(c) Solid fraction -

(d) Intrinsic liquid velocity [m/s]
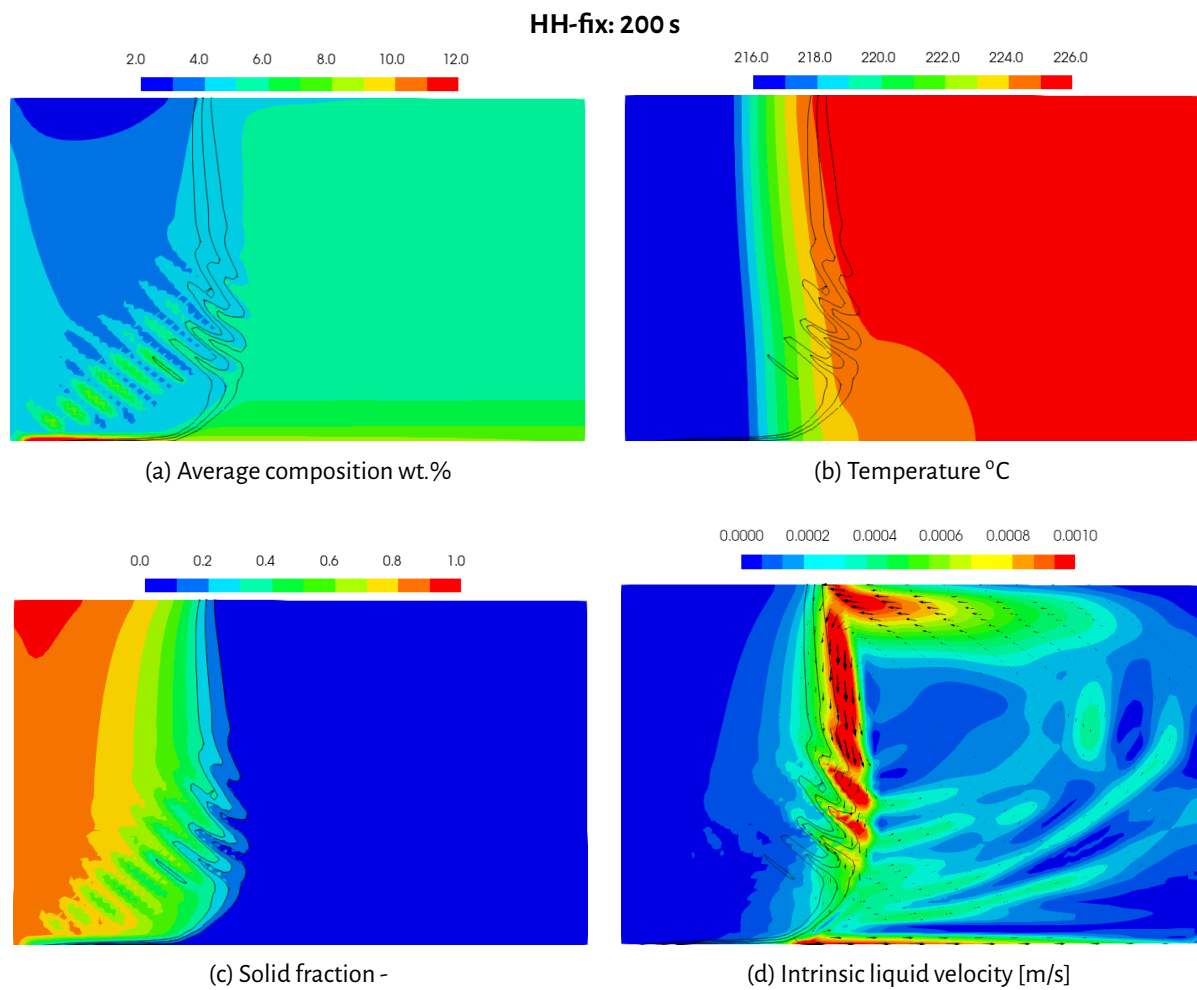
Figure 5.11 – Profiles for: a) liquid composition b) temperature c) solid fraction and d) intrinsic liquid velocity for **SOLID**®**th - const** at 200 s. The black iso-lines represent the solid fraction at 0.1, 0.2 and 0.3. Alloy: Sn - 5 wt.% Pb

HH-fix: 700 s

(a) Average composition wt.%

(b) Temperature °C

(c) Solid fraction -

(d) Intrinsic liquid velocity [m/s]
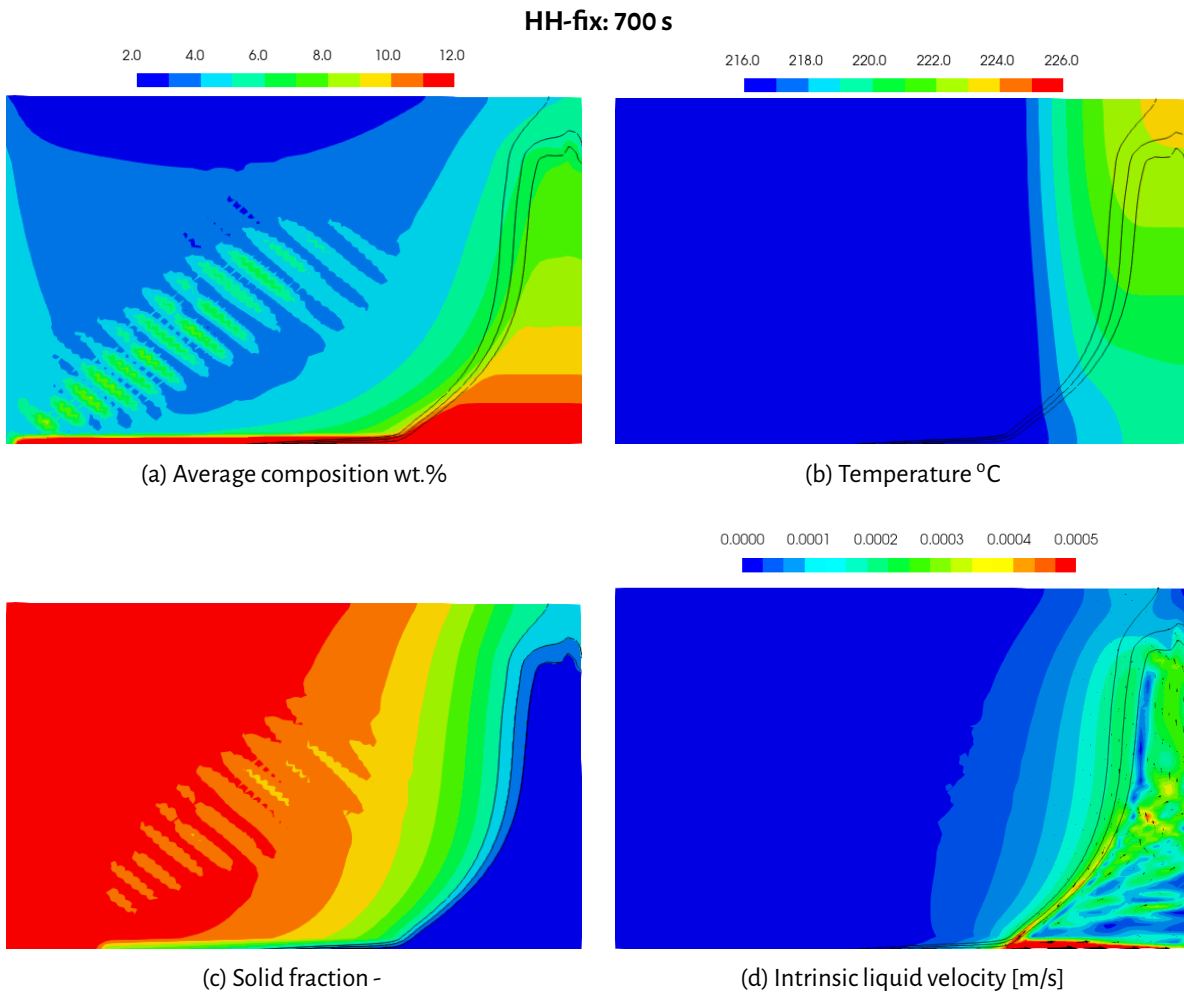
Figure 5.12 – Profiles for: a) liquid composition b) temperature c) solid fraction and d) intrinsic liquid velocity for **SOLID**®$_{th}$ **- const** at 700 s. The black iso-lines represent the solid fraction at 0.1, 0.2 and 0.3. Alloy: Sn - 5 wt.% Pb

HH-fix: Average composition wt.%

(a) **SOLID**®$_{th}$ **- const**
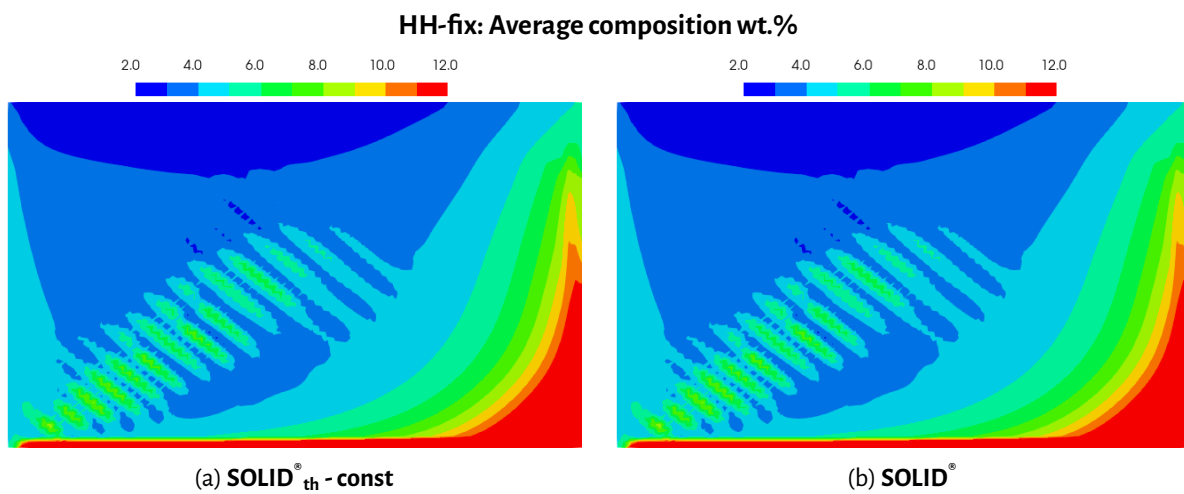
(b) **SOLID**®

Figure 5.13 – Final Pb segregation maps for a) **SOLID**®$_{th}$ **- const** and b) **SOLID**®
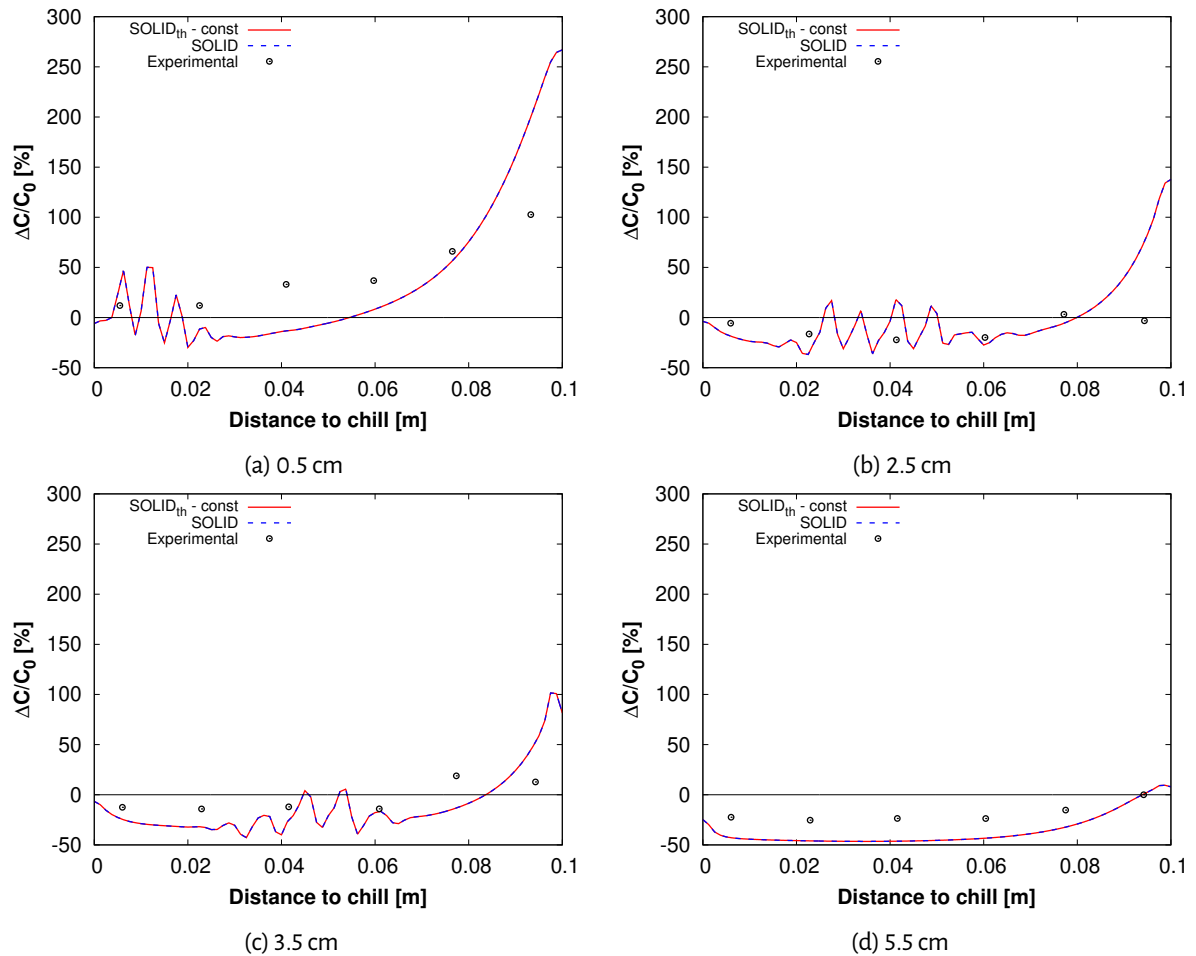
Figure 5.14 – Relative lead composition variation for Sn- 5 wt.% Pb alloy at the end of solidification as a function of the distance to the chill. Results for **SOLID**®**th - const** and **SOLID**® and with the experimental measurements corresponding to the heights of the cavity: a) 0.5 cm, b) 2.5 cm, c) 3.5 cm and d) 5.5 cm

HH-fix: Average composition wt.%

(a) **SOLID**®**ₜₕ - var**   (b) **SOLID**®**ₜₕ - const**
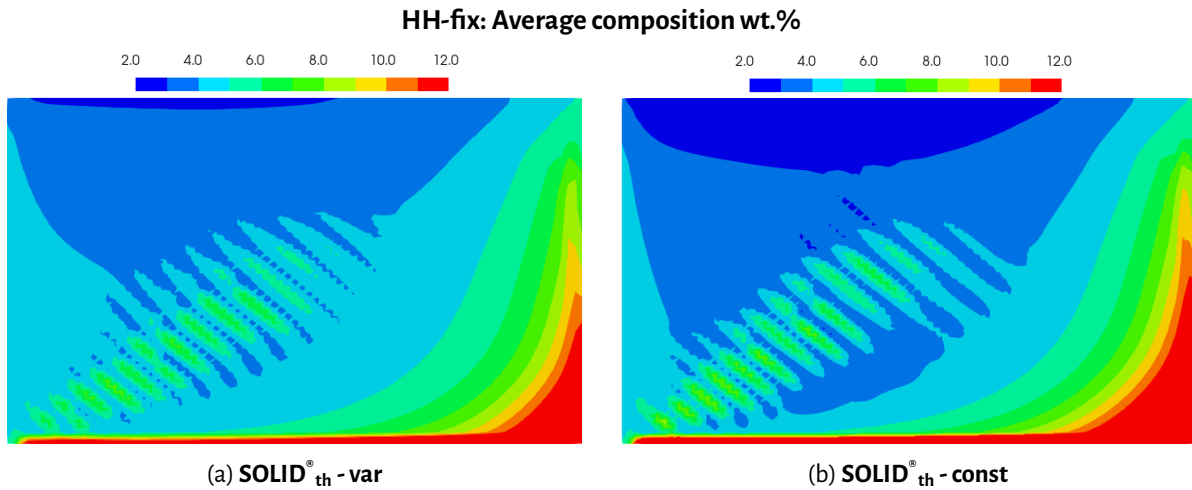
Figure 5.15 – Final Pb segregation maps for a) **SOLID**®**ₜₕ - var** and b) **SOLID**®**ₜₕ - const**

5.5 cm from the bottom boundary. The simulation results are in good agreement with the experimental measurements for most part of the domain except in the bottom (0.5 cm). All the profiles show an over-prediction in the magnitude of Pb segregation close to the right boundary. Fig. 5.13 also shows the segregation profiles obtained for **SOLID**® which is identical to the profiles for **SOLID**®**ₜₕ - const**, thus validating the implementation of the microscopic growth model within the framework of macroscopic solidification model. Table 5.3 lists the computational time used for **SOLID**® and **SOLID**®**ₜₕ - const** for the simulation. **SOLID**®**ₜₕ - const** uses slightly more computational time and the difference is attributed to the differences in regards to the implementation of the new microscopic growth model.

5.1.2.1 Impact of phase diagram parameters

Once the implementaion of the new microscopic growth model is validated, simulation is performed with new model accouting for variable phase diagram parameters - case **SOLID**®**ₜₕ - var**. Fig. 5.15 shows the comparison of the final Pb segregation maps for **SOLID**®**ₜₕ - var** and **SOLID**®**ₜₕ - const**. **SOLID**®**ₜₕ - var** results shows reduced segregation as compared to **SOLID**®**ₜₕ - const** results and are in accordance with trend observed in the control volume solidification simulation results shown in Fig. 5.6b. The overall modification is a combination of:

- Modification to the interfacial phase diagram parameters - partition coefficient and liquidus temperature

- Modification to the phase enthalpies

Modification to interfacial phase diagram parameters affects the local solidification kinetics as discussed in Section 5.1.1. Whereas the the phase enthalpies, while affecting the local solidification kinetics, also affects the heat transfer during solidification. Thus, analysing the results of **SOLID**®**ₜₕ - var** is not straight-forward. Hence, we perform further analyses by performing simulations with different sets of variable and constant phase diagram parameters (Table 5.1) from which certain conclusions are drawn which help understand the final result. In order to assess the impact of modified phase enthalpies alone, a simulation is performed assuming phase enthalpies are only dependent on temperature with a constant specific heat capacity (C_p) and latent heat (L_f), while keeping the interfacial phase diagram parameters identical to **SOLID**®**ₜₕ - var** (i.e. variable interfacial phase diagram parameters). This case is referred to as **SOLID**®**ₜₕ - ip**.

HH-fix: Average composition wt.%

(a) **SOLID**®th **- var** (b) **SOLID**®th **- ip**
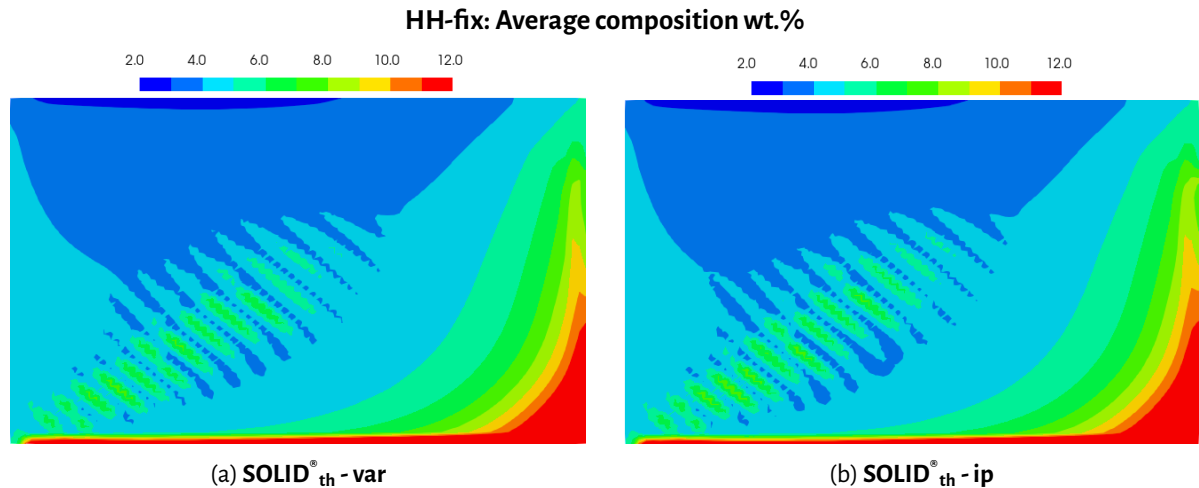
Figure 5.16 – Final Pb segregation map for a) **SOLID**®th **- var** and b) **SOLID**®th **- ip**

5.1.2.1.1 Assessing the impact of modification to phase enthalpies: Fig. 5.16 shows the final Pb segregation map for the case **SOLID**®th **- var** and **SOLID**®th **- ip**. We observe that the segregation maps for the two results are very similar. Further similarities are observed in the intrinsic liquid velocity map as shown in Fig.5.17. As the liquid velocity field is a direct consequence of the thermo-solutal convection, similarities in the liquid velocity field indicates similarities in the composition and the temperature fields in the liquid phase. Fig. 5.18 shows the liquid composition and temperature along an horizontal axis at the mid-height of 0.03 m. It is observed that the liquid composition and temperature are similar in the liquid domain for **SOLID**®th **- var** and **SOLID**®th **- ip**. As solidification begins, the temperature evolution starts to differ due to the variation in phase enthalpies, which also modifies the liquid composition. Fig. 5.19 shows the temperature evolution for **SOLID**®th **- var** and **SOLID**®th **- ip** for three points at an height of 30 mm, at a distance of 25, 50 and 75 mm from the chill. For all the three points, the temperature evolution is identical as long as the points are complete liquid. As solidification progresses, the temperature decreases faster for **SOLID**®th **- var** as compared to **SOLID**®th **- ip** on account of the larger value of latent heat in **SOLID**®th **- ip**. However, there is no significant difference in the composition evolution for the three points (hence not shown). Thus, the variation in temperature as solidification commences explains the slight difference in the intrinsic liquid velocity magnitude in the mushy zone as seen in Fig. 5.20. Fig. 5.20 shows the temporal evolution of the intrinsic liquid velocity magnitude at three points within the cavity. The points are located at mid-height (30mm) and at a distance of i) 25 mm ii) 50 mm and iii) 75 mm from the chill surface. It is observed that there are small differences in the intrinsic liquid velocity magnitude obtained for **SOLID**®th **- var** and **SOLID**®th **- ip**. These differences are only observed once solidification begins at those points.

Fig. 5.21 shows the average evolution of solid fraction in the whole domain. Large values of latent heat results in delayed solidification for **SOLID**®th **- ip** (and similar to **SOLID**®th **- const**) as compared to •®th - var. As a consequence, the total solidification time of the cavity is modified. However, these differences do not affect the final segregation map significantly (in the current case of columnar solidification) as seen in Fig. 5.26 where the segregation profiles along an axis obtained for **SOLID**®th **- var** and **SOLID**®th **- ip** almost superimpose. Thus, we conclude that the modification to phase enthlapies have minimal impact on the final segregation map. It is the interfacial phase diagram parameters which affect the final macrosegregation map for Sn-Pb alloy in **HH-fix**. Hence, further analysis will be done by analysing **SOLID**®th **- ip** and comparing with

HH-fix: Intrinsic liquid velocity [m/s]

(a) **SOLID**®**th - var** - 50 s

(b) **SOLID**®**th - ip** - 50 s

(c) **SOLID**®**th - var** - 100 s
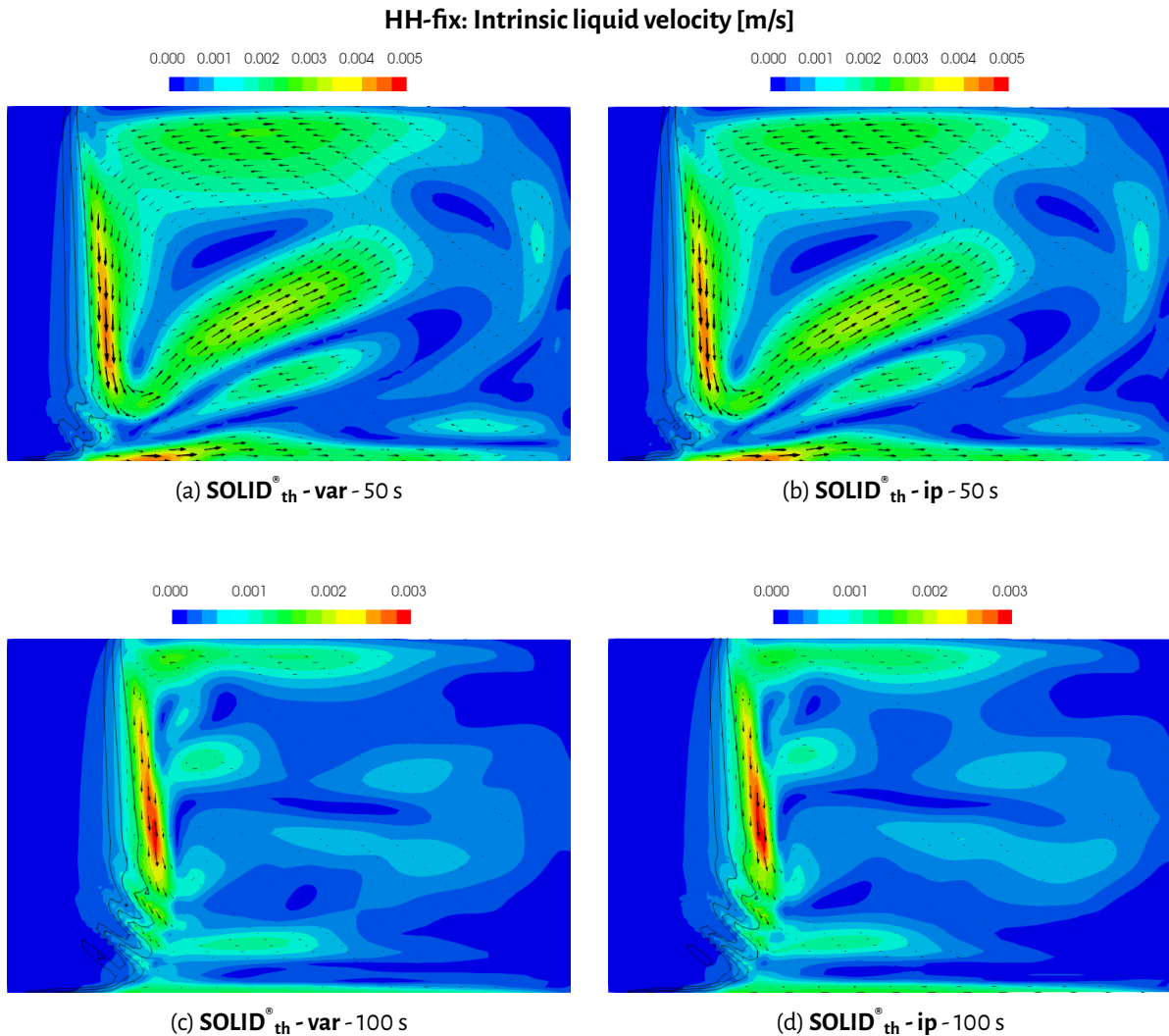
(d) **SOLID**®**th - ip** - 100 s

Figure 5.17 – Intrinsic liquid velocity map for **SOLID**®**th - var** and **SOLID**®**th - ip** at 50 s and 100 s

SOLID®**th - const**. Comparison with **SOLID**®**th - var** is not discussed further so as to reduce the number of variable parameters, allowing for simplified discussion.

5.1.2.1.2   Assessing the impact of modification to interfacial phase diagram parameter   Fig. 5.22 shows the Sn-Pb phase diagram obtained from Thermo-Calc® as well as the linearized Sn-Pb phase diagram for the hypo-eutectic domain obtained using the 'classical values' used in literature (Table 5.2). As observed in control volume solidification (Fig. 5.6b) as well as the **HH-fix** solidification (Fig. 5.15), results for **SOLID**®**th - const** has higher segregation as compared to **SOLID**®**th - ip** which can be attributed to low value of partition coefficient used in **SOLID**®**th - const**. Thus, we propose to modify the partition coefficient and liquidus slope while keeping the same pure melting temperature. The partition coefficient is chosen to be 0.157 which corresponds to the partition coefficient obtained from Thermo-Calc® for the nominal composition of 5 wt.% Pb. The liquidus slope is slightly modified from -1.286 to -1.3 K(wt.%)$^{-1}$. Fig. 5.22 shows the modified linear phase diagram as well.

Fig. 5.23 shows a comparison of the final segregation maps for **SOLID**®**th - ip** and **SOLID**®**th - const mod**. The **SOLID**®**th - const mod** results are an improvement over the **SOLID**®**th - const** results and is quite close to
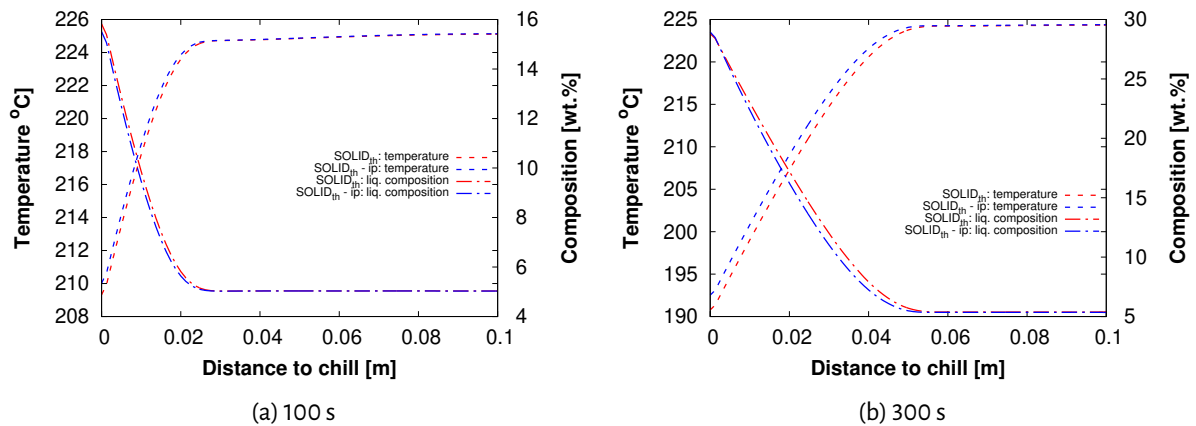
(a) 100 s

(b) 300 s

Figure 5.18 – Temperature and liquid composition variation at mid-height (0.03 cm) as a function of distance to the chill at a) 100 s and b) 300 s for **SOLID**®**th - var** and **SOLID**®**th - ip**
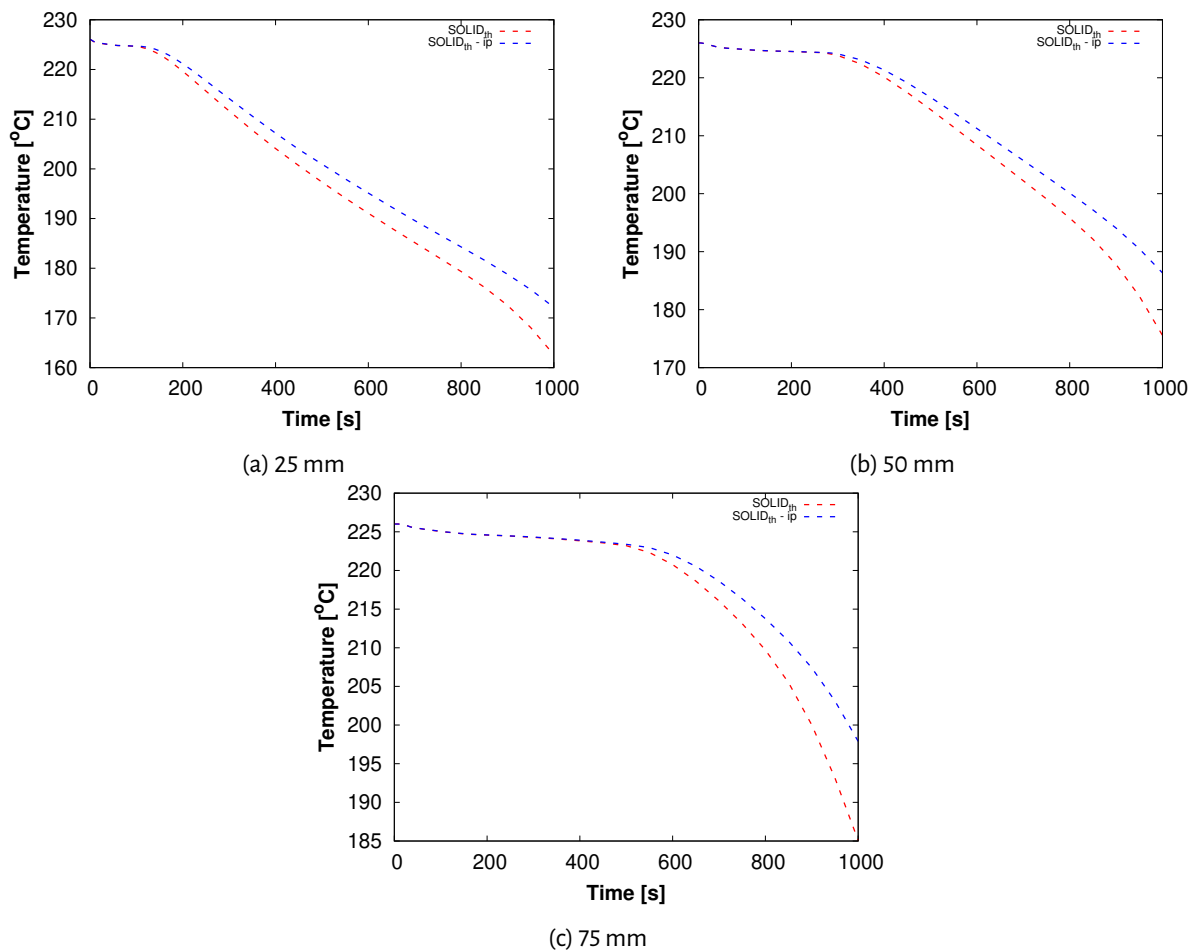
(a) 25 mm

(b) 50 mm

(c) 75 mm

Figure 5.19 – Comparison of temperature for **SOLID**®**th - var** and **SOLID**®**th - ip** at a height of 30 mm and varying diatance to the chill: a) 25mm b) 50 mm and c) 75 mm

SOLID®**th - ip** result. The segregation profiles shown in Fig. 5.26 further validate this point. However, the high value of partition coefficient (0.157) results in solidification finishing before T_{sol0} is reached. Fig. 5.24 shows the solidification path for two points at an height of 30 mm and at distance of 25 mm and 75 mm from the chill. The point 50 mm is not included due to the presence of segregation channels. The behaviour of the solidifi-
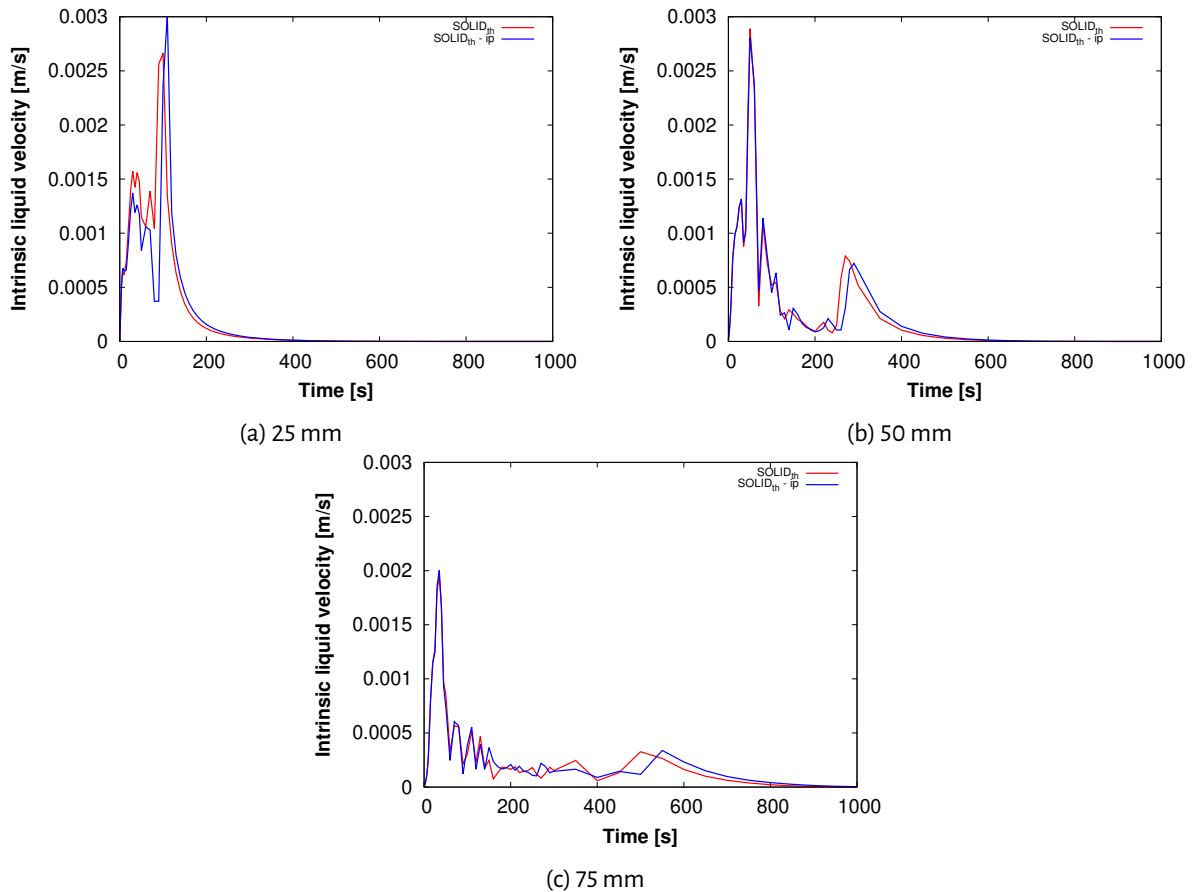
(a) 25 mm

(b) 50 mm

(c) 75 mm

Figure 5.20 – Comparison of intrinsic liquid velocity for **SOLID**®**th - var** and **SOLID**®**th - ip** at a height of 30 mm and varying distance to the chill: a) 25mm b) 50 mm and c) 75 mm
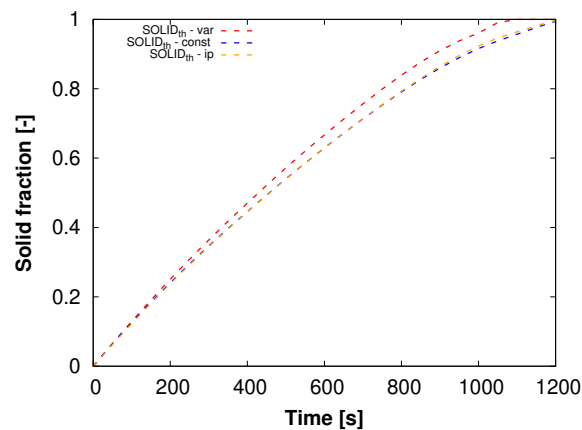
Figure 5.21 – Total solidification time for a) **SOLID**®**th - var** and b) **SOLID**®**th - ip** for the whole domain

cation path at both the points are similar. The solidification path for **SOLID**®**th - ip** follows that for **SOLID**®**th - const mod** up to a solid fraction of ≈ 0.8. It is only at the later stages of solidification that the solidification path for **SOLID**®**th - ip** diverges from that of **SOLID**®**th - const mod** towards **SOLID**®**th - const** due to the reduction in the partition coefficient, ending with quasi-eutectic solidification. Since most of the segregation develops at low solid fraction, divergence in solidification path does not affect the final segregation map significantly. Fig. 5.25 shows the distribution of quasi-eutectic solid phase. As the bottom-right corner of the cavity is the most
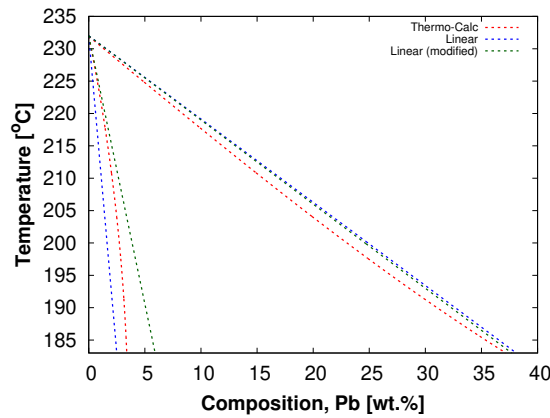
Figure 5.22 – Sn-Pb phase diagram obtained from Thermo-Calc®as well as the linearized Sn-Pb phase diagram for the hypo-eutectic domain obtained using partition coefficient value used in literature (0.0656 - linear) and the proposed modified value (0.157 - linear (modified k))

HH-fix: Average composition wt.%

(a) **SOLID®th - ip**

(b) **SOLID®th - const mod**
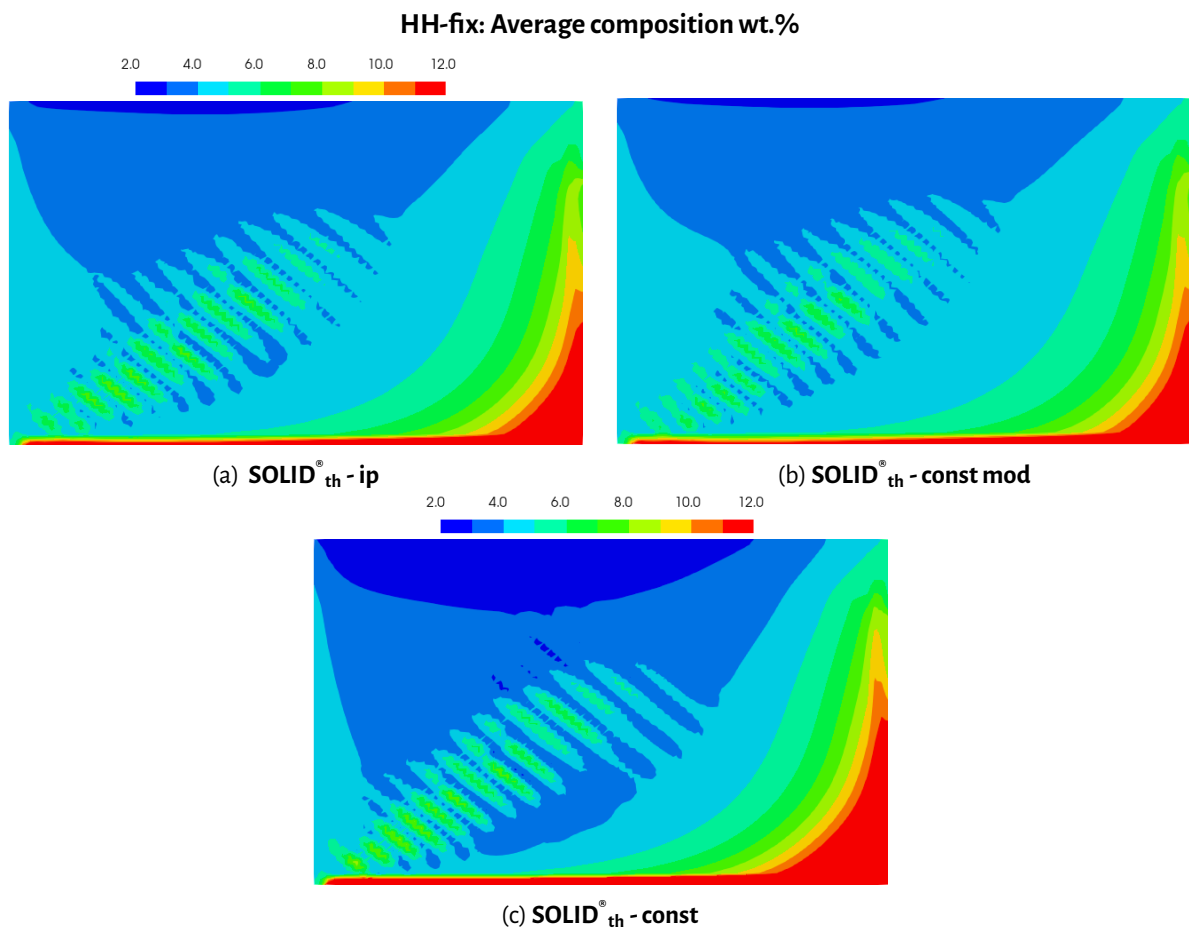
(c) **SOLID®th - const**

Figure 5.23 – Final Pb segregation map for a) **SOLID®th - ip**, b) **SOLID®th - const mod** and c) **SOLID®th - const**

Pb enriched zone, this zone has the highest phase fraction of quasi-eutectic solid phase. **SOLID®th - const** has the highest quasi-eutectic solid phase while **SOLID®th - const mod** has the lowest.

From the above discussion, we can draw the following inferences from the various simulations for **HH-fix**:

1. Coupling the simulation with variable phase diagram parameter improves the segregation prediction

(a) 0.5 cm

(b) 2.5 cm
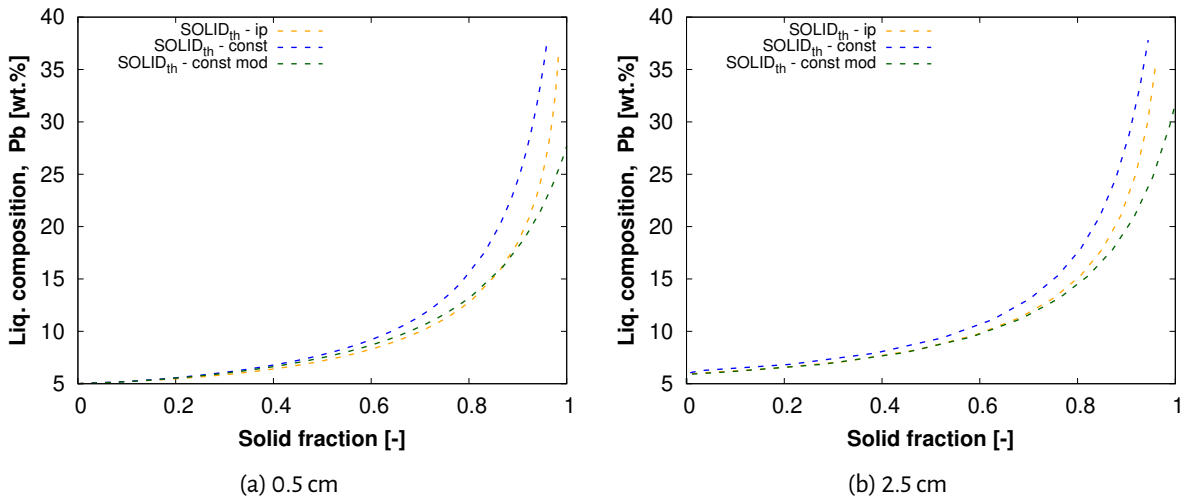
Figure 5.24 – Liquid composition evolution for **SOLID®$_{th}$ - ip**, **SOLID®$_{th}$ - const** and **SOLID®$_{th}$ - const mod** at a height of 30 mm for points a) 25 mm and b) 75 mm from the chill.

HH-fix: Eutectic phase fraction

(a) **SOLID®$_{th}$ - const**

(b) **SOLID®$_{th}$ - ip**
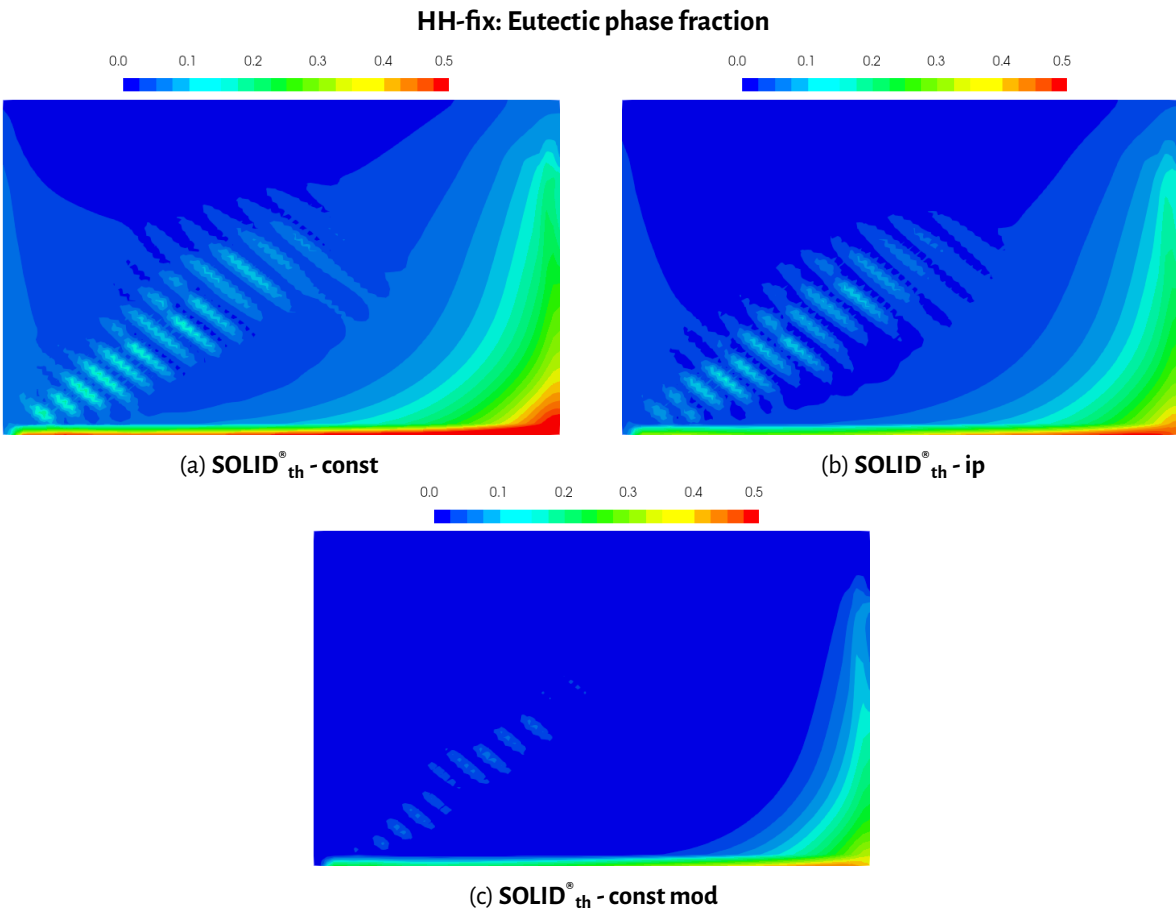
(c) **SOLID®$_{th}$ - const mod**

Figure 5.25 – Eutectic phase fraction map for a) **SOLID®$_{th}$ - const** b) **SOLID®$_{th}$ - ip** and c) **SOLID®$_{th}$ - const mod**

as compared to case with the 'classical' fixed parameters

2. Modification to phase enthalpies due to coupling with phase diagram data does not modify the macroseg-regation prediction significantly. However, it does modify the temperature and composition evolution
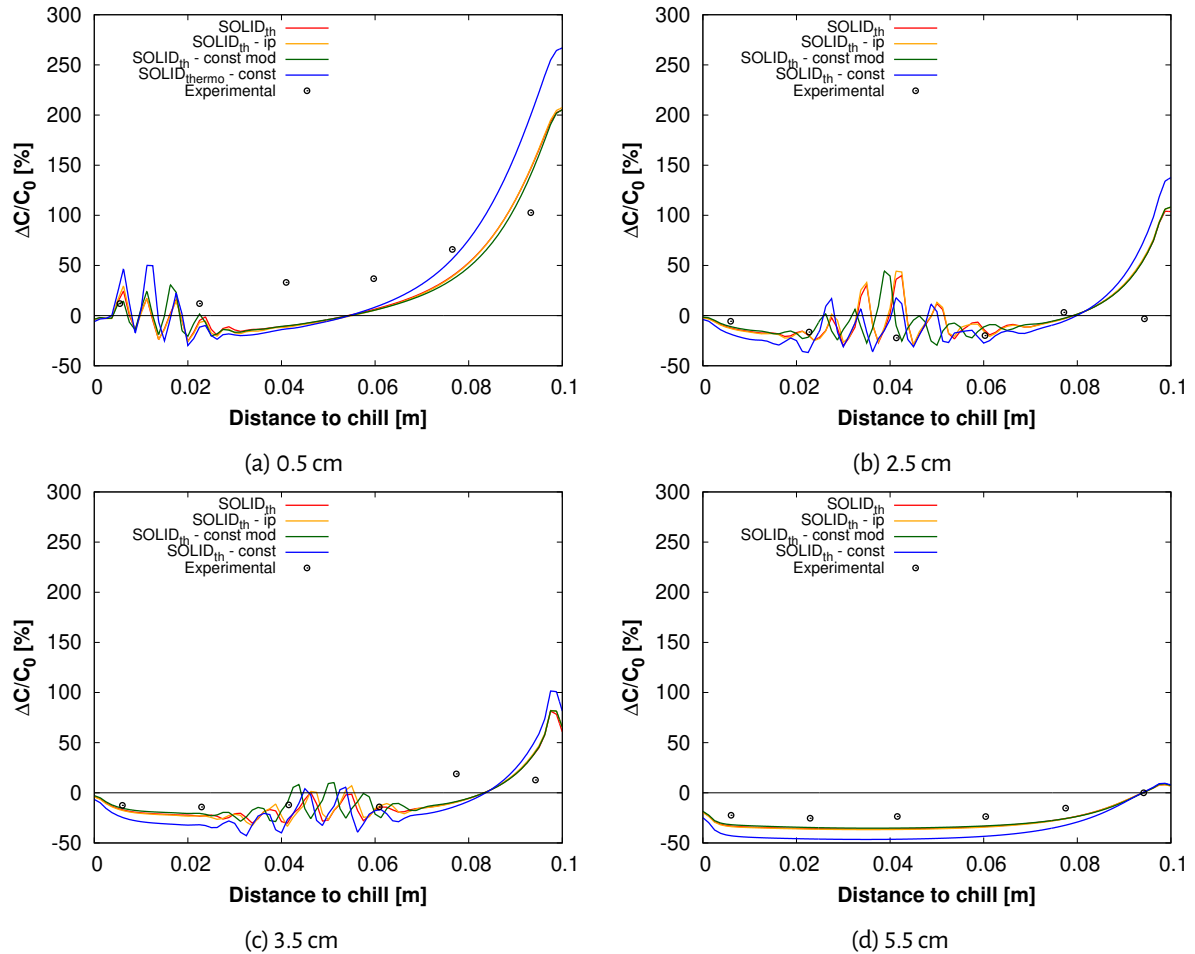
Figure 5.26 – Relative lead mass fraction variation for Sn- 5 wt.% Pb alloy at the end of solidification as a function of the distance to the chill. Simulation results are compared with the experimental measurements corresponding to the heights of the cavity: a) 0.5 cm, b) 2.5 cm, c) 3.5 cm and d) 5.5 cm

locally once solidification begins, which results in **SOLID$^{®}_{th}$ - var** having difference in temperature and liquid composition in the mushy zone when compared to **SOLID$^{®}_{th}$ - ip**.

3. The interfacial phase diagram parameters, specifically the partition coefficient is the critical parameter which influences the macrosegregation map when the simulations account for variable phase diagram parameters. Improved suggestion of constant partition coefficient values, improve the macrosegregation prediction, however, results in lower values of the eutectic phase fraction.

With regards to the discussion pertaining to the impact of the phase diagram parameters on the Hebditch-Hunt benchmark case, the primary focus has been on the case with fixed solid grains. In literature, the Hebditch-Hunt benchmark case has been simulated with moving equiaxed grains as a validation case. Unlike the fixed grain case where the domain of influence of variable enthalpies on the temperature is constrained to the left side of the cavity, the moving grains results in variation in temperature evolution and the heat transfer in the entire domain. Thus, for the discussion with moving solid phase, only the final result will be presented for the case with variable phase diagram parameters. However, before that, we present the result with constant phase diagram parameters. This result is presented to validate the implementation of the new micromodel for the case of moving equiaxed grains.

HH-move: 20 s

(a) Average composition wt.%

(b) Temperature °C

(c) Solid fraction -

(d) Grain density [m^{-3}]

(e) Intrinsic liquid velocity [m/s]

(f) Intrinsic solid velocity [m/s]

Figure 5.27 – Profiles for: a) liquid composition b) temperature c) solid fraction d) grain density e) intrinsic liquid velocity and f) intrinsic solid velocity for **SOLID**®$_{th}$ **- const** at 20 s. The black iso-lines represent the solid fraction at 0.1, 0.2 and 0.3. Alloy: Sn - 5 wt.% Pb

HH-move: 300 s

(a) Average composition wt.%

(b) Temperature °C

(c) Solid fraction -

(d) Grain density [m⁻³]

(e) Intrinsic liquid velocity [m/s]

(f) Intrinsic solid velocity [m/s]
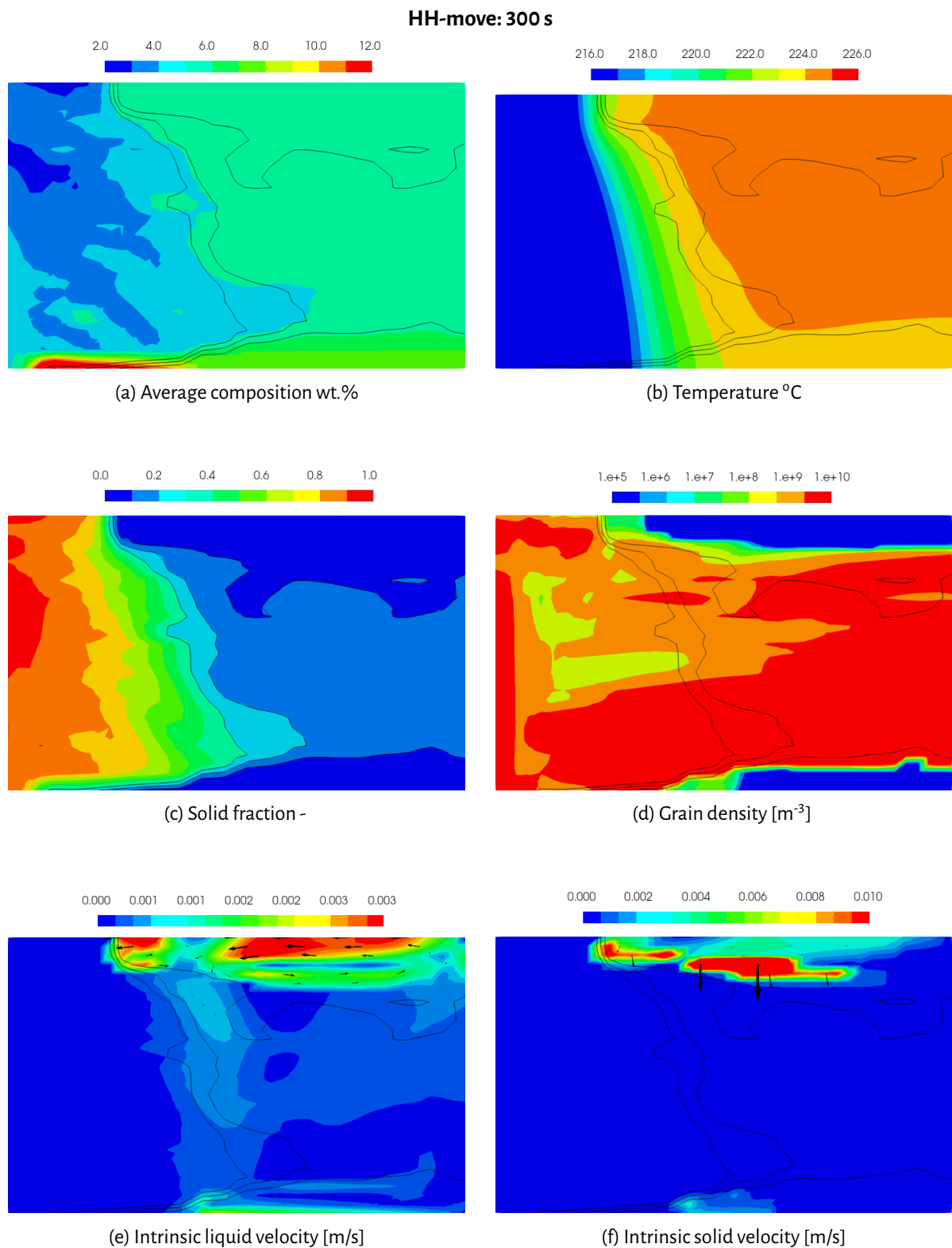
Figure 5.28 – Profiles for: a) liquid composition b) temperature c) solid fraction d) grain density e) intrinsic liquid velocity and f) intrinsic solid velocity for **SOLID**®**th - const** at 300 s. The black iso-lines represent the solid fraction at 0.1, 0.2 and 0.3. Alloy: Sn - 5 wt.% Pb

5.1.3   Hebditch-Hunt case: moving solid phase (HH-move)

Simulation in the presence of solid transport due to sedimentation and liquid convection are performed for the Hebdith-Hunt benchmark test case (further referred to as **HH-move**) with SOLID®$_{th}$. The simulation is performed with a three phase dendritic model. The thermo-physical properties used to perform the simulations are reported in B.6. The other simulation parameters are given in Table B.7. Due to time constraints, the results presented in this section are for a coarser mesh with rectangular shaped cells of 2.5 mm x 4 mm (40×30). Simulations are performed with a time step of 1.5×10^{-3} s with 10 micro time-steps. Nucleation of grains is simulated using the instantaneous nucleation model described in 2.6.2.1.

Fig. 5.27 and Fig. 5.28 shows the evolution of solid fraction, grain density, temperature, average composition, liquid and solid velocity at 20 and 300 s. Cooling starts at the left wall. As soon as the local nucleation conditions are satisfied, solid grains are introduced. These grains start sedimenting as their density is larger than that of liquid. The rejection of solute from the solid to the liquid phase results in enrichment of liquid, making it heavier in accordance with Fig. 5.6c. The thermo-solutal convection along with the moving grains results in a counterclockwise flow. Further, the solid grains are also transported by the counterclockwise flow. While the large grains settle, the smaller grains are also transported into the superheated bulk liquid where they remelt. The three black iso-lines represent the solid fraction at 0.1, 0.2 and 0.3. Due to settling and transport of solid grains, they begin getting accumulated along the bottom side of the cavity where the highest solid fraction is found. Fig. 5.27a shows the average segregation profile in the cavity. Negative segregation associated with the depositing equiaxed grains is observed. Solute rich liquid above this zone of sedimented grains is also observed.

By 300 s, the cavity is divided into two distinct areas: slurry and packed areas. The slurry region exists in the upper part of the cavity and the solid fraction is much smaller than 0.1. In the packed region, the solid velocity is zero. The settling of solute-depleted grains results in the negative segregation at the bottom of the cavity. However, at the bottom of the ingot, some positive segregation zone is observed. This is due to the intragranular flow. The direction of the liquid flow in the packed region relative to the temperature grains results in an increase in concentration. This is in accordance with the equation:

$$\frac{\partial c}{\partial t} = -g_l \vec{v_l}.\nabla \langle c_l^i \rangle^1 = -\frac{1}{m_l^i} g_l \vec{v_l}.\nabla \left(T \right) \tag{5.6}$$

With further progress of solidification, the mushy region spans the whole cavity. The solute enriched heavy intragranular flow descends and moves along the bottom wall of the cavity, which induces local solutal remelting in the region. This remelting creates a channel where the liquid fraction is higher. Similar phenomena is also observed in other regions in the cavity which results in strong segregation patches.

Fig. 5.29 shows the final Pb segregation and grain density maps for **HH-move** simulations. We observe that the left half of the cavity has lower composition than the right half. A high number of grains in the lower-right corner results from the combination of liquid advection and grain sedimentaion, accumulation and packing. Fig. 5.29 shows the final Pb segregation and grain density maps for **SOLID**®, **SOLID**®$_{th}$ **- const** and **SOLID**®$_{th}$ **- const**: Scheme μSOLID. We observe that the results for **SOLID**® and **SOLID**®$_{th}$ **- const** are quite close, thus validating the implementation of the new microscopic growth model for the case of moving grains and liquid convection. We also observe that the solution for the new time integration scheme: μSOLID is also in good accordance with the other results. The differences could be attributed to the strong non-linearity of the solidification model. Table 5.4 lists the computational time used for the three cases. The increase in computational time from 41 h to 51 h for **SOLID**®$_{th}$ **- const** is attributed to the differences in regards to the implementation of
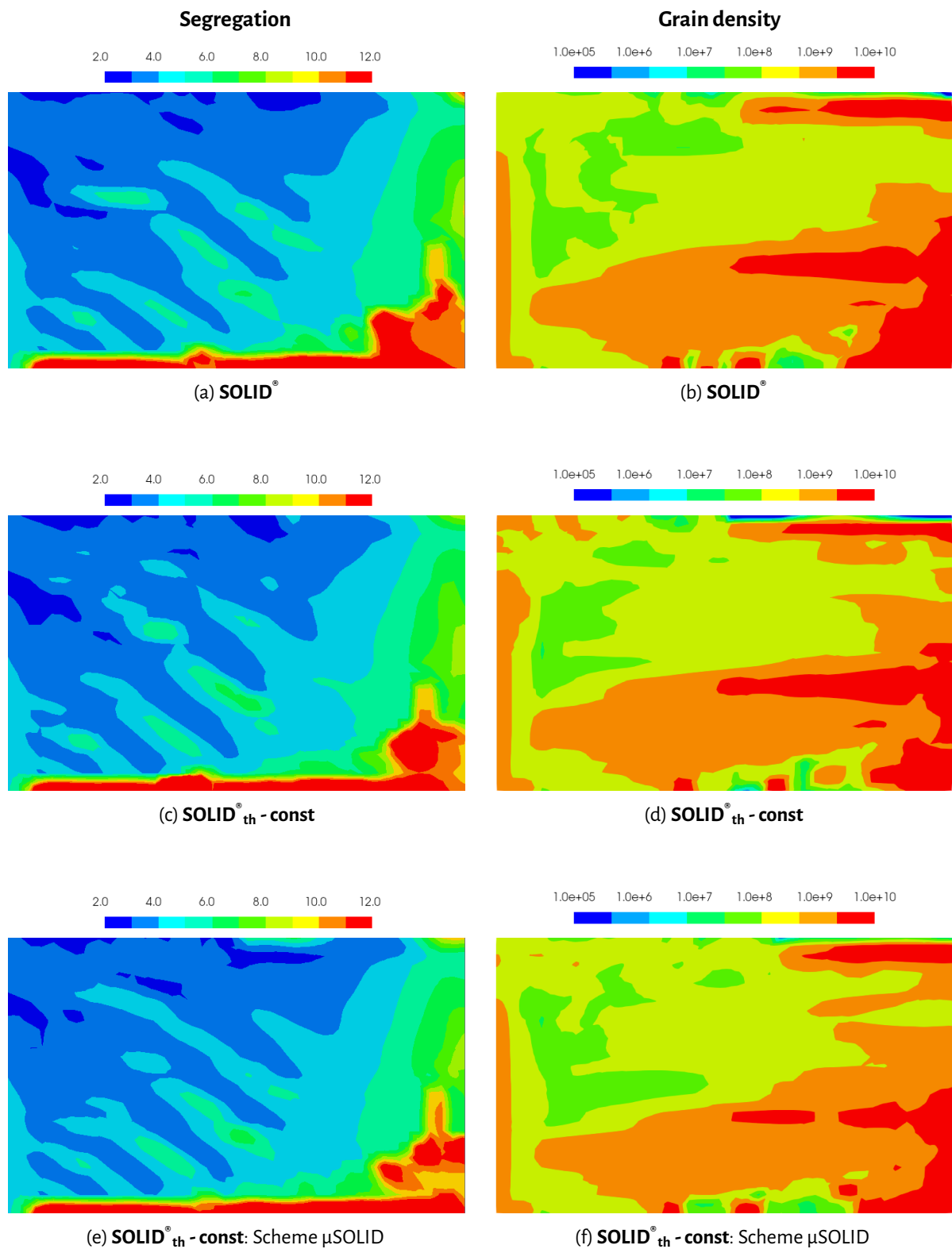
Figure 5.29 – Final Pb segregation and grain density maps for a) **SOLID**® b) **SOLID**®**th - const** and c) **SOLID**®**th - const**: Scheme μSOLID

the new microscopic growth model. A further increase in the computational time to 65 h for **SOLID**$^{®}_{th}$ **- const**: Scheme μSOLID is in accordance with discussion presented in 3.4.3.2. Further analysis needs to be done to understand the effect of scheme μSOLID on the final results. However, it is beyond the scope of this thesis and is a part of the future perspectives for the current work.

Table 5.4 – HH-move: Computational time

Simulation case	Computational time [h]
SOLID$^{®}$	≈ 41
SOLID$^{®}_{th}$ **- const**	≈ 51
SOLID$^{®}_{th}$ **- const**: Scheme μSOLID	≈ 65

HH-move

(a) **SOLID**$^{®}_{th}$ **- const**   (b) **SOLID**$^{®}_{th}$ **- var**
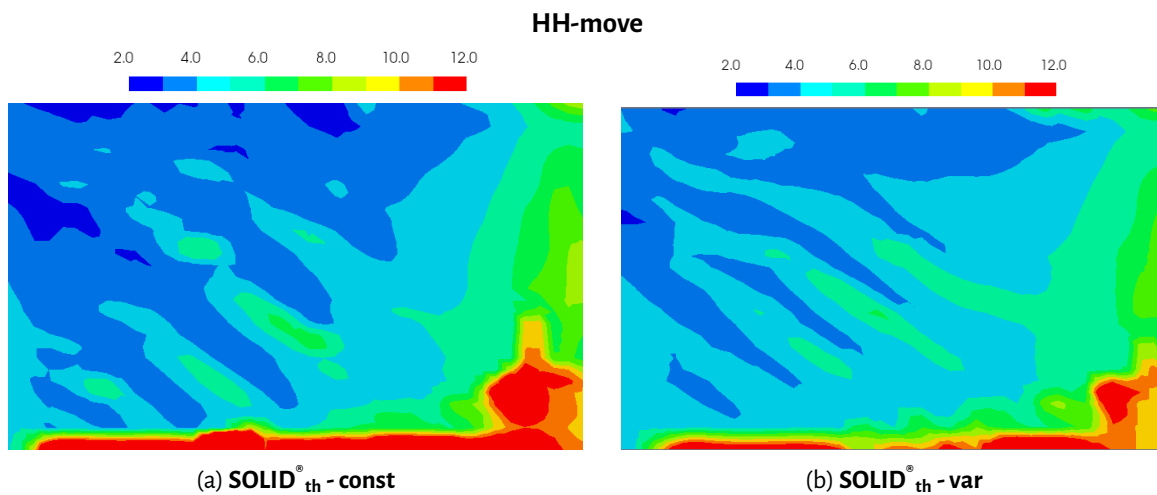
Figure 5.30 – Final Pb segregation and grain density maps for a) **SOLID**$^{®}_{th}$ **- const** and b) **SOLID**$^{®}_{th}$ **- var**

Fig. 5.30 shows the final Pb segregation map for **SOLID**$^{®}_{th}$ **- const** and **SOLID**$^{®}_{th}$ **- var**. The result for **HH-move: SOLID**$^{®}_{th}$ **- var** follows the similar trend as presented earlier for **HH-fix: SOLID**$^{®}_{th}$ **- var**. Coupling with CALPHAD data results in the reduction of macrosegregation and is primarily due the higher values of partition coefficient calculated for **SOLID**$^{®}_{th}$ **- var**. The position of the segregation channels remains unchanged. Fig. 5.31 shows the average solidification time for i) **HH-move: SOLID**$^{®}_{th}$ **- var** and ii) **HH-fix: SOLID**$^{®}_{th}$ **- var**. Solidification progresses faster when accouting for grain motion. This is due to the fact that when grain settle in the vicinity of the chill, it is replaced by a hotter liquid phase. Consequently, the heat transfer between the liquid metal and chill is higher which results in faster solidification. With no solid movement, the heat is extracted through the fixed solid layer.

5.2   Industrial application

In the previous section, SOLID$^{®}_{th}$ model was validated and applied to the simulation of Hebditch-Hunt benchmark case. The simulations were limited to model purely columnar or equiaxed solidification. However, in real
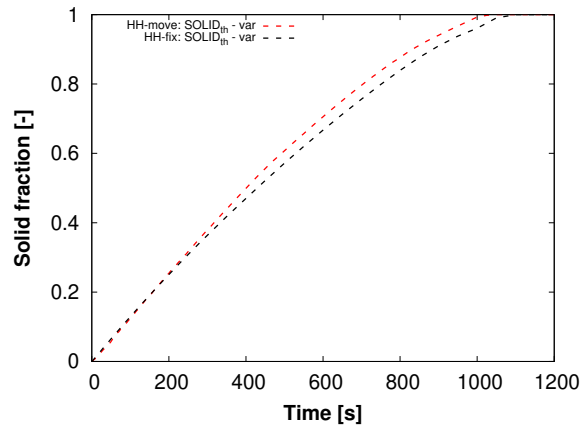
Figure 5.31 – Total solidification time for a) **HH-move: SOLID®_{th} - var** and b) **HH-fix: SOLID®_{th} - var** for the whole domain

ingots, transition in structure from columnar structure at the periphery to fine equiaxed structure at the center are observed. In this part, SOLID®_{th} model is applied to simulate the solidification of a 4.2 ton experimental research ingot cast by Industeel® as a part of the SOFT-DEFIS project. The model is used to explain the formation of observed structures and segregation during the solidification of the ingot.

5.2.1   Casting setup and observations

The main points concerning the ingot are recalled and summarized here. The setup of the ingot is shown in Fig. 5.32a. It has a square base of 0.55 m and height of 1.96 m. The mold is made of cast iron with a refractory cladding in the top 20 cm to create a hot top. Liquid steel fills the ingot from the base and a layer of protective powder is used during filling to prevent oxidation of the alloy and reduce heat loss. Once the ingot is filled, the liquid metal is covered with a layer of exothermal powder. The total solidification time of the ingot is around 2 h and 30 min (150 min). Thermo-couples have been placed in the mold to measure the evolution of temperature during casting. As a part of this investigation, 16 ingots were cast with four ingots per source plate. Fig. 5.33 shows a schematic representation of the casting configuration as well as the actual casting setup. The cast alloy is referred to as 18MND5 steel and the alloy composition is given in Table 5.5. No inoculants were used.

Table 5.5 – Chemical composition in wt% of 18MND5 steel

C	S	P	Si	Mn	Ni	Cr	Mo	Fe
0.197	0.002	0.0036	0.186	1.45	0.712	0.178	0.498	Balance

The cast ingot was analyzed by cutting it along its axis. macroetching was performed to identify the structure. Two distinct zones can be observed: columnar and equiaxed zone. Within the equiaxed zone, the grains can be further distinguished into large dendritic and fine equiaxed grains. The structure distribution of the cast ingot has been mapped and is shown in Fig. 5.34. The columnar zone is located along the mold wall and has a thickness in the range of 8-10 cm. The primary and the secondary dendrite arm spacing were measured. The experimental data was interpolated and is shown in Fig. 5.34. The large dendritic equiaxed grains are located in the top part of the ingot whereas the fine equiaxed grains were observed closer to the bottom part of the ingot. The dendritic equiaxed grains are located on the top part of ingot and are usually quite large ($\approx$ 10
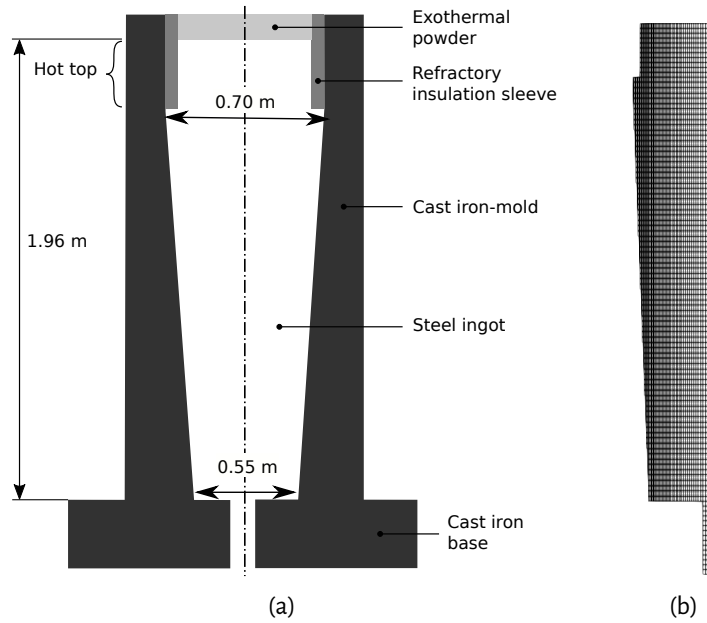
Figure 5.32 – a) Schematic representation of the casting alongwith the 2D geometry used for the simulations (not drawn to scale) and b) the mesh for the solidification domain.
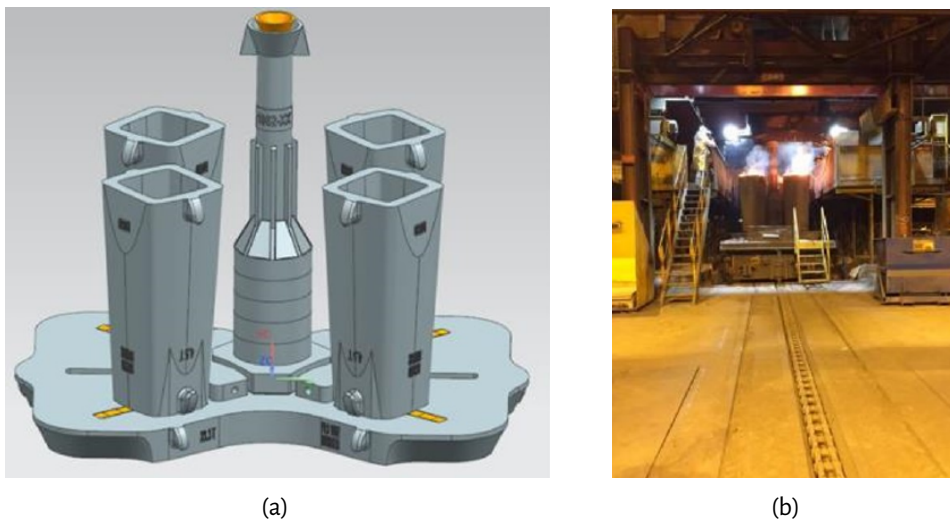
Figure 5.33 – a) Schematic representation of the casting setup and b) actual photo of the casting setup [161]

mm or more), whereas the fine equiaxed grains are smaller (less than 10 mm). Fig. 5.35 shows the three primary microstructures that have been observed. Further, to characterize the segregation profile, spectroscopy analysis was performed on sampled obtained from the open face of the ingot cross-section to measure the carbon segregation. Shallow holes of 8 mm were drilled and used for spectroscopy analysis. The segregation map shown in Fig. 5.34 plots the relative segregation value, i.e. $(c - c_0)/c_0$, with c_0 being the nominal composition. We observe a large negative segregation zone at the bottom of the ingot which is supposed to be mostly due to the settling of the equiaxed grains. The relative segregation values for carbon in this zone is $\approx$ -20% of the average composition. The top region, which is the last to solidify has a large positive segregation, with a maximum of +33% of the average composition. No composition measurements were performed in the hot top region and is thus not shown in Fig. 5.34.

a) Structures   b) PDAS (µm)   c) SDAS (µm)   d) Dendrite length (µm)   e) Relative segregation
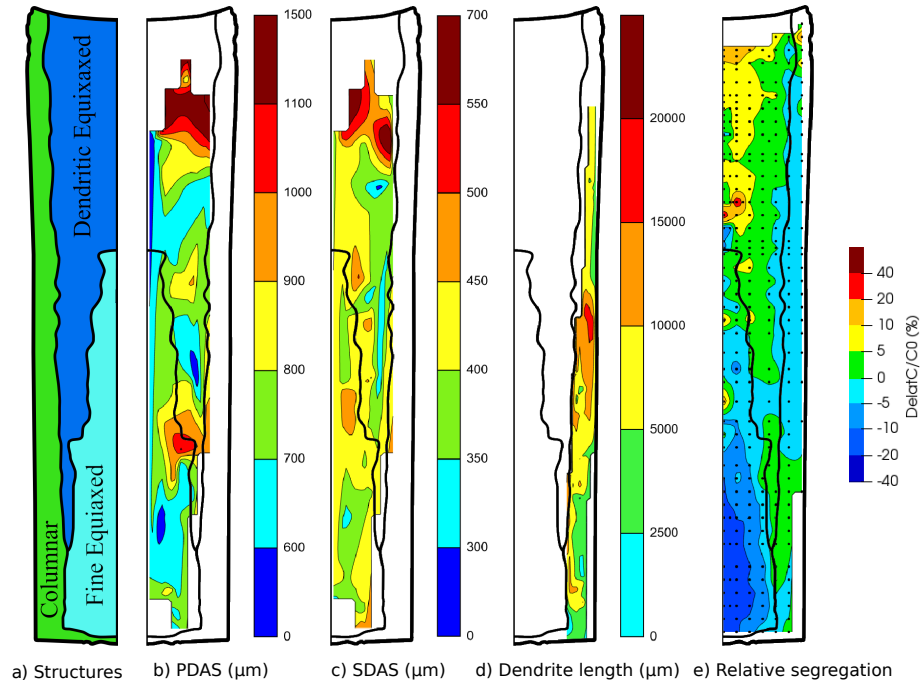
Figure 5.34 – Experimentally observed structure and segregation of 4.2 ton ingot [161]

(a)   (b)   (c)
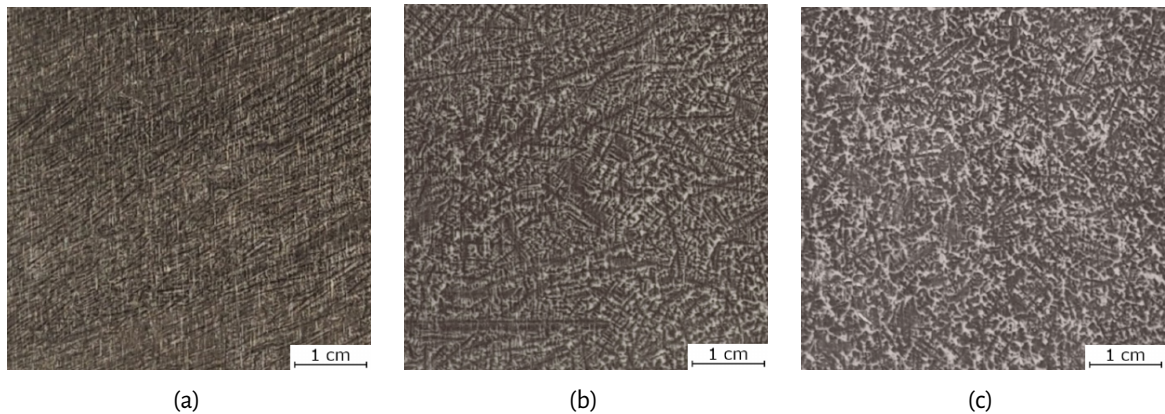
Figure 5.35 – The three types of experimentally observed structures in the 4.2ton ingot: a) columnar b) dendritic equiaxed and c) fine equiaxed. All the images were taken at an height of 45cm from the bottom of the ingot [161]

5.2.2 Simulation configuration

In the present simulation, we considered a ternary Fe-C-Cr alloy as highlighted in red in Table. 5.5, while neglecting the other alloying elements. In the present case, we limited the number of alloying elements to two, so as demonstrate the influence of multiple elements on the phase diagram parameters as well as the computational time of the simulations while keeping the result analysis simple. In the framework of our model, we consider a simplified 2D axis-symmetric geometry as shown in Fig. 5.32a. The mesh used for the simulation is shown in Fig. 5.32b. The mesh size at the center is 1 cm × 3 cm. The boundary condiditions applied on the various surfaces are given in the Table 5.7. The 'Mixed' condition in Table 5.7 corresponds to:

$$\text{Heat flux density} = h\left(T - T_{ext}\right) + \epsilon\sigma\left(T^4 - T_{ext}^4\right) \tag{5.7}$$

where h is the exchange coefficient, T_{ext} is the external temperature, ϵ is the emissivity and σ is the Stefan-Boltzmann constant. The thermophysical properties of the alloy are summarized in Table B.5. The phase diagram parameters corresponding to simulations with SOLID® have been listed in Table 5.6. The domain is discretized with rectangular shaper cells. The ingot is considered to be already filled by the liquid alloy with a temperature of 1523 °C, which corresponds to a superheat of 1 °C, at the start of the simulation. It is assumed that the main part of the superheat is evacuated during the filling stage.

Table 5.6 – Phase diagram parameters

Property	Symbol	Units	Value
Partition coeff. (C)	k_p^i	-	0.17
Partition coeff. (Cr)	k_p^i	-	0.91
Liquidus slope (C)	m_l^i	K(wt.%)$^{-1}$	-80.0
Liquidus slope (Cr)	m_l^i	K(wt.%)$^{-1}$	-1.3
Latent heat	L_f	kJkg^{-1}	292
Specific heat capacity	C_p	Jkg^{-1}K^{-1}	750

Table 5.7 – Boundary conditions

Boundary	Condition	Values
Ingot axis	Axis-symmetric	-
mold/air	Mixed	T_{ext}=20 °C, h=12 Wm^{-2}K^{-1}, ϵ = 0.7
Exothermal powder/air	Mixed	T_{ext}=100 °C, h=12 Wm^{-2}K^{-1}, ϵ = 0.7
Bottom of mold/ground	Constant temperature	T=20 °C
Ingot/exothermal powder	Perfect contact	-
mold/base	Thermal resistance	0.001 m^{2}KW^{-1}
Ingot/mold	Thermal resistance	0.0001 m^{2}K/W
Ingot/refractory sleeve	Thermal resistance	0.001 m^{2}KW^{-1}

Before presenting the results of the industrial ingot simulation, control volume Scheil solidification simulations were performed. This simulation helps assess the impact of variable interfacial phase diagram parameters, neglecting the impact of macrosegregation which can complicate the analysis of the final results.

5.2.3   Control volume solidification

Solidification simulations were performed for a closed control volume under the conditions of linear decreasing enthalpy. Fig. 5.4 shows the system dimension and the boundary condition used for the control volume

(a) Temperature

(b) Liquid density

(c) Liq. composition, C

(d) Liq. composition, Cr
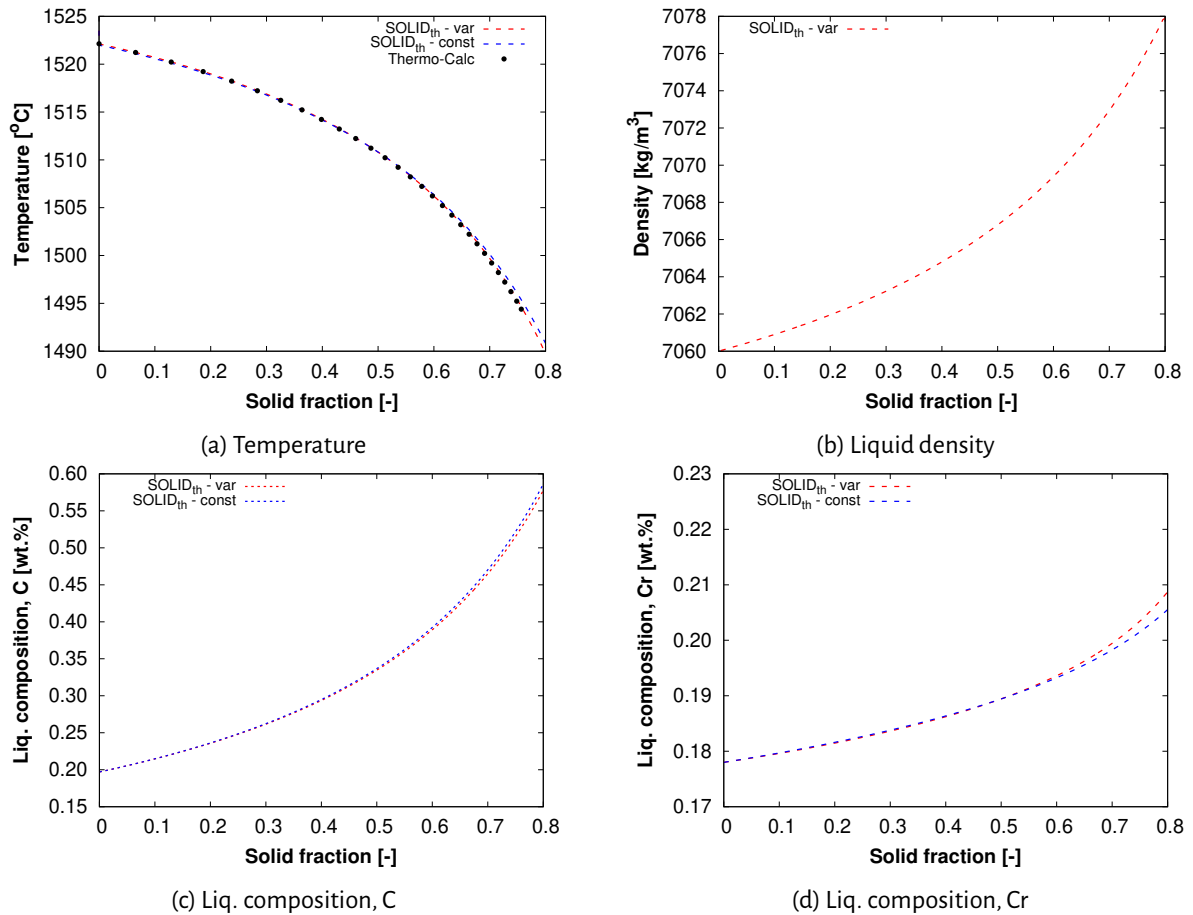
Figure 5.36 – a) Comparison of partial equilibrium solidification of the Fe-C-Cr alloy for **SOLID®th - const**, **SOLID®th - var** and Thermo-Calc® b) Density evolution during primary solidification for **SOLID®th - var** with the liquid composition evolution of c) carbon and d) chromium.

test case. As carbon is an interstitial element and chromium is a substitutional element, lever rule is assumed for carbon and Scheil solidification is assumed for chromium, and is further referred to as 'partial equilibrium solidification'. Primary solidification is assumed to finish as 1489.89 °C. Results are shown for three simulation cases:

– Thermo-Calc® using the TCFE9 database

– **SOLID®th - var**: simulations coupled to the phase diagram parameter using ANN-MLP

– **SOLID®th - const**: simulations assuming constant phase diagram parameters (Table 5.6)

Fig. 5.36a shows the evolution of temperature as a function of solid fraction. Thermo-Calc® results are retrieved by SOLID®th for the case **SOLID®th - var**. Thermo-Calc® results are only plotted upto a solid fraction of ≈ 0.75, as post this solid fraction, it predicts the solidification of secondary austenite (BCC_A2) phase due to which there is a change in the slope of the temperature vs solid fraction plot. Results for **SOLID®th - const** are quite close to the results for **SOLID®th - var**, with slight deviation towards the end of primary solidification. Similar trends are observed for the liquid composition evolution of carbon and chromium as shown in Fig. 5.36c and Fig. 5.36d. This deviation is attributed to the variations in the chromium composition evolution towards the end of solidification. This is the result of the variation in the partition coefficient of chromium as shown in Fig. 5.37d while the partition coefficient of carbon almost remains constant as shown in Fig. 5.37c.

(a) m_l^c (-80K(wt.%)$^{-1}$ for SOLID$^®$)

(b) m_l^{cr} (-1.3K(wt.%)$^{-1}$ for SOLID$^®$)

(c) k^c (0.17 for SOLID$^®$)

(d) k^{cr} (0.91 for SOLID$^®$)
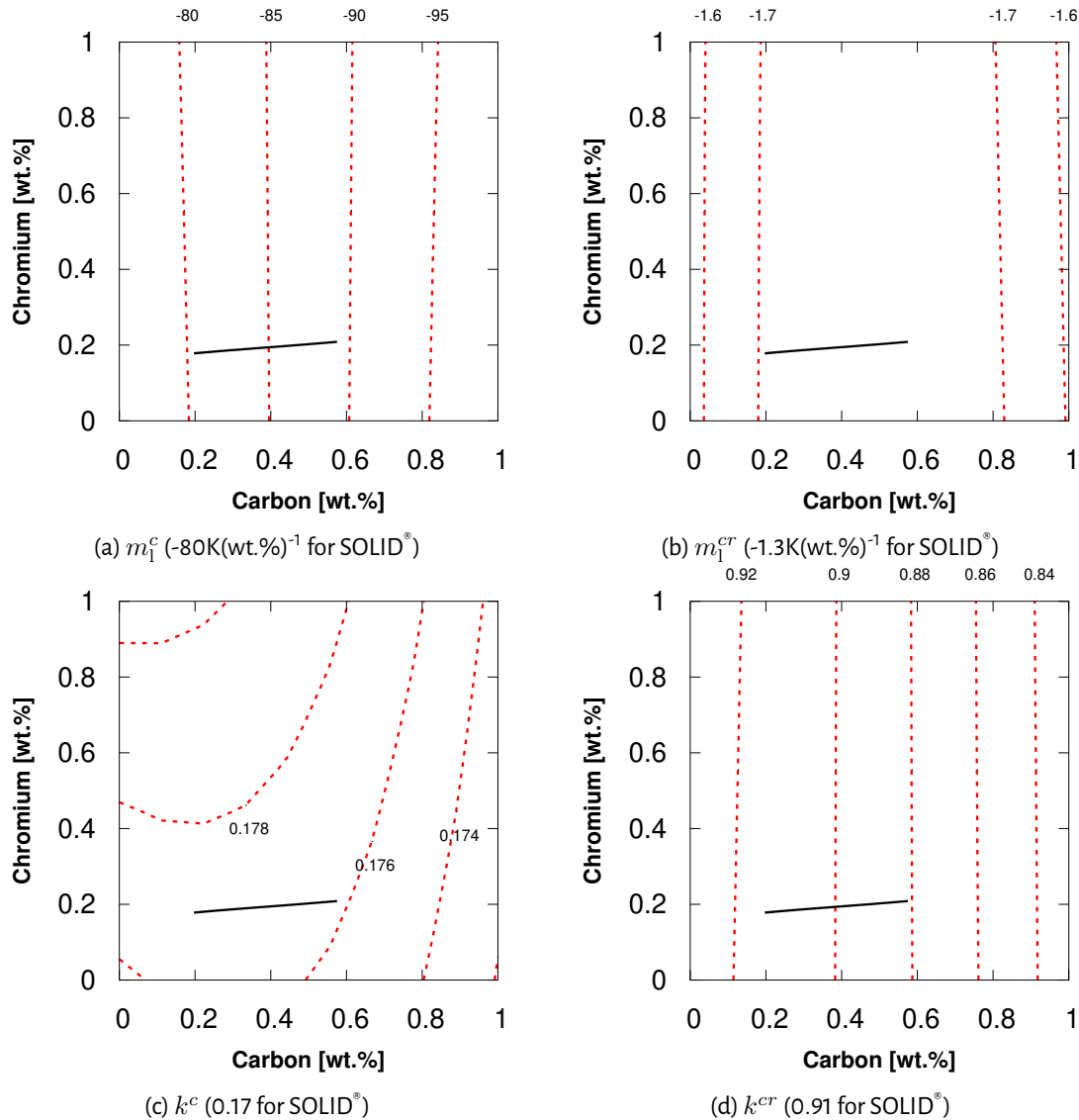
Figure 5.37 – Liquidus slope isolines (in red) for a) carbon and b) chromium and partition coefficient isolines (in red) for c) carbon and d) chromium for the Fe-C-Cr alloy with primary δ - ferrite phase along with the partial equilibrium solidification liquid composition evolution (in black)

However, as the magnitude of the liquidus slope of chromium is much smaller than carbon, the variation in liquid chromium composition does not affect the temperature evolution. The variation in the temperature evolution between **SOLID$^®$$_{th}$ - var** and **SOLID$^®$$_{th}$ - const** is a direct consequence of the liquidus slope of carbon as shown in Fig. 5.37a. Thus, as solidification progresses, the liquidus slope for carbon decreases and the equilibrium temperature predicted for **SOLID$^®$$_{th}$ - var** is lower than that for **SOLID$^®$$_{th}$ - const**. Fig. 5.36b shows the liquid density evolution for **SOLID$^®$$_{th}$ - var**. As the liquid composition evolution of **SOLID$^®$$_{th}$ - const** is similar to **SOLID$^®$$_{th}$ - var**, the liquid density evolution for **SOLID$^®$$_{th}$ - const** is not presented in Fig. 5.36b.

Fig. 5.38a shows the evolution of the phase enthalpy as well as the overall enthalpy evolution during primary solidification. The solid lines correspond to **SOLID$^®$$_{th}$ - var** while the dashed lines to **SOLID$^®$$_{th}$ - const**. The reference state for the enthalpy values are defined such that the enthalpy of the liquid phase at $g_s = 0$ is identical in both the data sets. The difference between the liquid and solid phase enthalpy obtained for **SOLID$^®$$_{th}$ - const** is higher on account of the larger latent heat value used. For **SOLID$^®$$_{th}$ - const**, this value cor-

(a)   (b)
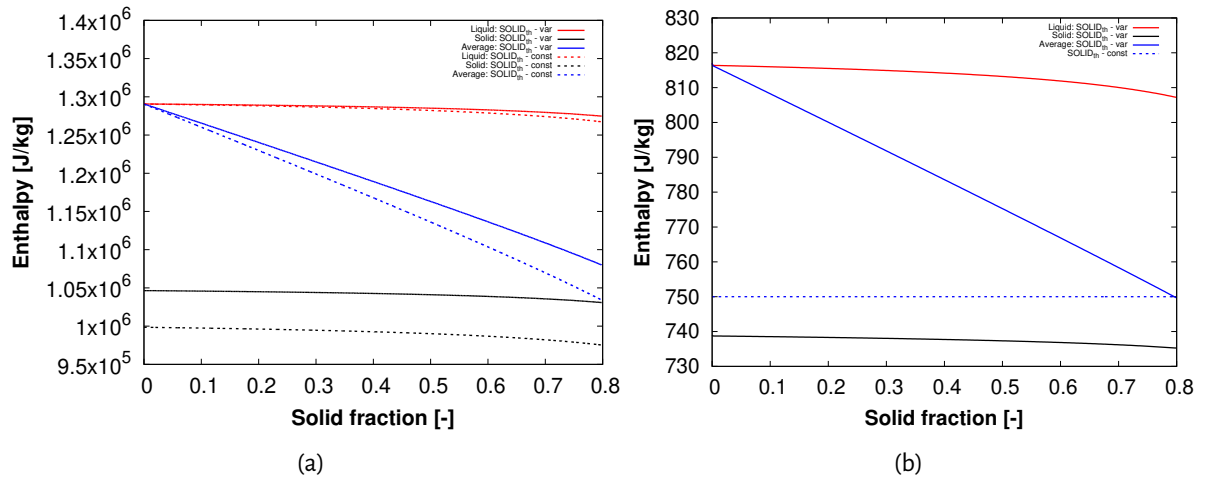
Figure 5.38 – Evolution of a) phase and average enthalpy and b) specific heat capacity obtained for **SOLID**[®]**th - var** and **SOLID**[®]**th - const** during partial-equilibrium solidification

Table 5.8 – Latent heat and specific heat capacity values used in literature

Reference	L_f [kJ kg^{-1}]	C_p(solid) [J kg^{-1} K^{-1}]	C_p(liquid) [J kg^{-1} K^{-1}]
Same C_p values for liquid and solid phase			
Ohnaka and Fukusako [162]	272	628	628
Combeau *et al.* [163] (δ - ferrite)	309	715	715
M'Hamdi *et al.* [164] (γ - austenite)	250	670	670
Combeau *et al.* [38] (δ - ferrite)	271	500	500
Li *et al.* [165] (δ - ferrite)	271	500	500
Li *et al.* [166] (δ - ferrite)	271	500	500
Cao *et al.* [167] (δ - ferrite)	270	625	625
Meng and Thomas [168] (δ - ferrite)	271	670	670
Sang *et al.* [169] (δ - ferrite)	299		
Different C_p values for liquid and solid phase			
Schneider and Beckermann [170] (γ - austenite)	270	650	800
Zhang *et al.* [171] (δ - ferrite)	271	760	824

responds to the fixed latent heat value of 292 kJ kg^{-1}, whereas for **SOLID**[®]**th - var**, this value is around of 244 kJ kg^{-1}. Further, the variation of the specific heat capacity of the liquid and solid phase is shown in Fig. 5.38b. Table 5.8 lists the latent heat and specific heat capacity values used for simulations for various steel grades. For most models, equal values of specific heat capacity are used for the solid and liquid phase. This is due to the constraint imposed by the model implemented. The works of Schneider and Beckermann [170] and Zhang *et*

al. [171] employ different values of specific heat capacity for the solid and liquid phase. While this list is non-exhaustive, this table highlights the large variations in the values of latent heat and specific heat capacity used in literature. The values of latent heat vary in the range of 250-310 kJkg^{-1}, which are usually much higher than the value of $\left(\langle h_l\rangle^l - \langle h_s\rangle^s\right)$ observed in the present simulation of 244 kJkg^{-1}. Similarly, the values of the specific heat capacity used are quite low when compared to the present simulation where the average specific heat capacity varies in the range of 815-750 Jkg^{-1}.K. The values employed by Zhang *et al.* [171] are closest to the values obtained for the present Scheil solidification simulation. However, these large variation in the values of latent heat and the specific heat capacity used in literature can significantly modify the simulation results as they impact solidification kinetics. In this regards, we would like to mention:

  – Employing CALPHAD data helps solve this issue (in concurrence with the aim of this thesis). While direct coupling may not be feasible for other models, an improved approximation of the phase diagram parameters can be suggested (similar to modified values of partition coefficient and liquidus slope suggested for the Hebditch-Hunt benchmark case in Section 5.1.2.1.2.)

  – In case of an alloy, the 'latent heat' term has no physical meaning, unless the effect of the alloying elements on the enthalpy is neglected. Since most models do not account for the effect of composition on the phase enthalpy, use of 'latent heat' is consistent. However, these quantities will be referred to as $\left(\langle h_l\rangle^l - \langle h_s\rangle^s\right)$ for **SOLID**®$_{\textbf{th}}$ **- var** results.

(a) **SOLID**®$_{\textbf{th}}$ **- var**   (b) **SOLID**®$_{\textbf{th}}$ **- const**
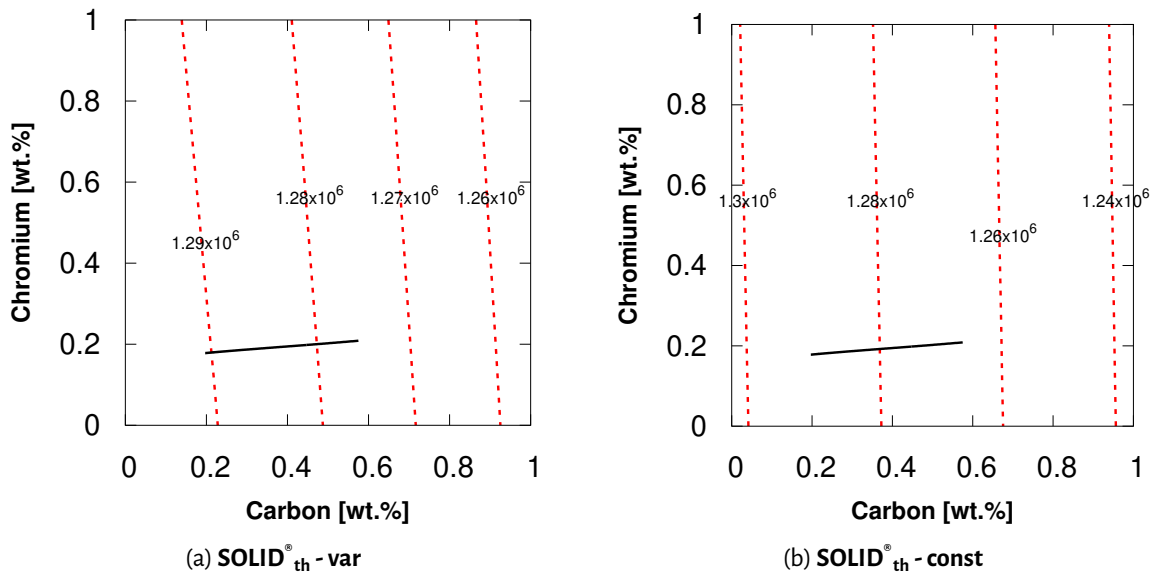
Figure 5.39 – Liquid enthalpy isolines (in red) at the liquidus temperature for a) **SOLID**®$_{\textbf{th}}$ **- var** and b) **SOLID**®$_{\textbf{th}}$ **- const** for the Fe-C-Cr alloy with primary δ - ferrite phase along with the partial equilibrium solidification liquid composition evolution (in black)

Fig. 5.39 shows the liquid enthalpy isolines at the liquidus temperature for **SOLID**®$_{\textbf{th}}$ **- var** and **SOLID**®$_{\textbf{th}}$ **- const**. The slope of the isolines obtained from the two models are different. The slope of the enthalpy isolines is a direct consequence of the liquidus surface, hence, the liquidus slope values used for carbon and chromium. Further, within the composition domain shown, the decrease in value of liquid enthalpy is larger for **SOLID**®$_{\textbf{th}}$ **- const**. This is attributed to the absence of composition effect on the phase enthalpy. Fig. 5.40 shows the evolution of the $\left(\frac{\partial \langle h_\phi\rangle^\phi}{\partial \langle c_\phi^i\rangle}\right)_{T,\langle c_\phi^{j\neq i}\rangle^\phi}$ for the elements carbon and chromium in both the phases during partial

equilibrium solidification. In the liquid phase, the $\left(\frac{\partial \langle h_1 \rangle^1}{\partial \langle c_1^i \rangle}\right)$ values for carbon and chromium are of the opposite sign with the magnitude of carbon being an order higher than chromium. This, coupled with the fact that the segregation of carbon is higher than chromium, we can assume that in the liquid phase, carbon dominates the liquid enthalpy change contribution due to composition change.

(a)   (b)
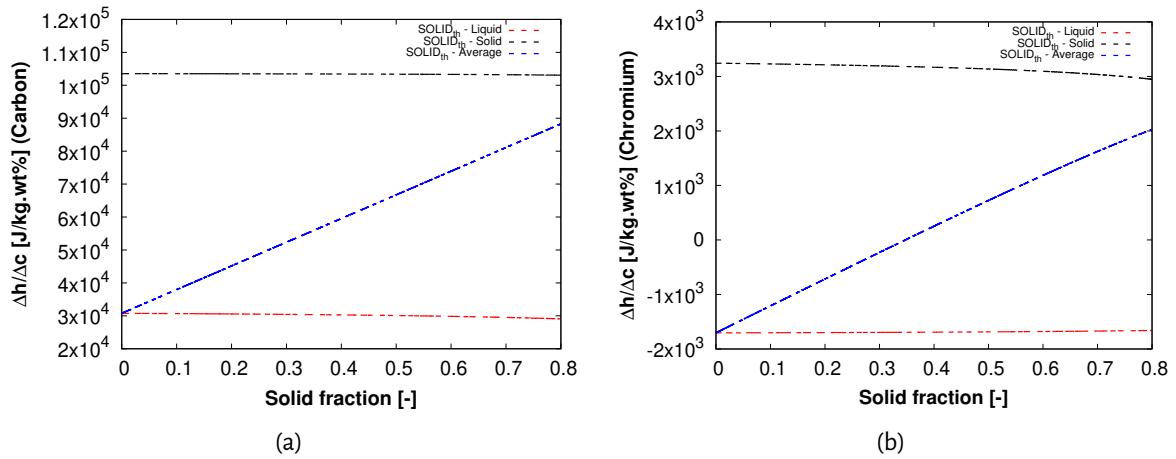
Figure 5.40 – Evolution of $\left(\frac{\partial \langle h_\phi \rangle^\phi}{\partial \langle c_\phi^i \rangle}\right)_{T, \langle c_\phi^{j \neq i} \rangle^\phi}$ parameter for a) carbon and b) chromium during partial equilibrium solidification
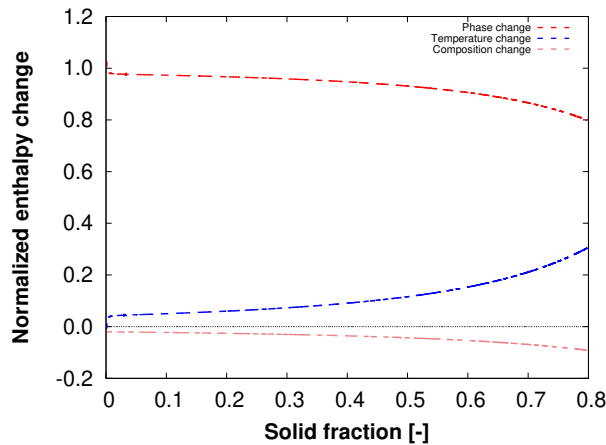
Figure 5.41 – Contribution of i) phase change ii) temperature change and iii) composition change to the decrease in enthalpy during partial-equilibrium solidification

As mentioned in chapter 3, the change in enthalpy is accounted to the change in the liquid fraction, temperature and composition. In the present model, they are the terms 'A', 'B' and 'C' in Eqn. 3.20 respectively. Restating the equation for the sake of convenience:

$$\mathrm{d}\langle h \rangle = A + B + C \tag{5.8}$$

$$A = \left(\langle h_1 \rangle^1 - \langle h_s \rangle^s\right) \mathrm{d}g_1 \qquad \text{Phase change}$$
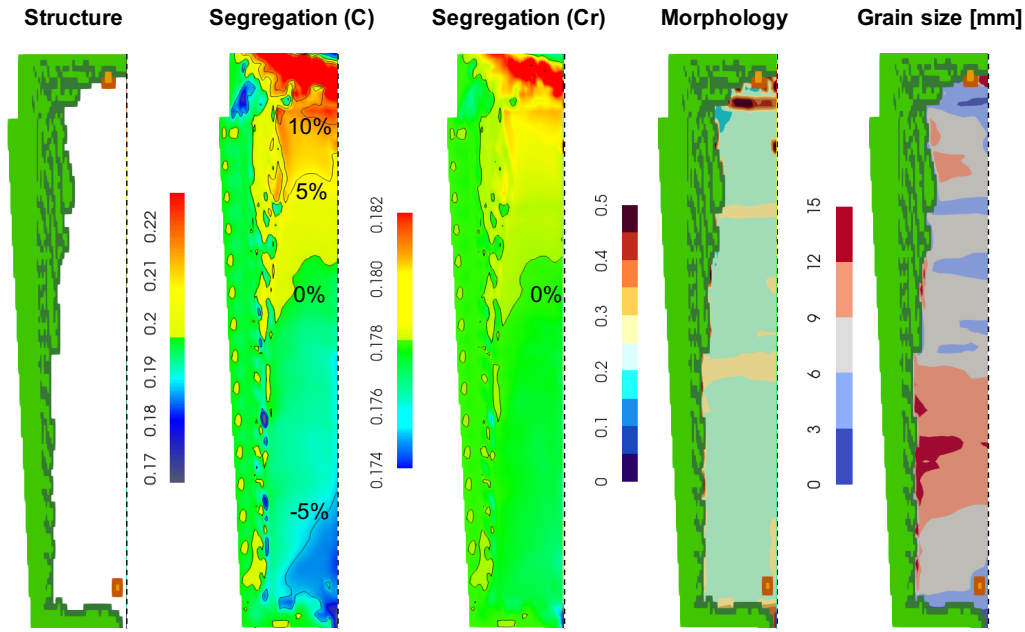
Figure 5.42 – Simulations results for **SOLID**$^{®}$**$_{th}$ - var**

$$B = \left[g_{s} \left(\frac{\partial \langle h_{s} \rangle^{s}}{\partial T} \right)_{\langle c_{s}^{i} \rangle^{s}} + (1 - g_{s}) \left(\frac{\partial \langle h_{l} \rangle^{l}}{\partial T} \right)_{\langle c_{l}^{i} \rangle^{l}} \right] \mathrm{d}T \qquad \text{Temperature change}$$

$$C = \left[g_{s} \sum_{i} \left(\frac{\partial \langle h_{s} \rangle^{s}}{\partial \langle c_{s}^{i} \rangle^{s}} \right)_{T} \mathrm{d} \langle c_{s}^{i} \rangle^{s} + (1 - g_{s}) \sum_{i} \left(\frac{\partial \langle h_{l} \rangle^{l}}{\partial \langle c_{l}^{i} \rangle^{l}} \right)_{T} \mathrm{d} \langle c_{l}^{i} \rangle^{l} \right] \qquad \text{Composition change}$$

For the Scheil solidification, these individual contributions were computed. Fig. 5.41 shows the normalized individual contributions of the three contributions. The values are normalized with the total enthalpy change. We observe that the enthalpy change due to phase change is the largest contribution to the total enthalpy change, with a subsequent decrease in this contribution as solidification progresses due to decrease in the rate of phase change. The temperature change contribution (sensible heat) is the second largest and also results in the decrease of enthalpy, similar to the phase change contribution. The composition contribution is the smallest and it results in an increase in enthalpy, unlike the other two contributions. Thus, we can conclude that the simulation results are most sensitive to the values of latent heat or $\left(\langle h_{l} \rangle^{l} - \langle h_{s} \rangle^{s} \right)$ and the specific heat capacity. The relative contribution of the latent heat or $\left(\langle h_{l} \rangle^{l} - \langle h_{s} \rangle^{s} \right)$ and the sensible heat is dependent on the solidification kinetics. Under limited diffusion in the liquid phase, the relative contribution can wary. Error introduced in the these values can have a significant impact on the solidification kinetics, specially for large ingots, as will be discusssed in the following section. Finally, enrichment of liquid during solidification results in an increase in liquid density as shown in Fig. 5.36b. The solid has a much higher density compared to liquid. The liquid and solid density have an impact on the liquid flow during ingot solidification, as will be seen in the following section.

(a) Centerline

(b) 0.12 m from centerline
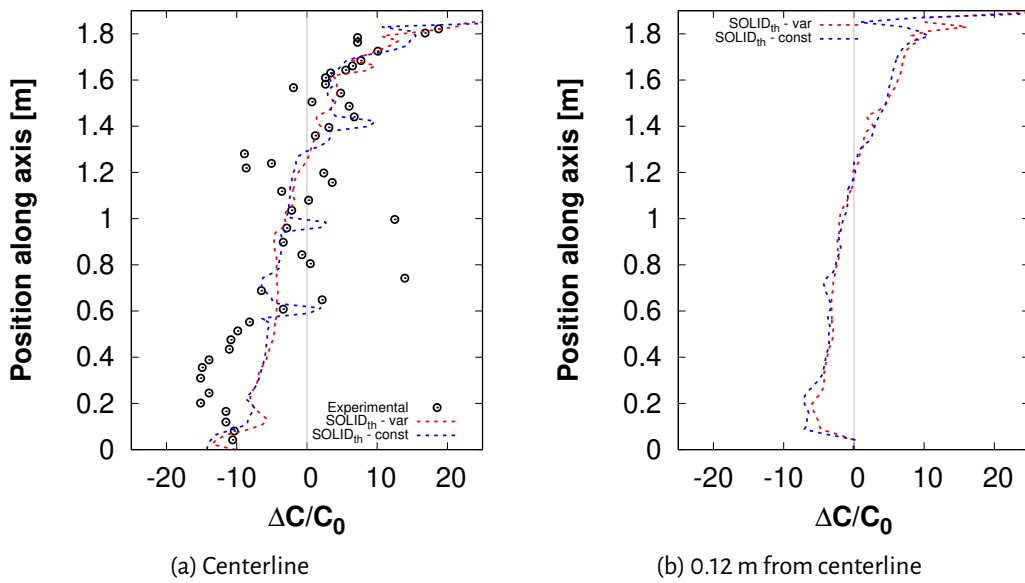
Figure 5.43 – Comparison of segregation ratio in carbon along the a) center-line and b) 0.12 m from centerline for for **SOLID**®_{th} **- var** and for **SOLID**®_{th} **- const** with the experimental results

(a) Centerline

(b) 0.12 m from centerline
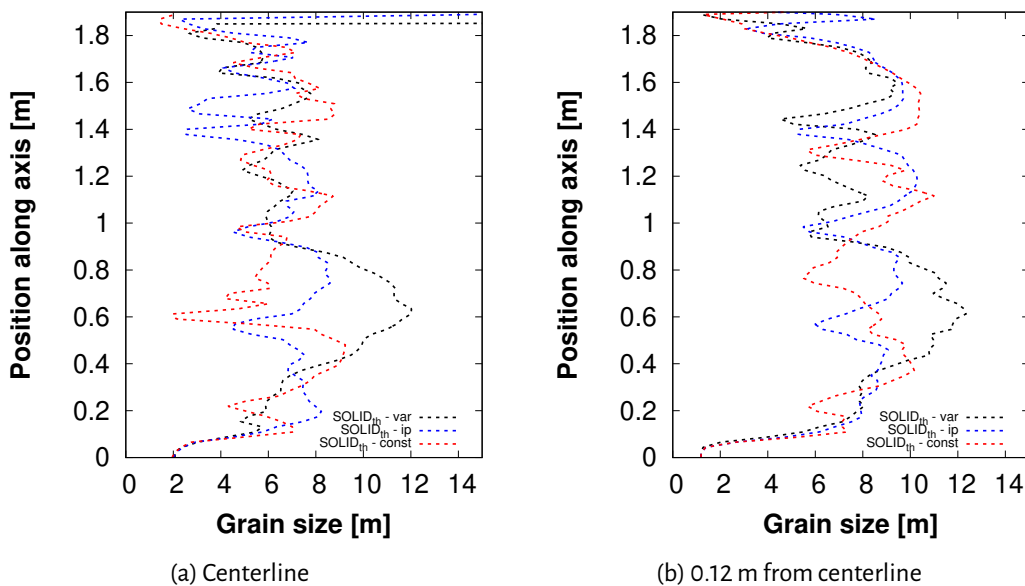
Figure 5.44 – Comparison of grain size along the a) center-line and b) 0.12 m from centerline for for **SOLID**®_{th} **- var** and for **SOLID**®_{th} **- ip** and **SOLID**®_{th} **- const**

Table 5.9 – Fragmentation parameters

Parameters	Value
Fragmentation flux density	500 m^{-2}s^{-1}
Thermal gradient activation threshold	100 Km^{-1}

5.2.4   Ingot solidification

Fig. 5.42 shows the simulation results obtained for **SOLID**®$_{th}$ **- var**. The columnar zone is in green and orange. The green color represents the primary columar grains growing from the mold wall, whereas the orange columnar grains represent the columnar grains that originate as a consequence of the equiaxed to columnar transition (ECT). The darker shades of the two colors represent the position of the columnar front. The rest of the zone is occupied by equiaxed grains. These equiaxed grains are produced by the fragmentation of the columnar grains. As mentioned in the previous chapter 3, the fragmentation flux is determined by two input variables: i) fragmentation flux density and ii) thermal gradient activation threshold. These two parameters are obtained by performing a sensitivity analysis such that the parameters which provide the results closest to the experimental ingot in terms of macrosegregation and structure is chosen. For the current simulations, the parameters associated with fragmentation are listed in Table 5.9.

The columnar zone thickness varies from around 8 cm in the lower domain to 14 cm at the upper domain. While the values in lower domain are in accordance with the observed columnar thickness, the values observed in the upper zone are not. It is observed that the thickness of the columnar grains is higher at the bottom as compared to top. The simulation do not capture this trend and could be attributed to the absence of mold filling [172]. The predicted equiaxed grain size is shown in Fig. 5.44. It is within the observed range, however, no distinct zones of large and small equiaxed grains are observed. This is due to the fact that grain size distribution is a direct result of the complex interaction between grain sedimentation and grain introduction due to fragmentation of the columnar grains, and will be discussed in detail in the following section. The equiaxed grains are quite dendritic as shown by the morphology distribution, the values of which are mostly in the range of 0.2-0.3. Similar to the grain size distribution, no distinct morphology zones (fine, dendritic), as observed in the experimental results are predicted. Finally, the segregation maps are shown for carbon and chromium. Following the centerline, the simulation predicts positive segregation of carbon and chromium and a transition to the negative segregation in the downward direction. Off the centerline, a conically shaped negative segregation zone at the bottom of the ingot is observed. These trends are in good agreement with the measured tendencies. The intensity of positive segregation in the hot top for carbon are in good agreement with the observed values, however, the intensity of negative segregation at the bottom is under-predicted. Fig. 5.43a shows the observed and simulated carbon segregation ratio along the centerline of the ingot. The experimental observations also show that below the positive segregated hot top, there is a small zone of negative segregation which is followed with a small positive segregated region. The simulated results do not capture such transitions.

5.2.4.1   Temporal evolution of ingot solidification

The evolution of the ingot solidification in the presence of free floating dendritic grains is shown in Fig. 5.45. The solidification starts with the formation of columnar grains at the surface of the ingot. At 60 s (Fig. 5.45a),
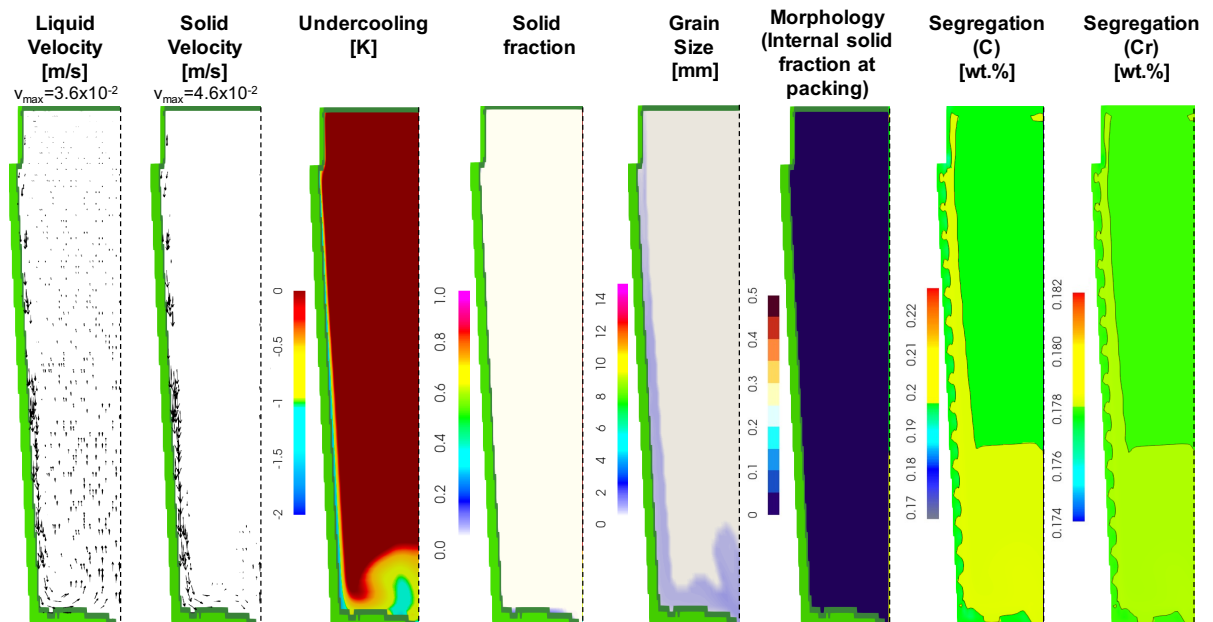
(a) 60 s
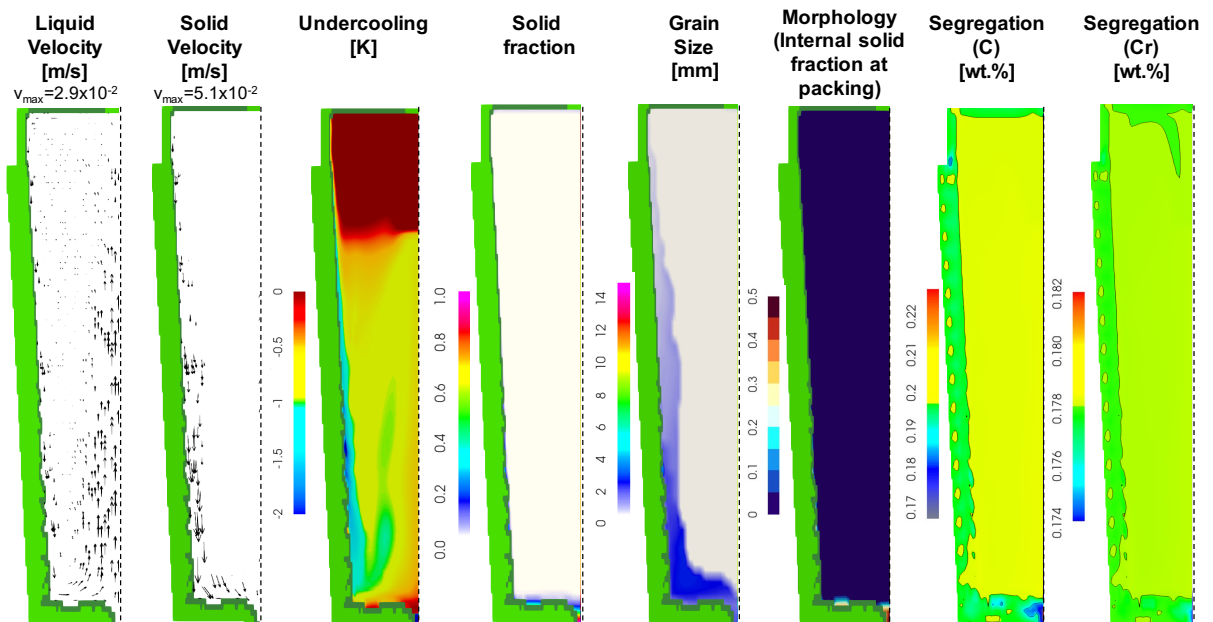
(b) 300 s
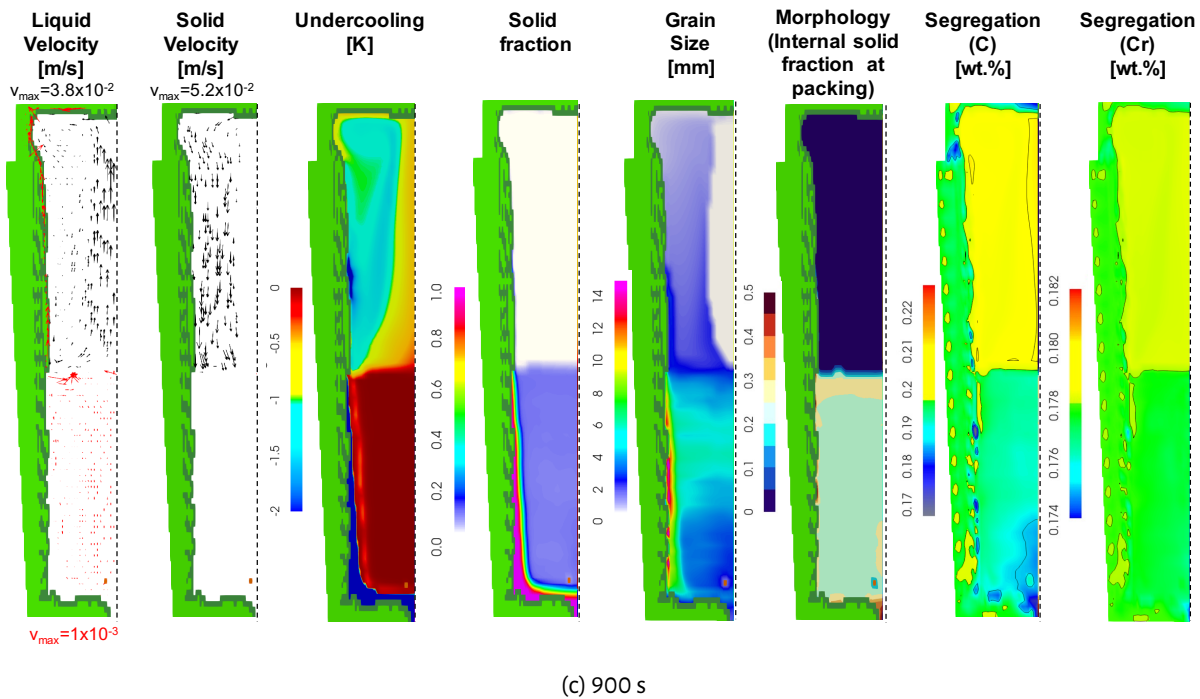
(c) 900 s

Figure 5.45 – Maps of various parameters at a) 60 s, b) 300 s and c) 900 s for the Q550 ingot simulation for case **SOLID®th - var**

the columnar structure is already a few centimeters thick, the thickness being higher at the base than at the vertical ingot surface due to faster cooling. The cooler liquid adjoining the ingot surface has a higher density and descends along the columnar grains. As solidification progresses and the local thermal conditions for fragmentation of the columnar dendrites are satisfied, equiaxed grains are introduced by a flux of fragments across the columnar front. Since the solid phase is heavier than the liquid phase, as shown in Fig. 5.36b, the equiaxed grains descend along the columnar zone and entrain the liquid to flow downward, creating a strong anti-clockwise flow in the core of the ingot. The local undercooling and the time before packing are the parameters which primarily determine the grain size. Equiaxed grains originating in the upper part of the ingot grow and sediment, while those originating in the lower part are small and are swept up into the superheated liquid, where they remelt. The sedimenting grains do not block the growth of the columnar front and are subsequently entrapped in the columnar zone.

At around 300 s (Fig. 5.45b), the sedimenting equiaxed grains block the columnar front. As the columnar grains in the bottom of the ingot are the first to be blocked, the thickness of the columnar zone is the lowest here. The equiaxed grains are assumed to be blocked at a grain fraction of $g_{env} = 0.4$. Most of the domain except for the top part of the ingot are undercooled. As solidification progresses, the undercooling increases and at around 550 s, most of the ingot is undercooled. The long distance the equiaxed grains travel before sedimenting, accompanied with a higher undercooling results in large dendritic grains. These dendritic grains occupy a much larger volume (g_{env}) as compared to the solute-lean solid (g_s). Thus, these grains quickly fill up the volume of the ingot core while depositing very little solid mass, due to which the tendency for negative segregation due to grain sedimentation is quite weak, and is shown in Fig. 5.45c (at 900 s). With time, as the equiaxed grains are packed, the solute segregation builds with time due to the movement of the intragranular liquid (shown in red in Fig. 5.45c) in the packed layer. Post 900 s, solidification progresses with the sedimentation of remaining equiaxed grains as well as the new grains originating from the top of the ingot. The whole

of the ingot is filled with equiaxed grains in about 6000 s which explains the thicker columnar region at the top. During this time, strong positive segregation at the top of the ingot develops. This enrichment originates from the global circulation of the intragranular liquid.

5.2.4.2   Impact of phase diagram parameters

(a) **SOLID®th - const**
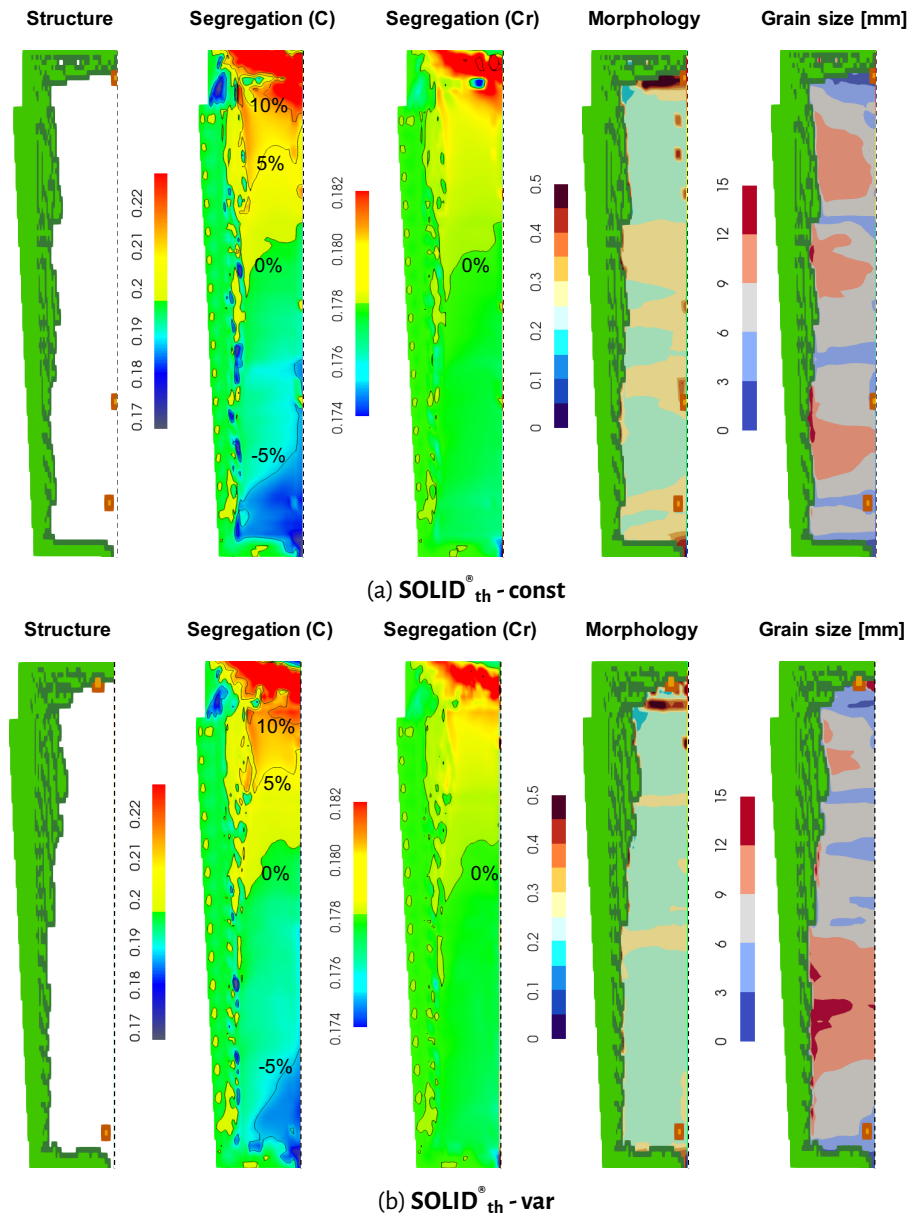
(b) **SOLID®th - var**

Figure 5.46 – Comparison of results for a) **SOLID®th - const** and b) **SOLID®th - var** at the end of solidification

To understand the impact of coupling the simulation with CALPHAD data, results for **SOLID®th - const** are compared with **SOLID®th - var**. Fig. 5.46 shows the results for **SOLID®th - const** and **SOLID®th - var**. It is observed that the segregations maps for carbon and chromium obtained for the two cases are very similar except for a slightly larger negative segregation cone at the base for **SOLID®th - const**. The axial segregation profile along the center-line and at a distance of 0.12 m from the centerline for the two models are quite similar as shown in Fig. 5.43. The similarities are in accordance with the discussion in section 5.2.3. The primary difference lies

in the structure obtained. The grain size and the morphology differ, and is a direct consequence of the difference in heat transfer and liquid flow conditions in the ingot. As mentioned earlier, the difference between the results for **SOLID**®**$_{th}$ - const** and **SOLID**®**$_{th}$ - var** is a combination of:

– Modification to phase enthalpies

– Modification to interfacial phase diagram parameters - partition coefficient and liquidus temperature
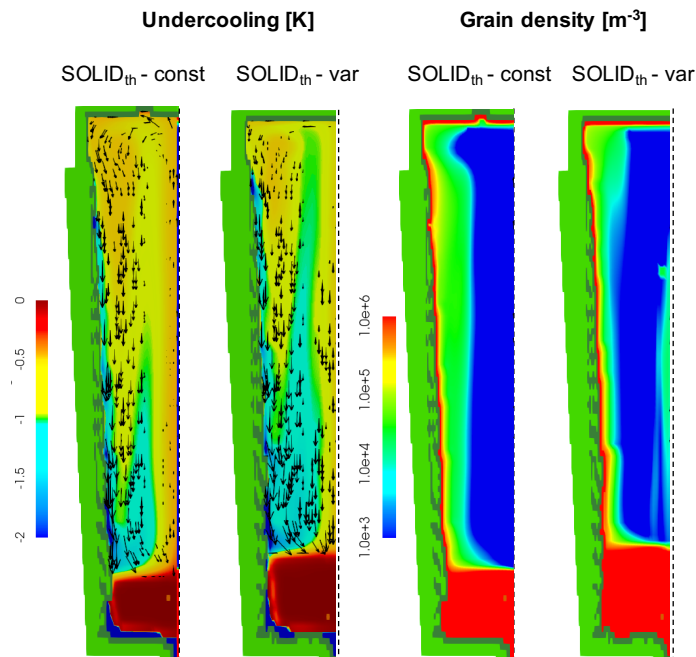
Figure 5.47 – Comparison of undercooling and grain density for **SOLID**®**$_{th}$ - const** and **SOLID**®**$_{th}$ - var** at 600 s
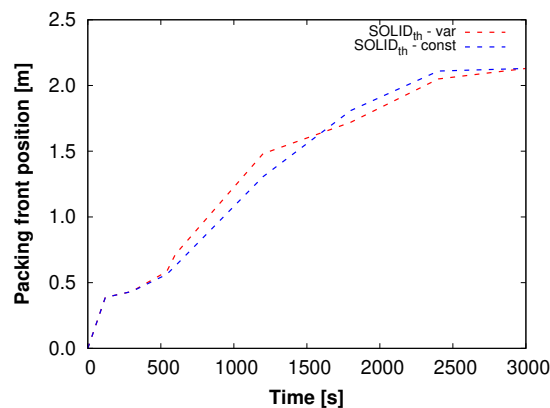
Figure 5.48 – Evolution of position of packing front for **SOLID**®**$_{th}$ - const** and **SOLID**®**$_{th}$ - var**

5.2.4.2.1 Assessing the impact of modification to phase enthalpies: Fig. 5.47 shows the undercooling and grain density for **SOLID**®**$_{th}$ - const** and **SOLID**®**$_{th}$ - var** at 600 s. Around this time, the equiaxed zone with large grains at the base of ingot for **SOLID**®**$_{th}$ - var** is being formed by the sedimentation of equiaxed grains. It is observed that undercooling observed for **SOLID**®**$_{th}$ - var** is higher than **SOLID**®**$_{th}$ - const**. This is attributed to

the lower values of $\langle h_l \rangle^l - \langle h_s \rangle^s$ in **SOLID®$_{th}$ - var** which results in more reduction of sensible heat, leading to a higher undercooling. Further, the grain density for **SOLID®$_{th}$ - var** is also lower. This results in the formation of equiaxed zone with grain size reaching a maximum of 12.5 mm for **SOLID®$_{th}$ - var**. For **SOLID®$_{th}$ - const**, the maximum grain size is around 10 mm. This also results in the grains being more dendritic for **SOLID®$_{th}$ - var**. It is around this point that the thickness of the packed equiaxed zone for increases faster for **SOLID®$_{th}$ - var**. The thermal condition prevaling within the ingot evolve with time. However, packing front movement can be correlated to the grain size observed. Fig. 5.48 shows the temporal evolution of packing front position for **SOLID®$_{th}$ - var** and **SOLID®$_{th}$ - const**. The packing front moves faster for **SOLID®$_{th}$ - var** at lower heights, and faster for **SOLID®$_{th}$ - const** at higher heights. This results in relatively larger grains for **SOLID®$_{th}$ - var** at lower heights and larger grains for **SOLID®$_{th}$ - const** at higher heights. This also influences the thickness of the columnar zone similarly. Faster movement of the packing front results in earlier blocking of the columnar front and a lower thickness of the columnar zone. While this effect is not significant at lower heights, at higher heights, it results in columnar zone for **SOLID®$_{th}$ - var** being 17.7 cm thick as compared to 12.5 cm for **SOLID®$_{th}$ - const**.
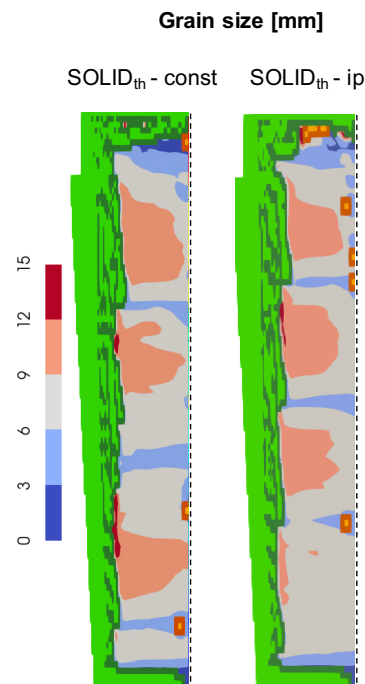
Figure 5.49 – Comparison of grain size map for **SOLID®$_{th}$ - const** and **SOLID®$_{th}$ - ip** at the end of solidification

5.2.4.2.2 Assessing the impact of modification to interfacial phase diagram parameter:

The partial equilibrium solidifcation for the Fe-C-Cr alloy showed almost identical solidification paths for **SOLID®$_{th}$ - const** and **SOLID®$_{th}$ - var**, thus, highlighting the minimal impact of the variable interfacial phase diagram parameters. To further confirm the small impact of the interfacial phase diagram parameters (liquidus slope and partition coefficient), simulations are performed for **SOLID®$_{th}$ - ip**. As structure of the ingot is of interest, only the equiaxed grain size and the columnar zone thickness is presented in Fig. 5.49. It is observed that the equiaxed grain size distribution as well as the columnar zone thickness are not similar for **SOLID®$_{th}$ - ip** and **SOLID®$_{th}$ - const**. This indicates that variation of partition coefficient and liquidus temperature is significant, such that it modifies the thermal conditions within the ingot, thus affecting the structure of the ingot. Figs. 5.44a and

5.44b shows the grain size along the centerline and at a distance of 0.12 m from the centerline respectively. The cause of this difference could be attributed to the impact of phase diagram parameters on the dendrite tip velocity. However, further investigation needs to be performed.
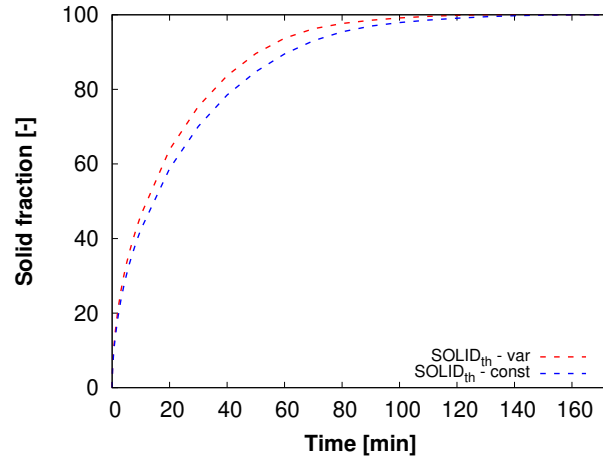
(a)

Figure 5.50 – Comparison of a) segregation profile along the centre axis
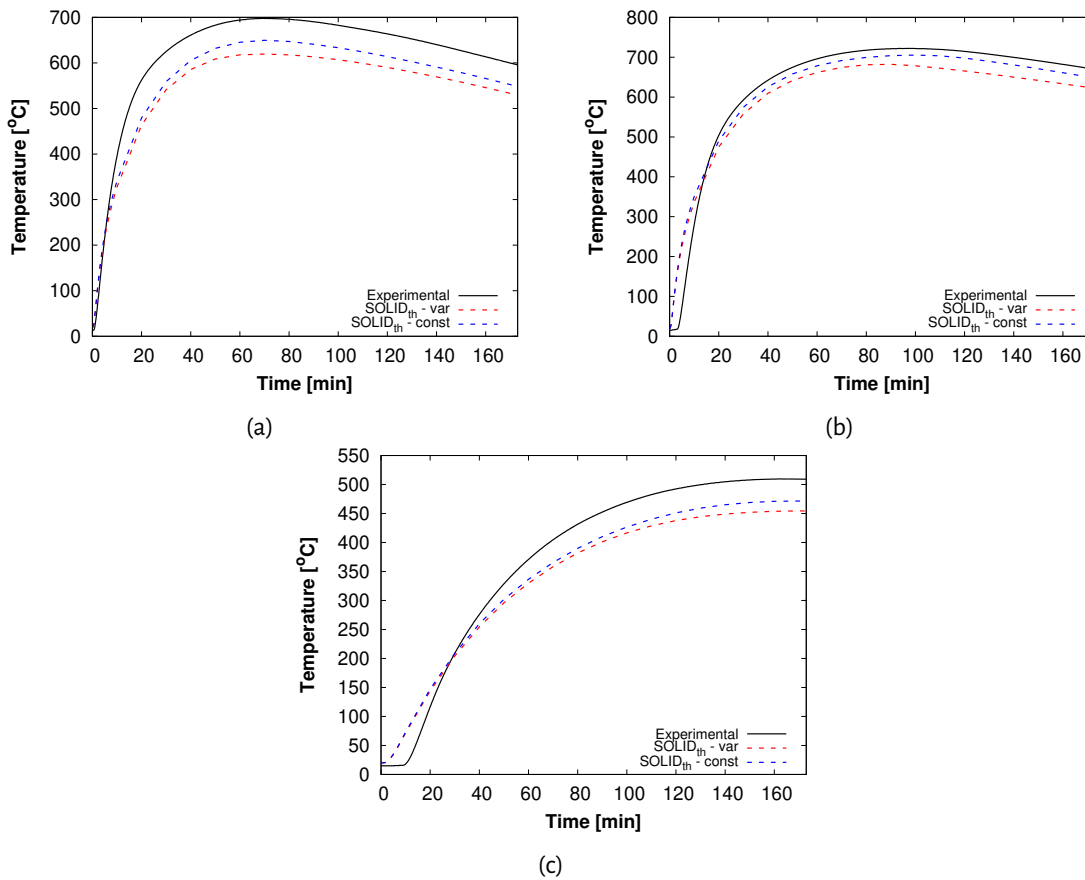
(a)

(b)

(c)

Figure 5.51 – Comparison of temperature evolution in the mold between the experimental measurments and simulation results obtained from SOLID® and SOLID®th. The experimental temperature evolution is the average of six thermo-couples for each height a) 0.3 m b) 0.89 m and c) 1.86 m

Table 5.10 – Computational time for various simulations cases

Model	Computational time [h]
SOLID®$_{th}$ **- const**	≈ 13
SOLID®$_{th}$ **- var**	≈ 21.5
SOLID®$_{th}$ **- ip**	≈ 16

Thus, unlike the Hebditch-Hunt benchmark case, modified constant phase diagram parameters cannot be suggested here. Both, the modification to phase enthalpies as well as the modification to the interfacial phase diagram parameter modifies the final structure of the cast ingot. A simulation was performed with a modified value of latent heat (244 kJ)kg^{-1}). The result produced was different to the above presented cases, and is hence not presented here. Fig. 5.50 shows the evolution of the average solid fraction in the ingot for **SOLID**®$_{th}$ **- const** and **SOLID**®$_{th}$ **- var**. The total solidification time for both the simulations are around 150 min which is in good accordance with the reported value. The **SOLID**®$_{th}$ **- var** case undergoes faster solidification. This is primarily due to the lower values of $\langle h_l \rangle^l - \langle h_s \rangle^s$. Fig. 5.51 compares temperature evolution in the mold obtained from the two models with the values obtained from the thermocouples. While the temperature evolution profile are similar, the values are lower for the simulations (lower for **SOLID**®$_{th}$ **- var** due to the lower values of $\langle h_l \rangle^l - \langle h_s \rangle^s$). Further improvements are needed with respect to the boundary conditions used in the simulations. Table 5.10 shows the computational time used by the simulations.

5.2.4.3 Impact of diffusion length model

Simulations were performed for **SOLID**®$_{th}$ **- var** with the new diffusion length model proposed in Chapter 4. The two diffusion length models will be further referred to as the 'Tveito model' (TM) and the 'Modified Martorano model' (MMM). Fig. 5.52 shows the results for **SOLID**®$_{th}$ **- var** with MMM and TM. It is observed that the results obtained for the two liquid diffusion length models are similar for most of the parameters, except for the grain morphology. Fig. 5.53 shows the grain size and morphology of the grain within the packed region for the two cases. The equiaxed grain size is similar upto a height of 1 m for both the cases. Similar observations are made for the thickness of the columnar zone. However, the morphology of the grains are significantly different. Upto a height of 1 m, the MMM diffusion length predicts $\approx 50\%$ more dendritic grains as compared to TM. As the grain size is also similar for the two cases, the highly dendritic grains for MMM is attributed to lower grain density. The low grain density is due to the less fragmentation of the columnar grains observed for MMM cases. It is hypothesized that the lower undercooling for MMM causes the thermal gradient criteria for fragmentation not to be satisfied. Further analysis needs to be performed to have a better understanding of the impact of the new diffusion length model.

5.3 Summary

The solidification model SOLID®$_{th}$ is applied to model the solidification of a benchmark experimental ingot (Hebditch-Hunt) and an industrial ingot. The main points of this chapter can be summarized as follows:

– **Hebditch-Hunt benchmark case for Sn- 5 wt.% Pb alloy:** For the Hebditch-Hunt benchmark case,

(a)

(b)
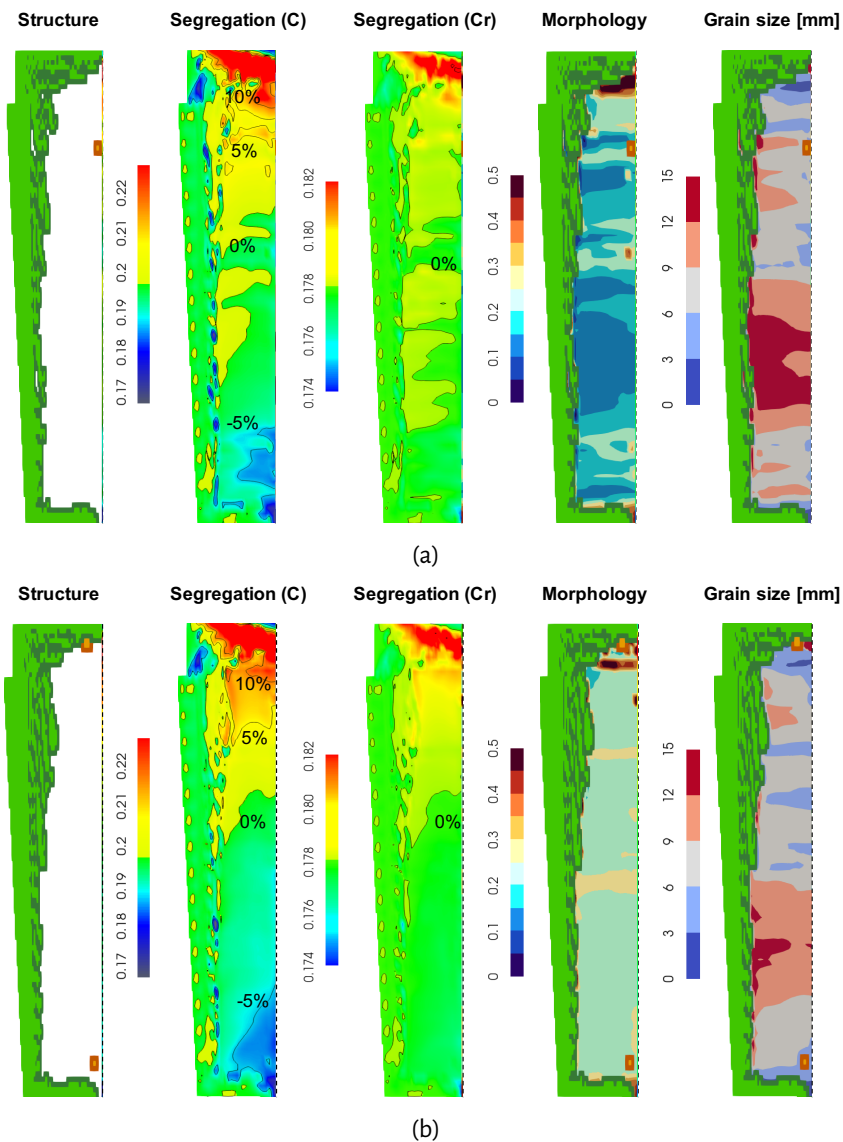
Figure 5.52 – Comparison of results from SOLID®th at the end of solidification for a)modified Martorano b) Tveito *et al.* [173] (re-stated for the sake of convenience) diffusion length models

two simulation cases are established. The first case corresponds to fixed solid grains and is used to simulate the growth of columnar grains in the Hebditch-Hunt setup. The first simulation was performed to validate the implementation of the new micromodel for cases pertaining to liquid convection. Subsequently, simulations are performed with constant and variable phase diagram parameters. It is observed that the simulations with variable phase diagram parameters predict lower segregation as compared to constant phase diagram parameters. This is primarily due to the large partition coefficient calculated using ANN-MLP. The partition coefficient used for the constant phase diagram corresponds to a composition close to the eutectic composition. However, since most of the segregation happens at higher liquid fraction, the modified partition coefficient value suggested corresponds to the nominal composition of the liquid. Using the new partition coefficient value, the segregation result predicted is similar to the result predicted using variable phase diagram parameters. However, using the modified partition coefficient results in a small amount of

(a) Centerline

(b) 0.12 m from centerline

(c) Centerline

(d) 0.12 m from centerline
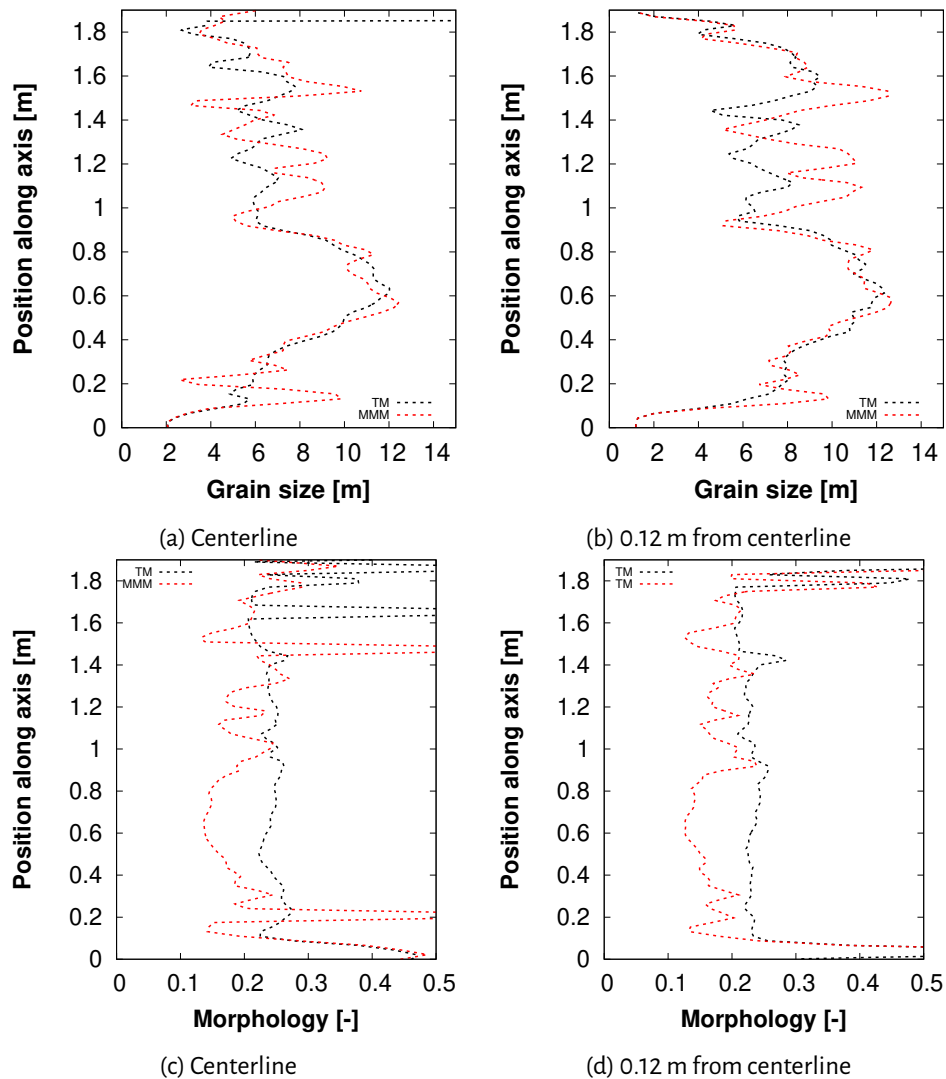
Figure 5.53 – Grain size and morphology along the a) centerline and b) 0.12 m from centerline for TM and MMM

eutectic phase fraction at the end of solidification.

Second set of simulations were performed for the Hebditch-Hunt setup with moving grains. Similar to the fixed grains case, the first simulation was performed to validate the implementation for cases pertaining to liquid convection and grain motion. Subsequently, simulations are performed with constant and variable phase diagram parameters. Similar to the fixed grains case, simulation with variable phase diagram parameters predicts lower segregation on account of the higher partition coefficient. The implementation of a new time integration scheme: μSOLID was also validated.

– **Q550 ingot for Fe- 0.197 wt.% C - 0.178 wt.% Cr alloy:** The simulations show the impact of grain movement on the ingot structure and segregation profile. Results obtained from simulations accounting for variable phase diagram parameters were compared with simulation with constant parameters. Accounting for variable phase diagram parameters does not affect the segregation maps for carbon or chromium. However, the structure of the ingot is significantly affected by the incorporation of the phase diagram parameters. Unlike the Hebditch-Hunt benchmark case, modified constant parameters could not be defined, thus highlighting the limitations of models with con-

stant phase diagram parameters. Simulation was performed with the new diffusion length model. The segregation maps for carbon and chromium are quite similar. However, the grains are predicted to be upto 50% more dendritic for this case.

Chapter 6 :   Conclusions and Perspectives

Contents

6.1 Conclusions

Solidification remains one of the most complex problems faced by industries on a regular basis. Computational methods have become an efficient tool to understand the influence of various phenomena on the final segregation and structure of the cast product. There are various limitations which pose significant problems to the accurate modeling of solidification. Two key limitations are:

- **Model assumptions:** Most of the models are based on certain simplifying assumptions which limit the prediction capability of a model

- **Constitutive models:** In a muti-scale approach to model solidification, accurate representation of micro-structural phenomena is critical

In this situation, the present thesis aims at improving the solidification model by focusing on improving the factors which limit their prediction capability. During the course of our work, four main tasks were accomplished. These can be summarized as follows:

- **Modification to the implementation of the microscopic growth model in SOLID**®

  - **Modification to account for variable phase diagram parameters**

    The microscopic growth model consists of solving a set of equations which describe the solute diffusion controlled grain growth kinetics. The set of equations are: i) enthalpy balance equation ii) interfacial solute balance equation, iii) interfacial equilibrium equation and iv) solute mass balance in the solid and liquid phase. To account for variable phase diagram parameters, the formulation and implementation of these equations are modified. The new formulation of the enthalpy balance equation (Eqn. 3.31) is able to account for the effect of composition change on the enthalpy change during solidification. This information was absent in the earlier formulation. The implementation of the new formulation poses problems with regards to the interfacial equilibrium equation (Eqn. 3.34). Access to the interfacial concentration when the initial state is complete liquid is non-physical. Special treatment for such cases have been implemented and discussed in Section 3.4.3. The microscopic growth model was implemented for equiaxed solidification (two phase globular as well as the three phase dendritic model) and was validated with single control volume solidification test-cases. The microscopic tip velocity model used for the dendritic grains is also modified so as to account for the variable phase diagram parameters. The new microscopic growth model formulation was also implemented and validated for the six phase model which accounts for columnar and equiaxed grains and is used to model columnar to equiaxed transition (CET).

  - **New time integration scheme (μSOLID)**

    An update to the splitting approach is presented. The new time integration scheme: μSOLID, is proposed with regard to coupling the microscopic growth model with the macroscopic model outputs. It is currently validated for equiaxed solidification and applied to the solidification of the Hebditch-Hunt benchmark test case. Preliminary results are presented for μSOLID scheme and show some differences in the results. The larger computation time of μSOLID scheme is attributed to the division of macroscopic contribution over each

micro time-step. However, detailed analysis needs to be performed to understand the impact of the new scheme.

— **Effecient approach to couple the solidification model to Thermo-Calc® data**

Accurate and efficient access to Thermo-Calc® data is critical to an accurate modeling of solidification. Earlier approaches to coupling the solidification model to Thermo-Calc® were directly coupling the solidification model using the TQ-Interface® or using a tabulation approach along with an interpolation technique. These approaches are deemed to be computationally expensive for multi-component systems. Thus, we propose a regression approach in which the required thermodynamic data , obtained with Thermo-Calc® are imported in terms of computationally cheap regression relationships. The first step was to identify the thermodynamic functions required from Thermo-Calc® (listed in Table 3.6). These thermodynamic functions affect the macroscopic heat transfer as well as the microscopic growth model. The thermodynamic functions identified were of varying nature. The varying nature of different thermodynamic functions results in different features that are used in the regression relations. Hence, instead of determining unique features for regression relations pertaining to individual thermodynamic functions, ANN-MLP is proposed as the choice to generate regression relationships. Quantitative validation of the regression relationships were performed using the Mean squared error (MSE) metric and have been presented for Al-Si, Sn-Pb and Fe-C-Cr systems. Directions to improve the use of Thermo-Calc® data for producing the regression relationships have also been discussed. Finally, the coupling of the Thermo-Calc® data with the solidification model has been validated by comparing the Scheil solidification results obtained from SOLID®th and Thermo-Calc®.

— **Extending the liquid diffusion length proposed by Martorano *et al.* [32] to account for liquid convection**

Multi-scale modeling of solidification requires accurate modeling of microstructural phenomena such as grain morphology and the solute profile in the phases. The solute profile in the liquid phase is approximated through a constitutive model for the diffusion length in the liquid phase. Various diffusion length models have been studied and compared to an exact solution for a pure diffusive test case. The study shows that the diffusion length proposed by Martorano *et al.* [32] gives the result closest to the exact solution. However, the model is limited to pure diffusive cases. Hence, using a stagnant film approach, the model is extended to account for liquid convection. The new diffusion length model has been applied to modeling of solidification in a large industrial ingot.

With the accomplishment of the tasks mentioned above, SOLID®th is validated and applied to model the solidification of ingots. To understand the influence of the variable phase diagram input parameters on the final results, simulations were performed with different sets of input parameters for the phase diagram data. The three sets of input parameters are: i) interfacial phase diagram parameters constant along with phase enthalpies modeled with constant C_p and L_f ii) variable interfacial phase diagram parameters along with phase enthalpies modeled with constant C_p and L_f and iii) variable phase diagram parameters as well as the phase enthalpies dependent on composition and temperature. The model is applied to two cases:

— **Hebditch-Hunt benchmark case for Sn- 5 wt.% Pb alloy**

For the Sn-Pb alloy, the initial analysis is performed for the Scheil solidification of a closed system. Accounting for variable interfacial phase diagram parameters results in lower segregation due to

the higher value of partition coefficient. Subsequently, simulations were performed for the test case. Most of the analysis was done with the case where solid grains were assumed to be fixed (columnar solidification). The influence of the modification with regards to the phase enthalpies being dependent on composition and temperature on the final Pb segregation in the cavity is found to be minimal. However, significant impact of the variable interfacial phase diagram parameters, specially the partition coefficient is observed. The results obtained are compared with the experimental results. The simulation results are in good agreement with the experimental data and are an improvement over the result obtained using fixed phase diagram parameters. Modified values of the fixed phase diagram parameters are proposed and used for a simulation. Notably we showed that the best choice for the partition coefficient is the value close to the liquidus temperature for the nominal concentration due to macrosegregation mainly developing at high liquid fraction. The segregation results obtained improve, however, the predicted amount of eutectic phase fraction is significantly reduced.

— **Q550 ingot for Fe- 0.197 wt.% C - 0.178 wt.% Cr alloy**

Similar to the approach for the Hebditch-Hunt benchmark case, the initial analysis is performed for the Scheil solidification of a closed system. Accounting for variable interfacial phase diagram parameters does not have an impact on the segregation result. This is due to the small variations in the liquidus slope and partition coefficient during the solidification domain. However, for the simulation of the large ingot, coupling the simulation with a variable phase diagram parameter results in modification of the result. The segregation profile remains largely unaltered which is in accordance with the Scheil solidification results. However, the grain size map changes substantially. This modification is attributed to the difference in latent heat and specific heat capacity of the phases which modifies the heat transfer along with the solid and liquid flow during solidification. Simulation is also performed with the new proposed liquid diffusion length. Modification to the liquid diffusion length affects the segregation map as well as the grain size and morphology. The segregation map obtained is closer to experimental observation as compared to the earlier simulation. The grains are $\approx 50\%$ more dendritic, which is attributed to the reduced fragmentation of columnar grains. This reduction of fragmentation is due to the modification to the temperature field.

Both the simulations highlight the importance of coupling the model with Thermo-Calc® data. While the relative importance of certain phase diagram parameters depends on the alloy system, coupling the models with Thermo-Calc® data has improved the result when compared to simulations with constant phase diagram parameters. During the course of this study, improved values corresponding to fixed phase diagram parameters have been suggested. While these improved parameters do not completely replicate the results of a simulation with all phase diagram variables, they improve the simulation results. The new proposed diffusion length model is also an improvement on the previously used diffusion length model. The CPU time for the various simulations were also compared in Chapter 5 (Table 5.10 for the industrial ingot solidification). We observe that the CPU time increases for SOLID®$_{th}$ model. The increase in CPU time can be attributed to: i) modification to the implementation of the microscopic growth model ii) calculation of the interfacial phase diagram parameters via ANN-MLP iii) calculation of the phase enthalpies via ANN-MLP. While the individual contribution of the three factors have not been quantified, it is generally observed that calculation of phase enthalpies via ANN-MLP is the major contribution to the increase in CPU time. Thus, for simulations where the interfacial phase diagrams are only critical, simulations with only varying the interfacial phase diagram parameters can be performed without a significant increase in the CPU time, highlighting the efficient ap-

proach towards coupling SOLID® with CALPHAD data. Even accounting for variable phase enthalpies does not drastically increase the CPU time. Thus, we can safely conclude that an original and an efficient way for coupling SOLID® with CALPHAD data has been proposed and implemented.

6.2 Perspectives

A solidification model accounting for variable phase diagrams has been implemented. While various issues have been worked and improved upon, there are still points that remain open to subsequent improvements as well as some further analysis on various aspects of the model. Several propositions can be made:

- **Application to higher order systems:** Currently, the model has only been applied to a binary (Al-Si, Sn-Pb) and ternary (Fe-C-Cr) system. It remains to be seen how the model performs for higher order systems. Initial observations with regards to the regression relationships for a quaternary system (Fe-C-Cr-Mn) are that the number of nodes in the hidden layer in ANN-MLP are not significantly different as compared to that for a ternary system, thus highlighting the ease of extensibility of this approach to a higher order system.

- **Incorporation of density data from Thermo-Calc®:** Density evolution plays a critical role in the development of the eventual liquid flow. Currently, the liquid density evolution for the thermo-solutal convection contribution is obtained via the Boussinesq approximation and the solid density is assumed to be constant. Fig. 6.1 shows the liquid and the solid density evolution for the Scheil solidification of Fe- 0.197 wt.% C - 0.178 wt.% Cr alloy obtained in SOLID® and Thermo-Calc® (with the TCFE9 database). While the profile for the density evolution are quite similar for both the models, the values are quite different and can have a significant impact on the segregation and structure of the cast ingot. Hence, better approximation of the parameters for the density evolution is proposed for future developments.

(a)   (b)
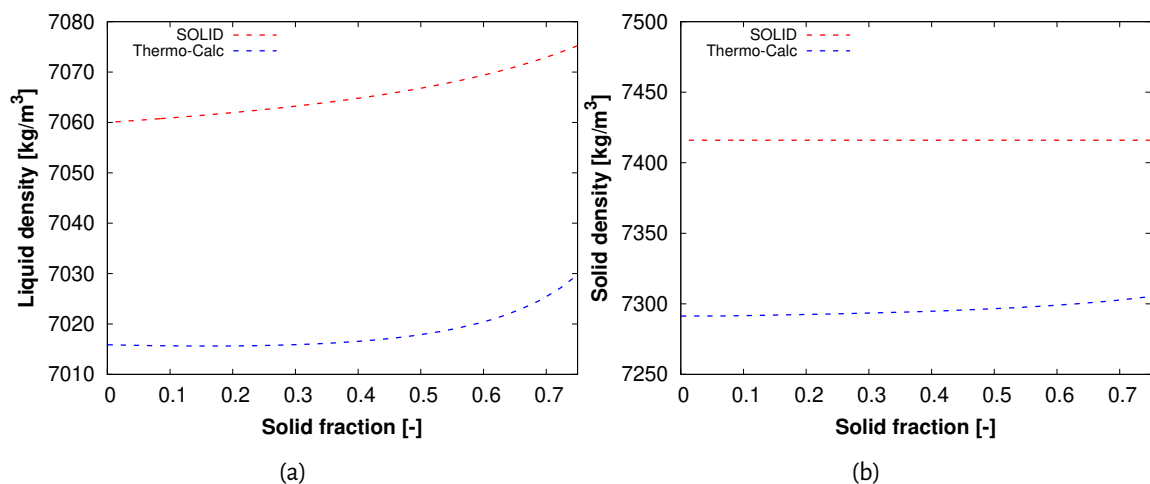
Figure 6.1 – Evolution of a) liquid density and b) solid density for the Scheil solidification of Fe- 0.197 wt.% C - 0.178 wt.% Cr alloy

- **Impact of the special treatment for a case where the initial state is pure liquid:** As pointed out earlier, for the implementation of the interfacial equilibrium relationship (Eqn. 3.34), if the initial

state is complete liquid, we perform a special treatment as given in Eqn. 3.40. Presenting Eqn. 3.40 again (for the sake of clarity)

$$\implies {}^{\mathbf{j+1}}T - T^* \left({}^{\mathbf{v+1}}[\langle c_l^i \rangle^l]^{\mathrm{tr}} \right) = \sum_i m_l^i ({}^{\mathbf{j+1}}c_l^{*i} - {}^{\mathbf{v+1}}[\langle c_l^i \rangle^l]^{\mathrm{tr}})$$

As mentioned earlier, the logic behind this treatment is that we need combination of temperature and composition which lies on the liquidus surface. Thus we compute the liquidus temperature (T^*) for the composition ${}^{\mathbf{v+1}}[\langle c_l^i \rangle^l]^{\mathrm{tr}}$, and it is used in the interfacial equilibrium relationship. However, it is observed that using the same approach with a modified composition $1.5 \times {}^{\mathbf{v+1}}[\langle c_l^i \rangle^l]^{\mathrm{tr}}$ (for a case where the liquid is highly undercooled, the interface liquid composition can be close to 1.5 times the average liquid composition) slightly modifies the segregation results for the Hebditch-Hunt benchmark test case. This issue was not further explored due to time constraint, hence, should be looked into in the future.

– **Peritectic transformation:** A peritectic reaction is defined as the reaction between the melt and primary solid phase to form a secondary solid phase. This reaction is quite important for steels (primary phase: δ-ferrite, secondary phase: γ-austenite) and can have a significant impact on the final segregation. However, it was realized that in the current implementation which uses a volume averaging approach, it is impossible to account for such transformation. The difficulty arises in averaging when solid grains with different histories: i) δ-ferrite ii) γ-austenite and iii) grain undergoing peritectic reaction in the same REV. Hence, we propose that for steel which undergo peritectic transformation, we generate two sets of regression functions, one for the δ-ferrite and another for the γ-austenite phase, and through a defined criteria, we employ the regression relationship for either the δ-ferrite or the γ-austenite phase.

– **Approach µSOLID:** The time integration scheme discussed in chapter 3 is currently only implemented for equiaxed solidification in SOLID®${}_{\mathrm{th}}$. The implementation of this approach for the columnar solidification remains to be done. However, the approach has already been implemented and validated for columnar and mixed columnar-equiaxed solidification in another solidification model (OpenSOLID®), currently being developed here in IJL, Nancy.

– **Regression algorithms:** In the current work, ANN-MLP has been used to obtain regression relationships for various thermodynamic functions. However, in the fast evolving domain of machine learning, efficient algorithms are being continuously developed which can be applied for regression analysis. These algorithms can be broadly classified into: i) bagging machine learning and ii) boosting machine learning. Algorithms within these broad categories have shown to be more accurate and/or efficient than ANN-MLP for regression analysis. These avenues could be further explored for an efficient coupling of the solidification model with Thermo-Calc® data.

Appendix A : Modification to microscopic growth model for CET

Contents

A.1 Modification to microscopic growth model for CET (columnar to equiaxed transition)

During the growth of columnar grains, two cases are encountered.

A.1.1 Columnar grains and no equiaxed grains:

The original set of equations proposed by Leriche [123] are:

$$\begin{cases} \left(k^i - 1\right)c_1^{*i}\dfrac{\Gamma_s^{\mathrm{col}}}{\rho} = \dfrac{S_v^{\mathrm{env,col}}D_1^i}{\delta_1^{i,\mathrm{col}}}\left(\dfrac{g_1^{\mathrm{col}}}{g_e^{\mathrm{col}}}\right)\left(c_1^{i*,\mathrm{col}} - \langle c_1^i\rangle^{\mathrm{l,col}}\right) + \dfrac{S_v^{\mathrm{s,col}}D_s^i}{\delta_s^{i,\mathrm{col}}}\left(k^i c_1^{i*,\mathrm{col}} - \langle c_s^i\rangle^{\mathrm{s,col}}\right) \\[3mm] \delta h_m^{\mathrm{col}} = C_p\left(T_f + \sum_i m_1^i c_1^{*i,\mathrm{col}} - {}^t T\right) - L_f\left(\dfrac{\Gamma_s^{\mathrm{col}}}{\rho}\delta t\right) \\[3mm] \delta h_m^{\mathrm{ec}} = C_p({}^{t+\delta t}T - {}^t T) \\[3mm] \sum_i m_1^i c_1^{i*,\mathrm{col}} = {}^{t+\delta t}T - T_f \\[3mm] \delta h_m^{tot} = g^{\mathrm{col}}\delta h_m^{\mathrm{col}} + \left(1 - g^{\mathrm{col}}\right)\delta h_m^{\mathrm{ec}} + \delta g^{\mathrm{col}}\left(h_m^{\mathrm{col},0} - h_m^{\mathrm{ec},0}\right) \end{cases} \tag{A.1}$$

where the superscript col and ec corresponds to parameters in the columnar and extra-columnar region respectively. $\delta h_m^{\mathrm{col}}$ and δh_m^{ec} are the change in enthalpy of the columnar and extra-columnar region at each micro time-step. δh_m^{tot} is the total enthalpy change due to growth of the columnar grains and the propogation of the columnar front during each micro time-step. The modified set of equations are as follows (notations used are similar to the one used for pure equiaxed solidification):

$$\begin{cases} \left({}^t k^i - 1\right){}^j c_1^{*i,\mathrm{col}}\dfrac{{}^{j+1}\Gamma_s^{\mathrm{col}}}{\rho} = \dfrac{S_v^{\mathrm{env,col}}D_1^i}{\delta_1^{i,\mathrm{col}}}\left(\dfrac{{}^{\mathbf{n}}[g_1]^{\mathrm{col}}}{{}^{\mathbf{n}}[g_e]^{\mathrm{col}}}\right)\left({}^{j+1}c_1^{i*,\mathrm{col}} - {}^{\mathbf{n}}[\langle c_1^i\rangle^{\mathrm{l}}]^{\mathrm{col}}\right) + \dfrac{S_v^{\mathrm{s,col}}D_s^i}{\delta_s^{i,\mathrm{col}}}\left({}^t k^i {}^{j+1}c_1^{i*,\mathrm{col}} - {}^{\mathbf{n}}[\langle c_s^i\rangle^{\mathrm{s}}]^{\mathrm{col}}\right) \\[3mm] \begin{cases} \delta h_m^{\mathrm{col}} = A + B + C \\[2mm] A = -\left({}^t[\langle h_1\rangle^{\mathrm{l}}]^{\mathrm{col}} - {}^t[\langle h_s\rangle^{\mathrm{s}}]^{\mathrm{col}}\right)\left(\dfrac{{}^{j+1}\Gamma_s^{\mathrm{col}}}{\rho}\delta t\right) \\[2mm] B = \sum_i\left[\left(1 - {}^t g_s^{\mathrm{col}}\right)\left({}^t\left[\dfrac{\partial[\langle h_1\rangle^{\mathrm{l}}]}{\partial[\langle c_l^i\rangle^{\mathrm{l}}]}\right]^{\mathrm{col}}\right)\left({}^{\mathbf{n}}[\langle c_l^i\rangle^{\mathrm{l}}]^{\mathrm{col}} - {}^t[\langle c_l^i\rangle^{\mathrm{l}}]^{\mathrm{col}}\right) + {}^t g_s^{\mathrm{col}}\left({}^t\left[\dfrac{\partial[\langle h_s\rangle^{\mathrm{s}}]}{\partial[\langle c_s^i\rangle^{\mathrm{s}}]}\right]^{\mathrm{col}}\right)\left({}^{\mathbf{n}}[\langle c_s^i\rangle^{\mathrm{s}}]^{\mathrm{col}} - {}^t[\langle c_s^i\rangle^{\mathrm{s}}]^{\mathrm{col}}\right)\right] \\[2mm] C = \left[\left(1 - {}^t g_s^{\mathrm{col}}\right)\left({}^t\left[\dfrac{\partial[\langle h_1\rangle^{\mathrm{l}}]}{\partial T}\right]^{\mathrm{col}}\right) + {}^t g_s^{\mathrm{col}}\left({}^t\left[\dfrac{\partial[\langle h_s\rangle^{\mathrm{s}}]}{\partial T}\right]^{\mathrm{col}}\right)\right]\left({}^{t+\delta t}T - {}^t T\right) \end{cases} \\[3mm] \delta h_m^{\mathrm{ec}} = \left[\left({}^t\left[\dfrac{\partial[\langle h_1\rangle^{\mathrm{l}}]}{\partial T}\right]^{\mathrm{col}}\right)\right]\left({}^{t+\delta t}T - {}^t T\right) \\[3mm] \sum_i {}^t m_1^i\left({}^{j+1}c_1^{i*,\mathrm{col}} - {}^t c_1^{i*,\mathrm{col}}\right) = {}^{j+1}T - {}^t T \\[3mm] \delta h_m^{tot} = {}^t[g]^{\mathrm{col}}\delta h_m^{\mathrm{col}} + \left(1 - {}^t[g]^{\mathrm{col}}\right)\delta h_m^{\mathrm{ec}} + \delta[g]^{\mathrm{col}}\left(h_m^{\mathrm{col},0} - h_m^{\mathrm{ec},0}\right) \end{cases}$$

$$\tag{A.2}$$

The modifications pertain to discussion with regards to modifications in the equiaxed growth model to account for variable phase diagram parameters. For the first micro time-step, specific treatment is performed with regards to the interface equilibrium relationship and has already been discussed earlier.

A.1.2 Columnar grains and equiaxed grains:

The original set of equations proposed by Leriche [123] are:

$$
\begin{cases}
\left(k^i - 1\right)c_1^{*i}\frac{\Gamma_s^{\rm col}}{\rho} = \frac{S_v^{\rm env,col}D_1^i}{\delta_1^{i,\rm col}}\left(\frac{g_1^{\rm col}}{g_e^{\rm col}}\right)\left(c_1^{i*,\rm col} - \langle c_1^i\rangle^{\rm l,col}\right) + \frac{S_v^{\rm s,col}D_s^i}{\delta_s^{i,\rm col}}\left(k^i c_1^{i*,\rm col} - \langle c_s^i\rangle^{\rm s,col}\right) \\[10pt]
\left(k^i - 1\right)c_1^{*i}\frac{\Gamma_s^{\rm eqx}}{\rho} = \frac{S_v^{\rm env,eqx}D_1^i}{\delta_1^{i,\rm eqx}}\left(\frac{g_1^{\rm eqx}}{g_e^{\rm eqx}}\right)\left(c_1^{i*,\rm eqx} - \langle c_1^i\rangle^{\rm l,eqx}\right) + \frac{S_v^{\rm s,eqx}D_s^i}{\delta_s^{i,\rm eqx}}\left(k^i c_1^{i*,\rm eqx} - \langle c_s^i\rangle^{\rm s,eqx}\right) \\[10pt]
\delta h_m^{\rm col} = C_p\left(T_f + \sum_i m_1^i c_1^{*i,\rm col} - {}^tT\right) - L_f\left(\frac{\Gamma_s^{\rm col}}{\rho}\delta t\right) \\[10pt]
\delta h_m^{\rm eqx} = C_p\left(T_f + \sum_i m_1^i c_1^{*i,\rm eqx} - {}^tT\right) - L_f\left(\frac{\Gamma_s^{\rm eqx}}{\rho}\delta t\right) \\[10pt]
\sum_i m_1^i c_1^{i*,\rm col} = \sum_i m_1^i c_1^{i*,\rm eqx} \\[10pt]
\delta h_m^{tot} = g^{\rm col}\delta h_m^{\rm col} + \left(1 - g^{\rm col}\right)\delta h_m^{\rm eqx} + \delta g^{\rm col}\left(h_m^{\rm col,0} - h_m^{\rm eqx,0}\right)
\end{cases}
\tag{A.3}
$$

where the superscript eqx corresponds to the equiaxed region. The modified set of equations are as follows:

$$
\begin{cases}
\left({}^tk^{i,\rm col} - 1\right){}^jc_1^{*i}\frac{{}^{j+1}\Gamma_s^{\rm col}}{\rho} = \frac{S_v^{\rm env,col}D_1^i}{\delta_1^{i,\rm col}}\left(\frac{{}^n[g_1]^{\rm col}}{{}^n[g_e]^{\rm col}}\right)\left({}^{j+1}c_1^{i*,\rm col} - {}^n[\langle c_1^i\rangle^{\rm l}]^{\rm col}\right) + \frac{S_v^{\rm s,col}D_s^i}{\delta_s^{i,\rm col}}\left({}^tk^{i,\rm col}{}^{j+1}c_1^{i*,\rm col} - {}^n[\langle c_s^i\rangle^{\rm s}]^{\rm col}\right) \\[10pt]
\left({}^tk^{i,\rm eqx} - 1\right){}^jc_1^{*i}\frac{{}^{j+1}\Gamma_s^{\rm eqx}}{\rho} = \frac{S_v^{\rm env,eqx}D_1^i}{\delta_1^{i,\rm eqx}}\left(\frac{{}^n[g_1]^{\rm eqx}}{{}^n[g_e]^{\rm eqx}}\right)\left({}^{j+1}c_1^{i*,\rm eqx} - {}^n[\langle c_1^i\rangle^{\rm l}]^{\rm eqx}\right) + \frac{S_v^{\rm s,eqx}D_s^i}{\delta_s^{i,\rm eqx}}\left({}^tk^{i,\rm eqx}{}^{j+1}c_1^{i*,\rm eqx} - {}^n[\langle c_s^i\rangle^{\rm s}]^{\rm eqx}\right) \\[10pt]
\begin{cases}
\delta h_m^{\rm col} = A + B + C \\[8pt]
A = -\left({}^t[\langle h_1\rangle^{\rm l}]^{\rm col} - {}^t[\langle h_s\rangle^{\rm s}]^{\rm col}\right)\left(\frac{{}^{j+1}\Gamma_s^{\rm col}}{\rho}\delta t\right) \\[8pt]
B = \sum_i\left[\left(1 - {}^tg_s^{\rm col}\right)\left({}^t\left[\frac{\partial[\langle h_1\rangle^{\rm l}]}{\partial[\langle c_l^i\rangle^{\rm l}]}\right]^{\rm col}\right)\left({}^n[\langle c_l^i\rangle^{\rm l}]^{\rm col} - {}^t[\langle c_l^i\rangle^{\rm l}]^{\rm col}\right) + {}^tg_s^{\rm col}\left({}^t\left[\frac{\partial[\langle h_s\rangle^{\rm s}]}{\partial[\langle c_s^i\rangle^{\rm s}]}\right]^{\rm col}\right)\left({}^n[\langle c_s^i\rangle^{\rm s}]^{\rm col} - {}^t[\langle c_s^i\rangle^{\rm s}]^{\rm col}\right)\right] \\[8pt]
C = \left[\left(1 - {}^tg_s^{\rm col}\right)\left({}^t\left[\frac{\partial[\langle h_1\rangle^{\rm l}]}{\partial T}\right]^{\rm col}\right) + {}^tg_s^{\rm col}\left({}^t\left[\frac{\partial[\langle h_s\rangle^{\rm s}]}{\partial T}\right]^{\rm col}\right)\right]\left({}^{t+\delta t}T - {}^tT\right)
\end{cases} \\[8pt]
\begin{cases}
\delta h_m^{\rm eqx} = A + B + C \\[8pt]
A = -\left({}^t[\langle h_1\rangle^{\rm l}]^{\rm eqx} - {}^t[\langle h_s\rangle^{\rm s}]^{\rm eqx}\right)\left(\frac{{}^{j+1}\Gamma_s^{\rm eqx}}{\rho}\delta t\right) \\[8pt]
B = \sum_i\left[\left(1 - {}^tg_s^{\rm eqx}\right)\left({}^t\left[\frac{\partial[\langle h_1\rangle^{\rm l}]}{\partial[\langle c_l^i\rangle^{\rm l}]}\right]^{\rm eqx}\right)\left({}^n[\langle c_l^i\rangle^{\rm l}]^{\rm eqx} - {}^t[\langle c_l^i\rangle^{\rm l}]^{\rm eqx}\right) + {}^tg_s^{\rm eqx}\left({}^t\left[\frac{\partial[\langle h_s\rangle^{\rm s}]}{\partial[\langle c_s^i\rangle^{\rm s}]}\right]^{\rm eqx}\right)\left({}^n[\langle c_s^i\rangle^{\rm s}]^{\rm eqx} - {}^t[\langle c_s^i\rangle^{\rm s}]^{\rm eqx}\right)\right] \\[8pt]
C = \left[\left(1 - {}^tg_s^{\rm eqx}\right)\left({}^t\left[\frac{\partial[\langle h_1\rangle^{\rm l}]}{\partial T}\right]^{\rm eqx}\right) + {}^tg_s^{\rm eqx}\left({}^t\left[\frac{\partial[\langle h_s\rangle^{\rm s}]}{\partial T}\right]^{\rm eqx}\right)\right]\left({}^{t+\delta t}T - {}^tT\right)
\end{cases} \\[8pt]
\begin{cases}
\sum_i {}^tm_1^{i,\rm col}\left({}^{j+1}c_1^{i*,\rm col} - {}^tc_1^{i*,\rm col}\right) = {}^{j+1}T - {}^tT \\[8pt]
\sum_i {}^tm_1^{i,\rm eqx}\left({}^{j+1}c_1^{i*,\rm eqx} - {}^tc_1^{i*,\rm eqx}\right) = {}^{j+1}T - {}^tT
\end{cases} \\[8pt]
\delta h_m^{tot} = {}^t[g]^{\rm col}\delta h_m^{\rm col} + \left(1 - {}^t[g]^{\rm col}\right)\delta h_m^{\rm eqx} + \delta[g]^{\rm col}\left(h_m^{\rm col,0} - h_m^{\rm eqx,0}\right)
\end{cases}
\tag{A.4}
$$

Two sets of thermodynamic parameters are computed for the columnar and equiaxed region. The interfacial equilibrium relationship is currently split into two. This allows us to use the liquid composition in the columnar

and equiaxed region and its corresponding liquidus temperature and liquidus slope for the first micro time-step. The liquid composition in the columnar and equiaxed region can be very different in some cases and this is the reason why the two equations have been kept separate.

Appendix B :   Data and simulation parameter

Contents

B.1   Al-5 wt.% Si alloy

Table B.1 – Thermophysical properties of Al-5 wt.% Si alloy

Property	Symbol	Units	Value
Partition coeff. (Si)	k_p^i	[-]	0.117
Liquidus slope (Si)	m_l^i	[K/wt.%]	-7.7
Solid diffusion coeff. (Si)	D_s^i	[m^2/s]	1×10^{-15}
Liquid diffusion coeff. (Si)	D_l^i	[m^2/s]	3×10^{-9}
Melting point of pure substance	T_f	[$^\circ$C]	660
Density	ρ_l	[kg/m^3]	2500
Latent heat	L_f	[J/kg]	3.8×10^5
Specific heat capacity	C_p	[J/kgK]	940

Table B.2 – Simulation parameters

Parameters	Symbol	Units	Value
Cooling rate	$\dot{T}$	[K/s]	-45
Nucleation undercooling	ΔT_{nuc}	[$^\circ$C]	1×10^{-6}
Time step	Δt	[s]	1×10^{-2}
Number of micro time-steps	n_{mic}	[-]	10

B.2   Al-7 wt.% Si alloy

Table B.3 – Thermophysical properties of Al-7 wt.% Si alloy

Property	Symbol	Units	Value
Partition coeff. (Si)	k_p^i	[-]	0.13
Liquidus slope (Si)	m_l^i	[K/wt.%]	-6.5
Solid diffusion coeff. (Si)	D_s^i	[m²/s]	1×10^{-12}
Liquid diffusion coeff. (Si)	D_l^i	[m²/s]	6.45×10^{-9}
Melting point of pure substance	T_f	[ºC]	663.5
Eutectic temperature	T_{eut}	[ºC]	577
Density	ρ_l	[kg/m³]	2452
Latent heat	L_f	[J/kg]	3.874×10^5
Specific heat capacity	C_p	[J/kgK]	1060
Liquid thermal conductivity	k_l	[W/mK]	70
Solid thermal conductivity	k_s	[W/mK]	70

Table B.4 – Simulation parameters

Parameters	Symbol	Units	Value
Mesh size	Δx	[m]	1×10^{-3}
Primary arm spacing	λ_1	[m]	5×10^{-4}
Nucleation undercooling	ΔT_{nuc}	[ºC]	0
Time step	Δt	[s]	1×10^{-2}
Number of micro time-steps	n_{mic}	[-]	10

B.3 Q550 ingot: Fe -0.197 wt.% C -0.178 wt.% Cr alloy

Table B.5 – Thermophysical properties of Fe-0.197 wt.% C -0.178 wt.% Cr alloy

Property	Symbol	Units	Value
Partition coeff. (C)	k_p^i	[-]	0.17
Partition coeff. (Cr)	k_p^i	[-]	0.91
Liquidus slope (C)	m_l^i	[K/wt.%]	-80.0
Liquidus slope (Cr)	m_l^i	[K/wt.%]	-1.3
Solid diffusion coeff. (C)	D_s^i	[m^2/s]	5×10^{-9}
Liquid diffusion coeff. (C)	D_l^i	[m^2/s]	7×10^{-9}
Solid diffusion coeff. (Cr)	D_s^i	[m^2/s]	1.2×10^{-12}
Liquid diffusion coeff. (Cr)	D_l^i	[m^2/s]	3×10^{-9}
Melting point of pure substance	T_f	[°C]	1538
Thermal expansion coefficient	β_T	[K^{-1}]	0.885×10^{-4}
Solutal expansion coefficient (C)	β_C	[wt.%$^{-1}$]	-1.416×10^{-2}
Solutal expansion coefficient (Cr)	β_C	[wt.%$^{-1}$]	-9.915×10^{-4}
Liquid reference density	ρ_l	[kg/m^3]	7060
Shrinkage coefficient	β_{sh}	[-]	0.048
Latent heat	L_f	[kJ/kg]	292
Specific heat capacity	C_p	[J/kgK]	750

B.4 Hebditch-Hunt benchmark case: Sn - 5 wt.% Pb alloy

Table B.6 – Thermophysical properties

Property	Symbol	Units	Value
Nominal concentration	c_0	$[\text{wt}\%]$	5.0
Partition coefficient	k_p	$[-]$	0.0656
Melting point of the pure substance	T_f	$[^\circ\text{C}]$	232.0
Liquidus slope	m_l	$[\text{K/wt}\%]$	-1.286
Liquid reference density	ρ_l	$[\text{kg/m}^3]$	7000.0
Solid density for grain buoyancy	ρ_s	$[\text{kg/m}^3]$	7142.9
Kinematic viscosity	ν_l	$[\text{m}^2/\text{s}]$	1.428571×10^{-7}
Thermal conductivity	k	$[\text{W/mK}]$	55.0
Solutal expansion coeff.	β_C	$[\text{wt}\%^{-1}]$	-5.3×10^{-3}
Thermal expansion coeff.	β_T	$[\text{K}^{-1}]$	6.0×10^{-5}
Latent heat	L_f	$[\text{J/kg}]$	6.1×10^4
Specific heat capacity	C_p	$[\text{J/(kgK)}]$	260.0
Liquid diffusion coeff.	D_l^i	$[\text{m}^2/\text{s}]$	1×10^{-8}
Solid diffusion coeff.	D_s^i	$[\text{m}^2/\text{s}]$	1×10^{-9}
Characteristic length for permeability	d_p	$[\text{m}]$	200.0×10^{-6}
Packing limit grain volume fraction	g_e^{pack}	$[-]$	0.3
Tortuosity	τ	$[-]$	$6/\pi$
Kozeny constant	K_k	$[-]$	5.0
Nuclei density	N_0	$[m^{-3}]$	10^{-9}
Initial diametere of nuclei	d_{g0}	$[m]$	10^{-6}

Table B.7 – Simulation parameters

Boundary	Condition
Initial liquid temperature	226 $^{\circ}$C
Nucleation undercooling	1×10^{-4} $^{\circ}$C
Macro time step	1.5×10^{-3} s
Number of micro time-steps	10

Appendix C :   Regression data

Contents

C.1 Fe-C-Cr alloy

Table C.1 – Regression analysis - Fe-C-Cr (δ) system

Inputs	Output	R^2	MSE
c_l^{c*}, c_l^{cr*}	T^*	>0.99	3×10^{-8}
c_l^{c*}, c_l^{cr*}	m_l^c, m_l^{cr}	>0.99	1.5×10^{-6}
c_l^{c*}, c_l^{cr*}	k^c, k^{cr}	>0.99	2×10^{-6}
$\langle h_l \rangle^l, \langle c_l^c \rangle^l ... \langle c_l^{cr} \rangle^l$	T_l	>0.99	3×10^{-7}
$\langle h_s \rangle^s, \langle c_s^c \rangle^s ... \langle c_s^{cr} \rangle^s$	T_s	>0.99	8×10^{-6}
$T, \langle c_l^c \rangle^l, \langle c_l^{cr} \rangle^l$	$\langle h_l \rangle^l$	>0.99	6×10^{-6}
$T, \langle c_s^c \rangle^s, \langle c_s^{cr} \rangle^s$	$\langle h_s \rangle^s$	>0.99	1.3×10^{-5}
$T, \langle c_l^c \rangle^l, \langle c_l^{cr} \rangle^l$	$\left(\frac{\partial \langle h_l \rangle^l}{\partial T} \right)_{\langle c_l^c \rangle^l, \langle c_l^{cr} \rangle^l}$	>0.99	6×10^{-6}
$T, \langle c_s^c \rangle^s, \langle c_s^{cr} \rangle^s$	$\left(\frac{\partial \langle h_s \rangle^s}{\partial T} \right)_{\langle c_s^c \rangle^s, \langle c_s^{cr} \rangle^s}$	>0.99	3.9×10^{-5}
$T, \langle c_l^c \rangle^l, \langle c_l^{cr} \rangle^l$	$\left(\frac{\partial \langle h_l \rangle^l}{\partial \langle c_l^c \rangle^l} \right)_{T, \langle c_l^{cr} \rangle^l}, \left(\frac{\partial \langle h_l \rangle^l}{\partial \langle c_l^{cr} \rangle^l} \right)_{T, \langle c_l^c \rangle^l}$	>0.99	8×10^{-6}
$T, \langle c_s^c \rangle^s, \langle c_s^{cr} \rangle^s$	$\left(\frac{\partial \langle h_s \rangle^s}{\partial \langle c_s^c \rangle^s} \right)_{T, \langle c_s^{cr} \rangle^s}, \left(\frac{\partial \langle h_s \rangle^s}{\partial \langle c_s^{cr} \rangle^s} \right)_{T, \langle c_s^c \rangle^s}$	>0.99	5×10^{-5}

C.2   Sn-Pb alloy

Table C.2 – Mapping data: Sn-Pb alloy

Phase data file: LIQUID

Temperature range	235 - 180 [^{o}C]
Composition rage	0 - 40 [wt.%]
Δ T	2.5 [^{o}C]
$\Delta \langle c^{pb} \rangle$	0.8 [wt.%]

Phase data file: BCT (solid)

Temperature range	235 - 100 [^{o}C]
Composition rage	0 - 40 [wt.%]
Δ T	5 [^{o}C]
$\Delta \langle c^{pb} \rangle$	0.8 [wt.%]

Interface equilibrium data file

Temperature range	235 - 180 [^{o}C]
Composition rage	0 - 40 [wt.%]
Number of data points	1000

Table C.3 – Regression analysis - Sn-Pb system

Inputs	Output	MSE
c_l^{pb*}	T^*	1×10^{-8}
c_l^{pb*}	m_1^{pb}	5×10^{-7}
c_l^{pb*}	k^{pb}	1.5×10^{-6}
$\langle h_1 \rangle^1, \langle c_1^{pb} \rangle^1$	T_1	1×10^{-7}
$\langle h_s \rangle^s, \langle c_s^{pb} \rangle^s$	T_s	4×10^{-7}
$T, \langle c_1^{pb} \rangle^1$	$\langle h_1 \rangle^1$	1×10^{-6}
$T, \langle c_s^{pb} \rangle^s$	$\langle h_s \rangle^s$	1.1×10^{-5}
$T, \langle c_1^{pb} \rangle^1$	$\left(\dfrac{\partial \langle h_1 \rangle^1}{\partial T} \right)_{\langle c_1^{pb} \rangle^1}$	1×10^{-6}
$T, \langle c_s^{pb} \rangle^s$	$\left(\dfrac{\partial \langle h_s \rangle^s}{\partial T} \right)_{\langle c_s^{pb} \rangle^s}$	5×10^{-6}
$T, \langle c_1^{pb} \rangle^1$	$\left(\dfrac{\partial \langle h_1 \rangle^1}{\partial \langle c_1^c \rangle^1} \right)_{T, \langle c_1^{pb} \rangle^1}$	3×10^{-6}
$T, \langle c_s^{pb} \rangle^s$	$\left(\dfrac{\partial \langle h_s \rangle^s}{\partial \langle c_s^c \rangle^s} \right)_{T, \langle c_s^{pb} \rangle^s}$	2×10^{-5}

List of Tables

List of Figures

196

Bibliography

[1] G. Lesoult. Macrosegregation in steel strands and ingots: Characterisation, formation and consequences. *Materials Science and Engineering: A*, 413-414:19 – 29, 2005. International Conference on Advances in Solidification Processes.

[2] J. Dantzig and M. Rappaz. *Solidification: -Revised & Expanded*. EPFL press, 2016.

[3] Hasse Fredriksson and Ulla Akerlind. *Materials processing during casting*, volume 210. Wiley Online Library, 2006.

[4] Ali Saad. *Numerical modelling of macrosegregation formed during solidification with shrinkage using a level set approach*. PhD thesis, PSL Research University, 2016.

[5] WA Tiller, KA Jackson, JW Rutter, and Bruce Chalmers. The redistribution of solute atoms during the solidification of metals. *Acta metallurgica*, 1(4):428–437, 1953.

[6] Adeline Buffet, Henri Nguyen-Thi, Aziz Bogno, Thomas Schenk, Nathalie Mangelinck-Noël, Guillaume Reinhart, Nathalie Bergeon, Bernard Billia, and J Baruchel. Measurement of solute profiles by means of synchrotron x-ray radiography during directional solidification of al-4 wt% cu alloys. In *Materials Science Forum*, volume 649, pages 331–336. Trans Tech Publ, 2010.

[7] A Bogno, H Nguyen-Thi, G Reinhart, B Billia, and J Baruchel. Growth and interaction of dendritic equiaxed grains: In situ characterization by synchrotron x-ray radiography. *Acta Materialia*, 61(4):1303–1315, 2013.

[8] Ch-A Gandin. From constrained to unconstrained growth during directional solidification. *Acta Materialia*, 48(10):2483–2501, 2000.

[9] H Esaka, W Kurz, and R Trivedi. Solidification processing 1987. *The Institute of Metals, London*, 168, 1988.

[10] Michel Rappaz and Ch-A Gandin. Probabilistic modelling of microstructure formation in solidification processes. *Acta metallurgica et materialia*, 41(2):345–360, 1993.

[11] Benjamin Gerin. Bibliography report, 2019.

[12] L Northcott. The influence of alloying elements on the crystallization of copper. part i. small additions and the effect of atomic structure. *J. Inst. Metals*, 62:101–136, 1938.

[13] WC Winegard and Bruce Chalmers. Supercooling and dendritic freezing in alloys. *Transactions of the American Society for Metals*, 46:1214–1224, 1954.

[14]

[15] Atsumi OHNO, Tetsuichi MOTEGI, and Hiroshi SODA. Origin of the equiaxed crystals in castings. *Transactions of the Iron and Steel Institute of Japan*, 11(1):18–23, 1971.

[16] KA Jackson, JD Hunt, DR Uhlmann, and TP Seward. On origin of equiaxed zone in castings. *Transactions of the Metallurgical Society of AIME*, 236(2):149, 1966.

[17] J Pilling and A Hellawell. Mechanical deformation of dendrites by fluid flow. *Metall. Mater. Trans. A*, 27(1):229–232, 1996.

[18] H Neumann-Heyme, K Eckert, and C Beckermann. Dendrite fragmentation in alloy solidification due to sidearm pinch-off. *Physical Review E*, 92(6):060401, 2015.

[19] T Sato, W Kurz, and K Ikawa. Experiments on dendrite branch detachment in the succinonitrile-camphor alloy. *Transactions of the Japan Institute of Metals*, 28(12):1012–1021, 1987.

[20] AE Ares and CE Schvezov. Solidification parameters during the columnar-to-equiaxed transition in lead-tin alloys. *Metallurgical and Materials Transactions A*, 31(6):1611–1625, 2000.

[21] Alicia Esther Ares, Liliana Mabel Gassa, Sergio Fabian Gueijman, and Carlos Enrique Schvezov. Correlation between thermal parameters, structures, dendritic spacing and corrosion behavior of zn–al alloys with columnar to equiaxed transition. *Journal of Crystal Growth*, 310(7-9):1355–1361, 2008.

[22] Alicia Esther Ares, Sergio Fabian Gueijman, and Carlos Enrique Schvezov. An experimental investigation of the columnar-to-equiaxed grain transition in aluminum–copper hypoeutectic and eutectic alloys. *Journal of crystal Growth*, 312(14):2154–2170, 2010.

[23] Jose Eduardo Spinelli, Ivaldo Leao Ferreira, and Amauri Garcia. Influence of melt convection on the columnar to equiaxed transition and microstructure of downward unsteady-state directionally solidified sn–pb alloys. *Journal of Alloys and Compounds*, 384(1-2):217–226, 2004.

[24] Lakhdar Hachani, Bachir Saadi, Xiao Dong Wang, Abdallah Nouri, Kader Zaidat, Aissa Belgacem-Bouzida, Linda Ayouni-Derouiche, Gaëtan Raimondi, and Yves Fautrelle. Experimental analysis of the solidification of sn–3 wt.% pb alloy under natural convection. *International Journal of Heat and Mass Transfer*, 55(7-8):1986–1996, 2012.

[25] L Hachani, K Zaidat, B Saadi, XD Wang, and Y Fautrelle. Solidification of sn–pb alloys: Experiments on the influence of the initial concentration. *International Journal of Thermal Sciences*, 91:34–48, 2015.

[26] Dong Rong Liu, Nathalie Mangelinck-Noël, Ch-A Gandin, Gerhard Zimmermann, Laszlo Sturz, H Nguyen Thi, and Bernard Billia. Structures in directionally solidified al–7 wt.% si alloys: Benchmark experiments under microgravity. *Acta materialia*, 64:253–265, 2014.

[27] Dong Rong Liu, Nathalie Mangelinck-Noël, Ch-A Gandin, Gerhard Zimmermann, Laszlo Sturz, Henri Nguyen-Thi, and Bernard Billia. Simulation of directional solidification of refined al–7 wt.% si alloys–comparison with benchmark microgravity experiments. *Acta Materialia*, 93:24–37, 2015.

[28] Guillaume Reinhart, Ch-A Gandin, Nathalie Mangelinck-Noël, Henri Nguyen-Thi, J-E Spinelli, Jose Baruchel, and Bernard Billia. Influence of natural convection during upward directional solidification: A comparison between in situ x-ray radiography and direct simulation of the grain structure. *Acta materialia*, 61(13):4765–4777, 2013.

[29] JD Hunt. Steady state columnar and equiaxed growth of dendrites and eutectic. *Mater. Sci. Eng.*, 65(1):75–83, 1984.

[30] VB Biscuola and MA Martorano. Mechanical blocking mechanism for the columnar to equiaxed transition. *Metall. Mater. Trans. A*, 39(12):2885–2895, 2008.

[31] TM Pollock and WH Murphy. The breakdown of single-crystal solidification in high refractory nickel-base alloys. *Metallurgical and Materials Transactions A*, 27(4):1081–1094, 1996.

[32] M. A. Martorano, C. Beckermann, and C. A. Gandin. A solutal interaction mechanism for the columnar-to-equiaxed transition in alloy solidification. *Metall. Mater. Trans. A*, 34(8):1657–1674, Aug 2003.

[33] C. Beckermann. Modelling of macrosegregation: applications and future needs. *International Materials Reviews*, 47(5):243–261, 2002.

[34] HD Merchant, DE Tyler, and E Henry Chia. Continuous casting of non-ferrous metals and alloys. *Chicago*, page 1989, 1988.

[35] Ch Gras, M Meredith, Kevin Gatenby, and JD Hunt. Defect formation in twin roll-cast aa 3xxx and 5xxx series aluminium alloys. In *Materials Science Forum*, volume 396, pages 89–94. Transtec Publications; 1999, 2002.

[36] Men G Chu and John E Jacoby. Macrosegregation characteristics of commercial size aluminum alloy ingot cast by the direct chill method. In *Essential Readings in Light Metals*, pages 819–824. Springer, 2016.

[37] Bruno Gariepy and Yves Caron. Investigation in the effects of casting parameters on the extent of centerline macrosegregation in dc cast sheet ingots. In *Essential Readings in Light Metals*, pages 831–841. Springer, 2016.

[38] Hervé Combeau, Miha Založnik, Stéphane Hans, and Pierre Emmanuel Richy. Prediction of macrosegregation in steel ingots: influence of the motion and the morphology of equiaxed grains. *Metall. Mater. Trans. B*, 40(3):289–304, 2009.

[39] G Lesoult. Macrosegregation in cast steel: historical considerations on products, casting processes, and segregation models. In *Solidification Science and Technology–Proceedings of the John Hunt International Symposium*, pages 269–292, 2011.

[40] Zhiye Chen, Dieter Senk, and Felix Firsbach. Experimental investigations on solidification of 500-kg steel ingots with laboratory trials. *Metallurgical and Materials Transactions B*, 49(5):2514–2532, 2018.

[41] FLEMINGS MC. Principles of control of soundness and homogeneity of large ingots. *SCAND. J. METALLURGY; SWED.; DA. 1976; VOL. 5; NO 1; PP. 1-15; BIBL. 30 REF.*, 1976.

[42] Merton C Flemings. Solidification processing. *Metallurgical transactions*, 5(10):2121–2134, 1974.

[43] Edward John Pickering. Macrosegregation in steel ingots: The applicability of modelling and characterisation techniques. *ISIJ International*, 53(6):935–949, 2013.

[44] RJ McDonald and JD Hunt. Convective fluid motion within the interdendritic liquid of a casting. *Metallurgical Transactions*, 1(6):1787–1788, 1970.

[45] Anthony F Giamei and BH Kear. On the nature of freckles in nickel base superalloys. *Metallurgical Transactions*, 1(8):2185–2192, 1970.

[46] J Comon and P Bastien. Etude expérimentale des relations entre la solidification et les hétérogénéités de lingots d'acier de 3 à 30 tonnes. *Revue de Métallurgie*, 65(1):13–23, 1968.

[47] C Maidorn and D Blind. Solidification and segregation in heavy forging ingots. *Nuclear engineering and design*, 84(2):285–296, 1985.

[48] Guanghua Yan, Lizhan Han, Chuanwei Li, Xiaomeng Luo, and Jianfeng Gu. Effect of macrosegregation on the microstructure and mechanical properties of a pressure-vessel steel. *Metallurgical and Materials Transactions A*, 48(7):3470–3481, 2017.

[49] George Krauss. Solidification, segregation, and banding in carbon and alloy steels. *Metallurgical and Materials Transactions B*, 34(6):781–792, 2003.

[50] J Comon, J Delorme, and P Bastien. Hétérogénéité des gros lingots de forge. étude de l'influence des impuretés et des éléments d'alliage sur la ségrégation. *Revue de Métallurgie*, 70(4):251–258, 1973.

[51] Kent D Carlson, Zhiping Lin, R Hardin, Christoph Beckermann, George Mazurkevich, and M Schneider. Modeling of porosity formation and feeding flow in steel casting. In *Proceedings of the 56th SFSA Technical and Operating Conference, Paper*, number 4.4, 2002.

[52] P-D Grasso, J-M Drezet, and M Rappaz. Hot tear formation and coalescence observations in organic alloys. Technical report, TMS Publ., 2002.

[53] Miha Založnik and Hervé Combeau. An operator splitting scheme for coupling macroscopic transport and grain growth in a two-phase multiscale solidification model: Part i – model and solution scheme. *Comput. Mater. Sci.*, 48(1):1 – 10, 2010.

[54] X. Doré, H. Combeau, and M. Rappaz. Modelling of microsegregation in ternary alloys: Application to the solidification of al–mg–si. *Acta Materialia*, 48(15):3951 – 3962, 2000.

[55] M. C Flemings and G. E. Nereo. Macrosegregation. Part. I. *AIME Met Soc Trans*, 239(9):1449–1461, 1967.

[56] M. C. Flemings, R. Mehrabian, and G. E. Nereo. Macrosegregation. Part II. *AIME Met Soc Trans*, 242(9):41–49, 1967.

[57] M. C Flemings and G. E. Nereo. Macrosegregation. Part. III. *AIME Met Soc Trans*, 242(9):50–55, 1967.

[58] R Mehrabian, M Keane, and MC Flemings. Interdendritic fluid flow and macrosegregation; influence of gravity. *Metallurgical and Materials Transactions B*, 1(5):1209–1220, 1970.

[59] David R Poirier, PJ Nandapurkar, and S Ganesan. The energy and solute conservation equations for dendritic solidification. *Metallurgical and Materials Transactions B*, 22(6):889–900, 1991.

[60] Jie Wanqi. Further discussions on the solute redistribution during dendritic solidification of binary alloys. *Metallurgical and Materials Transactions B*, 25(5):731–739, 1994.

[61] SD Ridder, S Kou, and R Mehrabian. Effect of fluid flow on macrosegregation in axi-symmetric ingots. *Metallurgical Transactions B*, 12(3):435–447, 1981.

[62] Weitao Liu. *Modélisation par éléments finis des phénomènes thermomécaniques et de macroségrégation dans les procédés de solidification*. PhD thesis, École Nationale Supérieure des Mines de Paris, 2005.

[63] WD Bennon and FP Incropera. A continuum model for momentum, heat and species transport in binary solid-liquid phase change systems—i. model formulation. *International Journal of Heat and Mass Transfer*, 30(10):2161–2170, 1987.

[64] WD Bennon and FP Incropera. A continuum model for momentum, heat and species transport in binary solid-liquid phase change systems—ii. application to solidification in a rectangular cavity. *International Journal of Heat and Mass Transfer*, 30(10):2171–2187, 1987.

[65] PJ Prescott, FP Incropera, and WD Bennon. reassessment of the continuum momentum equation. *Int. J. Hcut Mass Tran& Vol*, 34(9):2351–2359, 1991.

[66] Jun Ni and Frank P Incropera. Extension of the continuum model for transport phenomena occurring during metal alloy solidification—i. the conservation equations. *International Journal of Heat and Mass Transfer*, 38(7):1271–1284, 1995.

[67] Jun Ni and Frank P Incropera. Extension of the continuum model for transport phenomena occurring during metal alloy solidification-ii. microscopic considerations. *International Journal of Heat and Mass Transfer*, 38(7):1285–1296, 1995.

[68] Christopher J Vreeman, Matthew John M Krane, and Frank P Incropera. The effect of free-floating dendrites and convection on macrosegregation in direct chill cast aluminum alloys: Part i: model development. *International Journal of Heat and Mass Transfer*, 43(5):677–686, 2000.

[69] Matthew John M Krane, Frank P Incropera, and David R Gaskell. Solidification of ternary metal alloys—i. model development. *International journal of heat and mass transfer*, 40(16):3827–3835, 1997.

[70] Matthew John M Krane. Macrosegregation development during solidification of a multicomponent alloy with free-floating solid particles. *Applied Mathematical Modelling*, 28(1):95–107, 2004.

[71] Stephen Whitaker. Diffusion and dispersion in porous media. *AIChE Journal*, 13(3):420–427, 1967.

[72] J. Ni and C. Beckermann. A volume-averaged two-phase model for transport phenomena during solidification. *Metallurgical Transactions B*, 22(3):349, 1991.

[73] Stephen Whitaker. The forchheimer equation: a theoretical development. *Transport in Porous media*, 25(1):27–61, 1996.

[74] B Goyeau, T Benihaddadene, D Gobin, and M Quintard. Averaged momentum equation for flow through a nonhomogenenous porous structure. *Transport in porous media*, 28(1):19–50, 1997.

[75] P Bousquet-Melou, B Goyeau, Michel Quintard, F Fichot, and D Gobin. Average momentum equation for interdendritic flow in a solidifying columnar mushy zone. *International journal of heat and mass transfer*, 45(17):3651–3665, 2002.

[76] Christoph Beckermann. *Melting and solidification of binary mixtures with double-diffusive convection in the melt*. PhD thesis, Purdue University, 1987.

[77] C. Beckermann and R. Viskanta. Double-diffusive convection during dendritic solidification of a binary mixture. *PhysicoChemical Hydrodynamics*, 10(2):195–213, 1988.

[78] Beckermann C and Viskanta R. Mathematical modeling of transport phenomena during alloy solidification. *ASME. Appl. Mech. Rev.*, 46(1):1–27, 1993.

[79] S. Ganesan and D. R. Poirier. Conservation of mass and momentum for the flow of interdendritic liquid during solidification. *Metallurgical Transactions B*, 21(1):173, Feb 1990.

[80] Donald A Drew. Mathematical modeling of two-phase flow. *Annual review of fluid mechanics*, 15(1):261–291, 1983.

[81] M Rappaz and Ph Thevoz. Solute diffusion model for equiaxed dendritic growth. *Acta Metallurgica*, 35(7):1487–1497, 1987.

[82] C. Y. Wang and C. Beckermann. A multiphase solute diffusion model for dendritic alloy solidification. *Metallurgical and Materials Transactions A*, 24(12):2787–2802, Dec 1993.

[83] C.Y. Wang and C. Beckermann. A unified solute diffusion model for columnar and equiaxed dendritic alloy solidification. *Materials Science and Engineering: A*, 171(1-2):199–211, 1993.

[84] C.Y. Wang and C. Beckermann. Equiaxed dendritic solidification with convection: Part i. multiscale/multiphase modeling. *Metallurgical and materials transactions A*, 27(9):2754–2764, 1996.

[85] M C Schneider and C Beckermann. Formation of macrosegregation by multicomponent thermosolutal convection during the solidification of steel. *Metallurgical and Materials Transactions A*, 26(9):2373–2388, 1995.

[86] Miha Zaloznik and Hervé Combeau. The influence of the morphology evolution of free-floating equiaxed grains on the macrosegregation in a 3.3-ton steel ingot. *Proceedings of MCWASP XII, TMS, The Minerals, Metals and Materials Society*, pages 165–172, 2009.

[87] Arvind Kumar, Miha Založnik, and Hervé Combeau. Prediction of equiaxed grain structure and macrosegregation in an industrial steel ingot: comparison with experiment. *International Journal of Advances in Engineering Sciences and Applied Mathematics*, 2(4):140–148, 2010.

[88] Menghuai Wu and Andreas Ludwig. Modeling equiaxed solidification with melt convection and grain sedimentation—i: Model description. *Acta Materialia*, 57(19):5621–5631, 2009.

[89] Menghuai Wu and Andreas Ludwig. Modeling equiaxed solidification with melt convection and grain sedimentation—ii. model verification. *Acta Materialia*, 57(19):5632–5644, 2009.

[90] M. Wu, A. Fjeld, and A. Ludwig. Modelling mixed columnar-equiaxed solidification with melt convection and grain sedimentation – part i: Model description. *Computational Materials Science*, 50(1):32 – 42, 2010.

[91] M Wu, A Ludwig, and A Fjeld. Modelling mixed columnar-equiaxed solidification with melt convection and grain sedimentation–part ii: Illustrative modelling results and parameter studies. *Computational Materials Science*, 50(1):43–58, 2010.

[92] KO Tveito, Marie Bedel, Miha Založnik, Hervé Combeau, Mohammed M'Hamdi, Arvind Kumar, and Pradip Dutta. Numerical study of the impact of inoculant and grain transport on macrosegregation and microstructure formation during solidification of an al-22% cu alloy. In *IOP Conference Series: Materials Science and Engineering*, volume 33, page 012089. IOP Publishing, 2012.

[93] Marie Bedel, KO Tveito, Miha Založnik, Hervé Combeau, and M M'Hamdi. A model study of the impact of the transport of inoculant particles on microstructure formation during solidification. *Computational Materials Science*, 102:95–109, 2015.

[94] Knut Omdal Tveito, Akash Pakanati, Mohammed M'Hamdi, Hervé Combeau, and Miha Založnik. A simplified three-phase model of equiaxed solidification for the prediction of microstructure and macrosegregation in castings. *Metall. Mater. Trans. A*, 49(7):2778–2794, 2018.

[95] HongHao Ge, Jun Li, QingTao Guo, FengLi Ren, MingXu Xia, JianHua Yao, and JianGuo Li. Numerical simulation of a-segregation evolution in a 55-ton ingot using four-phase solidification model. *Metallurgical and Materials Transactions B*, pages 1–12, 2021.

[96] Miha Založnik. *Modeling of macrosegregation in direct chill casting*. PhD thesis, Univerza v Novi Gorici, Fakulteta za podiplomski študij, 2006.

[97] W Kurz and DJ Fisher. Fundamentals of solidification. *Trans Tech Publ*, page 293, 1989.

[98] Laurent Heyvaert. *Modélisation de la formation des structures et des microporosités durant la solidification d'alliages d'aluminium*. PhD thesis, Université de Lorraine, 2015.

[99] Mamoru Ishii and Takashi Hibiki. *Thermo-fluid dynamics of two-phase flow*. Springer Science & Business Media, 2010.

[100] Jun Ni and Christoph Beckermann. Modeling of globulitic alloy solidification with convection. *Journal of Materials Processing and Manufacturing Science*, 2:217–231, 1993.

[101] Andreas Ludwig and Menghuai Wu. Modeling of globular equiaxed solidification with a two-phase approach. *Metallurgical and Materials Transactions A*, 33(12):3673–3683, 2002.

[102] Thi-Thuy-My Nguyen. *Multiscale finite element modeling of macrosegregation and grain transport.(Modélisation multi-échelle d'éléments finis de la macroségrégation et du transport des grains)*. PhD thesis, Mines ParisTech, France, 2015.

[103] Laurent Heyvaert, Marie Bedel, Miha Založnik, and Hervé Combeau. Modeling of the coupling of microstructure and macrosegregation in a direct chill cast al-cu billet. *Metallurgical and Materials Transactions A*, 48(10):4713–4734, Oct 2017.

[104] Pradeep K Agarwal and Brian K O'Neill. Transport phenomena in multi-particle systems—i. pressure drop and friction factors: unifying the hydraulic-radius and submerged-object approaches. *Chemical engineering science*, 43(9):2487–2499, 1988.

[105] H. Combeau, J. M. Drezet, A. Mo, and M. Rappaz. Modeling of microsegregation in macrosegregation computations. *Metallurgical and Materials Transactions A*, 27(8):2314–2327, 1996.

[106] Hervé Combeau and Asbjørn Mo. Eutectic reaction and nonconstant material parameters in micro-macrosegregation modeling. *Metallurgical and Materials Transactions A*, 28(12):2705–2714, 1997.

[107] H. D. Brody and M. C. Flemings. Solute redistribution in dendritic solidification. *AIME Met. Soc. Trans.*, 236:615, 1966.

[108] TW Clyne and W Kurz. Solute redistribution during solidification with rapid solid state diffusion. *Metallurgical Transactions A*, 12(6):965–971, 1981.

[109] Itsuo Ohnaka. Mathematical analysis of solute redistribution during solidification with diffusion in solid phase. *Transactions of the Iron and Steel Institute of Japan*, 26(12):1045–1051, 1986.

[110] Sumio KOBAYASHI. A mathematical model for solute redistribution during dendritic solidification. *Transactions of the Iron and Steel Institute of Japan*, 28(7):535–542, 1988.

[111] VR Voller and C Beckermann. Approximate models of microsegregation with coarsening. *Metallurgical and materials transactions A*, 30(11):3016–3019, 1999.

[112] Yoshiyuki Ueshima, Shozo Mizoguchi, Tooru Matsumiya, and Hiroyuki Kajioka. Analysis of solute distribution in dendrites of carbon steel with δ/γ transformation during solidification. *Metallurgical Transactions B*, 17(4):845–859, Dec 1986.

[113] V. R. Voller and S. Sundarraj. Modelling of microsegregation. *Materials Science and Technology*, 9(6):474–482, 1993.

[114] L. Thuinet and H. Combeau. A new model of microsegregation for macrosegregation computation in multicomponent steels. part i: theoretical formulation and algorithm. *Computational Materials Science*, 45(2):294 – 304, 2009.

[115] L Thuinet and H Combeau. A new model of microsegregation for macrosegregation computation in multicomponent steels. part ii: Application to fe–ni–c alloys. *Computational materials science*, 45(2):285–293, 2009.

[116] Munekazu Ohno, Daichi Kimura, and Kiyotaka Matsuura. Prediction of microsegregation behavior in fe-based alloys based on machine learning. *Tetsu-to-Hagane*, 103(12):711–719, 2017.

[117] Munekazu Ohno, Daichi Kimura, and Kiyotaka Matsuura. Prediction of microsegregation based on machine learning and its extension to a macrosegregation simulation. *TETSU TO HAGANE-JOURNAL OF THE IRON AND STEEL INSTITUTE OF JAPAN*, 103(12):54–63, 2017.

[118] Qipeng Dong, Jiongming Zhang, Liang Qian, and Yanbin Yin. Numerical modeling of macrosegregation in round billet with different microsegregation models. *ISIJ International*, 57(5):814–823, 2017.

[119] L Thuinet and H Combeau. Prediction of macrosegregation during the solidification involving a peritectic transformation for multicomponent steels. *Journal of materials science*, 39(24):7213–7219, 2004.

[120] M Založnik and Hervé Combeau. Effects of solidification kinetics and liquid density in modeling of macrosegregation in castings. *Proceedings of MCWASP XII, A Publication of TMS, Warrendale, Pennsylvania*, pages 253–260, 2009.

[121] D. Tourret and Ch.-A. Gandin. A generalized segregation model for concurrent dendritic, peritectic and eutectic solidification. *Acta Materialia*, 57(7):2066 – 2079, 2009.

[122] Marie Bedel. *Étude de la formation des structures de solidification et des macroségrégations en coulée semi-continue d'aluminium*. PhD thesis, 2014. Thèse de doctorat dirigée par Combeau, Hervé et Založnik, Miha Sciences des matériaux Université de Lorraine 2014.

[123] Nicolas Leriche. *Etude de la Transition Colonnaire-Equiaxe dans les lingots et en coulée continue d'acier et influence du mouvement des grains*. PhD thesis, University of Lorraine, 2015.

[124] Benoît Appolaire. *Prise en compte du mouvement des cristaux equiaxes dans la modélisation de la solidification des lingots d'acier coules en fonderie*. PhD thesis, Vandoeuvre-les-Nancy, INPL, 1999.

[125] Ø Nielsen, A Mo, B Appolaire, and H Combeau. Measurements and modeling of the microstructural morphology during equiaxed solidification of al-cu alloys. *Metallurgical and Materials Transactions A*, 32(8):2049–2060, 2001.

[126] GP Ivantsov. Temperature field around a spherical, cylindrical, and needle-shaped crystal, growing in a pre-cooled melt. *Dokl Akad Nauk SSSR*, 58:567–569, 1947.

[127] G Horvay and JW Cahn. Dendritic and spheroidal growth. *Acta Metallurgica*, 9(7):695–705, 1961.

[128] Achilles Papapetrou. Untersuchungen über dendritisches wachstum von kristallen. *Zeitschrift für Kristallographie-Crystalline Materials*, 92(1-6):89–130, 1935.

[129] W1 Kurz, B Giovanola, and R Trivedi. Theory of microstructural development during rapid solidification. *Acta metallurgica*, 34(5):823–830, 1986.

[130] Ramagopal Ananth and William N Gill. Self-consistent theory of dendritic growth with convection. *Journal of crystal growth*, 108(1-2):173–189, 1991.

[131] Ch-A Gandin, Gildas Guillemot, Benoît Appolaire, and Ngadia Taha Niane. Boundary layer correlation for dendrite tip growth with fluid flow. *Materials Science and Engineering: A*, 342(1-2):44–50, 2003.

[132] B Cantor and A Vogel. Dendritic solidification and fluid flow. *Journal of Crystal Growth*, 41(1):109–123, 1977.

[133] Menghuai Wu, Andreas Ludwig, and Abdellah Kharicha. Volume-averaged modeling of multiphase flow phenomena during alloy solidification. *Metals*, 9(2):229, 2019.

[134] Tao Wang, Sergey Semenov, Engang Wang, Yves Delannoy, Yves Fautrelle, and Olga Budenkova. Effect of diffusion length in modeling of equiaxed dendritic solidification under buoyancy flow in a configuration of hebditch–hunt experiment. *Metallurgical and Materials Transactions B*, 50(6):3039–3054, 2019.

[135] Charles-André Gandin, Hervé Combeau, Miha Založnik, Michel Bellet, et al. Finite element multi-scale modeling of chemical segregation in steel solidification taking into account the transport of equiaxed grains. *Metallurgical and Materials Transactions A*, 49(5):1725–1748, 2018.

[136] Akash Pakanati, Mohammed M'hamdi, Hervé Combeau, and Miha Založnik. Investigation of macrosegregation formation in aluminium dc casting for different alloy systems. *Metallurgical and Materials Transactions A*, 49(10):4710–4721, 2018.

[137] MC Schneider, JP Gu, C Beckermann, WJ Boettinger, and UR Kattner. Modeling of micro-and macroseg-regation and freckle formation in single-crystal nickel-base superalloy directional solidification. *Metal-lurgical and Materials Transactions A*, 28(7):1517–1531, 1997.

[138] O Hunziker. Theory of plane front and dendritic growth in multicomponent alloys. *Acta materialia*, 49(20):4191–4203, 2001.

[139] Xinyan Yan, Fanyou Xie, M Chu, and Y.A Chang. Microsegregation in al–4.5cu wt.% alloy: experimental investigation and numerical modeling. *Materials Science and Engineering: A*, 302(2):268 − 274, 2001.

[140] X. Yan, S. Chen, F. Xie, and Y.A. Chang. Computational and experimental investigation of microsegrega-tion in an al-rich al–cu–mg–si quaternary alloy. *Acta Materialia*, 50(9):2199 − 2207, 2002. Computational Thermodynamics and Materials Design.

[141] A Jacot and M Rappaz. A pseudo-front tracking technique for the modelling of solidification microstruc-tures in multi-component alloys. *Acta Materialia*, 50(8):1909–1926, 2002.

[142] Qing Chen, Anders Engström, Lars Höglund, Henrik Strandlund, and Bo Sundman. Thermo-calc pro-gram interface and their applications-direct insertion of thermodynamic and kinetic data into mod-elling of materials processing, structure and property. In *Materials Science Forum*, volume 475, pages 3145–3148. Trans Tech Publ, 2005.

[143] Hongwei Zhang, Charles-André Gandin, Haithem Ben Hamouda, Damien Tourret, Keiji Nakajima, and Jicheng He. Prediction of solidification paths for fe–c–cr alloys by a multiphase segregation model cou-pled to thermodynamic equilibrium calculations. *ISIJ international*, 50(12):1859–1866, 2010.

[144] Q Du, DG Eskin, and L Katgerman. Modeling macrosegregation during direct-chill casting of multicom-ponent aluminum alloys. *Metallurgical and materials transactions A*, 38(1):180–189, 2007.

[145] Ali Saad, Charles-André Gandin, and Michel Bellet. Temperature-based energy solver coupled with tabulated thermodynamic properties–application to the prediction of macrosegregation in multicom-ponent alloys. *Computational Materials Science*, 99:221–231, 2015.

[146] W. S. McCulloch and W. Pitts. A logical calculus of the ideas immanent in nervous activity. *The bulletin of mathematical biophysics*, pages 115–133, 1943.

[147] N Haghdadi, A Zarei-Hanzaki, AR Khalesian, and HR Abedi. Artificial neural network modeling to pre-dict the hot deformation behavior of an a356 aluminum alloy. *Materials & Design*, 49:386–391, 2013.

[148] Ying Han, Guanjun Qiao, JiaPeng Sun, and Dening Zou. A comparative study on constitutive relation-ship of as-cast 904l austenitic stainless steel during hot deformation based on arrhenius-type and arti-ficial neural network models. *Computational Materials Science*, 67:93–103, 2013.

[149] S Krajewski and J Nowacki. Dual-phase steels microstructure and properties consideration based on artificial intelligence techniques. *Archives of Civil and Mechanical Engineering*, 14(2):278–286, 2014.

[150] Jiapeng Sun, Liang Fang, and Jing Han. Optimization of concrete hollow brick using hybrid genetic al-gorithm combining with artificial neural networks. *International Journal of Heat and Mass Transfer*, 53(23-24):5509–5518, 2010.

[151] Cross-validation: evaluating estimator performance. `https://scikit-learn.org/stable/modules/cross_validation.html`. Accessed: 2021-10-29.

[152] Mlpregressor: Neural network module of sklearn. `https://https://scikit-learn.org/stable/modules/generated/sklearn.neural_network.MLPRegressor.html`. Accessed: 2021-15-29.

[153] Gildas Guillemot, Ch-A Gandin, Hervé Combeau, and Romulo Heringer. A new cellular automaton—finite element coupling scheme for alloy solidification. *Modelling and Simulation in Materials Science and Engineering*, 12(3):545, 2004.

[154] Tommy Carozzani, Hugues Digonnet, and Ch-A Gandin. 3d cafe modeling of grain structures: application to primary dendritic and secondary eutectic solidification. *Modelling and Simulation in Materials Science and Engineering*, 20(1):015010, 2011.

[155] DJ Hebditch and JD Hunt. Observations of ingot macrosegregation on model systems. *Metallurgical transactions*, 5(7):1557–1564, 1974.

[156] Miha Založnik, Arvind Kumar, and Hervé Combeau. An operator splitting scheme for coupling macroscopic transport and grain growth in a two-phase multiscale solidification model: Part ii − application of the model. *Computational Materials Science*, 48(1):11–21, 2010.

[157] Nasir Ahmad, J Rappaz, J-L Desbiolles, Tuomas Jalanti, M Rappaz, H Combeau, G Lesoult, and Christian Stomp. Numerical simulation of macrosegregation: a comparison between finite volume method and finite element method predictions and a confrontation with experiments. *Metallurgical and Materials Transactions A*, 29(2):617–630, 1998.

[158] Miha Založnikand Arvind Kumar and Hervé Combeau. An operator splitting scheme for coupling macroscopic transport and grain growth in a two-phase multiscale solidification model: Part ii − application of the model. *Computational Materials Science*, 48(1):11 − 21, 2010.

[159] David R Poirier and P Nandapurkar. Enthalpies of a binary alloy during solidification. *Metallurgical Transactions A*, 19(12):3057–3061, 1988.

[160] Jyrki Miettinen. Calculation of solidification-related thermophysical properties for steels. *Metallurgical and materials transactions B*, 28(2):281–297, 1997.

[161] Benjamin Gerin, Hervé Combeau, Miha Založnik, Isabelle Poitrault, Maya Cherif, Laurent Carroz, Matthieu Morel, and Chantal David. Prediction of solidification structure in 4.2t steel ingot, 2021.

[162] Itsuo OHNAKA, Tatsuichi FUKUSAKO, and Kiyoaki NISHIKAWA. Solidification analysis of steel ingots with consideration of fluid flow. *Tetsu-to-Hagane*, 67(3):547–556, 1981.

[163] Hervé Combeau, Arvind Kumar, Miha Založnik, Isabelle Poitrault, Gilbert Lacagne, Andrew Gingell, Thierry Mazet, and Gérard Lesoult. Macrosegregation prediction in a 65 ton steel ingot. In *1st International Conference on Ingot Casting, Rolling and Forging, Aachen, Germany, Brüssel-Saal, Ingot Casting-Simultion, June*, 2012.

[164] M M'Hamdi, H Combeau, and G Lesoult. Modelling of heat transfer coupled with columnar dendritic growth in continuous casting of steel. *International Journal of Numerical Methods for Heat & Fluid Flow*, 1999.

[165] Jun Li, Menghuai Wu, Andreas Ludwig, and Abdellah Kharicha. Modelling macrosegregation in a 2.45 ton steel ingot. In *IOP Conference Series: Materials Science and Engineering*, volume 33, page 012091. IOP Publishing, 2012.

[166] Jun Li, Honghao Ge, Bin Wang, Menghuai Wu, and Jianguo Li. Numerical simulation of multi-mini-pot pouring process of a 13-ton steel ingot. In *IOP Conference Series: Materials Science and Engineering*, volume 84, page 012009. IOP Publishing, 2015.

[167] Yanfei Cao, Dianzhong Li, Xing-Qiu Chen, Chen Liu, Yun Chen, Paixian Fu, Hongwei Liu, Xiaoping Ma, Yang Liu, Yikun Luan, et al. Inducing mechanism and model of the critical oxygen content in homogenized steel. *Materials & Design*, 205:109723, 2021.

[168] YA Meng and Brian G Thomas. Heat-transfer and solidification model of continuous slab casting: Con1d. *Metallurgical and materials transactions B*, 34(5):685–705, 2003.

[169] Baoguang Sang, Xiuhong Kang, and Dianzhong Li. A novel technique for reducing macrosegregation in heavy steel ingots. *Journal of Materials Processing Technology*, 210(4):703–711, 2010.

[170] Marc C Schneider and Christoph Beckermann. Simulation of micro-/macrosegregation during the solidification of a low-alloy steel. *ISIJ international*, 35(6):665–672, 1995.

[171] Chunping Zhang, Mohammad Jahazi, and Paloma Isabel Gallego. On the impact of microsegregation model on the thermophysical and solidification behaviors of a large size steel ingot. *Metals*, 10(1):74, 2020.

[172] Benjamin Gerin, Hervé Combeau, Miha Založnik, Isabelle Poitrault, and Maya Cherif. Prediction of solidification structures in a 9.8 tonne steel ingot. In *IOP Conference Series: Materials Science and Engineering*, volume 861, page 012032. IOP Publishing, 2020.

[173] KO Tveito, M Bedel, Miha Založnik, H Combeau, and M M'Hamdi. The effect of finite microscopic liquid solute diffusion on macrosegregation formation. In *IOP Conference Series: Materials Science and Engineering*, volume 27, page 012040. IOP Publishing, 2012.

Abstract

The present work aims at refining existing models in SOLID® by developing capabilities for improved prediction of the solidification process. Multiphase solidification models incorporate transport equations, which are closed by interphase transfer terms that are governed by microscopic constitutive relationships. These analytical relationships rely on the accurate representation of the microstructural phenomena such as the grain morphology and solute profile in the phases, along with the assumptions of diffusion-controlled solidification with thermodynamic equilibria at the solid-liquid interfaces. This work focuses on two aspects: i) coupling solidification model with the thermodynamics of multicomponent alloys and ii) incorporating a new liquid diffusion length model for improved prediction of solute profile in the liquid phase. A methodology is proposed for incorporating phase diagram data into multiphase volume average solidification models. Previous instances of coupling the model with thermodynamic software packages include direct coupling with the software and a tabulation and interpolation technique. Direct coupling is time-consuming, whereas the tabulation approach becomes infeasible with increasing number of components in the system. We present a novel approach of using Artificial Neural Networks - Multi-layer perceptron (ANN-MLP) on tabulated thermodynamic data to obtain regression relationships, which can be easily coupled with the solidification model. This approach is computationally much more efficient than the above mentioned methods. The coupling procedure is described and validated with Thermo-Calc® Scheil solidification. Further simulations were performed on the Hebditch & Hunt benchmark case as well as an industrial ingot. Results obtained from the model, while improving the segregation prediction, also highlight the critical phase diagram parameters which help us propose modified values of these parameters for simulations which assume them to be constant. Secondly, the liquid diffusion length relationship proposed by Martorano *et al.* was extended to account for liquid convection. Simulation of the industrial ingot with the new diffusion length relationship shows significant impact on the grain size and grain morphology.

Keywords: Solidification, numerical modeling, Thermo-Calc®, artificial neural networks, liquid diffusion length

Résumé

Le présent travail vise à affiner les modèles existants dans SOLID® pour une meilleure prédiction des macroségrégations et des structures de solidification. Les modèles de solidification mis en œuvre dans le code SOLID sont multiphasiques et multiéchelles. Les équations de transport qui le constituent sont fermées par des termes de transfert interphase régis par des relations constitutives microscopiques. Ces termes de transfert interphase reposent sur la représentation aussi précise que possible des phénomènes microstructuraux tels que la morphologie des grains,le profil des solutés dans les phases, et les équilibres thermodynamiques aux interfaces solide-liquide. Ce travail se concentre sur deux aspects : i) le couplage du modèle de solidification avec la thermodynamique des alliages multiconstitués et ii) l'incorporation d'un nouveau modèle de longueur de diffusion pour la phase liquide intervenant dans les termes de transfert interphase. Une méthodologie est proposée pour incorporer les données du diagramme de phase dans le modèle de solidification du code SOLID. Les exemples présents dans le littérature concernant le couplage d'un modèle de solidification avec des progiciels thermodynamiques (de type CALPHAD) ont été réalisé en considérant : soit le couplage direct entre les logiciels, soit une technique de tabulation permettant ensuite le calculs des grandeurs thermodynamiques par interpolation. Le couplage direct prend beaucoup de temps, tandis que l'approche par tabulation devient impossibleavec l'augmentation du nombre de constituants de l'alliage. Nous présentons une nouvelle approche consistant à mettre en oeuvre des réseaux de neurones pour obtenir à partir de données thermodynamiques issus de codes de type CALPHAD, des relations de régression. Ces relations de régression peuvent ensuite être facilement couplées à un modèle de solidification de type de celui implémenté dans le code SOLID. Cette approche est beaucoup plus efficace sur le plan informatique que les méthodes mentionnées ci-dessus. La procédure de couplage est décrite et validée à partir de comparaisons avec des calculs CALPHAD sur des cas simples de solidification. D'autres simulations ont été effectuées sur le cas de référence Hebditch & Hunt ainsi que sur un lingot industriel. Les résultats obtenus par le modèle, tout en améliorant la prédiction de la ségrégation, mettent également en évidence les paramètres critiques du diagramme de phase, ce qui nous permet de proposer des valeurs modifiées de ces paramètres pour les simulations qui les supposent constants. Deuxièmement, la relation de longueur de diffusion dans la phase liquide proposée par Martorano *et al.* a été étendue pour tenir compte de la convection de la phase liquide. La simulation du lingot industriel avec cette nouvelle relation de longueur de diffusion montre un impact significatif sur la taille et la morphologie des grains.

Mots-clés: Solidification, modélisation numérique, Thermo-Calc®, réseau de neurone, modélisation multi-échelle, multiphysique